Intermetallic Phase Selection in Dilute Al-Fe-Si alloys

Steven James Maggs

Submitted in accordance with the requirements for the degree of Ph.D

The University of Leeds, School of Materials

January 1996

The candidate confirms that the work submitted is his own and that appropriate credit has been given where reference has been made to the work of others.

Intermetallic Phase Selection in Dilute Al-Fe-Si Alloys

S.J.Maggs

The DC casting of 1000 series Al-Fe-Si alloys often results in the formation of a defect known as the Fir Tree Zone (FTZ) caused by variations in the type of binary Al-Fe eutectic intermetallic phase. These include Al_3Fe, which is the equilibrium phase, and Al_6Fe, Al_mFe and Al_xFe which are all common metastable phases found in DC cast ingots. Variation in the solidification conditions across a DC cast ingot, in particular, the cooling rate and local solidification velocity, bring about transitions from one intermetallic phase to another. The composition of the alloy, especially the presence of minor trace elements is also known to affect the transitions, but its effect has been less well studied.

Equipment was constructed which reliably simulated DC casting conditions and enabled the FTZ to be reproduced. Experiments were conducted to examine the effect of the concentration of Fe, Si (and Fe:Si ratio) and of low levels (<0.04 wt %) of Mg, Ti, Ti-B, V and Mn on the occurrence of phases causing the defect. Intermetallic phases extracted from the matrix by dissolution in hot butanol were identified by XRD. It was found that presence of Ti-B grain refiner had a large effect on the intermetallic phase selection, whilst the other trace element additions had lesser effects. In order to understand the way in which each element was affecting phase selection, experiments were conducted using DSC and a Bridgman furnace to isolate the variables of cooling rate and growth velocity respectively. A curve fitting technique was used to obtain values of eutectic nucleation onset temperature from DSC data where the primary aluminium and eutectic peaks overlapped. A technique was developed to extract intermetallic particles from DSC samples for examination in the TEM.

It was found that the addition Ti-B grain refiner affected the phase selection by altering the nucleation temperature. The addition of Mg was found to stabilise the equilibrium phase by its affect on both growth temperature and nucleation temperature The effect of Ti was less clear in that it stabilised the equilibrium phase in the DSC experiments but tended to stabilise the metastable phase in the Bridgman experiments.

Acknowledgments

Table of Contents

List of Figures appearing at the end of each chapter

Chapter 5

1.0 Introduction

Aluminium lithographic sheet is used in the printing industry for large scale printing operations. The alloy used for this type of sheet is a high quality 1050 alloy, the main alloying elements being approximately 0.25 wt. % Si and 0.40 wt. % Fe. Similar alloys are used for architectural cladding and other applications requiring a good surface finish and/or colouring. The composition limits of this series of alloys are shown in table 1.01.

Element	Fe	Si	Cu	Mn	Mg	Zn	Ti	Cr,V,Li
wt. %	0.40	0.25	0.05	0.05	0.05	0.07	0.05	<0.03

Table 1.01: Chemical composition limits for 1050 aluminium alloy [1].

As an introduction to the problems encountered by some users of this type of sheet alloy, the process used to make lithographic printing sheet will be described briefly. Similar processes are used for preparing and colouring architectural cladding and other components requiring colour.

The sheet alloy is cast using the Direct Chill (DC) casting process (which will be described in some detail later), then homogenised, hot rolled to 3.5 mm and finally cold rolled to 0.3 mm. The sheet is then cleaned prior to delivery to the customer. On delivery, the customer then puts it through various processing stages. The sheet is cleaned and then electrograined by passing the sheet through a bath in which it is pitted electrolytically by the passage of an alternating current. The aim is to produce a uniform coverage of a distribution of pit sizes. After electrograining, an oxide film is deposited on to the pitted surface by anodising in a sulphuric or phosphoric acid bath. This oxide film evenly coats the pitted surface but does not change its topography. The sheet is then coated with a phosphate layer by passage through a phosphating bath. This phosphate layer affects the wetting and adhesion properties of the surface which is then coated with an ultra-violet (UV) light sensitive layer of photoresist polymer. The sheet is then chopped to size and sent to the printer.

At the printer the sheets are exposed to UV light through a negative or positive mask which causes the photoresist exposed to the UV light to harden. The unexposed photoresist is then washed away and the sheet is heated in an oven to strengthen the remaining photoresist. The sheet is now ready for printing. The lithographic printing process exploits the propensity of grease-based inks to adhere to areas where the photoresist is

retained and of water-based inks to adhere to those areas denuded of the photoresist. The surface quality of the rolled aluminium alloy sheet before any processing has taken place is, therefore, of paramount importance as any surface defects which exist in the sheet are likely to affect the quality of the finished product. If, for example, the anodising response of the sheet were affected by the surface properties of the 'as-rolled' sheet then the areas of sheet unexposed to the UV light and thus bare of photoresist would also be affected. This is, in fact, what happens in practice when the as-cast ingot contains a defect known as the Fir Tree Zone (FTZ). This defect is known to be caused by certain solidification conditions in the DC casting process [2,3,4] and is such that it will still manifest itself in the rolled and treated product.

The problem of the FTZ forms the basis of this work. The DC casting process is at the root of the problem and where its solution lies. It will now be described in some detail.

1.01   The Direct Chill (DC) Casting process.

All sheet ingot produced in Europe and the majority produced elsewhere is semi-continuously cast using the Direct Chill (DC) casting method. In this technique molten alloy is poured onto a starter block in a water chilled mould (see figure 1.01). As the ingot solidifies it is withdrawn from below. A skin or shell of solidified metal forms on contact with the chilled mould surface and a sump of liquid metal forms inside the ingot. This is cooled by the direct chill water curtain below the mould. The ingot, typically, has a rectangular cross section having dimensions of 600 mm by 1350 mm and varies in length, depending on the producer, from around 6 m up to 11 m. Circular cross-section DC cast ingots are also produced for extrusion billets and sometimes contain the FTZ. This study will concentrate on alloys used for the rectangular sheet ingots intended for rolling.

1.01.1 Solidification in the DC Cast Ingot

During casting there are two ways by which the cooling occurs, the cooling inside the mould and the secondary cooling of the direct chill water curtain outside the mould; hence two microstructurally distinct regions are formed in the ingot.

The first of these is the shell zone. The shell zone is the part of the ingot which has been solidified, initially by direct contact with the mould wall, and then, as solidification shrinkage pulls the ingot away from the mould, by air cooling (see figure 1.02). The extraction of heat by conduction through the mould wall and via air cooling is less efficient

than by water cooling. The cooling rate in the shell is, therefore, lower than in the next zone immediately adjacent to the shell. This was shown by Westengen [5] who determined the variation in cooling rate and cell size as a function of the distance from the ingot edge(figure 1.03). The solidification shrinkage which pulls the solidified shell away from the mould wall can produce defects in the ingot surface such as 'bleed blands' and cold shuts. Consequently, process parameters, in particular casting rate, are tightly controlled. When a surface of a product is important, such as in sheet used for applications where anodising is necessary, the shell is removed entirely by scalping the surface before rolling takes place. The shell does, however, play a role in the determination of the microstructure of the main body of the ingot, which is of interest in this study

The solidification behaviour and the resulting microstructure of the main body of the DC cast ingot can be better understood by considering the way in which the heat is extracted. Two types of heat must be extracted from a liquid for it to solidify: the superheat and the latent heat. The heat flow is limited and therefore so is the rate of solidification. The solid/liquid interface sweeps through the liquid at an ever decreasing rate. The distance travelled by the interface, d, is proportional to the square root of time, t, :- $d \propto t^{1/2}$. The local grain structure is determined by the local rate of interface advance. Partition of solute ahead of the interface can lead to constitutional supercooling and the nucleation of grains ahead of the interface. Alloying and the addition of grain refiners can be used to control these two effects.

The two main factors which determine the microstructures found on solidification are the composition of the liquid metal (including grain refiners) and the local solidification rate. The latter depends on heat extraction rate which is, in turn, dependent on the casting parameters: the effectiveness of the chill, the casting speed and the ingot dimensions. If a simple bar of metal is solidified from one end using a chill, the grain structure will be fine and equiaxed at the chill, followed by a columnar region parallel to the direction of heat extraction and finally a coarse, equiaxed zone furthest from the chill. The dendrite arm spacing and size of the interdendritic particles increase with distance away from the chill. This is a crude model of what occurs in the DC cast ingot. In reality heat is extracted in, not one, but three dimensions and the interface is not parallel with the mould walls but is curved. This is illustrated figure 1.04 which shows a series of metal bars solidified unidirectionally The bars show the interface advance after a fixed time has passed. The rate of interface advances with the square root of time but the ingot is lowered at a constant rate. The

interface assumes an approximate parabolic shape as shown in the diagram. The favoured growth direction is perpendicular to the local interface and therefore changes with distance from the chilled surface. The interface in a pure aluminium ingot would be macroscopically smooth, defining the 660°C isotherm. When alloyed there is no longer a smooth interface as the solidification occurs over a temperature range and a mushy zone several millimetres wide is seen. This zone is part liquid and part solid and the concept of a macroscopically smooth interface is no longer valid. This is especially true near the centre line of the ingot where a mush of floating crystals is found. The last liquid to solidify in the ingot does so from a mush of floating crystals and solute-rich liquid. This area can be microstructurally coarse and segregation effects can easily be observed. The interface takes a finite time to pass from the edge to the centre of the ingot and a liquid sump forms as a result. The sump can vary in depth and can be up to a metre deep. Sump depth can be controlled in two ways; by varying the casting speed and by varying the ingot thickness.

The most common way to eliminate the structural variations mentioned above is to use grain refiner. This suppresses columnar growth and increases the randomness of the structure by supplying many nucleation sites. Grains nucleate ahead of the interface and grow possessing no preferred orientation. The increased number of grains restricts their size thus reducing the average grain size. The most commonly used grain refiner for most commercial aluminium alloys is a titanium and boron mixture (proportions vary but 5Ti:1B is not untypical). The grain refiner is added as a pre-alloyed bar of aluminium and known proportions of Ti and B.

1.02   The Fir Tree Zone.

If a vertical section of a DC cast ingot is caustically etched or anodised in dilute H_2SO_4 it will sometimes show a pattern of light and dark regions called the Fir Tree Zone. The transition between the light and dark areas is macroscopically distinct and the pattern looks, typically, like the silhouette of a fir tree, see figure 1.05. The defect can result in the patchy appearance of sheet after anodising and surface treatments and poor quality anodised products. Sheet containing the defect is usually deemed unacceptable for lithographic sheet.

The defect shows up on the surface when the ingot has been scalped in the intermediate zone between the fir tree 'branches'. It is therefore desirable to alter the casting practice so that the FTZ is either driven out to the surface of the ingot or closer to the centre. This is most commonly done by changing the casting rate (the rate at which the ingot

is withdrawn from the mould). The effect of lowering the casting rate is to force the FTZ out to the surface and this has proven to be the most reliable method of overcoming the problem. This is not entirely satisfactory, however, as it slows down the overall rate of ingot production. Increasing the casting rate can also solve the problem by pushing the boundary in towards the centre of the ingot, but causes other defects on the surface of the ingot.

The FTZ is known to be a direct result of the variation in solidification conditions across the ingot. The change in cooling rate and associated change in local solidification velocity cause the type of binary Al-Fe eutectic intermetallic to change. The binary phase, Al_3Fe, forms under near equilibrium cooling conditions as the intermetallic phase in the interdendritic eutectic. At higher cooling rates it is possible for other, metastable, binary phases to form. The common binary metastable phases formed in DC casting are Al_6Fe and Al_mFe [6] and, reported more recently, Al_xFe [7,8]. The transition from one type of binary intermetallic phase to another at different positions in the ingot causes the FTZ defect.

Phase	Bravais Lattice/ Point Group	Lattice constants	Density /Mg m^{-1}	References
Al_3Fe $Al_{19}Fe_6$ $Al_{13}Fe_4$ Al_7Fe_2	monoclinic c2/m	a= 1.549 nm b= 0,808 nm c= 1.245 nm β= 107.75°	3.8	16,17,18,19
Al_mFe m=4-4.4	I$_4$mm or I$_4$/mmm	a= 0.884 nm c=2.106nm		5,20,21,22,23,24,25
Al_xFe x=5-5.8	monoclinic (?)	a=2.160 nm b=0.930 nm c= 0.879 nm		5,6,8,22
Al_6Fe	orthorhombic Ccmm or Ccm2	a= 0.649 nm b=0.744 nm c= 0.879 nm	3.45	26,27,28,29
Al_bFe	bcc	a=1.03 nm		11
Al_3Fe_2	monoclinic	a= 0.890 nm b=0.635 nm c= 0.632 nm β= 93.40°		30,31

Table 1.02 Crystallographic data for binary phases found in the Al-Fe and Al-Fe-Si system.

The variation in cooling rate is not simply a steady reduction with distance from the ingot edge. Molten metal poured into the DC mould comes immediately in contact with the mould walls and is cooled rapidly. This cooling is dependent on the contact between the solidified ingot and the mould wall. As the ingot pulls away from the mould wall due to solidification shrinkage, the physical contact is lost and the cooling rate becomes relatively

low due to the poor thermal conduction of the air gap. After some time, depending on the casting rate, the ingot surface comes into contact with the water spray and the cooling rate rises rapidly. The cooling rate then steadily decreases as solidification front moves towards the centre of the ingot and the heat must be conducted away through more and more solid. The varying cooling rate brings about changes in the type of eutectic binary intermetallic phase. The slowest cooling rates result in Al_3Fe, the highest in Al_mFe and the intermediate in Al_6Fe [9]. Al_3Fe is reported to form at intermediate cooling rates from close to the upper limit for Al_3Fe to just above the lower limit for Al_6Fe[8].

One of the major factors which affects the FTZ, other than solidification conditions is the composition of the alloy itself. The composition of the alloys can be varied in different ways to affect the FTZ. The levels of Fe and Si and, in particular, the iron to silicon ratio (Fe:Si) influence the FTZ [3,4,5,10,11], as does the level of some elements at trace levels [12,13,14] and the addition of grain refiner in the form of Ti and Ti-B hardener [14].

Before the factors affecting the FTZ are examined, the physical characteristics and solidification behaviour of the various binary and ternary phases in the Al-Fe-Si system which are known to be involved will be presented. Tables 1.02 and 1.03 show the crystallography of the binary and ternary phases; figure 1.06 shows schematically the compositional limits of some of the major phases.

1.03   Binary Aluminium Iron Phases

The binary phases described below are those which form the intermetallic phase of the eutectics which solidify in dilute Al-Fe (-Si) alloys such as the 1050 series. Iron is one the main impurity elements in these aluminium alloys and most of it is found in secondary particles due to its relatively limited solubility in aluminium (the equilibrium partition coefficient 0.027 [15]). The first solid to crystallise from the molten metal in Al-Fe alloys is primary α-aluminium; a solid solution of iron atoms in aluminium. This grows dendritically under normal solidification conditions and rejects the solute Fe atoms ahead of the solidification interface. When the liquid reaches the eutectic composition it transforms into a eutectic comprising primary aluminium coupled with an intermetallic Al-Fe phase. The nature of the eutectic depends strongly on the solidification conditions. Slow cooling results in the formation of the equilibrium $Al-Al_3Fe$ eutectic. Non-equilibrium, fast cooling allows metastable eutectic intermetallics to grow in preference to $Al-Al_3Fe$.

1.03.1 Al₃Fe

The aluminium rich corner of the Al-Fe phase equilibrium diagram is shown in figure 1.07 [32]. Aluminium has an FCC structure and a lattice parameter 0.4049 nm. The equilibrium maximum solid solubility of Fe in Al is 0.04 wt. %. The equilibrium eutectic reaction (L - α-Al + Al₃Fe) occurs at 655°C and 1.8 wt. % [33]. Al₃Fe has also been reported as Al₂₃Fe₇ and Al₁₉Fe₆ [32] and Al₁₃Fe₄ [18] but the generally accepted formula, and the one which will be used herein, is Al₃Fe. The Bravais lattice, lattice parameters and density of Al₃Fe are shown in table 1.02. Liu and Dunlop [34] found the following 3 orientation relationships between α-Al and Al₃Fe.

OR I

(200)$_{Al_3Fe}$ ‖(200) $_{Al}$

(010)$_{Al_3Fe}$ ‖(010) $_{Al}$

[001]$_{Al_3Fe}$ ‖[001] $_{Al}$

OR II

(100)$_{Al_3Fe}$ ‖(100) $_{Al}$

(020)$_{Al_3Fe}$ ‖(020) $_{Al}$

[001]$_{Al_3Fe}$ ‖[002] $_{Al}$

OR III

(100)$_{Al_3Fe}$ ‖(10 $\bar{1}$)$_{Al}$

(020)$_{Al_3Fe}$ ‖(020) $_{Al}$

[001]$_{Al_3Fe}$ ‖[202]$_{Al}$
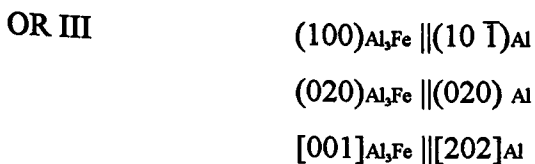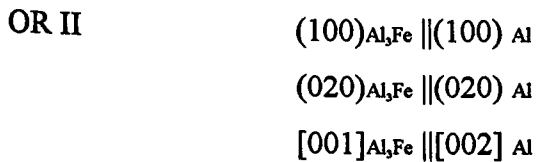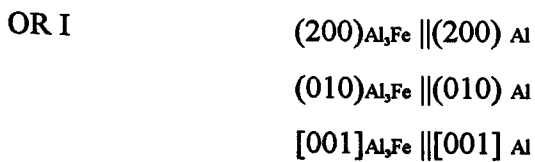
The eutectic grows as plates in a continuous aluminium matrix, the unit cell of Al₃Fe containing 100 atoms [32]. Adam and Hogan [35] examined the effects of growth rate and temperature gradient on the solidification morphology of directionally solidified high purity Al-Fe alloys and stated that Al₃Fe exhibits no consistent interphase interfaces with the aluminium and is considered to be an anomalous eutectic. The morphology of the eutectic was reported to vary with imposed growth rate (U) and temperature gradient (G). At high values of G/U the eutectic grew as alternating lamellae of Al and Al₃Fe. As the ratio drops, the Al₃Fe in the eutectic became more and more branched. The increase in branching was influenced by both G and U but it was found that G exerted the strongest influence. Both the interparticle spacings and the length to breadth ratios of the particles (viewed on transverse sections) decreased with an increase in U, this effect being mostly independent

of G.

Adam and Hogan [33] proposed the following relationship between interphase spacing, λ, and imposed growth rate for the Al-Al$_3$Fe eutectic. :

$$\lambda^{2.6}U = 3180 \ (\mu m^{3.6}/ \ sec \ )$$ 1.01

1.03.2 Al$_6$Fe

It has been reported [13,36] that considerable undercoolings are required for the nucleation of Al$_3$Fe on primary Al. As a result, metastable binary phases may frequently form in preference to Al$_3$Fe when the cooling rate or solidification rate is increased. The most commonly reported metastable phase is Al$_6$Fe. The eutectic reaction (L - α–Al + Al$_6$Fe) occurs at 650°C and at 3.5 wt. % Fe [33]. The Bravais lattice, lattice parameters and density are shown in table 1.02. The unit cell of Al$_6$Fe contains 28 atoms [16].

The eutectic grows with the Al$_6$Fe forming rods with [001] parallel to the imposed direction of growth and is considered to be a normal eutectic. Adam and Hogan proposed the following relationship between the interphase spacing and solidification rate for the Al-Al$_6$Fe eutectic-

$$\lambda^2 U = 10.2 \ (\mu m^{3}/ \ sec \ )$$ 1.02

The following unique orientation relationship between Al and the Al$_6$Fe was reported .

$(\bar{1}00)_{Al_6Fe} \ \| \ (\bar{1}11)_{Al}$

$(130)_{Al_6Fe} \ \| \ (\bar{1}1\bar{1})_{Al}$

$(3\bar{1}0)_{Al_6Fe} \ \| \ (002)_{Al}$

$[001]_{Al_6Fe} \ \| \ [001]_{Al} \ \| \ \text{Growth direction}$

The interphase interface is a low energy partially coherent one [35]

1.03.3 Al$_m$Fe

Another metastable eutectic intermetallic has been reported to form at higher cooling rates than those when Al$_3$Fe and Al$_6$Fe are found. The body centred tetragonal binary phase, Al$_m$Fe (where m $\approx$ 4.4) was first reported by Japanese workers [37]. The physical characteristics of this phase are shown in table 1.01. It is reported to have 118 atoms in each unit cell [23] and to possess a heavily faulted crystal structure [24]. Its morphology was reported to be 'dendrite-like' in samples extracted from a commercial purity DC cast alloy. Al$_m$Fe can contain as much as 3 wt. % Si whereas Al$_6$Fe can accommodate less than 0.5 wt.

% [15] (see figure 1.06).

1.03.4 Al_xFe

The formation of an intermediate phase at intermediate cooling rates between those where formation of Al_3Fe and Al_6Fe is expected was reported by Clyne and Young [8] in controlled velocity Bridgman growth experiments and by Westengen [7] from the examination of commercially cast DC ingots. A monoclinic structure with $\beta=94^\circ$, $a=2.16nm$, $b=0.93nm$ and $c=0.905nm$ was proposed by Clyne and Young based on TEM analysis and XRD of rolled foils. A composition was proposed corresponding to a value of $x = 5$. Westengen had difficulty in indexing diffraction patterns from the phase and suggested that it has a heavily faulted structure. Skerpje [6] examined Al_xFe in commercially cast DC ingots and suggested a different structure (orthorhombic, $a=0.6nm$, $b=0.7nm$ and $c= 8.79nm$). and composition ($x = 5.7$) from that of Clyne and Young. He also suggested that the diffraction patterns analysed by Clyne and Young and by Westengen were not necessarily from the same phase. In the commercially cast Al- 0.25 wt. % Fe - 0.13 wt. % Si alloy examined by Skerpje, appreciable levels of Si and Ni were detected in Al_xFe suggesting that the structure was a modification of Al_xFe capable of accommodating more Si.

There are considerable differences in the nature of the phase usually termed Al_xFe. That there is a binary phase, commonly termed Al_xFe, which is seen at intermediate cooling rates (and/or solidification velocities) between Al_3Fe and Al_6Fe is certain but its stoichiometry and crystal structure are unclear.

1.03.5 Other Binary Phases

A binary phase with a bcc structure, Al_pFe ($p \approx 4.5$), was reported by Ping et al [11] to form in fast cooled Al-Fe-Si alloys but has not been reported elsewhere. Simensen et al reported the presence of another metastable phase Al_9Fe_2 [31]. The crystal structure of this metastable phase is listed in table 1.02. The alloy this phase was discovered in contained silicon and the conditions under which it formed are unclear.

Phase	Stoichiometric formulae	Bravais lattice	lattice parameters /nm	References
α	$Al_{12}Fe_3Si$ $Al_{15}Fe_3Si$ $Al_{11.3}Fe_3Si_{1.6}$ $Al_{10.9}Fe_3Si_{1.9}$ $Al_{12.7}Fe_3Si_{1.0}$ $Al_{12.9}Fe_3Si_2$	cubic Pm3 cubic (Im3)	a= 1.252 a=1.256	38,39,40, 32, 41
α'	$Al_{11.8}Fe_3Si_{1.7}$ $Al_{12}Fe_3Si_2$ Al_9Fe_2Si $Al_{12.6}Fe_3Si_{1.6}$ $Al_{12}Fe_3Si_2$	Hexagonal (P6$_3$/mmc)	a=1.23 c=2.62	38, 42,32, 43
α_v	$Al_9Fe_2Si_2$ $Al_{14.6}Fe_3Si_1$ $Al_{12.4}Fe_3Si_{2.1}$	monoclinic	a=0.869 b=0.635 c=0.632 β=93.4•	6,44
α'', q_1		c-centred orthorhombic	a=0.1.27 b=3.62 c=1.27	7,11,19
α_T		c-centred monoclinic	a=2.195 b=3.062 c=2.073 β=97.74•	6
β	$Al_9Fe_2Si_2$ Al_9FeSi $Al_{13}Fe_{3.6}$ $Al_{13.3}Fe_3Si_{3.7}$ $Al_{13.6}Fe_3Si_{3.4}$	monoclinic	a=0.612 b=0.612 c=4.16 α=91.0•	42,43,45
β'		monoclinic	a=0.890 b=0.490 c=4.16 b=92.0•	7,39
q_2		monoclinic	a=1.25 b=1.23 c=1.97 β=111•	11,19
γ	Al_3FeSi	c-centred monoclinic	a=1.78 b=1.025 c=0.890 β=132•	11,20
δ	Al_4FeSi_2	Tetragonal	a=0.614 c=0.948	6,42,43

Table 1.03 Crystallographic data for ternary intermetallic phases found in the Al-Fe-Si system.

1.04 Ternary Aluminium Iron Silicon Phases.

Silicon has a higher solid solubility in aluminium than that of iron and, therefore is not found in secondary intermetallic particles to the same degree. The main secondary

constituents of dilute Al-Fe-Si alloys are the binary Al-Fe phases. Excess Si is often accommodated within the Al-Fe binaries as well as in solid solution within the primary Al. The amount of silicon able to be accommodated varies from phase to phase. Figure 1.06 shows schematically how much Si each of the commonly found intermetallics can accommodate. However, in commercial alloys and under fast cooling conditions, ternary AlFeSi phases are not uncommon. The equilibrium ternary phases at the aluminium rich corner of the phase diagram (see figure 1.08) are usually termed α and β. Many metastable variations of these phases have been reported (table 1.03).

The liquidus projection of the aluminium-rich corner of the Al-Fe-Si phase equilibrium diagram is shown in figure 1.08. Apart from the binary monoclinic Al$_3$Fe, two ternary phases, hexagonal α' AlFeSi and monoclinic β-AlFeSi [11] are predicted under equilibrium solidification along with primary Al. These equilibrium phases dominate in slow cooled cast materials but, depending upon the exact composition and cooling rate a number of intermediate non-equilibrium phases can form [20]. The cubic α-AlFeSi metastable phase appears at sufficiently high cooling rates [6] and is stabilised by some trace elements, in particular Mn, Cr, Mo, V, W and Cu [20]. The lattice parameters, Bravais lattice and stoichiometric formula for these and other reported ternary α-AlFeSi phases are shown in table 1.03.

The β AlFeSi phase has also been reported in many different forms. β-Al-Fe-Si is relatively concentrated in Fe and Si and is rarely found in the dilute alloys which are the subject of this work. However, table 1.02 shows some of the data available on these together with phases termed γ and δ found in AlFeSi alloys.

1.05 Binary Al-Fe Phase Selection

The local solidification conditions vary considerably in a DC cast ingot and the dominant intermetallic phase which solidifies will vary accordingly. The important variables include alloy composition, cooling rate, solidification rate, temperature gradient across the solid liquid interface and ease of nucleation and growth of a particular phase. Much work has been conducted on quantifying the critical cooling rates required during solidification for the appearance of metastable phases. However, it will be shown that the critical parameter may not be the cooling rate itself but the local solidification velocity. The distinction depends on whether phase selection is based on the ability of a phase to nucleate at a higher temperature than others or its ability to grow faster for . a given interface

temperature. The nucleation temperature is governed by cooling rate whereas the growth temperature is governed by local solidification velocity. The rate of heat extraction controls the cooling rate *and* the local growth velocity. Therefore, if two phases can nucleate with equal ease at a given cooling rate then the local solidification velocity becomes the more important factor in phase selection. Thus, in order to understand phase selection in DC casting, it is necessary to consider the mechanisms of both nucleation and growth.

1.05.1 The Al-Al$_3$Fe to Al-Al$_6$Fe Eutectic Transition

The transition between Al-Al$_3$Fe and Al-Al$_6$Fe eutectics has been extensively studied. A fibrous eutectic, distinct from the plate-like equilibrium Al-Al$_3$Fe was first observed by Dix [26] in fast-cooled Al -1.7 wt. % Fe. Hollingsworth *et al.* [29] subsequently identified the intermetallic phase in this new eutectic as Al$_6$Fe in fast-cooled Al - 2 wt. % Fe. Al$_6$Fe was created by dropping 6mm diameter molten alloy droplets into water. The Al$_6$Fe was identified by the fact that the surface of the sample containing the Al$_6$Fe was black after anodising whereas the rest, containing the Al$_3$Fe, was essentially white. This method of identifying areas containing different phases by surface treatment is summarised in table 1.04. It is also a method of identifying the presence of the FTZ. Backerud [36], using an Al-1wt % Fe alloy, found that a cooling rate of 3.3 °C s^{-1} or less was needed for the Al-Al$_3$Fe eutectic to grow in the 655-650°C temperature range. A considerable undercooling was needed before the Al$_3$Fe would nucleate. It was suggested that the nucleation of Al$_3$Fe on α-Al is difficult and that the nucleation probably occurs on floating particulates in the melt. The Al-Al$_6$Fe eutectic grew at cooling rates in excess of 3.3 °C s^{-1} at temperatures less than 650°C and needed no detectable undercooling. There is good reason to suspect, therefore, that the Al$_6$Fe nucleates easily on the α-Al, probably due to the low energy partially coherent interface [35] between the α-Al and the Al$_6$Fe.

Intermetallic compound	Etching with 0.5 % aq. HF	Anodic oxidation in 15% H$_2$SO$_4$	Anodic oxidised film colour
Al$_3$Fe	Dark brown	oxidised	light grey
Al$_6$Fe	light brown	not oxidised	dark grey
Al$_m$Fe	dark brown	oxidised	light grey
α–Al Fe Si	colourless	oxidised	light grey
β–Al Fe Si	dark brown	not oxidised	grey

Table 1.04. Effect of HF etching and anodising on the oxide film colour in dilute Al-Fe-Si alloys. [13]

The critical cooling rate obtained by Backerud for the transition of the $Al-Al_3Fe$ eutectic to the $Al-Al_6Fe$ eutectic in an Al-1 wt. % Fe alloy is close to that obtained by Adam and Hogan [36].in an Al-2 wt. % Fe alloy (2.5°C s^{-1}) and by Japanese authors [9,46] in dilute Al-Fe and Al-Fe-Si alloys (1 to 2° C s^{-1}).Thus, in hypoeutectic alloys, the cooling rate at which the transition from the $Al-Al_3Fe$ eutectic to the $Al-Al_6Fe$ eutectic occurs is approximately 2°C s^{-1}. The variation between the recorded values is probably due to different measuring techniques and to slight differences in impurity levels which, as will be shown, can strongly affect the transition. In a hypereutectic Al-3.5 wt. % Fe alloy the value was found to be 11.6°C s^{-1}; furthermore the Fe content increased so did the cooling rate necessary to suppress primary Al_3Fe in favour of eutectic Al_6Fe [36].

The effect of the temperature gradient (G) and solidification velocity (U) on the transition was investigated by Adam and Hogan. They found that the transition was somewhat dependent on G but considerably more so on U. Relationships were determined between the interparticular spacings, λ and the solidification velocity for the two eutectics.

$Al-Al_6Fe$ $\qquad$ $\lambda^2 U = 10.2 \ (\mu m^3/s)$

$Al-Al_3Fe$ $\qquad$ $\lambda^{2.6} U = 3180 \ (\mu m^{3.6}/s)$

$\qquad$ λ = eutectic particle spacing (μm)

$\qquad$ U = solidification rate ($\mu m s^{-1}$).

The relationship for the $Al-Al_3Fe$ eutectic was similar to one found by Iglessis et al.[21] in an Al-0.4% Fe-0.13% Si alloy at cooling rate less than 3.3°Cs^{-1}.

In the relationship $\lambda^n U$ = constant, Tiller [47] proposed that for a value of n = 2 (as in the $Al-Al_6Fe$ eutectic) the rate determining process for growth is diffusion of the solute species at the interface. This relationship is satisfied by various eutectic systems whose growth, therefore, is controlled by diffusion. If, however, the value of n > 2 (as in the $Al-Al_3Fe$ eutectic and some other systems), it was proposed that the rate determining process for the growth of the eutectic phase is the atomic attachment kinetics. In this context the $Al-Al_3Fe$ can be considered the anomalous eutectic and the $Al-Al_6Fe$ the normal eutectic. The transition from $Al-Al_3Fe$ to $Al-Al_6Fe$ on increasing growth rate was attributed to the fact that the rigid, faceted growth mode of Al_3Fe hinders the adjustment of interphase spacing. $Al-Al_6Fe$ can easily accommodate increases by adjustment of spacing and, consequently, can grow at higher growth rates and become the stable growth form.

The critical value of U (above which no Al_3Fe grows) was found to be 100 μm s^{-1} for a 2 wt. % Fe alloy. Jones and Hughes [48] also found a value of 100 μm s^{-1} for the

transition velocity in alloys in the composition range 2 - 6 wt. % Fe. Furthermore they determined that the critical velocity for the change from the Al-Al$_3$Fe to Al-Al$_6$Fe eutectic was practically independent of Fe content (even in concentrated alloys containing primary Al$_3$Fe). The data were collected using a Bridgman directional solidification furnace with a temperature gradient of 20 °C mm^{-1}. This critical value of U was subsequently verified by further Bridgman furnace work on an Al-3.00 wt. % Fe alloy by Liang and Jones [49] who found a value of 110 μm s^{-1}. They measured the growth temperatures of both eutectics which obeyed a linear relationship with the square root of the growth velocity, see figure 1.09.By interpolation they determined the equilibrium eutectic temperatures to be 655.1 ± 0.1•C for the Al-Al$_3$Fe eutectic and 652.9 ± 0.2•C for the Al-Al$_6$Fe eutectic. These results are in good agreement with those from other studies [22].

1.05.2 The Al$_6$Fe to Al$_m$Fe Eutectic Transition

There is generally good agreement between the published values for the critical cooling rate for the Al-Al$_3$Fe to Al-Al$_6$Fe transition. The same, however, can not be said for the results for the Al-Al$_6$Fe to Al-Al$_m$Fe transition, although this has received rather less attention owing to the fact that Al$_m$Fe is a relatively newly discovered phase.

The body centred tetragonal binary phase Al$_m$Fe (m ≈ 4.4) was reported by Japanese workers to form at cooling rates in excess of 10° C s^{-1} [21] in Al - 0.6 wt. % Fe alloys solidified in wedge shaped moulds and 20 °C s^{-1} [37] in the same alloy using unidirectional solidification. However, Asami et al [50] stated that the transition from Al$_6$Fe to Al$_m$Fe occurred at cooling rates in excess of 35 °C s^{-1} in Al - 0.5 wt.% Fe. Brobak and Brusethaug [10] compared directionally solidified Al-Fe-Si alloys to DC cast alloys and found that although Al$_m$Fe was present (co-existing with other binary phases) at cooling rates as low as 1-2 °Cs^{-1} in DC cast commercial Al-Fe-Si alloys with Fe:Si ratios of 2 it was not present at similar cooling rates in the same alloys produced by directional solidification

It would appear that the critical cooling rate for the transition from Al-Al$_3$Fe to Al-Al$_6$Fe is rather sensitive to silicon concentration in Al-Fe-Si alloys.The limited evidence available suggests that the critical cooling rate is Raised by the presence of Si in these alloys. ·

1.05.3 The Al$_3$Fe to Al$_x$Fe Eutectic Transition

The transition from Al-Al$_3$Fe to Al-Al$_x$Fe was reported by Clyne and Young [8] to

be an intermediate stage in the transition from Al-Al$_3$Fe to Al-Al$_6$Fe in a hypoeutectic Al-0.5 wt. % Fe alloy. Furthermore, they state that Al$_x$Fe had been mistaken for Al$_6$Fe in previous studies due to their similar appearance. This intermediate transition was held responsible for the disparities between the values of critical cooling rate reported for the Al-Al$_3$Fe to Al-Al$_6$Fe. The Al-Al$_x$Fe eutectic was reported to grow in a cooling rate range of 0.5 to 5 K s^{-1} which overlaps the top end of the cooling rate regime for the Al-Al$_3$Fe eutectic and the bottom end of that for the Al-Al$_6$Fe eutectic. In a directionally solidified commercially pure alloy, Brobak and Brusethaug [10] also detected the formation of Al$_x$Fe at a cooling rate of 2.8 °C s^{-1} which falls within the range proposed by Clyne and Young.

However, Brusethaug [10], Westengen [5] and Skerpje [6] all detected Al$_x$Fe coexisting with Al$_3$Fe, Al$_6$Fe, and Al$_m$Fe in DC cast ingots of commercial purity aluminium. This coexistence is forbidden according to the criteria set out by Clyne and Young [8], which suggests that the presence of impurities in the alloy can change the cooling rate ranges over which the phases can form. This will be discussed in more detail later.

1.06   Intermetallic Phase Selection and the FTZ in Directionally Solidified and DC Cast Ingots

Alloys cast by the DC casting method are invariably for commercial use. These contain both alloy additions and impurities. The fact that the alloys are not simple Al-Fe binaries introduces complexity when trying to predict the intermetallic phases which will form. The most common way of describing the ingot's microstructure has been to take samples at set distances from the ingot surface and to identify the phases present. This is then usually related to the cooling rate at that point inferred from the dendrite arm spacing. In these complex alloys phase transitions between different intermetallics are not as simple to understand as in the simple binary alloys . There is often more than one phase present at a particular distance from the ingot surface and one or sometimes two of the phases tend to be dominant. The composition of the alloy is thought to allow the coexistence of multiple phases locally: iron to silicon ratio, the presence of impurities at very low levels and the addition of Ti or Ti-B grain refiner at different levels can affect both the intermetallic phases formed and the size and nature of the fir tree zone.

It is not always possible to carry out experiments using full scale DC casting equipment due to the costs involved and the availability of equipment. Thus many workers have used purpose built directional solidification equipment which simulates DC casting to

investigate intermetallic phase selection and the origin of the FTZ [4,12,14,21,46].

Prior to a detailed discussion of this work, the terminology used in describing the FTZ needs to be defined. Many authors use different terms to describe the FTZ which can sometimes be confusing. A consistent approach will be adopted here whereby the area inside the boundary of the differential etching or anodising response on a DC cast ingot will be known as the FTZ. This is the region which has undergone the slower cooling. This definition also applies to any directionally solidified test samples: the area on the side of the boundary furthest from the chill or water cooling spray will be known as the FTZ (see figure 1.05).

Westengen [5][7] examined a commercial purity (1050) DC cast ingot which had been grain refined and was cast at 100 mm min^{-1}. The FTZ was revealed in a section through the ingot by etching in 10% NaOH for 20 min at 70°C. TEM was used to identify intermetallics present at 15 and 50 mm from the ingot edge. Outside the FTZ (15mm from the edge) the dominant phases found were α"-AlFeSi (see table 1.03) and Al_mFe whilst inside the FTZ (50mm from the edge) the dominant phases were found to be Al_6Fe and Al_xFe. The α"-AlFeSi was said to be a low Si modification of α–AlFeSi. Cooling rates of 10 °C s^{-1} at 15mm from the edge and 5° C s^{-1} at 50 mm were estimated from measurements of cell sizes.

These results are in good agreement with the work of Miki *et al.*[21] who determined the following relationships between the cooling rate and the intermetallic phases which formed in Al-0.6 wt. % Fe alloys:

Cooling Rate / °C s^{-1}	<1	1-10	>10
Intermetallic Phase	Al_3Fe	Al_6Fe	Al_mFe

Table 1.04: Cooling rate ranges over which intermetallic phases form in Al-0.6 wt. % Fe [21]

Furthermore, the border of the FTZ was found to correspond to a cooling rate of 8 °C s^{-1} which fits well the findings of these authors. However, the presence of Al_xFe at the lower cooling rate of 10 °C s^{-1} is not in accordance with the cooling rate range suggested by Young and Clyne [8] of ≈ 0.5 to 6 °C s^{-1} for the formation of Al_xFe.

Westengen [5,7] found that the different etching response of the zones in this ingot were eliminated by annealing at 590 °C for 5 hours. After annealing, the Al_6Fe and Al_mFe

had wholly or partially transformed to Al_3Fe whereas the α''-AlFeSi and Al_xFe were still present. The conclusion which may be drawn from this is that the FTZ in this case was caused by the different etching responses of Al_6Fe and Al_mFe.

Ping Liu *et al.* [11] examined the formation and stability of intermetallic phases in three directionally solidified Al-Fe-Si alloys:, one with Fe:Si = 4:1 (commercial purity) and two with Fe:Si = 2:1 (one commercial purity, the other high purity). The commercial purity alloy with the Fe:Si ratio of 2 was very similar to that used by Westengen [5,7] except that it was not grain refined. Samples were taken from the parts of the ingots which had experienced cooling rates of 1°C s^{-1} and 10 °C s^{-1} and the intermetallic phases present were identified using TEM and EDX. It was found that, in all the alloys studied, the lower cooling rate always resulted in the formation of Al_3Fe. At the higher cooling rate in the alloy with Fe:Si = 4:1 the intermetallics found were Al_3Fe (dominant), Al_6Fe, Al_mFe, a new phase with a similar composition to Al_6Fe but with no Si present, denoted Al_pFe (also dominant) and α-AlFeSi. In the alloy with the Fe:Si = 2:1, the dominant phase at the higher cooling rate was found to be α-AlFeSi although some Al_3Fe and Al_pFe were reported in the high purity alloy. From this it seems that the lower Fe:Si ratio favours the precipitation of α-AlFeSi over binary intermetallics, as was the case in the alloy investigated by Westengen. What is remarkable in the work of Liu *et al.*[11] is the relative proportions of the binary phases observed in the microstructure: Al_xFe was not found, Al_6Fe and Al_mFe are only found in small quantities and the only dominant binary intermetallic phase found was the equilibrium intermetallic Al_3Fe. The overall dominance of α-AlFeSi and Al_3Fe over the metastable binary phases commonly reported by other workers in similar alloys is probably due to the presence of impurity elements at trace levels. As will be shown later (chapters 3,4 and 5) , the presence of certain trace elements can markedly affect the phase selection in these alloys.

Skerpje *et al.*[6,23] examined a DC cast alloy with an Fe:Si ratio of 2:1 and a composition similar to the alloy used by Westengen (Al-0.25 wt.% Fe- 0.13 wt.% Si and similar impurity levels except for high levels of Zn and Ga). Intermetallic compounds were identified using transition electron microscopy and quantitative EDX. Cooling rates at different point in the ingot were both calculated using a DC casting simulator and inferred from measurements of dendrite arm spacings.

The phases found at 10 and 50 mm from the ingot edge corresponding to a calculated cooling rate of 8 to 6°C s^{-1} were Al_mFe, α-AlFeSi and α_T-AlFeSi, a monoclinic ternary

phase with a similar composition to α–AlFeSi, see table 1.03. The phases found at the position corresponding to a cooling rate of 1•C s^{-1} were Al_3Fe, Al_xFe, Al_mFe, cubic α–AlFeSi and orthorhombic α''-AlFeSi. When compared to the other authors'findings these results are surprising firstly because no Al_6Fe was identified and secondly because Al_xFe and Al_mFe phases were found in parts of the ingot which had suffered the lower cooling rates. At the time, Skerpje asserted that the phase Al_xFe was related to Al_6Fe in that it had the same Bravais lattice (C centred orthorhombic) and similar lattice parameters and iron content (26.2 wt.% Fe in Al_xFe and 25.6 wt.% Fe in Al_6Fe) the main difference being that the Al_xFe contained some silicon which he suggested, had caused some kind of complex stacking. Al_xFe is, however, now known to be unrelated to Al_6Fe and to have its own unique but complex crystal structure. This suggests, therefore, that Skerpje may have incorrectly identified Al_6Fe as Al_xFe and that Al_6Fe was indeed present in the region of the ingot which had experienced a cooling rate of 1 °C s^{-1}. The overall conclusion is that the there is a shift from (α-AlFeSi/α_T–AlFeSi/α''-AlFeSi) and Al_mFe at high cooling rates to Al_6Fe(Al_xFe) and Al_3Fe at lower cooing rates.

Brusethaug et al.[3] investigated the effect of casting speed, secondary cooling, Fe and Si content and grain refinement on the FTZ and intermetallic phases formed in DC cast unalloyed sheet (99.5 % Al). They found that an Fe:Si ratio of 2:1 resulted in the maximum depth of the FTZ boundary (i.e. the narrowest FTZ); increasing or decreasing the Fe:Si ratio moved the boundary out towards the ingot surface. They also found that the FTZ was present when Al_mFe was the dominant phase in the outer region of the DC cast ingot. α-Al Fe Si was found in all the regions of the Fe:Si =2 alloy. This is consistent with previous work [5,6,7,23].lowering the Fe:Si ratio to 1 was found to be unacceptable as a method of overcoming the problem of the FTZ since it affected the ability of the rolled sheet to be effectively electrograined. Therefore, they found that the only acceptable way of reducing or eliminating the FTZ by means of adjusting the Fe:Si ratio was to raise it. With an Fe:Si of 2:1 the dominant intermetallic phase in the area of highest cooling rate was found to be Al_mFe and a FTZ was present. With the Fe:Si ratio at 5:1 the dominant intermetallic phase in this region was found to be Al_6Fe and no FTZ was present. A reduction in casting speed from 75-80 mm/min to 65-60 mm/min increased the width of the FTZ in the alloy with an Fe:Si of 2 to such an extent that it was wider than the normal scalping depth. This is not the solution to the whole problem, however, as Brusethaug et al. state that a FTZ is sometimes found at lower casting speeds and suggest that other factors, presumably alloy composition

and grain refinement, could be involved

Brobak and Brusethaug [10] used directional solidification to solidify two alloys (those with Fe:Si = 2:1 and 5:1). which had been DC cast by Brusethuag *et al.*[3], however, the equipment used was not capable of producing solidification velocities high enough to result in the formation of Al_mFe. Even at lower solidification velocities, though, considerable differences were observed between the intermetallics found in the directionally solidified and DC cast ingots. In the alloy with an Fe:Si ratio of 5:1, the dominant phase was found to be a dendritic phase which could not be identified, rather than Al_6Fe. In the alloy with an Fe:Si ratio of 2:1, α- AlFeSi was the dominant intermetallic at high cooling rates, but it was found in neither alloy at low cooling rates. In both alloys, Al_3Fe was the dominant intermetallic at the lower cooling rate but formed at a growth velocity greater than that found by other workers for the transition to Al_6Fe. The comparison between this work and that of Brusethaug *et al.*[3] graphically illustrates the difficulty of using the results of simple directional solidification experiments to understand the intermetallic phase selection in DC cast ingots.

Tezuka and Kamino [14] used directional solidification equipment which was designed to simulate the solidification conditions which apply during DC casting. They solidified a number of binary Al-Fe and ternary Al-Fe-Si alloys containing 0.3 and 0.5 wt. % Fe, with Si levels in the range 0.1 to 0.4 wt. % Si to give Fe:Si ratios from 1;1 to 5:1. The dominant intermetallic phase in both the binary alloys was found to be Al_6Fe. On addition of 0.1 wt. % Si to both of these alloys, the dominant intermetallic changed to Al_3Fe. In none of these alloys however, was a FTZ observed. Adding greater amounts of Si produced different effects in the 0.3 wt. % Fe alloys to those observed in the 0.5 wt. % Fe alloys. In the 0.3 wt. % Fe alloys, increasing the Si content above 0.1 wt. % changed the dominant intermetallic from Al_3Fe to Al_mFe and finally to α-AlFeSi at Si levels of 0.25 wt. % and above. A FTZ was only observed with a Si content of 0.15 wt. %, when Al_mFe was the dominant intermetallic outside the FTZ (where the cooling rates were highest) and Al_3Fe was the dominant intermetallic inside the FTZ. In the 0.5 wt. % Fe alloys, increasing the Si content above 0.1 wt. % led to the formation of α-AlFeSi in the more rapidly cooled parts of the ingot. A FTZ was observed in the alloy containing 0.2 wt. % Fe, the differential etching response being produced by the presence of α-AlFeSi outside, and the Al_3Fe within, the FTZ. In the alloy containing 0.3 wt. % Si, a double FTZ was observed as a result of three different levels of etching response associated with regions of the ingot where α-

AlFeSi, Al_mFe and Al_3Fe were the dominant intermetallic.

These results are in agreement with previous results [7,10] in that the FTZ is found to be present in samples with Fe:Si ratios close to 2:1 and not in samples with higher or lower ratios. The occurrence of the FTZ, however, in the absence of Al_mFe, is contrary to previous findings [5,7]. In the two 0.5 wt. % Fe samples with 0.2 and 0.25 wt. % Si, the FTZ is caused by the different anodising response of Al_3Fe and α–AlFeSi. Previous work states that the presence of the FTZ is consistent with the presence of Al_mFe in the outer region of the ingot and Al_6Fe with or without Al_3Fe in the centre. There is a possibility that small quantities of Al_mFe were not detected by the Debye-Scherrer X-ray camera used for phase identification. On the other hand there is the possibility that Al_mFe does not need to be present for the FTZ to occur.

In directionally solidified 1100 series alloys, Asami [4] found very small quantities of Al_mFe accompanying Al_3Fe on the slow cooled side of a FTZ boundary. On the other side of the FTZ boundary Al_6Fe was the dominant intermetallic phase accompanied by small amounts of Al_3Fe. This is surprising as it suggests that Al_mFe formed at lower cooling rates than Al_6Fe. In comparison a 5005 alloy solidified in the same way contained Al_mFe as the dominant phase outside the FTZ with Al_3Fe and Al_6Fe coexisting inside the FTZ. 5005 alloys contain 0.7 wt. % Fe and 0.3 wt. % Si, 1100 series alloys contain 0.95 wt.% (Si + Fe). Asami does not state the actual composition.

Despite these results, it still must be noted that Tezuka and Kamino [14] are the only workers to find FTZs without any Al_mFe accompanying them. They conclude that in Al-Fe-Si ternary alloys the major crystallised phases change from Al_6Fe and Al_3Fe to Al_3Fe, Al_mFe and α–AlFeSi with an increase in Si content. Another point to note from their work is that there is only one, or at the most two, intermetallic phases found in each region of the directionally solidified samples made up from high purity ingredients. This is in marked contrast to DC cast ingots where three phases coexisting in the same region is common but as many as six phases have been found present in the same region [11]. This has been discussed by Brobak and Brusethaug [10] who also found a difference in the number of phases in DC cast and directionally solidified samples. They attributed this difference to the different solidification conditions during DC casting and directional solidification: the controlled and uniform growth conditions in directional solidification (ie temperature gradient, growth rate and cooling rate).The existence of minor instabilities and local variations in directional solidification may give rise to solidification conditions favouring the

growth of two phases. The situation in DC cast ingot is different in that the solidification conditions are position dependent. In a DC cast ingot the coexistence of multiple phases in the same region is attributable to fact that solidification conditions, in particular the local solidification velocity, are constantly changing. This, however, does not account for the fact that Tezuka found no more than two phases in at any one point in samples directionally solidified in what is essentially a DC casting simulator with a range of cooling rates mimicking those experienced by an actual DC cast ingot. The only other explanation can be that the purity of the alloys used by Tezuka must restrict the number of phases. The effect of impurities and trace level of other element will be discussed later.

In summary it seems safe to say that the FTZ is brought about by the presence of different binary Al-Fe phases at different positions in the DC cast ingot. The phase which appears to be responsible for the largest difference in surface etching response is Al_mFe. When an alloy containing Al_mFe and a FTZ is homogenised by high temperature annealing the Al_mFe and other metastable binary phases tend to transform to the stable Al_3Fe and the FTZ disappears. The conditions needed, therefore, for the formation of the most vivid FTZ are those needed for the formation of Al_mFe in the outer part of the DC cast ingot with Al_6Fe, or a mixture of Al_3Fe and Al_6Fe, in the inner part. It is possible, however, to obtain a less vivid FTZ without Al_mFe being present, if instead α AlFeSi is present in the outer region of the ingot. Whatever the particular phases required, the transition from one phase to another at a particular position in the ingot is brought about by providing a sufficiently high cooling rate and, consequently, solidification velocity for the metastable phase to form in the outer region of the ingot. In DC casting this is achieved by increasing the casting rate which results in an increase in both cooling rate and solidification velocity.

The ratio of iron to silicon in the alloy seems to have an effect on the formation of the FTZ. In the alloys considered above a FTZ was always present with Fe:Si = 2:1. Lowering this value eliminates the FTZ but renders the material unsuitable for electrograining. Increasing the Fe:Si ratio also eliminates the FTZ by changing the dominant intermetallic phase within the outer region of the ingot. There is a trend for alloys with Fe:Si ratio = 2:1 and a FTZ to also contain the ternary metastable phase cubic α–AlFeSi in all regions of the ingot, not just the FTZ. This is surprising in that the cubic α–AlFeSi will only form at high rates of solidification in dilute alloys. This is because the solidification needs to be sufficiently rapid to suppress the eutectic reaction (liq - Al+Al_3Fe) so that the peritectic point can be reached (liq + Al_3Fe - Al + α–AlFeSi). The α–AlFeSi phase was not seen at

higher Fe:Si ratios of 5:1. (It must be stressed that the alloys with Fe:Si = 2:1 were all of similar compositions *ie* around 0.25. wt. % Fe and 0.13 wt. % Si. No results have been published on alloys with a markedly different composition and the same Fe:Si ratio).

The values of critical cooling rate suggested for the transition from one type of intermetallic phase to another are by no means fixed .. This is in keeping with a general theme of inconsistencies between different authors results. For example, Al_mFe was found in one alloy at a position corresponding to a cooling rate around 6 °C s^{-1} and in the same alloy Al_xFe, Al_mFe and α–AlFeSi phases were found at a position with a cooling rate of 1°C s^{-1} [6]. No Al_6Fe was found. The α–AlFeSi phases were often found in all areas of the ingot [6,10] with a Fe:Si of 2 but not always [10]. In general, phases found at different positions within similar alloys cast under similar conditions varied. These inconsistencies could result from slight differences in the way in which the alloys were cast, or in the way the phases were identified, or in the ways in which the cooling rates were calculated. More likely than this would be that the inconsistencies are caused by minor differences in the actual alloy compositions, in particular the presence of certain elements, as impurities or otherwise, at very low levels.

1.07   The Effect of Trace Elements on the FTZ

Apart from Fe and Si, commercial 1000 and 1050 alloys contain low levels of trace elements, predominantly Ti or Ti-B added as grain refiner, Mg, Mn, Ni, V, Zn, Cr, Cu, and sometimes Ca and Ga. The elements are either alloy additions or are unavoidably present in the alloy, perhaps as an impurity which was present in the raw materials and whose removal is deemed either unnecessary of prohibitively expensive. The joint effect of the trace elements on the formation of intermetallic phases which are responsible for the FTZ is not known but the individual effect of each element has been studied by using high purity base alloys and adding only the element under scrutiny.

The effect of adding relatively high levels of elements to an Al 0.5 wt.% Fe alloy was reported [13] on the critical cooling rate, Φ_c, for the transition from Al_6Fe to Al_mFe in directional solidification. It was found that the addition of up to 2.9 wt. % Mg had the effect of reducing the value of Φ_c as did the addition of silicon up to 0.17 wt.% and Cu up to 0.3 wt.%. The addition of 4.3 wt. % Mg took the value of Φ_c back to the same level as when none present. In DC casting, the effect of reducing the critical cooling rate needed for the formation of Al_mFe would be to push the FTZ boundary back into the ingot. In effect, the

Al_mFe, which forms at higher cooling rates, would have a larger range of cooling rates over which it could form before Al_6Fe was able grow. When Ti-B grain refiner was added a reduction in Φ_c for Al_mFe was seen. No effect was seen on the value of Φ_c by the addition of 0.1-2.1 wt.% Zn, 0.1-0.3 wt.% Mn, 0.1 - 0.3 wt.% Cr, and 0.01 - 0.1 wt.% Ti.

The effects of the addition grain refiner and trace levels of Li, Be, Ca, K and Ba on the FTZ were studied on a commercially pure 1100 alloy [13]. The larger the amount of grain refiner added, the further the boundary of the FTZ moved towards the centre of the ingot. Li, Be, K, Ba had no effect on the position of the FTZ boundary but the addition of Ca at levels of only 30 to 50 ppm shifted the boundary towards the centre of the ingot. This effect was exacerbated when grain refiner was added along with the calcium. However, the addition of trace elements to commercially pure material in order to gauge their effect is not entirely reliable. Industrially pure 1100 alloys can contain over 0.1 wt. % impurity [1] (mostly Fe and Si with some Cu, Mn and Zn). Any individual effect seen on the addition of a trace element may be 'swamped' by the effect of the presence of other impurities. The most reliable method to characterise the effect of individual elements is to start with very pure base alloys. Only when the nature and magnitude of the effect of an individual addition has been established can the synergistic effects of multiple elements be tackled.

Otani et al.[4] found that, in combination with the correct level of grain refiner, Ca eliminated the FTZ in 1000 and 5000 series aluminium alloys cast by unidirectionally solidification methods simulating DC casting. The FTZ was eliminated if the grain size was kept below 100 μm and the Ca below 0.03 wt.%. The intermetallic particles which were present in the FTZ in the ingots were identified which revealed that, with Ca present, Al_6Fe had been converted to Al_3Fe in the 1100 and Al_6Fe and Al_mFe had been converted to Al_3Fe in the 5005 alloy. This result does not agree with those cited above [13] where Ca, in the presence of grain refiner, was found to shift the FTZ boundary towards the centre of the ingot, promoting metastable phase formation.

Tezuka and Kamino [14] added B, Ca, Co, Mg, Si, and Ti to Al - 0.3 and 0.5 wt. % Fe - 0 to 0.4 wt. % Si alloys made up from high purity starting materials. The unidirectional solidification equipment used was designed to more accurately simulate the conditions inside a solidifying DC cast ingot than is the case with standard directional solidification equipment. This was achieved by using a removable chill plate at the base of the mould so that water could be sprayed directly onto the base of the ingot once it had solidified sufficiently that the plate could be removed safely. The cooling rate profile

(cooling rate *vs.* distance from the base of the ingot) was more representative of that obtained in a DC cast ingot in that it started off high, dropped rapidly, then increased even more rapidly (on removing the chill plate and spraying the water directly onto the base of the ingot) and finally gradually reduced the further up the ingot the solidification front moved.

In an Al-0.5 wt. % Fe alloy cast using the apparatus described above the dominant intermetallic phase throughout the ingot was found to be Al_6Fe and no FTZ was seen. It was found that the addition of small amounts of Co to these alloys brought about the appearance of Al_mFe by lowering the critical cooling rate necessary for its formation. Thus, at Co levels of 0.044 and 0.053 wt. %, Al_mFe was dominant in the lower cooling rate regions within the FTZ with Al_6Fe dominant elsewhere. This is the reverse of the formation sequence proposed by Miki *et al.*[21] for Al_mFe and Al_6Fe since here the Al_mFe formed at the lower cooling rates. Tezuka and Kamino [14] observed that the Al_mFe phase contained small quantities of Co which was not the case for Al_6Fe. This suggests that the promotion Al_mFe found in this work may have resulted from an increased relative thermodynamic stability of Al_mFe over Al_6Fe due to this differential solubility. At higher levels of Co (0.067 wt. %), only Al_mFe was present in the ingot and the FTZ disappeared. Increasing the Co content further, caused the appearance of $Al_9(Fe,Co)_2$. At a level of 0.076 wt. % Co, this was only found in the high cooling rate region of the ingot and a FTZ was formed with Al_mFe the dominant intermetallic phase within. With a Co content of 0.130 wt. %, however, $Al_9(Fe,Co)_2$ was dominant throughout the ingot and the FTZ disappeared again.

The addition of 0.5 wt.% Mg to an Al-0.3 wt.% Fe-0.15 wt. % Si ternary alloy suppressed the formation of Al_mFe in favour of Al_3Fe and Al_6Fe. When 0.03 wt. % Ti - 0.005 wt. % B was added to the Mg containing alloy, the effect was to strongly promote the formation of α–AlFeSi to such an extent that it dominated the whole ingot. This could have been due to a synergistic effect between the two additions or due to the fact that the magnitude of the effect caused by the Ti-B addition was much greater than that of the Mg addition.

The addition of 0.004 to 0.11 wt. % Ca to an Al - 0.5 wt. % Fe alloy promoted the formation of Al_3Fe over Al_6Fe. This is in agreement with Otani *et al.*[4] who found that Ca could eliminate the FTZ by completely suppressing the formation of metastable phases. The effect of adding Ca was even more pronounced in ternary alloys containing Si. It could be said, therefore, that these two elements act in conjunction with one-another.

The effect of adding Ti-B grain refiner to ternary Al-Fe-Si alloys was to change the major intermetallic phases from Al_3Fe and Al_mFe to Al_mFe and α–AlFeSi. The effect of B on its own in Al-Fe-Si alloys was somewhat confusing in that at low levels (0 to 50 ppm) it promoted the formation of a mixture of Al_3Fe and Al_6Fe and eliminated a FTZ consisting of Al_3Fe and Al_mFe (at low and high cooling rates respectively). However, at levels above 50 ppm, Al_mFe re-emerged as the dominant intermetallic phase and at 150 ppm was the only crystallised phase in the main body of the ingot. No explanation for this behaviour was offered. A summary of the reported effects of trace elements on phase selection in Al-Fe and Al-Fe-Si alloys is shown in table 1.05.

From the results of the work conducted on the effect of individual trace elements on phase selection it can be seen that the dominant intermetallic phase formed in an ingot can be greatly influenced by the presence of even very small amounts of these elements. Consequently, whether a FTZ is formed, and the position of its boundary or boundaries, is also influenced by these additions. If the transition from Al_mFe to some other intermetallic is taken, for the sake of argument, to be responsible for FTZ formation in these alloys then any element which lowers the critical cooling rate for the formation of Al_mFe such that it is possible for it to form during DC casting is, then, responsible for the formation of the FTZ. This also holds true if the element alters any other solidification parameter in such a way as to make FTZ formation possible. A mixture of such effects will be found in a commercial alloy where many impurities and alloying additions are present. It would be a considerable task indeed to predict the joint effect of all the elements in one particular commercial alloy. The effect of just two trace elements in Al-Fe-Si alloys is not usually known. The relative magnitude of their individual effects needs to be considered as a weak effect in one may be completely dwarfed by the by the strong effect of another. Moreover, the two elements together may complement one anothers' effects , nullify them, or have a totally different effect altogether. In order to develop a model which explains the phase selection in a complex alloy, the individual effect of each element must first be known and, as importantly, the precise mechanism by which it affects phase selection must also be known. Only then would it be possible to usefully predict the effects of mixtures of trace elements. The aim of this study is primarily to examine the individual effect of trace element additions on phase selection in model alloys (binary and ternary alloys made from very pure starting materials).

1.08   The Effects of Cooling Rates and Growth Velocity on Phase Selection

The intermetallic phase selection discussed in the sections above was expressed usually as a function of cooling rate: one intermetallic phase formed at a low cooling rate and a different intermetallic at a high cooling rate. Some workers, however, chose solidification velocity as the parameter to quantify phase selection [3,5,7,10,35,48,49].

Alloy	Addition	Effect	Reference
Al-0.5 wt.% Fe	None	Fully Al_6Fe	14
Al-0.5 wt.% Fe	Co	Promotes Al_mFe and $Al_9(Fe,Co)$ over Al_6Fe	14
Al-0.5 wt.% Fe	Ca	Promotes Al_3Fe over Al_6Fe and Al_mFe	14 13
Al-0.5 wt.% Fe + Si	Ca	As above but more so	14 13
Al-0.3 wt.% Fe-0.15 wt.% Si	0.5 wt.% Mg	Promotes Al_6Fe and Al_3Fe over Al_mFe	14.13
Al-0.3 wt.% Fe-0.15 wt.% Si +Grain Refiner	0.5 wt.% Mg	Promotes α–Al Fe Si over all other phases	14
Al-Fe-Si	Ti and Ti-B	Promotes Al_mFe and α–Al Fe Si over Al_3Fe and Al_mFe	14

Table 1.05 Summary of some of the effects, of trace elements on phase selection in dilute Al-Fe and Al-Fe-Si alloys [4,13,14,22].

Cooling rate is important primarily in terms of its effect on the nucleation temperature of a phase. At low cooling rates, the equilibrium phase is expected to nucleate as there is plenty of time for nuclei to form in the melt. At higher cooling rates, however, it is possible for metastable phases to nucleate. Metastable phases have melting temperatures below those of their stable counterparts. If the cooling rate is high enough, the situation may arise where there is not enough time for the stable phase to form a nucleus before the metastable phase (which may require less undercooling below its melting temperature) can do so. If this is the case the metastable phase will be that which is found in the cast microstructure (assuming that the metastable is not a good nucleant for the stable phase when competitive growth applies). Thus, there will be a critical cooling rate at which the transition to the metastable phase transition occurs.

The solidification velocity is the controlling parameter if the phase selection is based on growth rather than nucleation. The theory of competitive growth states simply that the

phase which can grow at the highest temperature for a given growth velocity will be that which forms (assuming that both phases can nucleate with equal ease). More simply still, the phase which grows the fastest will outgrow any competitors. The assumption in this theory that both phases can nucleate with equal ease become very important when the nucleation and growth characteristics of the competing phases are different. Some intermetallic eutectic phases grow in a continuous manner because their non-faceted growth mode allows easy adjustment of spacing to accommodate changes in velocity, whilst other eutectic intermetallic phases have a faceted growth mode which hinders spacing adjustment [35]. At high growth velocities some phases may need to repeatedly nucleate in order to carry on growing. Therefore, the problem of phase selection is not one defined solely by cooling rate or solidification velocity but by a complex interaction between the two.

1.09   Aims of the Experimental Work

The aim of the experiments described in the following chapters was to examine how the composition of alloys, based on the 1000 series affected phase selection. This was done by conducting a matrix of experiments. The first set of experiments set out to give a broad picture of phase selection in DC casting. by simulating the DC casting process in the laboratory. The composition of alloys cast in this way were varied and the effect noted. The aim of the experiments was to give an overview of the how composition affected the phase selection with particular reference to the phases forming the FTZ. The equipment was able to scan a range of solidification velocities and cooling rates and to give a general idea as to what effect each variation in composition was having.

In order to gain a more precise idea of the parameters controlling the phase selection in these castings, two sets of experiments were conducted whose aim was to isolate either the cooling rate or the solidification velocity as the single variable parameter.

The effect of cooling rate was examined in binary alloys using differential scanning calorimetry. The nucleation temperature of the eutectic intermetallic phases were measured over a range of cooling rates with the aim of determining whether a phase transition occurred. and if it did so, the critical cooling rate for that transition. Trace additions were made to the alloys and the same set of experiments conducted in order to examine the effect of these trace elements on the critical cooling rate for the transition.

The effect of solidification velocity on phase selection in fully eutectic alloys was examined using a Bridgman furnace. The growth temperature was measured for a range of

solidification velocities with the aim of discovering whether, and at what critical velocity, a phase transition occurred. Trace elements were added to the alloys and the same experiments conducted in order to examine the effect of the trace elements on the critical velocity of the phase transition.

The overall aim was to gain a knowledge of whether transitions between different intermetallics were controlled primarily by cooling rate or solidification velocity or a combination of both. The effect of the addition of trace elements on transitions would show whether they affected the growth or the nucleation behaviour of individual phases. With this knowledge, it was hoped that some of the effects seen in the casting experiments could be explained.
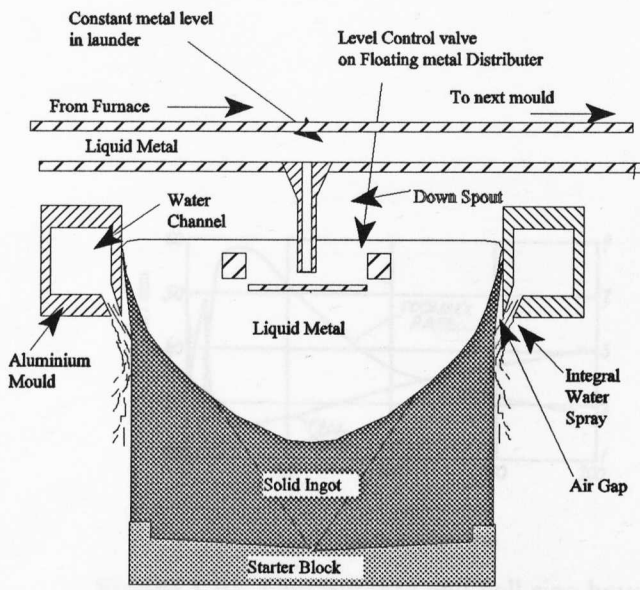
Figure 1.01. Schematic diagram of The Vertical DC Casting process
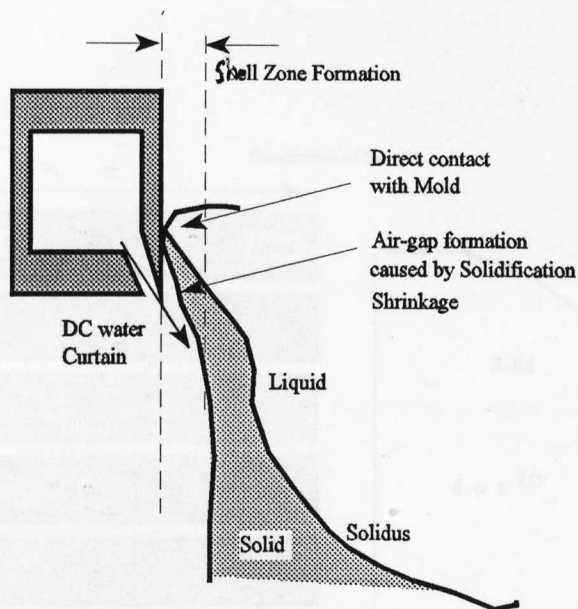
Figure 1.02. Diagram showing the formation of the Shell Zone in DC Casting.

Figure 1.03. Cooling rate and cell size have been plotted against the distance from the ingot edge.(After Westengen [5])
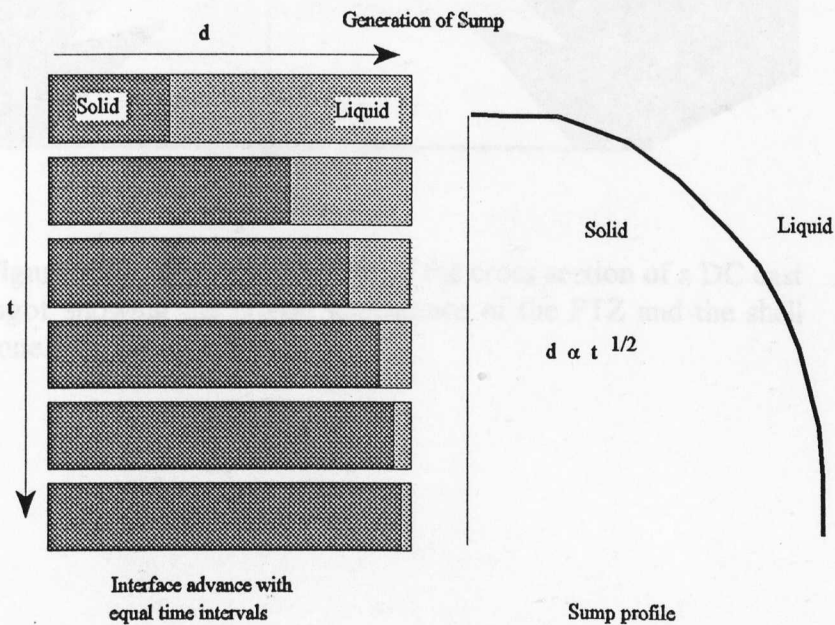
Figure 1.04. A metal bar being solidified from one end, at a constant heat extraction rate, shown at equal time intervals. The shape of the interface assumes a parabola when plotted against time. This is akin to the sump shape in DC casting.
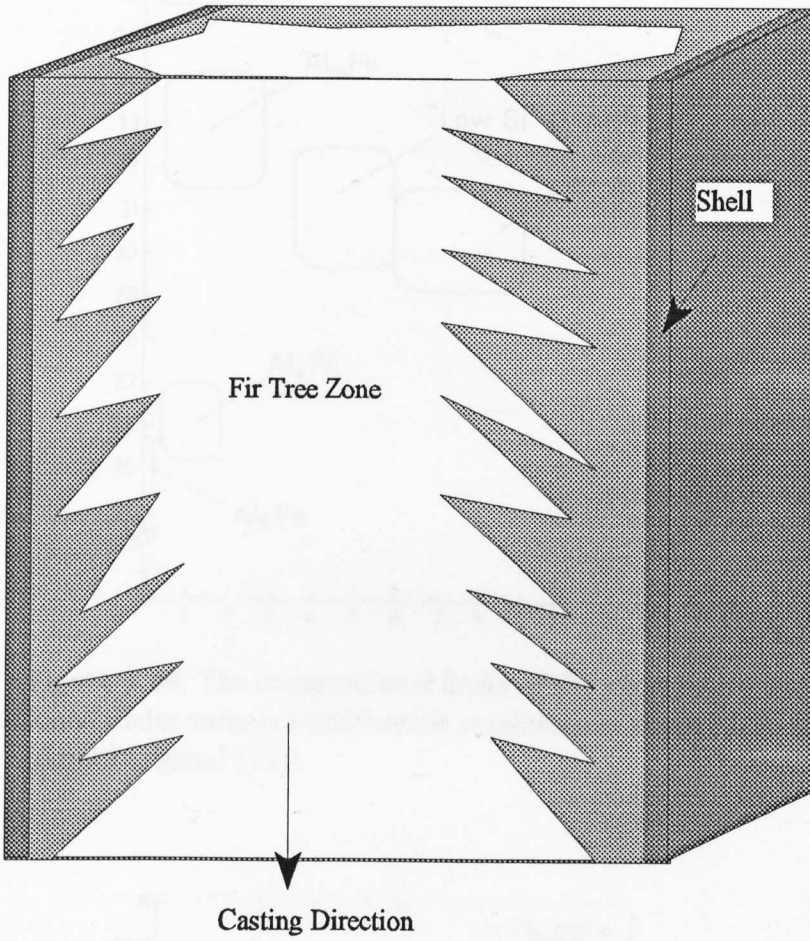
Figure 1.05. Schematic diagram of the cross section of a DC cast ingot showing the typical appearance of the FTZ and the shell zone.
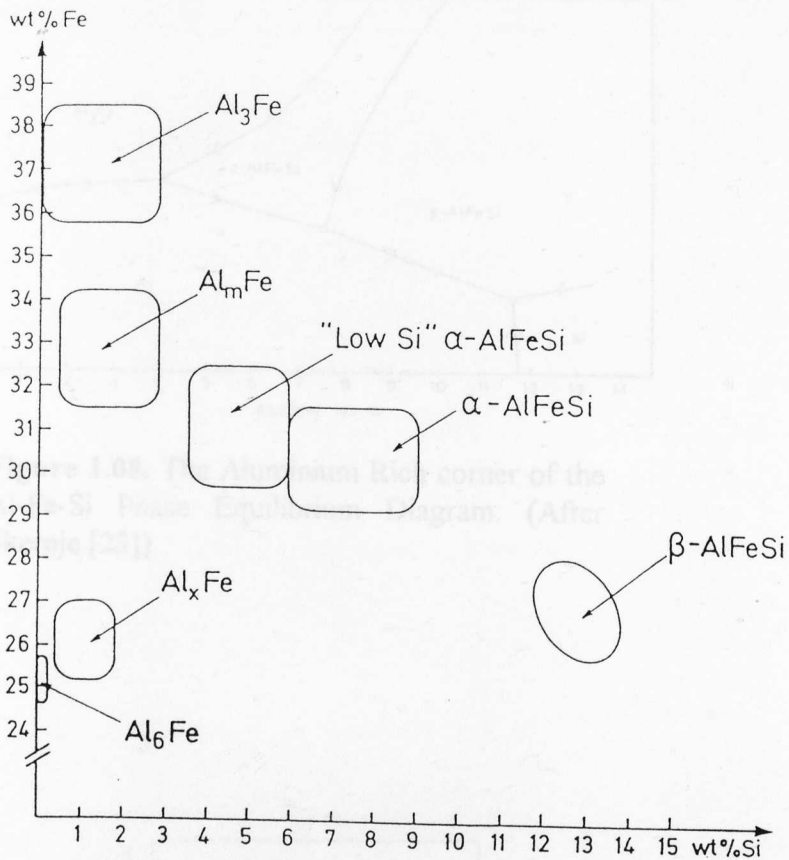
Figure 1.06. The compositional limits of the main binary and ternary found under various solidification conditions in dilute Al-Fe-Si alloys. (After Langsrud [15])
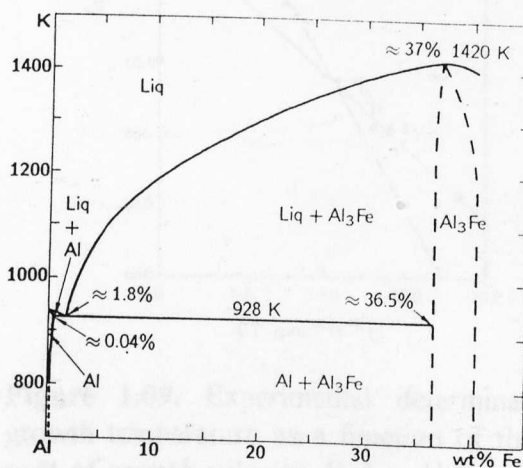
Figure 1.07. The Al rich corner of the Binary Al-Fe Phase Equilibrium Diagram.
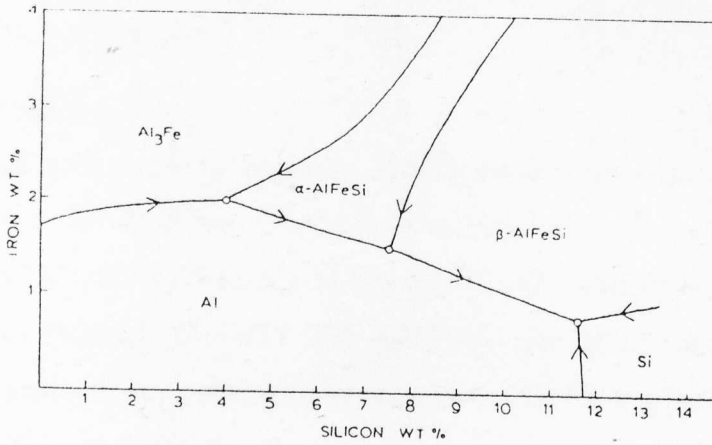
Figure 1.08. The Aluminium Rich corner of the Al-Fe-Si Phase Equilibrium Diagram. (After Skerpje [23])
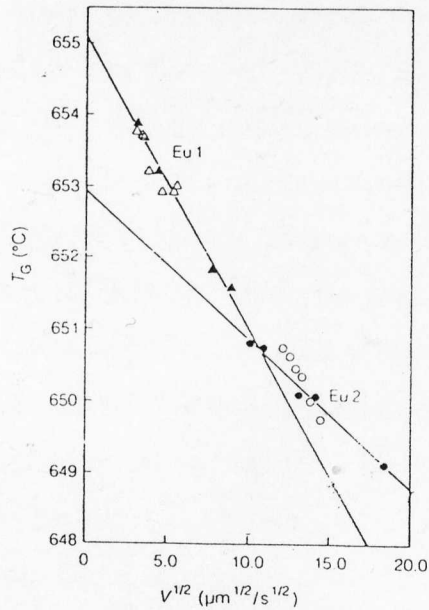
Figure 1.09. Experimental determinations of growth temperature as a function of the square root of growth velocity. Eu1 = Al_3Fe and Eu2= Al_6Fe. The critical velocity at which Al_3Fe is outgrown by Al_6Fe, is given at the point where the lines cross (110mms^{-1}).(After Liang and Jones[49]).

2.0   Particle Extraction

2.1   Introduction

In this work, a new technique (the SINBUT process) was used to extract intermetallic particles from the aluminium matrix for identification purposes. The technology was developed by the SINTEF Group of Norway [51,52]. The name is an abbreviation of SINTEF and Butanol (SI-BUT). The basic principle of operation is to dissolve the aluminium matrix in dry butanol under inert gas while leaving the intermetallic particles unaffected. This is carried out by placing the sample and butanol in an autoclave, the elevated temperature and pressure greatly accelerating the dissolution of the matrix. The aluminium reacts with the butanol forming aluminium butoxide which is soluble at high temperatures.

$$2Al + 6C_4H_9OH \rightarrow 2Al(OC_4H_9)_3 + 6H$$

There are advantages to particle extraction/examining extracted intermetallics over examining them in-situ in the aluminium matrix. The main disadvantage of in-situ examination is that the volume fraction of intermetallic phases in these alloys is too low for XRD detection. The alloys used in this study are very dilute and, consequently, have a relatively small volume fraction of intermetallic phase with the result that the contribution of the matrix to the X-Ray Diffraction (XRD) plot tends to 'swamp' any intermetallic contribution. The extraction of the particles from the matrix allows identification without any matrix effect. In the case of Energy Dispersive X-ray (EDX) in the TEM, the primary aluminium matrix also hinders reliable identification. Characteristic X-rays used in identification are emitted from a 'tear drop' shaped volume of material (the interaction volume) directly underneath the probe where the electron beam enters the material to be identified. If this interaction volume is larger or deeper than the particle (which, indeed, it was in this study) then the matrix will contribute to any reading. By extracting intermetallic particles, the matrix contribution is eliminated. Additionally, the morphology of intermetallic phases is clearer when they have been extracted. Metallographic examination of sectioned, polished and etched samples only reveal a two-dimensional picture of particle morphology...extracted particles give a much more revealing three-dimensional morphology useful for interpretation.

2.0   Particle Extraction

2.1   Introduction

In this work, a new technique (the SIBUT process) was used to extract intermetallic particles from the aluminium matrix for identification purposes. The technology was developed by the SINTEF Group of Norway [51,52]. The name is an abbreviation of SINTEF and Butanol (SI-BUT). The basic principle of operation is to dissolve the aluminium matrix in dry butanol under inert gas while leaving the intermetallic particles unaffected. This is carried out by placing the sample and butanol in an autoclave, the elevated temperature and pressure greatly accelerating the dissolution of the matrix. The aluminium reacts with the butanol forming aluminium butoxide which is soluble at high temperatures:

$$2Al + 6C_4H_8OH \rightarrow 2(C_4H_8O)_3Al + 6H_2$$
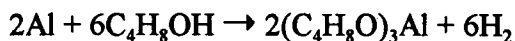
There are advantages gained from examining extracted intermetallics over examining them *in-situ* in the aluminium matrix. The main disadvantage of *in-situ* examination is that the volume fraction of intermetallic phases in dilute alloys is too low for XRD detection. The alloys used in this study are very dilute and, consequently, have a relatively small volume fraction of intermetallic phase with the result that the contribution of the matrix to the X-Ray Diffraction (XRD) plot tends to 'swamp' any intermetallic contribution. The extraction of the particles from the matrix allows identification without any matrix effect. In the case of Energy Dispersive X-ray (EDX) in the TEM, the primary aluminium matrix also hinders reliable identification. Characteristic X-rays used in identification are emitted from a 'tear drop' shaped volume of material (the interaction volume) directly underneath the point where the electron beam enters the material to be identified. If this interaction volume is larger or deeper than the particle (which, indeed, it was in this study), then the matrix will contribute to any reading. By extracting intermetallic particles, the matrix contribution is eliminated. Additionally, the morphology of intermetallic phases is clearer when they have been extracted. Metallographic examination of sections through polished and etched samples only reveal a two-dimensional picture of particle morphology : extracted particles give a much more revealing, three-dimensional image which needs no interpretation.

2.2   Experimental Techniques

Two techniques were used based on the SIBUT process. The first was used to extract intermetallics from samples cut from ingots cast in the DC simulator and Bridgman furnace (see chapters 3.0 and 5.0). These intermetallics were then identified by XRD to determine the intermetallics present at different locations within the ingots (particularly, those on either side of a FTZ boundary). The second technique was used to identify the main intermetallic phases present in Differential Scanning Calorimetry (DSC) samples (see chapter 4.0). XRD could not be used to identify phases extracted from these samples as there was not enough intermetallic present to give reliable measurements. Instead, a TEM with a quantitative EDX facility was used to examine carbon extraction replicas of the DSC samples.

2.2.1 The SIBUT Apparatus.

The basic apparatus for both techniques was essentially the same and worked on the same principle. Specially dried butanol was required for the dissolution of the aluminium matrix since any water present in the butanol would have formed insoluble aluminium hydroxide which would have contaminated the samples. Analar butanol contains 0.1 wt. % H_2O, which, although quite low, was still too high for this application. Consequently, a still was used to dry the butanol further. Slightly different stills were used for the two different techniques, see figures 2.01a and 2.01b, but the principle of operation was the same: the main difference was that the still used for the production of XRD samples had an extra chamber, figure 2.01a, where the processed butanol could be collected and tapped off into an autoclave. The stills work by heating the butanol to its boiling temperature, 121°C, under argon. The inert gas prevents any oxidation of the aluminium sample and keeps out airborne water vapour. Pure aluminium foil was added to the butanol in order to speed up the drying process by reacting with water in the butanol. The butanol and any water not reacting with the aluminium in the butanol will evaporate. The water cooled coil allows water vapour and hydrogen gas (evolved in the butanol/aluminium reaction) to escape through the open top of the still while butanol vapour condenses and drips back into the lower flask.

2.2.2 The SIBUT Extraction Technique for the production of samples for XRD Identification

This technique was used to identify phases occurring in the DC simulator cast ingots and Bridgman samples. Samples for extraction were cut from the regions of interest in the DC simulator ingots and from the middle section of the Bridgman growth specimens using a hacksaw. The optimum mass of sample for XRD was found to be 460 mg. This amount gave enough extractate to yield a good XRD pattern without taking an unreasonably long time to extract and without over-pressurising the autoclaves in which the extraction took place.

Samples for extraction were first cleaned for 2 minutes by chemical polishing in a solution of 2.5 parts by volume of nitric acid, 40 parts phosphoric and 5 parts sulphuric acid at 90°C. This removed surface grease and dirt and, more importantly, it removed the oxide layer present on the surface of the sample which would have interfered with the extraction process. Samples were than washed in a series of dry ethanol baths and then dried under vacuum in a Schlenk tube. The samples were then stored under argon in the Schlenk tubes to prevent further oxidation.

The dissolution of the matrix took place in a stainless steel autoclave, see figure 2.02, fitted with a pressure gauge and a 0.1 μm grade Teflon filter in the base. The autoclave was first washed in water in an ultrasonic bath for 5 minutes before being rinsed thoroughly with distilled and deionised water and dried in an oven for 2 hours at 135°C. It was then taken from the oven and the pre-weighed PTFE filter inserted. Whilst still warm, the autoclave was evacuated and purged with argon, this evacuation and purging being repeated twice before the weighed sample was inserted into the top of the autoclave (which was still under an argon purge so that there was a positive argon pressure ensuring that no air could enter).

A quantity (100 ml) of dry butanol, obtained from the still was poured into the autoclave which was subsequently sealed and placed in an oven at 135°C. The dissolution took around 4 hours to complete during which a pressure rise in the autoclave of 5 to 7 atm resulted from the superheating of the butanol and the evolution of hydrogen gas as a by-product of the aluminium / butanol reaction. Once the dissolution was finished the autoclave was removed and the bottom seal was opened, allowing the internal pressure to force the liquor out, during which the intermetallic particles, suspended in the liquor, were collected on the Teflon filter. When the autoclave had reached atmospheric pressure it was filled with

argon from the top. To wash the extractate, and to ensure that all the aluminium matrix had dissolved, the autoclave was filled with 50 ml of dry butanol, while still under an argon purge, sealed and heated in the furnace at 135°C for a further 30 minutes and emptied in the same way. The vapour pressure of the butanol was sufficient to force most of the remaining liquid from the autoclave; the remainder of the solution was forced out applying a top pressure of argon. This procedure was then repeated. When the autoclave had cooled to between 80 and 50°C, the lower valve was closed and connected to a water vacuum pump. The autoclave was then rinsed twice with 15ml of ethanol which was sucked out by opening the lower valve. The lower part of the autoclave, containing the filter paper and extractate was then placed in a covered beaker and left to dry overnight in an oven at 75°C. The filter paper with the extractate was subsequently weighed and the weight fraction of the intermetallic calculated.

2.2.3 XRD identification of extracted intermetallics.

The intermetallic phases were extracted as described above, which yielded a Teflon filter paper with a layer of intermetallic particles covering one side. The thickness of this layer was dependent on the size of the sample and the volume fraction of intermetallic phase contained therein. It was possible to perform X ray analysis on this as a whole; however, in order to save some of the sample for subsequent analysis and to concentrate the X-ray beam, it was necessary to concentrate some of the particles on a smaller part of the filter paper. This also reduced any reflection from the filter itself.

The filter paper and its contents were placed in a clean Petri dish which was filled with fresh methanol. This was then floated in a beaker of water in an ultrasonic bath. The effect of the ultrasound was to remove the particles from the filter and leave them suspended in the methanol. This suspension was poured into an agate mortar and the methanol evaporated by placing the mortar on a hotplate. When dry, the particles were ground to a fine powder with an agate pestle and sprinkled on onto a zero reflection silicon wafer smeared with a thin film of petroleum jelly, the particles being subsequently flattened down with a microscope slide. The purpose of grinding the particles was to ensure a random orientation of crystallographic planes within the sample; without this precaution, intermetallic phases with a plate-like morphology tended to lie flat on the silicon wafer giving a preferred orientation within the sample with the result that the relative peak

intensities observed did not correspond with those listed in the JCPDS powder diffraction file.

All X-ray diffraction was carried out on a Phillips PW 1830 diffractometer using Co $K\alpha$ radiation. Diffractometer traces were recorded over the range 15° to 90° 2θ.

2.2.4 Intermetallic Phase Identification by EPMA.

It was initially hoped that quantitative analysis of extracted intermetallic particles could be performed using Electron Probe Micro Analysis (EPMA). The EPMA was initially used to scan samples on the filter paper they were collected on. Although there was no doubt that the EPMA could accurately identify a single species of intermetallic held on a filter by using area scans, there was a problem when there was a mixture of phases was present. If the volume fraction of each phase in a mixture was not known, then the result of a scan covering a number particles would not be able to positively identify the phases present since the value of Fe content obtained would lie between the values of the two component phases. More ambiguity would be introduced if there were more than two phases present (which was, not infrequently, the case). A technique was, therefore, required which would enable the EPMA to analyse a single intermetallic particle at a time. The particles carried on the filter paper could not be analysed individually as they tended to overlap one another. As EPMA analysis takes its signal from an interaction volume which extends approximately 1 μm below the surface of the sample being analysed, if two dissimilar particles (of less than 1 μm thickness) overlapped unambiguous analysis would be impossible. Consequently, the particles needed to be taken off the filter paper and arranged on a substrate such that they would not overlap.

A method was evaluated whereby the particles were removed from the filter paper by immersion in acetone and the application of ultrasound vibration. The suspension of particles in acetone was transferred to an agate mortar where they were ground down with a pestle to negate any chance of preferred orientation. The acetone was then evaporated using a hot plate. Cold setting Araldite epoxy resin was prepared and mixed with varying amounts of carbon black in order that it become electrically conductive. Graphite flake was also experimented with as a conductive medium. Both carbon black and graphite flake were mixed into the resin until it was saturated and could not accommodate any more or became too viscous to be easily handled. The inside of a mounting mould was smeared with a thin

layer of petroleum gel. The ground up extractate was smeared on the bottom surface of the mould and the epoxy / carbon black mixture was poured on top and left to set.

The aim of this technique was to produce a thin layer of re-embedded intermetallic particles held in a conductive medium which could then be individually analysed in the EPMA. The reason for using carbon black was that it is a conductive powder which has a high surface area. With enough carbon black powder mixed into the epoxy a conductive network of interconnected particles would complete the circuit between the embedded particles and the sample holder required for EPMA analysis.

2.2.5   SIBUT Carbon Extraction Replica Technique for EDX Identification in the TEM.

Typical DSC specimens (see chapter 4.0) were 3mm diameter discs weighing approximately 5 mg. These would not yield a sufficient mass of extractate using the technique described in section 2.2.2 for analysis of the intermetallic phases present by XRD. Thus, a different technique was needed for their extraction and identification; the intermetallic particles were extracted on carbon film using a modified SIBUT process which allowed EDX identification in a TEM.

Figure 2.03 shows the steps taken in the preparation of the samples for examination in the TEM. Initially, the samples were rolled down to 100 μm thickness which broke up the intermetallic colonies allowing more accurate EDX analysis in the TEM. Additionally, rolling was to produced a thinner sample which took less time to dissolve in the butanol. Discs of 3mm diameter were punched from the rolled specimens and cleaned on both sides using a fine emery cloth. The samples were then electropolished in a Struers Tenupol-3 automatic twin-jet electropolisher using a solution of 2 wt. % potassium iodide in ethanol at 20 V D.C for 60 seconds at room temperature. This partially removed the aluminium matrix leaving the intermetallic particles standing proud of the surface. One side of the jet polished sample was then carbon coated in an Edwards Coating System E306A.

The uncoated side of the sample to be extracted was scored and scraped clean with a scalpel whilst submerged in cold butanol. This removed any remaining dirt and the oxide layer on the surface of the sample. By keeping it submerged in butanol, further oxidation was suppressed. It was found that the reaction of the aluminium matrix and butanol was hindered by the presence of the oxide layer and that its removal speeded up the process.

The distillation apparatus shown in figure 2.01b was then used to completely dissolve the aluminium matrix leaving the intermetallics held in the carbon film. Before use,

the spherical flask used to hold the butanol was cleaned and rinsed with warm butanol. A fresh charge of butanol was dried for 15 minutes in the still with argon gas flowing and the condenser working. A small piece of pure aluminium foil (99.999 wt. %) was added to the flask to speed up the drying process. The temperature of the butanol was maintained at 121°C so that it was just at its boiling temperature.

The clean sample was then placed in the flask with the boiling butanol. The reaction took between 1 and 3 hours to complete. (The time taken to dissolve a 5 mg sample in this way is only an hour or two less than that needed to dissolve a 460 mg sample in an autoclave (see section 2.2.2). This demonstrates how much the increased pressure in the autoclave increased the rate of reaction). When the reaction was complete, which was evident from the lack of effervescence of the sample, the heater was turned off and the flask emptied into a clean beaker. The fragments of carbon film carrying intermetallics were picked up on a copper TEM grid and transferred to another beaker containing fresh butanol at ≈100 °C. By rinsing in hot butanol any aluminium butoxide (which is insoluble in butanol at low temperatures) was removed from the samples. The carbon films were then transferred to cold butanol where they were picked up, individually, on 3 mm diameter, 400 mesh, carbon and Formvar coated copper TEM grids. The carbon and Formvar coating provided support for the weak carbon films. These samples were then examined in a JEOL 2000 FX TEM with LINK analysis software.

2.3 Results

In this section the relative success and advantages gained from particle extraction via the SIBUT technique will be discussed. Individual results from DC simulator, DSC and Bridgman experiments will be discussed in their respective chapters.

2.3.1 The SIBUT Extraction Technique for XRD specimens.

The SIBUT extraction technique has allowed phases to be positively identified without the need for time consuming TEM diffraction pattern analysis. Even with low yields of intermetallic particles (<3 mg of extractate from a 400 mg sample) the plots obtained from the diffractometer showed definite peaks and good reproducibility. The results can be said to be statistically sound due to the large numbers of particles in each sample. By

contrast, it was not possible to positively identify by XRD the intermetallic phase *in-situ* in the aluminium matrix even in a fully eutectic Al-Fe sample grown in a Bridgman furnace since the signal gained from the intermetallic phase was too weak to be seen against the intensity of the signal from the matrix. The technique allowed standard plots for the common phases found in dilute Al-Fe and Al-Fe-Si alloys to be obtained which could then be compared to experimentally grown samples allowing confident and fast identification without the need for time consuming analysis of TEM diffraction patterns. It was also possible to determine when a mixture of phases was present by comparison of experimentally obtained plots to the standard plots. The exact proportions of the phases in a mixture could not be obtained by this method; however, it was possible to estimate whether one phase was dominant over the other or others in the mixture by comparing the intensities of some of the stronger peaks from each phase.

XRD plots and micrographs of extracted particles of Al_3Fe, Al_xFe, Al_mFe, Al_6Fe and cubic α are shown in the following experimental chapters.

2.3.2 The Re-embedding Technique for EPMA specimens

The technique for re-embedding the extractate in a conductive epoxy resin was not as successful as had been hoped. The particles of carbon black (and graphite flake) did create the conductive network required. The samples which were made using this technique did retain a single layer of particles close to the surface which were easily visible in the microscope. The problem encountered was related to the size of the particles themselves. The interaction volume in the EPMA was larger and deeper than the particles and this tended to give unreliable results from individual particle analyses.

2.3.3   SIBUT Carbon Extraction Replica Technique for EDX analysis in the TEM

This technique was successful in that intermetallic particles could be extracted from the DSC specimens and viewed in the TEM. Some difficulties were, however, encountered with specimen contamination. The need for cleanliness in this technique is paramount. It was found that the best way to avoid contamination was to thoroughly clean all the equipment between each specimen extraction. Photomicrographs of particles extracted in this manner are shown in chapter 4. The determination of the composition of intermetallics extracted in this way is possible with a knowledge of the particle thickness and density. However, some problems were encountered in this respect which are also discussed in chapter 4.
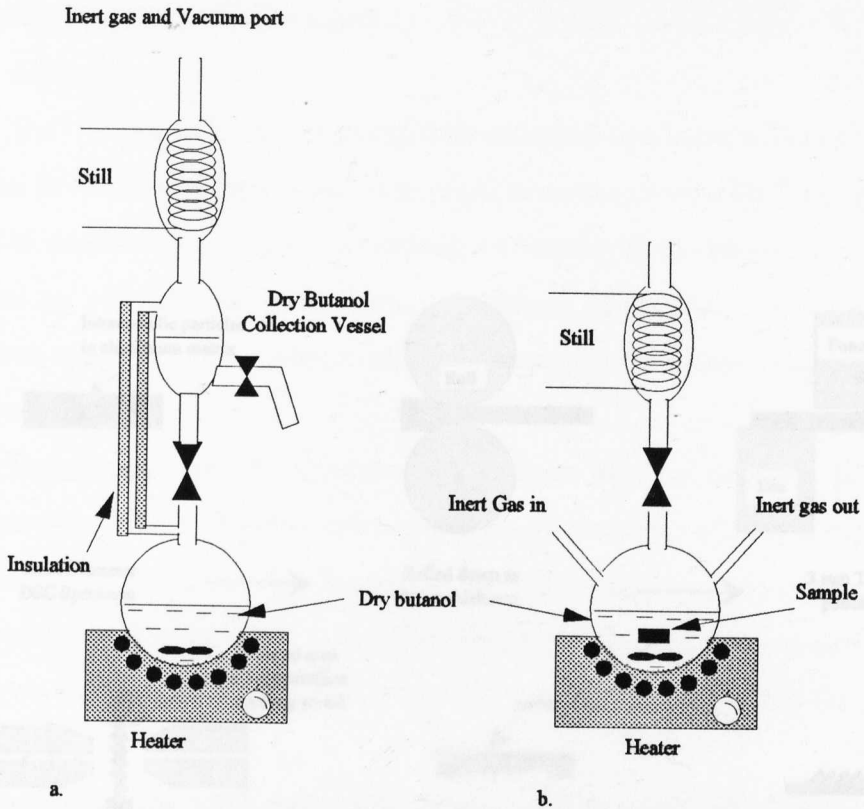
Figure 2.01. Two slightly different stills were used to dry the butanol. The still shown in **a** was used for the production of XRD samples and has a collection chamber for tapping off butanol to fill an autoclave. The still shown in **b** was used to produce extraction replicas for EDX analysis.
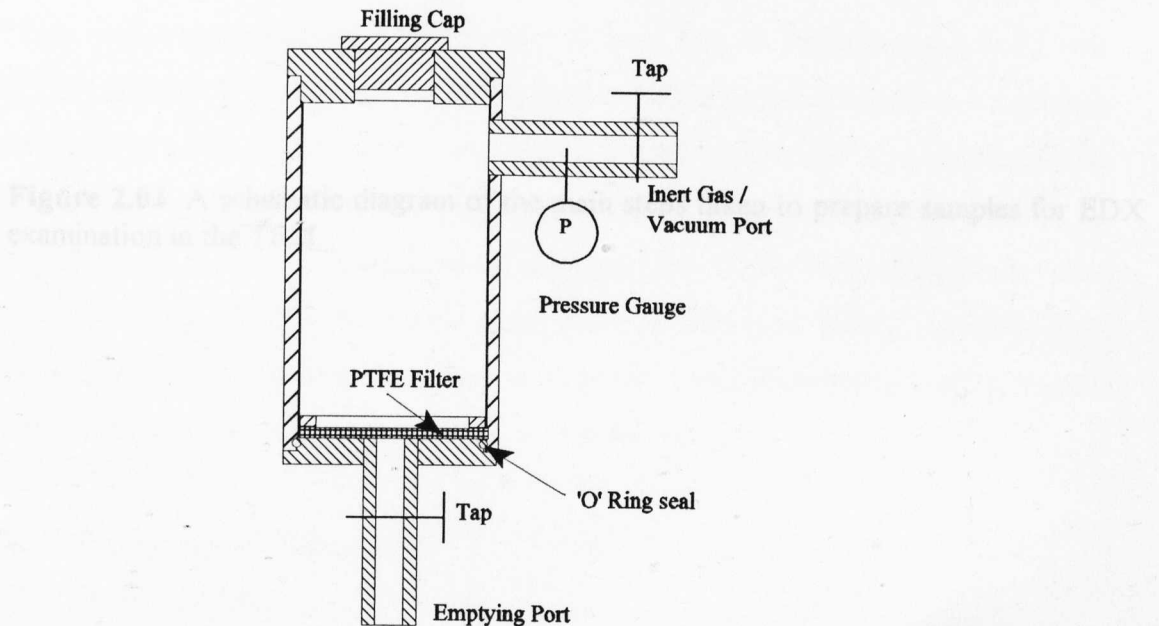
Figure 2.02. Cross section of the autoclave used to produce XRD samples.

Figure 2.03. A schematic diagram of the main steps taken to prepare samples for EDX examination in the TEM.

3.0   DC Simulator Experiments

3.1   Aims

The DC casting process is a large scale industrial operation with capital and running costs that make it unfeasible to conduct multiple experiments on a Ph.D budget. In order to be able to conduct experiments concerning DC casting in the laboratory, equipment was designed to simulate the solidification conditions experienced in a DC caster. The equipment, called the DC simulator, allowed repeated experiments to be conducted on the bench top at low cost.

The aims of the DC simulator experiments were to examine the possibility of reproducing the FTZ in the laboratory and to gauge the effect of alloy composition on the FTZ. The SIBUT technique, described in the previous chapter, provided a method whereby the phases responsible for the FTZ could be confidently identified. Thus the effects of Fe and Si and trace element concentrations on intermetallic phase selection and the ability to form the FTZ could be measured.

The specification for 1050 series sheet alloys, used for applications requiring a surface treatment such as anodising, allows up to 0.25 wt. % Si and 0.4 wt. % Fe. Minor alloying elements include Cu, Mn, Mg, Ti (<0.05 wt. % each) and Zn (<0.07 wt. %). The total level of Cr, V and Li is also limited (< 0.03 wt. %). In higher quality alloys, designed specifically for lithographic printing sheet these limits are more tightly controlled. The problem of the FTZ is sometimes attributed to the Fe and Si level and, in particular, the Fe:Si ratio [7,11,14]. In order to examine the effect of these parameters on phase selection, superpurity based, 99.999 wt % Al (5N) ternary alloys were chosen with Fe and Si levels which were within the 1050 series specification. By eliminating the trace elements mentioned above, the effect of varying the Fe and Si levels could be gauged. By casting binary superpurity based Al-Fe, alloys the effect of Fe content alone could be examined. Finally, the addition of selected trace elements individually to each of these alloys would enable their effect on both intermetallic phase selection and the FTZ to be determined.

3.2   Experimental Techniques

3.2.1   Alloy Selection.

Two binary Al-Fe base alloys (A1x and A2x) were chosen to examine the effect of varying Fe level. Three Al-Fe-Si base alloys (A1, A2, and A3) were chosen to examine the

effect of varying Fe and Si levels and the Fe:Si ratio. The nominal base alloy compositions are shown in table 3.01.

Trace elements were added individually to each of the base alloys in order to examine their effect. Mg, Mn, V, Ti, and Ti-B were added to the ternary base alloys and Mg, Ti and Ti-B were added to the binary base alloys, the nominal levels added are shown in table 3.02.

Alloy	Fe / wt. %	Si / wt. %	Fe:Si
A1x	0.2	-	-
A2x	0.4	-	-
A1	0.2	0.1	2
A2	0.4	0.1	4
A3	0.4	0.2	2

Table3.01 Base alloy nominal compositions

Addition	Mg / wt. %	Mn / wt. %	V / wt. %	Ti / wt. %	Ti+B / wt. %
Ternary alloys	0.02	0.02	0.02	0.04	0.04
Binary Alloys	0.02	-	-	0.04	0.04

Table 3.02 Nominal Trace element additions

The choice of the trace elements to be examined, and the levels thereof, were based on the impurity levels found in an alloy cast by Alcan which was known to be susceptible to the FTZ defect.

The base alloys were made up by melting the appropriate amounts of superpure (5N) Al and superpurity based Al - 5 wt. % Fe and, in the ternary alloys, Al - 5 wt. % Si master alloy in an electrical resistance furnace. Approximately 10 kg batches of each alloy was made. Trace additions were made just prior to casting in the DC simulator. The spectrographical analysis for the binary/ternary alloys are shown in tables 3.03 and 3.04 respectively.

3.2.1 The DC Simulator Design.

The purpose of the DC simulator was to allow fast, low cost experiments to be conducted which simulated the solidification conditions experienced within the DC ingot

during casting. In particular, the DC simulator was designed to allow a range of solidification velocities and cooling rates to be scanned. In order to do this, the design had to allow for the two stage cooling associated with DC casting. In the first stage of cooling which takes place within the mould, the region known as the shell zone solidifies. This consists of a layer of highly chilled material resulting from initial contact of liquid metal with the mould wall and a layer of slower cooled due to the formation of an air gap between the mould wall and the ingot skin as a result of solidification shrinkage. In the second stage, where heat is extracted by the cooling water curtain the remainder of the ingot solidifies at progressively lower and cooling rates.

Alloy	Fe / wt.%	Mg wt. %	Ti / wt. %	Ti-B / wt.% *
A1x	0.21	<0.001	<0.001	<0.001
A1x + Mg	0.21	0.029	<0.001	<0.001
A1x + Ti	0.19	<0.001	0.036	<0.001
A1x + Ti-B	0.21	<0.001	<0.001	0.044
A2x	0.41	<0.001	<0.001	<0.001
A2x + Mg	0.41	0.029	<0.001	<0.001
A2x + Ti	0.42	<0.001	0.42	<0.001
A2x + Ti-B	0.40	<0.001	<0.001	0.045

Table 3.03 Spectrographic analysis of binary alloys cast in The DC Simulator.(* added as grain refiner)

A schematic diagram of the DC simulator is shown in figure 3.01 and a more detailed cross section is shown in figure 3.02. The basic design consists of a vertical furnace containing a removable stainless steel crucible. The furnace is heated by six vertical cartridge heating elements located at equal intervals around the furnace. A thermocouple is connected to a furnace controller which maintains the correct current into the heating elements to keep the furnace at a preset temperature. The crucible has a slight taper in its bore to allow easy removal of the solidified ingot. The insulation around the base of the ingot (Carborundum mouldable ceramic) prevents ingot solidification from the sides of the crucible at the base where it was found to be slightly cooler. The arrangement beneath the furnace consists of a tightly fitting plug which locates into the furnace base and is held in place by a clamp. The whole apparatus described above sits above a water jet and water catchment bath. The

clamp is designed so that the base plug can be quickly removed and swung out of the way enabling the water jet to impinge directly on the base of the solidifying ingot.

Alloy	Si / wt. %	Fe / wt.%	Mn / wt.%	Mg wt. %	Ti / wt. %	V / wt.%	B / wt. %
A1	0.11	0.21	<0.001	<0.001	<0.001	<0.001	-
A2	0.11	0.40	0.001	0.001	<0.001	<0.001	-
A3	0.22	0.40	0.001	0.001	<0.001	<0.001	-
A1+Mg	0.11	0.21	<0.001	0.022	<0.001	<0.001	-
A2+Mg	0.11	0.40	0.001	0.023	<0.001	<0.001	-
A3+Mg	0.22	0.39	0.001	0.023	<0.001	<0.001	-
A1+Mn	0.11	0.21	0.02	0.001	<0.001	<0.001	-
A2+Mn	0.11	0.40	0.019	-	-	<0.001	-
A3+Mn	0.22	0.40	0.019	-	-	<0.001	-
A1+V	0.11	0.21	<0.001	-	-	0.021	-
A2+V	0.11	0.39	-	-	<0.001	0.021	2
A3+V	0.21	0.39	-	-	<0.001	0.20	2
A1+Ti	0.10	0.20	-	-	0.041	<0.001	1
A2+Ti	0.10	0.38	-	-	0.39	<0.001	2
A3+Ti	0.21	0.36	-	-	0.043	<0.001	2
A1+Ti-B	0.10	0.20	-	-	0.041	<0.001	14
A2+Ti-B	0.10	0.38	-	-	0.039	<0.001	13
A3+Ti-B	0.21	0.39	-	-	0.039	0.001	13

Table 3.04 Spectrographic analysis of ternary alloys cast in The DC Simulator.

3.2.3 Operation of the DC Simulator

The top surface of the base plug and the inside of the stainless steel crucible were painted with graphite paint to prevent the solidified metal from alloying with or sticking to the crucible. The mouldable ceramic insulation was applied to the base of the crucible and hardened in a separate electrical furnace at 110°C for 10 to 15 minutes. In tests, it was found that the lack of insulation around the base of the furnace allowed some solidification to begin low down on the crucible walls. The added insulation provided by the mouldable ceramic prevented this without affecting the solidification from the base.

With the top of the crucible insulated with Kaowool refractory wool, the DC simulator was preheated to 740°C. The pre-weighed base alloy to be cast was melted in an induction furnace and superheated to a temperature of 720°C. Each charge, weighing approximately 0.7 kg, gave an ingot height of around 250 mm. The correct weight of trace addition was added 1 minute before the alloy was cast. This was particularly important in the case of the Ti-B grain refiner addition as it has been shown [52] that its effect can fade with time due to settling of the TiB_2 nucleant particles. In the case of Mn, V and Ti, additions were made using previously-alloyed master alloy containing 5 wt. % of the said element in 5N Al. Mg was added as 99.9. wt. % purity metal and the Ti-B was added using commercial purity 5:1 refiner (5 wt. % Ti-1 wt. % B in Al).

Just prior to casting, the furnace was turned off for safety purposes and the water jet was turned on to a preset level. The water jet impinged on the recessed bottom surface of the base plug. This was done by pointing the water jet at an angle from the side. The top insulation was removed before the metal was poured in and replaced afterwards to prevent solidification occurring from the top.

After 30 seconds, the base plug was removed and swung out of the way to allow the water jet to impinge directly onto the base of the solidifying ingot. In this way, the two stage cooling was achieved: the first stage of cooling while the metal was in contact with the water-cooled base plug and when the plug was removed (when the shell was formed) and the second stage when the water spray was directly in contact with the bottom surface of ingot (and the main bulk of the alloy solidified at a gradually decreasing rate). When the ingot had fully solidified, the water jet was turned off and the crucible removed. The ingot was extracted from the crucible by tapping the crucible on a hard surface.

3.2.3   Preparation of DC Simulator Ingots for Macroscopic Examination

Ingots cast in the DC simulator were sectioned longitudinally along the central axis using a band saw. One half was then linished on coarse, 80 grit emery paper to produce a flat surface. This surface was then ground on progressively finer emery paper (120, 240, and 600 grit) and polished using 15 μm diamond paste and spray.

The polished ingots were then macro-etched to show up any fir tree effect. Using large scale treatment tanks, the ingots were prepared in large batches. The following series of treatments were used to provide the most vivid effect:-

- 10 min in an agitated water-based degreasant;

- 1 min water rinse;

- 5 min caustic etch in an aqueous solution of 5 % NaOH and 4 % NaNO$_3$
  at 60°C;

- 2 min (30% v/v) nitric acid desmut;

- 1 min water rinse;

- 40 min anodising in a solution of 165 gl^{-1} sulphuric acid at 17-18 V DC and 150 A m^{-2} at 20 °C;

- 60 min seal in water at 98°C.

The differential etching response of the different phases could be seen after the caustic etch. The anodising process made the surface harder and more able to resist scratching by growing the oxide film. The final seal in near boiling water further strengthens the film by closing over any pits present in the film surface [53].

3.2.4   Determination of Cooling Rates in the DC Simulator.

Thermocouples were used to determine the cooling rate on solidification at three different positions within the DC Simulator. The object of this was to get an idea of the magnitude of the cooling rates in the apparatus so that a comparison with the DC casting process was valid. Horizontal holes were drilled through both sides of the crucible at 20, 50 and 100 mm from the base of the stainless steel crucible. Alumina sheaths, of 1.3 mm outside diameter and 1.1 mm inside diameter, were inserted through the holes and cemented in place with Autostick ceramic cement. Type-k thermocouples were inserted into the sheaths and cemented in place so that their tips were situated along the centre line of the crucible. The thermocouples were connected to a Schlumberger data logger interfaced with a PC and an experiment carried out as described in section 3.2.3. with the temperature in the three different positions logged from the time just before the metal was poured until the solidification front had passed the third thermocouple.

3.3   Results

3.3.1.1 Ternary Al-Fe-Si Alloys

The SEM micrographs in figure 3.03 show typical examples of each of the main phases extracted from the ingots, with corresponding XRD traces for each phase. The phases detected were: Al$_3$Fe, Al$_6$Fe, Al$_m$Fe, Al$_x$Fe, cubic α-Al-Fe-Si and one other phase, designated u2, whose diffraction pattern did not match the standard patterns for phases in

this system. The phase u2 was only found in small quantities in the sample A1+Mg and its crystal structure has not been established. The morphology of each of the phases is clearly different: the plate like Al_3Fe, the more branched Al_6Fe and the more obviously regular eutectic morphologies of Al_mFe and cubic α.

Figure 3.04 shows the distribution of intermetallic phases found in each of the ingots together with the FTZ boundaries where present. In many cases XRD indicated that more than one phase was present at a given position: dominant phases are indicated first with phases detected at low levels shown in parentheses. In the ingots cast in this work, the FTZ is defined as the area of differential etching closest to the top of the ingot. In most cases, although clearly visible to the naked eye, the FTZ was difficult to record photographically. The samples where a photographic record could be made (alloys A2+Ti-B, A3 and A3+V) are shown in figure 3.06. The A2+Ti-B sample showed the most vivid contrast between the FTZ to lower part of the ingot.

The effect of the trace additions on the intermetallic phases can be explained by considering the range of solidification velocities or cooling rates over which each phase can grow. For example, consider a hypothetical base alloy in which the phases cubic α, Al_6Fe and Al_3Fe are found in three different regions of the ingot, see Figure 3.07. The addition of an element at trace level which extended the range of solidification velocities or cooling rates over which, say, Al_3Fe could form would push the boundary between Al_3Fe and Al_6Fe down towards the base of the ingot , figure 3.07b, reducing the size of the region where Al_6Fe is found in the ingot. Alternatively, if the range over which cubic α could form were extended, the cubic α/Al_6Fe boundary would be pushed upwards, as in figure 3.07c. This will be discussed in more detail below.

The results shown in figure 3.04 will now be discussed in more detail. The effect of the addition of Ti-B refiner will be treated separately to the effects of other trace addition.

3.3.1.2 Base Alloys

A consideration of the results for A1 and A3 shows that the type of intermetallics that occur are not just a function of Fe:Si ratio but depend also on the Fe concentration. Alloys A1 and A3 both have Fe:Si = 2 but A3 has twice the amount of Fe as alloy A1. Cubic α exists at high cooling rates in both alloys. At lower cooling rates, Al_xFe appears in alloy A1 but Al_6Fe appears in alloy A3. Al_3Fe is found in both the alloys A1 and A3 at the lowest cooling rates. A double FTZ was clearly visible in alloy A1 corresponding to the transitions

from cubic α to Al_xFe and from Al_xFe to Al_3Fe. Only a single FTZ, due to the cubic α to Al_6Fe transition, was seen in alloy A3. An Al_6Fe to Al_3Fe transition was present higher up the ingot but this transition did not give rise to any observable differential response to macroetching. In alloy A2, with Fe:Si = 4 but the same Fe concentration as alloy A3, Al_6Fe forms at the highest solidification rates rather than cubic α which was seen in A3.

The solidification sequence seen in the three base alloy ingots may be summarised as follows:

high cooling rate and solidification velocity		low cooling rate and solidification velocity		
cubic α	$\rightarrow$ Al_xFe	$\rightarrow$	Al_3Fe	A1: 0.2%Fe, 0.1%Si, Fe:Si=2
Al_6Fe	$\rightarrow$ Al_3Fe	$\rightarrow$	Al_3Fe	A2: 0.4%Fe, 0.1%Si, Fe:Si=4
cubic α	$\rightarrow$ Al_6Fe	$\rightarrow$	Al_3Fe	A3: 0.4%Fe, 0.2%Si, Fe:Si=2

Thus:

● Keeping the Fe:Si ratio constant and doubling the Fe concentration alters the type of intermetallics found in the FTZ from Al_3Fe and Al_xFe in alloy A1 to Al_3Fe and Al_6Fe in A3.

● Doubling the Fe:Si ratio for a constant Fe level (alloy A2 vs. alloy A3) moves the Al_6Fe/cubic α and Al_3Fe/Al_6Fe boundaries down to such an extent that the cubic α is eliminated.

No Al_mFe was detected in the base alloys in the work reported here. This is in disagreement with the results of Japanese workers who have reported a transition from Al_mFe to Al_6Fe to Al_3Fe in Al-Fe and Al-Fe-Si alloys on decreasing cooling rate [4,9]. They did not detect cubic α in their alloys but its appearance at high cooling rates and low Fe and Si levels has been reported elsewhere [7].

The phase termed Al_xFe was identified by workers at Alcan International by comparison with a standard XRD plot obtained from other experiments on dilute Al-Fe alloys. Its XRD trace did not match Al_3Fe, Al_6Fe, Al_mFe (m≈4.2), cubic α, hexagonal α or monoclinic β. Its stoichiometry was found by TEM/EDX to be close to Al_4Fe, but its crystallographic structure has not yet been established.

More than one intermetallic phase could exist at a given location in an ingot. For example, Al_6Fe and Al_3Fe co-existed in A3. A gradual transition between intermetallic types

might explain why a FTZ is not always revealed by macroetching. This will be discussed later.

3.3.1.3 The Effect of Mn and Ti on the Visible FTZ.

Mn and Ti eliminated the visible FTZ boundary otherwise revealed on macroetching. This must be due to the effect of the elements on the etching response of the surface since there is little or no change in the intermetallic phases found in these ingots.

3.3.1.4 The Effect of Trace Element Additions to the base alloy A1

The phase Al_xFe was present only in the A1 base alloy. The addition of V, Ti, or Mn eliminated Al_xFe by moving the Al_3Fe boundary down to meet the cubic α boundary. The addition of Mg also moved the FTZ boundary down, replacing the cubic α near the base with Al_6Fe and another unidentified phase, u2. It appears that Mg hinders the formation of cubic α since none was observed in this alloy. Mg, V, Ti and Mn may favour Al_3Fe by extending the range of solidification velocities over which it can form.

Al_6Fe was scarce in the A1 alloys when compared to the A2 and A3 alloys and their variants. Indeed, Al_6Fe is only found in the A1 alloy with Mg added and then only in a very small region outside the FTZ whereas Al_6Fe is found in every ingot in the A2 and A3 series. This absence of Al_6Fe in the A1 series must be due to the Fe and Si level as this is the only constant in these alloys.

3.3.1.5 The Effect of Trace Element Additions to the base alloy A2

The trace elements had minor effects. They did not change the intermetallic phases found: there was always Al_6Fe at high cooling rates and Al_3Fe at low ones. The addition of V had no effect. With Mn, Al_3Fe was found at trace levels in the lower region of A2. This could be because the addition expanded the Al_3Fe phase field or because the shell zone was slightly larger than normal, reducing the initial cooling rate and solidification velocity and, in effect, moving the Al_3Fe/Al_6Fe boundary down towards the base of the ingot.

No cubic α was found in any of the A2 alloys. This effect must be brought about by the Fe and Si content of the A2 alloys, as this is their only common factor.

3.3.1.6 The Effect of Trace Element Additions to the Base alloy A3

The A3 base alloy contained cubic α near the base, then Al_6Fe in the region above and, with a diffuse boundary, Al_3Fe above that. The addition of V has moved the Al_3Fe and Al_6Fe phase fields down whilst maintaining a visible FTZ. The cubic α phase field has been 'pushed out' of the base of the ingot by the Al_6Fe. The fact that a visible boundary exists between the Al_3Fe and Al_6Fe in the alloy with the addition and not in the base alloy will be discussed later.

The effect of Ti is to move the Al_3Fe and Al_6Fe phase fields down towards the base of the ingot. A mixture of approximately equal proportions of cubic α and Al_6Fe is found in the fast solidified region, indicating that the Al_6Fe, so clearly distinct from the cubic α in the base alloy, can form under similar solidification conditions to cubic α when Ti is added.

The addition of Mn has moved the Al_3Fe/Al_6Fe boundary down and 'pushed' the cubic α out of the base of the ingot. Substantial additions of Mn tend to stabilise Al_6Fe [54], which is isostructural with Al_6Mn, forming $Al_6(Fe,Mn)$. This might be expected to expand the range of solidification conditions where Al_6Fe could form. But in these alloys, because the Mn does not segregate heavily and the levels are so low, any effect on the thermodynamic stability of Al_6Fe will be very small.

The addition of Mg has had no effect in the region outside the FTZ which is approximately the same size and contains cubic α as the dominant intermetallic. Inside the FTZ, however, the Al_6Fe in the base alloy has been substituted by Al_3Fe as the dominant phase. The range of solidification conditions over which Al_3Fe forms has expanded at the expense of Al_6Fe, but with no effect on the FTZ.

3.3.1.7 The Effect of Addition of Ti-B Refiner to the Base Alloys

Ti-B grain refiner added to DC cast aluminium alloys contains TiB_2 particles and excess Ti. It is added, typically, as a master alloy containing 5 wt. % Ti and 1 wt. % B in Al. When added to the molten metal, the TiB_2 acts as a nucleant for primary aluminium and the excess Ti dissolves. The addition of Ti-B refiner introduces TiB_2 particles and seems to have a much larger effect than the addition of free Ti. Consequently, the considerable differences in the phases found in the ingots with Ti-B refiner addition when compared to the base alloys must be due mainly to the effect of the TiB_2. It seems likely that any effect on the intermetallic phase selection would be produced by *some* of the TiB_2 particles promoting the nucleation of one (or more) intermetallic phases over all others. Alternatively, the change

in the morphology of the solidification structures, equiaxed dendrites as opposed to columnar, could affect the growth of certain intermetallics. Phases which find it difficult to alter their growth direction may have a growth disadvantage in the grain refined solidification structure over those which can.

TiB$_2$ seems to favour cubic α. When added to the A1 and A3 base alloys it caused cubic α to become the dominant intermetallic phase and eliminated a visible FTZ boundary. Some Al$_6$Fe occurred at lower cooling rates, away from the chill, but at trace level. The range of cooling rates at which cubic α forms has been extended to much lower values than in the base alloys, and Al$_x$Fe and Al$_3$Fe have been suppressed entirely.

In the A2 alloys the most obvious effects of TiB$_2$ addition were the relative promotion of Al$_6$Fe over Al$_3$Fe and the appearance of Al$_m$Fe. The FTZ was more visible in the A2 alloy with TiB$_2$ present than in any of the other alloys and was due to the transition from Al$_m$Fe, near the base, to Al$_6$Fe, higher up. This alloy was the only one in which Al$_m$Fe was detected. Westengen [5,7] attributed the FTZ to the different etching responses of Al$_m$Fe and Al$_6$Fe, and, indeed, the transition between these two species does produce a markedly more pronounced effect than associated with other transitions. However, the observations reported here show that the Al$_6$Fe / Al$_m$Fe transition is by no means the only one which can produce a visible FTZ. Note that in alloy A2 (as in alloys A1 and A3) the TiB$_2$ seems to have introduced some cubic α near the base of the ingot, albeit at trace level.

3.3.2.0 Binary Alloys

Figure 3.05 shows the distribution of intermetallic phases and the location of the visible FTZ boundary when present in the DC simulator binary alloys A1x and A2x. The micrographs of typical phases extracted from these samples together with corresponding XRD traces are shown in figure 3.03. The comparison of the binary Al-Fe to the ternary Al-Fe-Si ingots will show how the presence of Si influences phase selection as well as the individual effects of Mg, Ti and Ti-B trace additions.

3.3.2.1 Base Alloys

The different levels of Fe in the 1Ax and 2Ax alloys has had no effect on the macrostructure of the DC simulator cast ingots. Both displayed no visible FTZ and subsequent identification of intermetallics by SIBUT and XRD revealed that only Al$_6$Fe was present in the main bulk of the ingot. These findings are in   agreement with those of

Griger *et al* [55] who found that Al_6Fe was the only phase formed at low cooling rates in high purity hypoeutectic Al-Fe alloys with similar Fe concentrations to the alloys used in this study. This is in stark contrast to the ternary alloys where, in the presence of Si, the Fe concentration was shown to have a significant effect on intermetallic phase selection. Clearly, there is no ternary Al-Fe-Si cubic α present in the binary alloys. The more significant difference is that the presence of Si has surpressed the formation of Al_6Fe at positions in the ingot where it was common in the binary samples. Al_6Fe is present in the binary samples where before, in the ternary samples, Al_3Fe was found. This would suggest that the addition of Si encourages Al_3Fe to form at lower cooling rates or solidification rates than when it is absent. This corresponds with the findings of other workers [55,56] who have also stated that the formation metastable phases such as Al_6Fe (Al_xFe and Al_mFe) can be suppressed by increasing the amount of Si present. Figure 1.06 shows schematically the compositional limits of common phases found in dilute Al-Fe-Si alloys. From this it can be seen that Al_3Fe can contain a significant amount of Si whereas Al_6Fe is by no means so accommodating.. This does not, however, mean that the absence of Si necessarily precludes the formation of Al_3Fe, rather that the presence of Si inhibits the formation of Al_6Fe. The results from the experiments in this work show that the lack of Si favours the formation of Al_6Fe in high purity binary Al-Fe alloys solidified at low growth and cooling rates.

3.2.2.2 The Effect of Trace Additions.

As with the ternary alloys the effect of Ti and Mg additions will be dealt with separately to that of the addition of Ti-B refiner addition.

3.3.2.3 The Effect of Trace Element Additions to the A1x Base alloy.

The addition of Mg to A1x has not changed the phases found in the lower region of the ingot. However, higher up in the ingot a very faint FTZ boundary was visible. Only Al_6Fe was found below the boundary whereas Al_6Fe coexisted with Al_3Fe above the boundary. This result is consistent with the results from the experiments on ternary alloys where it was found that Mg favoured the formation of Al_3Fe.

The addition of Ti produced a visible FTZ at the fast cooled end of the ingot. Al_6Fe was found in the upper part of the ingot as in alloy A1x. The small area showing a different etching response adjacent to the shell was found to contain Al_mFe. In hypoeutectic binary alloys the critical cooling rate for the formation of this phase is not clear. The reported

values of critical cooling rates vary from 10°C s^{-1} [8] to over 35 °Cs^{-1} [4] and even over 500°Cs^{-1} [55] in high purity (4N) Al - 0.25 and 0.5 wt. % Fe alloys. In this alloy (Al - 0.2 wt. % Fe), Ti has had the effect of introducing Al$_m$Fe in the fast cooled region of the ingot. The shell zone of this particular ingot was thinner than others and the cooling rate and growth rate were, therefore, higher than in other ingots and it is possible that this contributed to the rather surprising result. The effect of Ti on the ternary ingots was small and, in all cases, eliminated a visible FTZ boundary between cubic α and Al$_3$Fe and Al$_6$Fe and Al$_3$Fe. The addition of Ti to the A1x binary alloy, however, results in a FTZ when the boundary is between Al$_6$Fe and Al$_m$Fe. This combination of intermetallics is known, however, to produce the most vivid FTZ due to the large difference in oxidation response between Al$_6$Fe and Al$_m$Fe.

3.3.2.4 The Effect of Trace Element Additions to the A2x Base Alloy

The addition of Mg and Ti to the A2x base alloys resulted in no change in the intermetallic phases in the ingots. The increase in Fe content in this alloy compared with the A1x base alloy has stabilised Al$_6$Fe even in the presence of the trace elements. The effect of increasing the Fe content in the ternary alloys with Mn and Ti additions was somewhat similar: in the low Fe alloy A1 (0.2 wt. % Fe) no Al$_6$Fe was seen whereas in both A2 and A3 alloys where the Fe content was higher (0.4 wt. % Fe) Al$_6$Fe was found in the faster-cooled area of the ingot with Al$_3$Fe in the slower cooled region.

The results are complex. It would appear that a lack of Si encourages the formation of Al$_6$Fe and that the higher the Fe content, the more this effect is seen. Mg is confirmed as promoting the formation of Al$_3$Fe, especially in the presence of Si, but, again, a higher Fe content may counter this effect.

3.3.2.5 The Effect of the addition of Ti-B Refiner to the Binary Alloys

As discussed in section 3.3.1.7, the effect of Ti-B grain refiner is probably on the nucleation behaviour of intermetallic phases and is treated separately as a result. The addition of Ti-B has had the largest effect on the intermetallic phases found in the binary alloys. This confirms the surprising conclusion, drawn from the ternary alloy results, that it not only affects nucleation of the primary aluminium dendrites but also the interdendritic eutectic.

The main effect of the addition of Ti-B refiner to the ternary alloys was to promote the formation of cubic α. Cubic α could not form, however, in the binary alloy where no Si was present. Despite this, as with the ternary alloys, the FTZ was the most visible in the binary alloys with a Ti-B addition.. In the A1x alloy a double FTZ was seen with Al_xFe being the only phase found in the region adjacent to the shell and Al_6Fe in the region above it. A mixture of approximately equal proportions of Al_6Fe and Al_3Fe was found in the FTZ above this. The presence of Al_xFe in a region having suffered a higher cooling rate than that where only Al_6Fe was discovered is surprising in that Al_xFe has been reported to form in binary alloys at intermediate cooling rates which straddle the Al_3Fe to Al_6Fe transition [8].

In the A2x base alloy with the Ti-B addition, a single FTZ was observed with a mixture of mainly Al_mFe and some Al_6Fe found in the region adjacent to the shell. As this region was so narrow, it is probable that, although care was exercised, the sample taken for extraction contained material from both above and below the boundary. It is likely then, that this region contained only Al_mFe and that the Al_6Fe was there as a result of sampling error. The region above this, within the FTZ, contained a mixture of Al_6Fe and Al_3Fe.

3.3.3 Cooling Rates in the DC Simulator

The cooling rates were determined from the temperatures logged by the thermocouples inserted in the samples. The cooling rates ranged from approximately 16 °C s^{-1} at 20 mm from the base, through 3 °C s^{-1} at 50 mm and 0.7 °C s^{-1} at 100 mm. The cooling rates experienced in commercial DC casting vary depending on the size of the ingot and casting conditions. Quoted values range from 1 up to between 10 to 20 °C s^{-1} [7,24]. The cooling rates found in the DC simulator are within this range. More importantly, it was possible to reproduce the FTZ observed in DC cast ingots, in the DC simulator and hence examine the effect of alloy composition on the formation of the FTZ.

3.4 Discussion

The effects of V and Ti additions on phases formed in the ternary alloys are small. In alloys A1 and A2 the effect was minimal and only slightly more marked in A3. In the binary alloys the effect of Ti was also small. However, the fact these elements have had any effect at all is surprising as they both partition to the solidifying Al rather than the liquid. The slight effects observed, however, show that very small levels of impurity can affect solidification behaviour.

From these results, it might seem that the answer to the problem of the FTZ in low Fe-low Si aluminium alloys may be to add Mn or Ti at the stated levels and, regardless of the phases actually present, the FTZ would be eliminated. In commercial practice, however, the alloys used do not have the same levels of purity   as the alloys used in this work. Individual impurity elements can exist in commercial purity alloys at levels as high as 0.07 wt. % and financial considerations make it impossible to achieve any higher level of purity than this. Consequently, a full understanding of how each element affects the solidification behaviour is needed before the problem of the FTZ can be fully eradicated in commercial alloys.

3.4.1 The Effect of Trace Elements on the Growth Velocities of Intermetallic Phases

The effects of each of the trace additions to these alloys has been described already in some detail, and it would be appropriate to speculate on the mechanisms which cause the changes in intermetallic found in the ingots. If the transitions between the phases occur in the base alloys at defined local solidification front velocities (U) then a plot of U against solidification front temperature, T, can be used to explain the transition in terms of a competitive growth model. This has been used often to describe eutectic growth in binary Al-Fe systems [49,57,58]. Essentially, this model assumes that the phase which can grow fastest at a given temperature will be that which forms. Implicit in this assumption is that all phases which are thermodynamically possible to form can nucleate with equal ease. Figure 3.08 shows how a phase selection model based on competitive growth applies to the DC Simulator ingots. A more detailed examination of this concept is conducted in chapter 5. Figure 3.08 shows a schematic of U versus T for the two phases Al_3Fe and Al_6Fe with and without a trace element present (these two phases are used as an example), the effect of the trace addition on the transition velocity, and the resultant movement of the FTZ boundary. Plots of velocity vs. growth temperature have been produced for the Al_3Fe to Al_6Fe transition in an Al-3 wt. % Fe directionally solidified in a Bridgman furnace [49]. The plots give an indication of the solidification velocity needed for one phase to displace another as the dominant intermetallic.

The addition of trace elements could alter the growth velocity of a phase at given interface temperature thus causing it to lose out to another competing phase. This might occur because either:

(i)   the trace element poisons the site at which liquid atoms attach to the solid intermetallic. This mechanism might lead to a significant decrease in growth velocity if the intermetallic possessed a faceted interface which advanced by step-wise growth rather than a non-faceted interface growing in a continuous manner. Or

(ii)   the trace element segregates positively in the liquid at the liquid intermetallic interface. This would increase the solutal undercooling at the intermetallic front and depress the growth velocity.

Those elements which segregate positively into the interdendritic liquid and out of the aluminium dendrites prior to the formation of the intermetallic particles will tend to be effective at a lower trace level.

The dotted line in the U-T diagram shown in figure 3.08c shows the effect of an addition which decreases the growth velocity for the Al_6Fe phase. The transition velocity from Al_3Fe to Al_6Fe has increased, causing the Al_6Fe/Al_3Fe boundary to move closer to the base of the ingot. This is only one possible scenario and assumes that the addition affects the growth velocity of one phase only. The situation becomes more complex when, say, three phases can form in the growth velocity range experienced in the ingot and the addition affects the growth velocities of more than one phase. Also, it is possible that an addition could alter growth velocities to such an extent that one phase would never be seen as the transition velocity becomes higher than any experienced in the DC simulator. The simple competitive growth model, however, does show conceptually how the FTZ may be extended or reduced in size, and how one phase might disappear from the ingot as a result of the addition of another element at trace level.

3.4.2   On the Existence of Multiple Phases in the Same region in the Ingot

The occurrence of two phases in the same place in the ingot was mentioned earlier. In most case, only one phase is found near the base of an ingot, but higher up, in the region of the lower solidification rates, it was not uncommon to find two phases co-existing. Where two phases were found together, usually one was dominant and the other was at a trace level. This can be explained in terms of the solidification velocity profile in figure 3.08b. The transition which causes the FTZ is usually found in the region where the highest solidification rates are encountered. At this time in the solidification of the ingot, the rate of change of solidification velocity is also the highest. If a transition between one type of intermetallic occurs over a range of solidification velocities, it will occur over a shorter

distance at the chill end of the ingot than it will higher up. Thus, the boundary will be more diffuse in the region where solidification occured more slowly and this would cause any change in surface etching response to be less visible. There are several reasons why the transition could happen over a range of solidification velocities. Firstly, it is known that the phase Al_3Fe, when growing as a eutectic, can have difficulties in adjusting its interphase spacing as a result of its rigid growth mode [35]. Even if it is the phase which would grow the fastest under optimum conditions, if it cannot alter its spacing quickly enough then Al_6Fe may still be able to grow in preference and two phases may then co-exist locally. Secondly, if Al_3Fe does not grow in a continuous manner but needs repeated nucleation over a range of cooling rates then Al_6Fe may continue to grow for a considerable distance before being completely replaced by Al_3Fe. Thirdly, because of the presence of trace components (particularly if they concentrate in the interdendritic liquid), even in a nominally binary Al-Fe alloy, it may be possible for more than one intermetallic to grow over a range of temperatures.

When two phases are found co-existing in the same area, the sample was probably taken from near the centre of a diffuse phase transition. When one phase is dominant, it probably means that the sample was taken from one side of the diffuse transition.

3.4.3 The effect of Ti-B and Trace Elements on the Nucleation Behaviour of Intermetallic Phases

The change in intermetallic solidification behaviour when any addition is made which affects the ability of one or more phases to nucleate, in particular, Ti-B grain refiner, can be explained in terms of an isothermal nucleation diagram (IND). The schematic IND in figure 3.09 shows the nucleation 'C' curves for two different intermetallics P1 and P2, where P1 is the equilibrium phase such as Al_3Fe and P2 is a metastable phase such as Al_6Fe. If the cooling rate $\phi1$ is employed, the first phase to nucleate will be P1. If a higher cooling rate $\phi2$ is employed, the first phase to nucleate will be P2.

The cooling rate profile along the DC simulator ingot is similar in form to the solidification rate profile shown schematically in figure 3.08b. The addition of grain refiner can assist the nucleation of a particular phase, as can be seen in alloys A1 and A3: when TiB_2 is added, cubic α has nucleated at a much lower cooling rate than in the base alloys whereas in the A2 alloy the addition of TiB_2 has assisted the nucleation of Al_mFe. This is probably because hexagonal TiB_2 promotes the nucleation of phases with higher symmetry,

such as cubic α and tetragonal Al_mFe, rather than those with lower symmetry, such as orthorhombic Al_6Fe and monoclinic Al_3Fe. This can be seen on the schematic IND as a shifting to the left of, say, the P2 curve. With the addition of Ti-B grain refiner, it can be seen that both cooling rates $\phi1$ and $\phi2$ will bring about the nucleation of P2 only. In effect, the range of cooling rates over which P2 can nucleate has been extended.

3.4.4 The Combined Role of Cooling Rate and Growth Velocity in Intermetallic Phase Selection

The effect of the addition of Ti-B grain refiner on intermetallic phase selection suggests that there are limitations to the application of a purely competitive growth model in these systems. It thus appears that both the nucleation and growth aspects of solidification need to be considered when attempting to understand phase selection and its effect on the formation of the FTZ. It is true that some additions may only affect growth behaviour whilst others only affect nucleation behaviour. However, in the context of the DC casting of commercial purity aluminium alloys, rather than the model alloys used in this study, a mixture of impurity and alloying elements which can affect either or both of these parameters makes the situation complex indeed.

In order to quantify the effect of some of the elements used as trace additions, experiments need to be conducted which isolate either the growth velocity or the cooling rate as a single variable. By using base alloys, and then making trace element additions and comparing the results it will be possible to see whether the addition is having an effect on the growth temperature at a given velocity or the nucleation temperature at a given cooling rate. The following two chapters describe an attempt to quantify the effect of individual elements on intermetallic phase selection in terms of their effect on growth velocity and nucleation temperature.
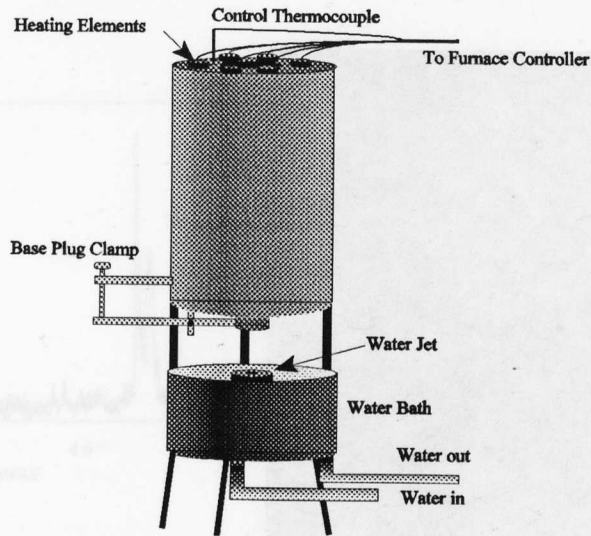
Figure 3.01. A Sketch of the DC Simulator and water cooling apparatus
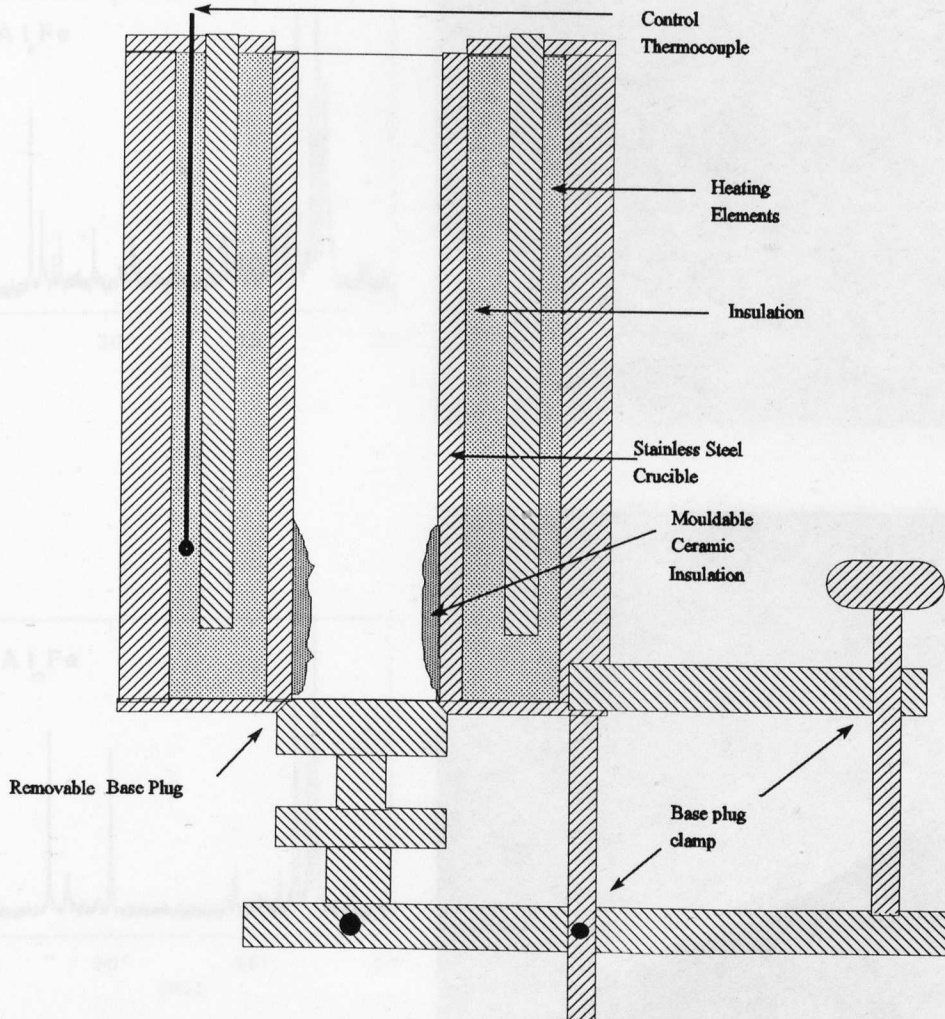
Figure 3.02. A cross section of the DC simulator showing the base clamp arrangement.
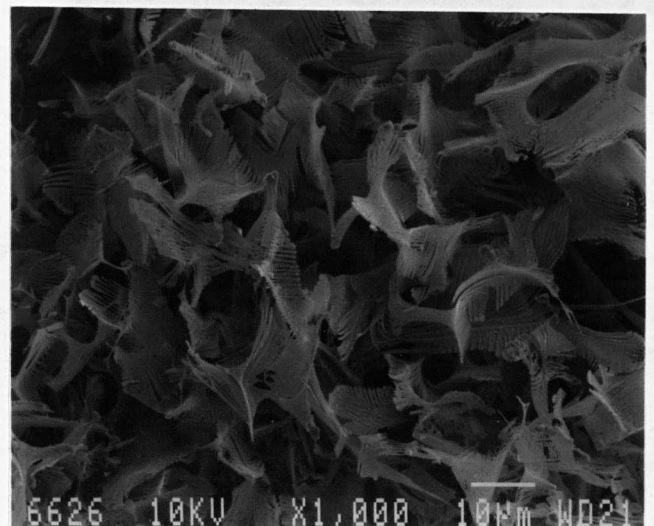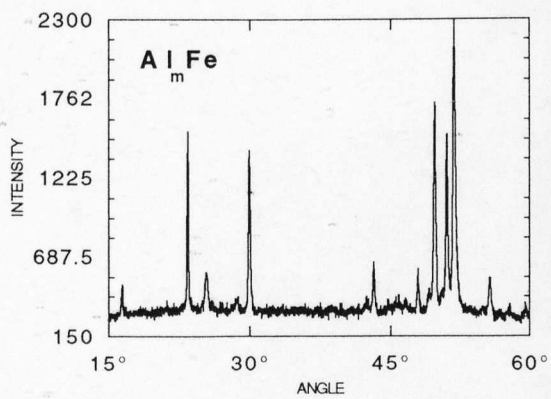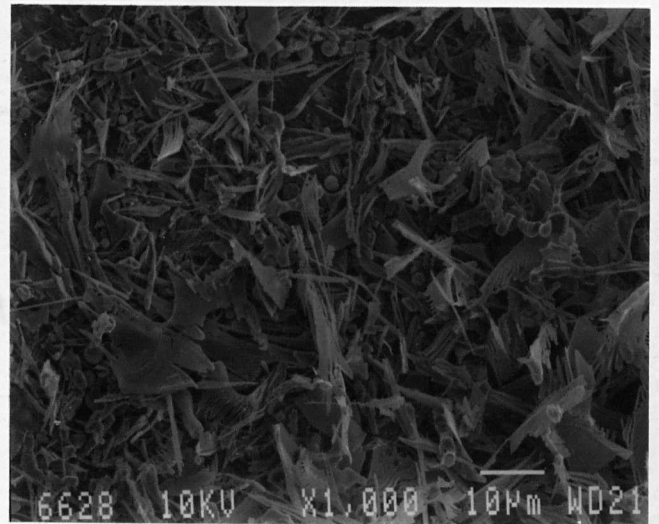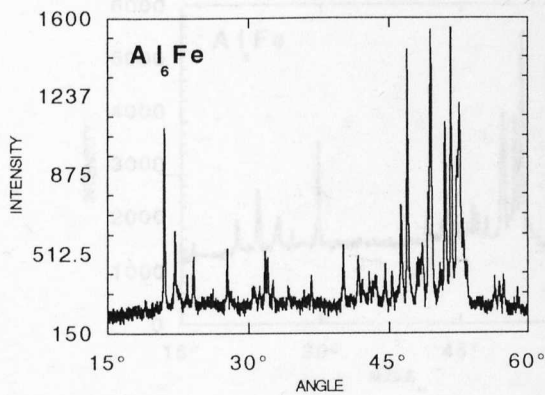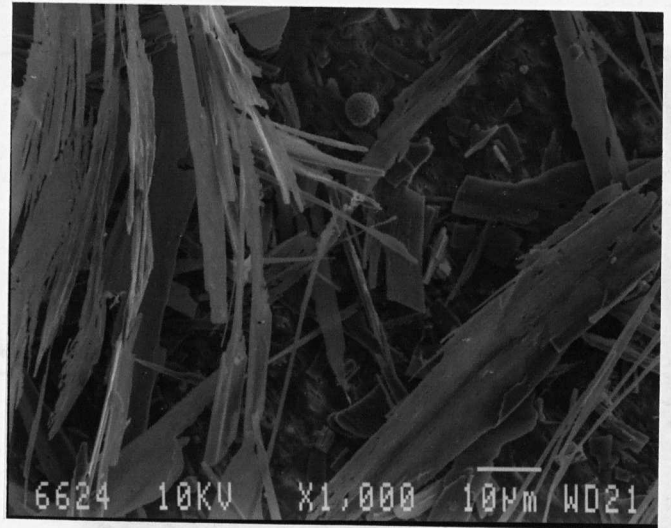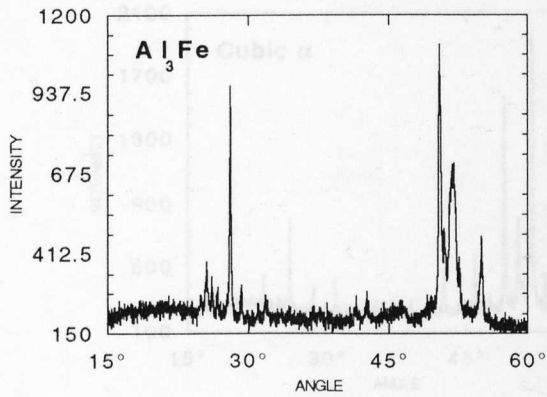
Figure 3.03: Typical XRD and SEM traces of the intermetallic phases extracted from
the DC simulator ingots.
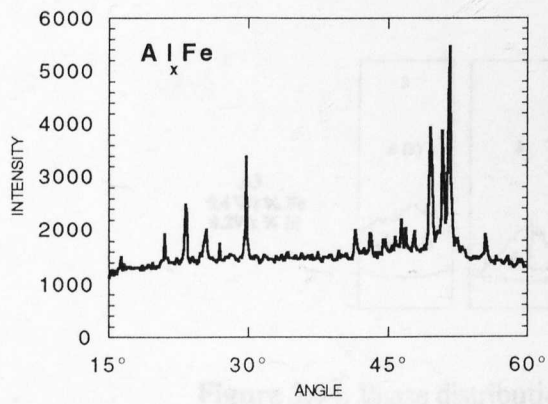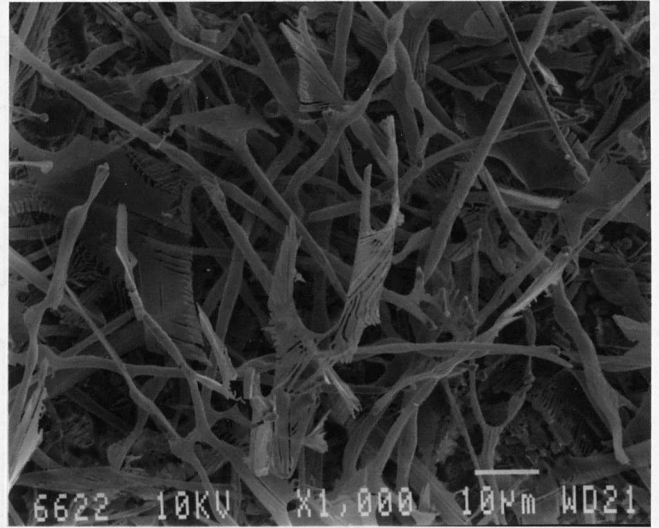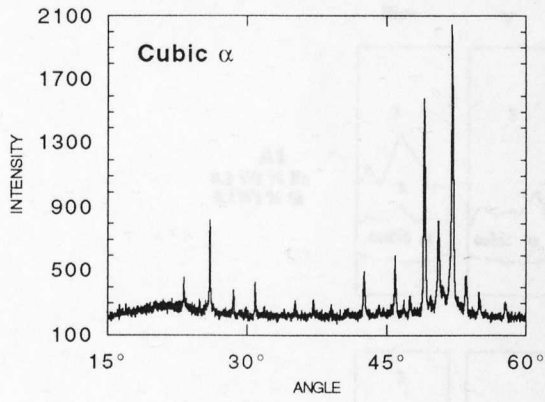
Figure 3.03: Typical XRD and SEM traces of the intermetallic phases extracted from the DC simulator ingots.
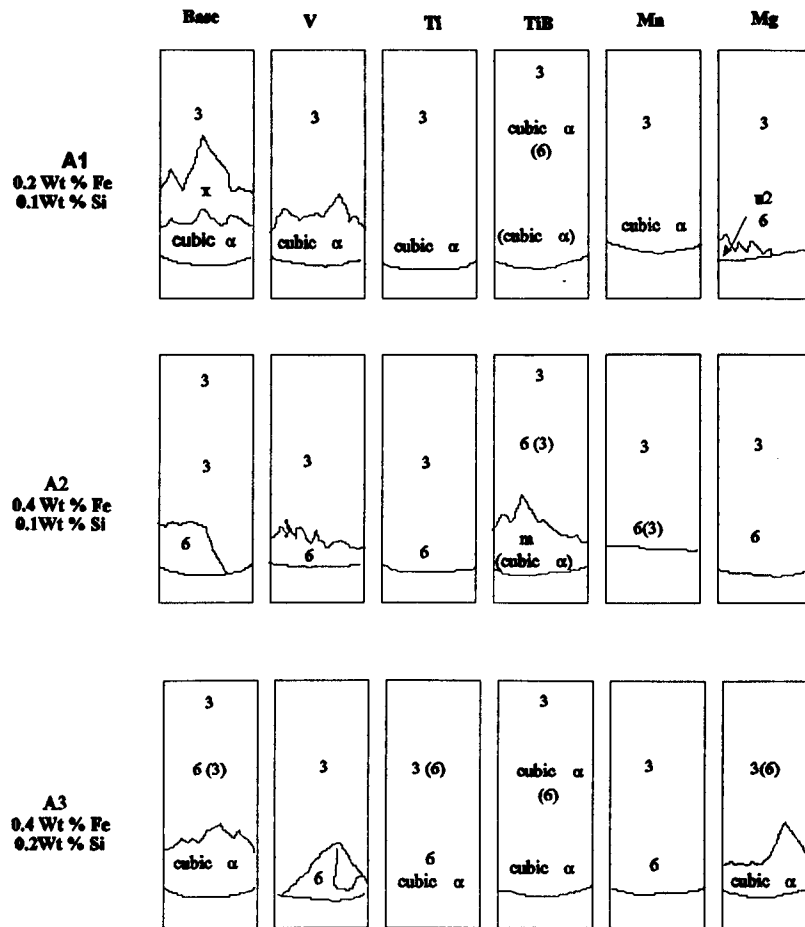
Figure 3.04. Phase distribution in ternary AlFeSi ingots.(For key see previous page).

69

Key to figures 3.03 and 3.04 3 = Al$_3$Fe, 6 = Al$_6$Fe, x = Al$_x$Fe, m = Al$_m$Fe, α = cubic α AlFeSi. Where more than one phase was present, the phase shown in parentheses was less dominant.
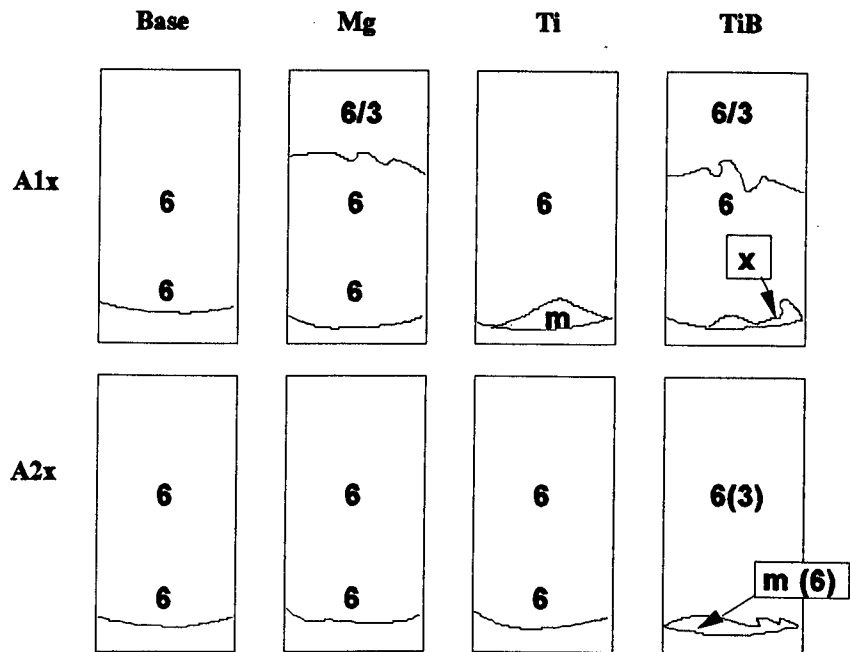
Figure 3.05 Phase distribution in Binary Al-Fe ingots.
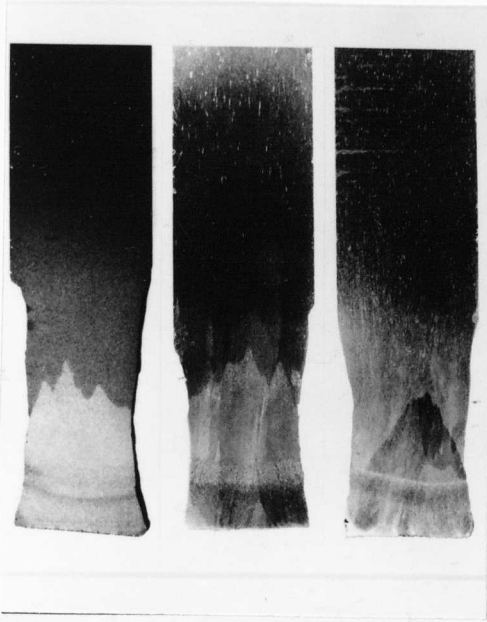
Figure 3.06a. Photographs of some FTZs in the ternary alloys: left to right - A2TiB, A3 and A3V.
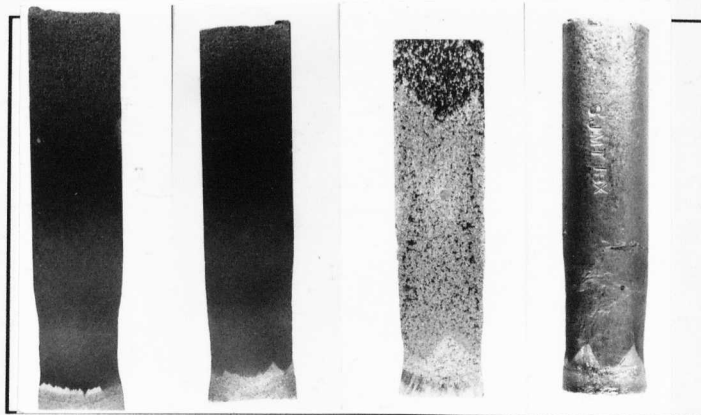
Figure 3.06b, Photographs of some FTZs in the binary ingots; left to right - A1xTiB, A2xTiB and A1xTi (front and back).
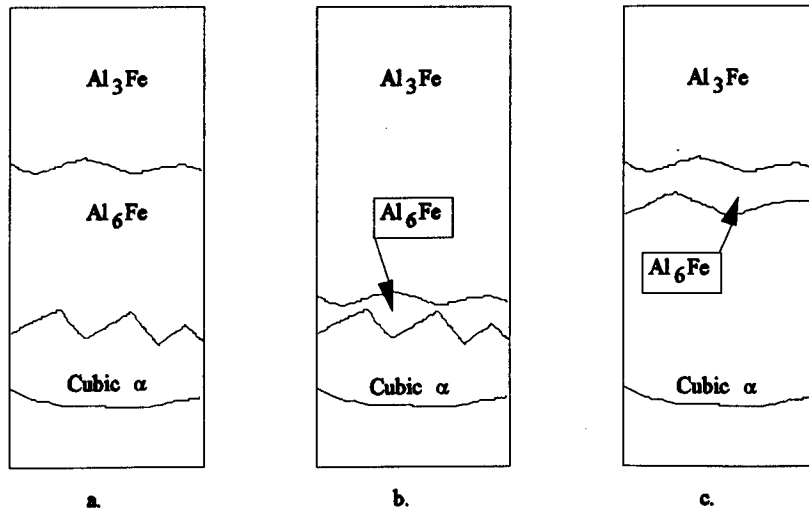
Figure 3.07. The possible effects of trace elements on phase fields in DC Simulator ingots. a.shows a possible situation with no trace element present. b. shows the same ingot with an addition which promotes Al_3Fe over Al_6Fe.c. shows the situation with an element which promotes cubic α over Al_6Fe
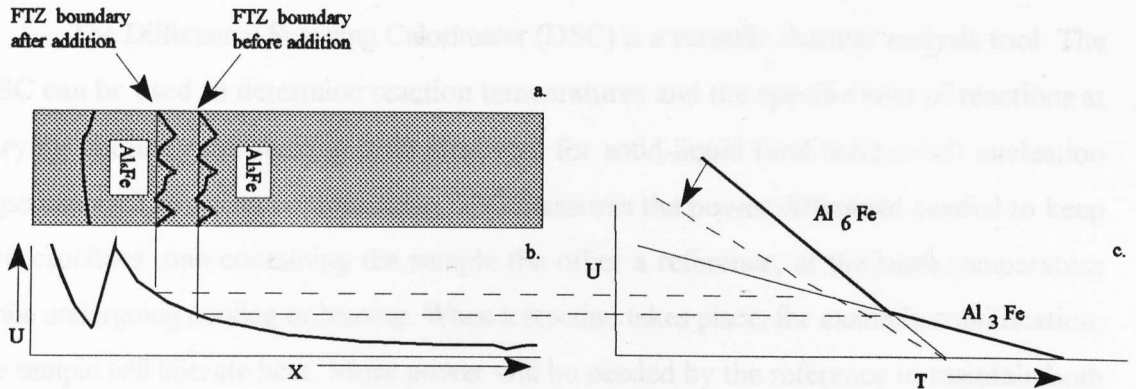
Figure 3.08. The competitive growth theory applied to phase selection in the DC Simulator ingot. **a.** shows a sketch of the ingot macrostructure. The two different FTZ boundaries represent the case with and without a trace element addition. **b.** shows the schematic variation in solidification velocity, U, with distance from the base of the ingot: the transition velocity in the presence of the trace addition occurs closer to the base of the ingot. **c.** explains how this could happen in terms of the growth temperature. The variation in growth temperature for the two competing eutectics Al-Al$_3$Fe and Al-Al$_6$Fe are shown. The continuous lines represent the base alloy, the broken lines show the effect of a trace addition which lowers the growth velocity of the Al-Al$_6$Fe eutectic, for a given growth temperature, while leaving the other eutectic unaffected. The addition of the trace element has increased the transition velocity and moved the FTZ boundary nearer the base of the ingot.
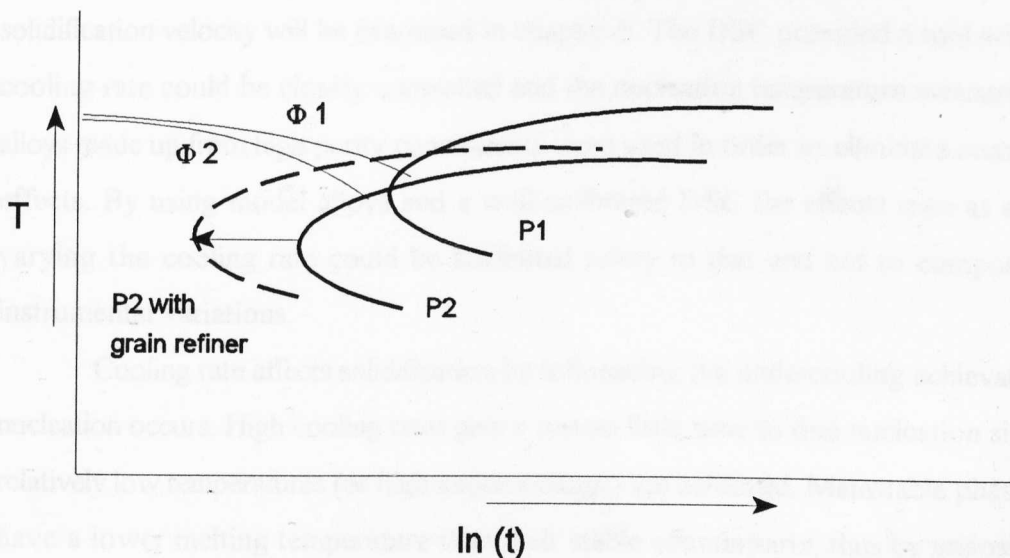
Figure 3.09. The schematic isothermal nucleation diagram for two phases P1 and P2. With no grain refiner present, at a cooling rate Φ1, the phase P1 nucleates, whereas at cooling rate Φ2 the phase P2 nucleates. With grain refiner present, which favours the nucleation of P2, both cooling rates result in the nucleation of P2.

4.0 Differential Scanning Calorimetry (DSC)

4.0.1 Introduction

The Differential Scanning Calorimeter (DSC) is a versatile thermal analysis tool. The DSC can be used to determine reaction temperatures and the specific heat of reactions at varying cooling rates making it an ideal tool for solid-liquid (and solid-solid) nucleation experiments. The power compensating DSC measures the power difference needed to keep two crucibles, one containing the sample the other a reference, at the same temperature while undergoing cooling or heating. When a reaction takes place, for example solidification, the sample will liberate heat. More power will be needed by the reference to maintain both at the same temperature. The DSC measures the differential power and can plot this against a time or temperature scale. Information can be derived from this regarding the reaction: the reaction onset temperature, the specific heat of reaction (endothermic and exothermic) and the peak temperatures. More specifically, the cooling rate can be varied so that its effect on the reaction can be established, and it is this facility which is employed here.

4.0.2 Aims

The main aim of the DSC experiments was to isolate the effect of cooling rate on the nucleation of the eutectic phase. The two main factors affecting phase selection, other than the composition of the alloy itself, are cooling rate and solidification velocity. The effect of solidification velocity will be examined in chapter 5. The DSC provided a tool whereby the cooling rate could be closely controlled and the nucleation temperature measured. Model alloys made up from high purity constituents were used in order to eliminate compositional effects. By using model alloys and a well-calibrated DSC the effects seen as a result of varying the cooling rate could be attributed solely to that and not to compositional or instrumental variations.

Cooling rate affects solidification by influencing the undercooling achievable before nucleation occurs. High cooling rates give a system little time to find nucleation sites before relatively low temperatures (or high undercoolings) are achieved. Metastable phases always have a lower melting temperature than their stable counterparts; thus by imposing a high cooling rate it is possible to cool the system below the melting temperature of a metastable phase before any of the stable phase has had time to nucleate. If the metastable phase does not need such a large undercooling below its melting temperature to nucleate then it is possible that the stable phase will be replaced by the metastable phase. This occurs in the Al-

Fe system with the binary eutectics Al-Al$_3$Fe and Al-Al$_6$Fe where Al$_3$Fe has nucleation difficulties in that it does not easily nucleate heterogeneously on α-aluminium whereas Al$_6$Fe has less of a problem. Consequently, although the eutectic temperature of Al-Al$_3$Fe is 3 to 5 °C above that of Al-Al$_6$Fe, the nucleation temperature at high cooling rates is, in fact, lower. The aim of the following set of experiments was to examine, firstly, how the nucleation temperature varies with cooling rate in two dilute model binary Al-Fe alloys and to see if a change in intermetallic phase could be detected and, secondly, to examine whether trace additions of Mg, Ti and Ti-B grain refiner affect the nucleation temperatures and/or the phase transition.

The addition of trace elements was examined in Chapter 3. It was found that they can have a significant effect on the intermetallic phase selection. By isolating a single variable, the cooling rate, it was hoped that some of the effects seen in those experiments could be explained.

The most definitive method of phase identification is the analysis of TEM diffraction patterns. These give a unique fingerprint of a material as long as the material has been well characterised in terms of its crystallography. The major drawback of TEM diffraction pattern analysis is the time scale and the skill level needed to obtain meaningful results. The aim of the EDX analysis part of this work was to develop a technique for the identification of intermetallics in the dilute Al-Fe system which was quick and relatively easy to use. The technique relied on the fact that the iron level in each of the possible intermetallics was different and, that by removing them from the matrix, they could be identified unambiguously by EDX.

4.1 Experimental Technique

4.1.1 Alloy Selection

Binary Al-Fe alloys were used in the DSC experiments. Two base alloys were selected: Al-0.2 wt. % Fe and Al- 0.4 wt. % Fe. These were made up from superpurity Al and Al-Fe master alloy. The additions were made using 5N purity Mg, Al-Ti master alloy (Al-5 wt. % Ti) and commercial purity Ti-B refiner. The alloy compositions are shown in table 4.01. The level of trace element additions were based on the levels of these elements commonly found as impurities in certain alloys produced by Alcan. The levels of these additions were the same as those made to alloys cast in the DC simulator experiments.

Alloy Designation	wt.% Fe	wt. % Mg	wt. % Ti	wt. % Ti-B
1x	0.2	-	-	-
2x	0.4	-	-	-
1xMg	0.2	0.02	-	-
2xMg	0.4	0.02	-	-
1xTi	0.2	-	0.04	-
2xTi	0.4	-	0.04	-
1xTiB	0.2	-	-	0.04
2xTiB	0.4	-	-	0.04

Table 4.01: Composition of alloys used in the DSC experiments.

4.1.2 Sample Preparation

Samples were prepared for DSC experiments by melting 200 g of the above alloys in an induction furnace and casting into a small conical mould. Spectrographic analysis of these castings was used to determine their chemical composition. A small block was sawn from each casting and from this a 0.5 mm slice was cut using a Buehler ISOMET low speed saw with a diamond cutting wheel. Discs were punched from these samples using a 3 mm diameter hand punch. Each sample was cleaned on both sides and ground to a mass of 5 mg (± 0.3 mg) using emery paper. It was important to know and define the mass of the specimens so that the instrument calibration (described below) was valid.

4.1.3 Calibration of the DSC

Before any experiments could be carried out the DSC required two different calibrations. The first calibration ensured that the DSC was measuring the correct temperatures and was performed by the DSC internal software. The second calibration took into account the thermal lag of the instrument.

To perform a temperature calibration, the instrument required two melting temperatures to be measured on heating. The melting temperature is not affected by heating rate in the same way that solidification is since, whilst it is relatively easy to undercool a melt prior to solidification, it is virtually impossible to superheat a solid prior to melting. The melting temperature of pure Zn and pure Al samples weighing approximately 5 mg were measured at a heating rate of 10 °C min^{-1}. The measured melting temperatures and the

accepted melting temperatures were entered into the computer calibration software which could then automatically compensate for any discrepancy.

The second calibration took into account the different thermal lag brought about by varying the cooling rate. At high cooling rates the delay between the actual reaction onset and the time when the instrument senses it is higher than at low cooling rates. This delay is called the instrumental thermal lag. A second order reaction, whose reaction temperature was not dependent on cooling rate was used to calibrate for this. Solidification temperature could not be used as both the actual undercooling and the thermal lag vary with cooling rate and would not be separable. The Curie transformation of nickel is a well defined second order transformation which is measurable in the DSC. The transformation occurs at 358°C. A pure Ni (99.999 wt. %) sample, weighing 5 mg, was cooled through the Curie point at cooling rates ranging from 5 to 80 °C min^{-1} (the range of cooling rates over which the experiments would be conducted). Because the transformation was second order, and not affected by cooling rate, any variation in the reaction onset temperature could be attributed to instrumental thermal lag. The measured Curie temperatures were plotted against cooling rate using the Kaleidagraph spreadsheet software on an Apple Macintosh computer. A straight line was fitted to the data using a least mean square analysis built into the software and a relationship was found to describe it in terms of the cooling rate and observed Curie temperature. The relationship was then used to adjust results from the following experiments so that the thermal lag effect was eliminated. All values of nucleation temperature quoted below have had the thermal lag calibration applied to them.

4.1.4 Nucleation Onset Temperature Experiments.

A Perkin-Elmer DSC-7 with a TAC7/PC instrument controller linking the DSC with an IBM model 50Z personal computer was used for these experiments. Glassy carbon crucibles (of 5 mm internal diameter) with lids were used in the DSC to contain the samples. The DSC was cooled with liquid nitrogen and Pureshield argon provided an inert gas atmosphere for the furnaces.

Each sample was cooled from fully liquid to solid at cooling rates spanning two orders of magnitude; 1, 5, 10, 20, 40 ,60, and 80 °C min^{-1}. Each sample was taken up to above 700°C and held at that temperature to ensure complete melting. At least one minute of cooling was allowed before any solidification would take place to ensure that a baseline had been established and that any transient effects had been eliminated. Data were collected

in the form of power difference versus temperature (the DSC software converts the time scale to temperature) and stored on floppy disc for subsequent analysis. In most cases the same sample could be used for a full set of experiments by remelting it for each different cooling rate. However, the samples with Ti-B additions were changed for every run because the effect of the TiB_2 phase, responsible for enhanced nucleation, has been shown to fade with repeated melting [32]. This effect is thought to be related to the settling of the TiB_2 particles responsible for the grain refinement. Samples solidified at 1 and 80 °C min^{-1} were saved for phase identification by EDX in the TEM (see chapter 2).

4.1.5   Deconvolution of DSC Peaks

The data required from the DSC experiments were the nucleation or onset temperatures of the eutectics. The plots of differential power (P) versus temperature (T) showed peaks corresponding to the nucleation of the primary aluminium at the beginning of solidification and that of the eutectic towards the end of solidification, see figure 4.01. Variations in cooling rate do not necessarily alter the undercooling needed for nucleation of the primary aluminium and the eutectic by the same amount and higher cooling rates cause peak broadening. At low cooling rates the two peaks were clearly separate, see figure 4.01a, and the onset temperature for the eutectic phase was easily inferred from the plot by finding the point where the eutectic peak met the baseline. However, the higher cooling rates (approximately 20 °C min^{-1} and above) caused the peaks to overlap obscuring this point, see figure 4.01(b). In order to determine the eutectic onset temperature, a curve fitting routine was employed which deconvoluted the two peaks by describing them as two asymmetrical Gaussian functions. With a mathematical description of the peak the onset temperature could be calculated. Although there is no theoretical justification for such a representation, the shape of a DSC solidification peak is, indeed, similar in shape to a Gaussian peak and this technique has been employed for other alloy systems [59]

In this work, the DSC cooling curve P(T) is represented as a sum of three functions:

$$P(T) = B(T) + G_{Al}(T) + G_{Eu}(T) \qquad\qquad 4.01$$

B(T) is a 3rd order polynomial representing the DSC baseline in the region of the primary aluminium and eutectic peaks:

$$B(T) = a_0 + a_1 T + a_2 T^2 \qquad\qquad 4.02$$

$G_{Al}(T)$ and $G_{Eu}(T)$ are asymmetric Gaussian functions representing the primary aluminium and eutectic peaks respectively:

$$
G_{Al}(T) = G_{Al}^0 \exp\left(-\frac{(T - T_p^{Al})^2}{\sigma_1^2}\right) : T \geq T_p^{Al}
$$

$$
= G_{Al}^0 \exp\left(-\frac{(T - T_p^{Al})^2}{\sigma_2^2}\right) : T \leq T_p^{Al}
\qquad 4.03
$$

$$
G_{Eu}(T) = G_{Eu}^0 \exp\left(-\frac{(T - T_p^{Eu})^2}{\sigma_3^2}\right) : T \geq T_p^{Eu}
$$

$$
= G_{Eu}^0 \exp\left(-\frac{(T - T_p^{Eu})^2}{\sigma_4^2}\right) : T \leq T_p^{Eu}
\qquad 4.04
$$

where G_{Al}^0 and G_{Eu}^0 are the peak heights, T_p^{Al} and T_p^{Eu} are the peak temperatures and σ_1, σ_2 and σ_3, σ_4 are the pairs of half breadths (peak breadth at half height) for the primary aluminium and eutectic solidification reactions respectively.

Asymmetric Gaussian functions in this form, i.e.:

$$
G(T) = G^0(T) \exp\left(-\frac{(T - T_p)^2}{\sigma_1^2}\right) : T \geq T_p
$$

$$
= G^0(T) \exp\left(-\frac{(T - T_p)^2}{\sigma_2^2}\right) : T \leq T_p
\qquad 4.05
$$

are shown in figure 4.02 (a) (where $\sigma_1 = \sigma_2$ and a conventional symmetric Gaussian peak results) and figure 4.02(b). As may be seen, figure 4.02 does bear a marked resemblance to a typical DSC peak for solidification of these alloys (figure 4.01a). Furthermore, this mathematical description of the DSC peaks gives a smooth function, whose first derivative is continuous at the peak temperature, and which is amenable to least-squares fitting to

experimental data. The fitting routine returns the peak temperature directly and, as will be shown in section 4.1.6, the onset temperature is a simple function of the peak temperature and the half breadth.

The function P(T) was fitted to the experimental data from the DSC for each of the experiments in turn by employing the least squares fit method. The adjustable parameters were (a_0 to a_2), G_{Al}^0, G_{Eu}^0, T_p^{Al}, T_p^{Eu}, σ_1, σ_2, σ_3, and σ_4. Whilst a computer program could have been written to perform this, it was convenient to employ the solver routine in the Microsoft Excel spreadsheet package, an example of which is shown in figure 4.03. The first column shows the raw differential power data obtained from the DSC. The second column shows the measured temperature(T). The third column contains actual differential power derived from the data in the first column by multiplying by a scaling factor obtained from the DSC data file. The next three columns contain computed values of the polynomial baseline B(T) and asymmetrical Gaussian functions for each of the peaks $G_{Al}(T)$ and $G_{Eu}(T)$. which when added together formed a set of data which was fitted to the measured data by adjustment of the peak and baseline parameters.

The spreadsheet was designed to allow the initial values of the fitting parameters to be adjusted by the operator to obtain a reasonable fit before the least means square fitting routine was employed. This reduced the time taken to fit curves to the large data files involved and prevented the fitting routine from finding divergent solutions. The box to the right of the data columns contains these variable parameters. Each fitting routine took between 20 and 120 minutes to complete, depending on the size of the data file.

4.1.6 Calculation of Onset Temperature from Fitted Curves

In these experiments it was assumed that the nucleation temperature T_N was the same as the onset temperature T_0 and that this was defined as the temperature at which the solidification peak met the base line. The DSC manufacturers recommended method of finding onset temperatures for a single peak was described in the Perkin Elmer DSC 7 users' manual. The point of intersection of a tangent to the point of the steepest gradient on the peak with the base line is defined as the onset temperature. The fitted Gaussian function descriptions of the peaks allowed this intersection to be mathematically derived.

In order to derive an expression for the onset temperature for the eutectic reaction, we need only to consider the Gaussian description of the eutectic peak in the temperature range $T \geq T_p^{Eu}$, i.e.

$$G_{Eu} = G_{Eu}^0 \exp\left(-\frac{(T - T_p^{Eu})^2}{\sigma_3^2}\right) \qquad 4.06$$

The steepest gradient of this function, i.e. where dG_{Eu} / dT is a maximum, occurs at the point of inflection, (T', G'_{Eu}) where $d^2G_{Eu} / dT^2 = 0$ (figure 4.02 (c)). At this point:

$$\frac{dG_{Eu}}{dT}\bigg|_{T=T'} = G_{Eu}^0 \frac{2(T_p^{Eu} - T')}{\sigma_3^2} \exp\left(-\frac{(T' - T_p^{Eu})^2}{\sigma_3^2}\right) \qquad 4.07$$

and

$$\frac{d^2G_{Eu}}{dT^2}\bigg|_{T=T'} = G_{Eu}^0 \left[-\frac{2}{\sigma_3^2} \exp\left(-\frac{(T' - T_p^{Eu})^2}{\sigma_3^2}\right) + \left(\frac{2(T' - T_p^{Eu})}{\sigma_3^2}\right)^2 \exp\left(-\frac{(T' - T_p^{Eu})^2}{\sigma_3^2}\right)\right] = 0$$

$$4.08$$

The non-trivial solution to the equation (4.08) gives:

$$T' = T_p^{Eu} + \frac{\sigma_3}{\sqrt{2}} \qquad 4.09$$

and the gradient of the tangent to this point is:-

$$\frac{dG_{Eu}}{dT}\bigg|_{T=T'} = -\sqrt{2}\frac{G_0^{Eu}}{\sigma_3} \exp\left(-\frac{1}{2}\right) \qquad 4.10$$

Substituting equation 4.09 into 4.06 gives

$$G'_{Eu} = G_{Eu}^0 \exp\left(-\frac{1}{2}\right) \qquad 4.11$$

The equation of a the tangent to G_{Eu} (T) at (T', G'_{Eu}) is thus:

$$G = -\left(\sqrt{2}\frac{G_{Eu}^0}{\sigma_3} \exp\left(-\frac{1}{2}\right)\right) T + \left(2 + \sqrt{2}\frac{T_p^{Eu}}{\sigma_3}\right) G_{Eu}^0 \exp\left(-\frac{1}{2}\right) \qquad 4.12$$

which intersects the T-axis at the point $(T_0, 0)$, where T_0^{Eu} is the onset temperature of the peak. Thus:

$$\left(\sqrt{2} \ \frac{G_{Eu}^{0}}{\sigma_3} \ exp\left(-\frac{1}{2} \right) \right) T_0^{Eu} + \left(2 + \sqrt{2} \ \frac{T_p^{Eu}}{\sigma_3} \right) G_{Eu}^{0} \ exp \left(-\frac{1}{2} \right) = 0 \qquad 4.13$$

which leads to the simple expression:

$$T_0^{Eu} = \sqrt{2} \ \sigma_3 + T_p^{Eu} \qquad 4.14$$

By a similar argument, the onset temperature for the primary aluminium solidification reaction could also be determined:

$$T_0^{Al} = \sqrt{2} \ \sigma_1 + T_p^{Al} \qquad 4.15$$

These simple formula were written into two cells in the spreadsheet described above so that the onset temperature was automatically calculated after the DSC peaks had been deconvoluted by the fitting routine. Examples of the fitted curves shown with the experimentally obtained data are shown in figure 4.04. The calculated curves fit well around the eutectic peak with those obtained from the experiments.

The values for eutectic onset temperature were plotted against cooling rate for each of the alloy systems investigated. The technique only allowed confident peak deconvolution for cooling rates up to 80 °C min^{-1}. Above this cooling rate the least mean square fitting routine within Microsoft Excel could not find a convergent solution. This restricted the range of cooling rates to relatively low values (80 °C min^{-1} = 1.33 °C s^{-1}).

The error in onset temperature was estimated to be just less than 1 °C by repeating the same DSC experiment on some of the samples 3 to 4 times, calculating the onset temperatures in each case and determining an average value of scatter in the results for an individual sample. This value dictated the size of the error bars shown on the plots of onset temperature vs. cooling rate in figure 4.05.

4.1.7 DSC Experiments on an Al 1 wt. %-Ni Alloy

The Al-Ni system contains a eutectic between α-Al and Al$_3$Ni. Which, in contrast to the Al-Fe system, is known not to form any metastable eutectic phases. The same set of DSC experiments run on the Al-Fe alloys were run using an Al -1 wt. % Ni alloy, a composition estimated to contain approximately the same volume fraction of intermetallic

phases as the Al-Fe alloys. The purpose of running these experiments was to examine how the nucleation temperature of a stable eutectic varied with imposed cooling rate in the knowledge that the intermetallic part of the eutectic was the same regardless of cooling rate. Thus, deviations from this type of behaviour in the Al-Fe binary alloys would be strong evidence for a transition in intermetallic type.

4.1.8 EDX identification of DSC samples.

Intermetallics were extracted from the DSC samples using the technique described in chapter 2. The resulting sample consisted of a 400 mesh, 3 mm diameter, carbon and Formvar polymer, TEM grid carrying the intermetallic particles held in a carbon extraction film. This was inserted into a JEOL 2000FX TEM equipped with a LINK AN10000 EDX analysis system. Electron transparent intermetallic particles, commonly found in clusters, were analysed using the LINK system in the TEM mode. Where possible, 5 to 10 analyses were taken from each sample, although some samples were heavily contaminated and less than 5 analyses could be obtained. All analyses were stored on disc for subsequent quantification .

The RTS-2/FLS software, provided with the LINK system, was used to process the X-Ray spectra. To perform quantitative analyses of the Fe and Al contents of each sample, an estimate of the sample thickness and density was required. A density of 3 Mg m^{-3} was used (see table 1.02) . A thickness of 300 nm was entered for all particles analysed. The system requires these value to perform a ZAF (Atomic number(Z), Absorption(A), Fluorescence(F)) correction. This correction takes account of differences in atomic number between the two elements analysed, the absorption of characteristic X-rays from the lower atomic number Al by Fe and the fluorescence of Al by Fe X-rays.

A common difficulty encountered when using quantitative EDX in the TEM is that of thickness and density estimation. The density of the phase being identified is always an unknown by virtue of the fact that the phase being identified *is* unknown. For this reason, the value of density entered is always a carefully considered guess. It is possible to obtain an accurate value of the thickness of a sample by various methods. Measurement of thickness fringe spacing is one and the contamination spot method is another. These techniques take some skill and considerable time. One of the aims of this work was to develop a quick and relatively easy technique for phase identification of binary Al-Fe

intermetallics. For this reason, what was considered to be a reasonable value was used rather than measuring the thickness in each sample.

The sensitivity of the calculated Fe level to different density and thickness values was determined for a single analysis. A single particle was analysed and the analysis stored. The calculation Fe concentration was then repeatedly performed while varying the density and then the thickness. A range of densities from 2.8 to 4 g cm^{-1} were entered while keeping the thickness value constant (at 300 nm) and then a range of thicknesses from 50 to 1000 nm were entered while keeping the density constant (at 300 Mg m^{-3}). The range of values chosen were thought to contain all likely actual values.

4.1.9 EDX Determination of Mg and Ti Concentration in Intermetallic Phases

The trace element additions Mg and Ti behave in different ways when Al alloys containing them solidify. Mg forms a eutectic with Al which means that it partitions to the liquid on solidification of primary aluminium. Ti forms a peritectic with Al which means that it partitions to the solidifying primary aluminium. The particles extracted from the samples containing Mg and Ti were re-analysed by EDX to determine the Mg and Ti level, respectively, in the intermetallic phases found. This was done by modifying the calculation performed by the EDX software to look for the said elements.

4.2   DSC Results

4.2.1 Introduction

The results of the DSC experiments are shown in figure 4.05. The eutectic nucleation onset temperatures, calculated using the spreadsheet and curve fitting routines described above, are plotted against the cooling rate for each alloy. The equilibrium nucleation temperatures (T_n°) of the eutectics, which is defined as the temperature at which the eutectic would nucleate under conditions of infinitely slow cooling, were obtained by extrapolating the data back to zero cooling rate. The values of T_n° for each alloy are shown in table 4.02

	T_n° /$^{\circ}$C ($\pm$ 0.5°C)			
Iron content	Base	+ Mg	+ Ti	+ Ti-B
0.2 wt. % (1x)	651.5	650.5	651.5	653
0.4 wt. % (2x)	652.5	652.5	652.5	654

Table 4.02 Estimated values of T_n° for each of the DSC alloys

The lower iron content in the 1x series of alloys meant that the volume fraction of eutectic was lower. Therefore the resulting eutectic peaks on the DSC plots were smaller due to smaller enthalpy change on eutectic solidification. This had the advantage of improving the peak resolution in the more dilute alloy. This effect is shown in figure 4.06 where, although the peak area is smaller the peak is narrower and hence overlaps the primary aluminium peak to a lesser degree. This allowed onset temperatures for the more dilute alloys to be obtained at higher cooling rates without the need for the deconvolution.

4.2.2 Nomenclature of Samples

In this work samples solidified in the DSC are denoted by their base alloy first then their trace addition and finally the cooling rate in °C min^{-1}. The nomenclature takes the following form:-

XX YY ZZ

where   XX is the base alloy, either 1x or 2x,

         YY is the trace element addition, either Mg, Ti or Ti-B,

and   ZZ is the cooling rate in °C min^{-1}, from 01 to 80.

For example, 1xMg80 is the base alloy 1x with a trace element addition of Mg, which has been cooled at 80 °C min^{-1}.

4.2.3.1 Base Alloys.

The variation of nucleation onset temperature with cooling rate for the base alloys 1x (0.2 wt. % Fe) and 2x (0.4 wt. % Fe) are shown in figure 4.05(a). 1x initially shows a sharp fall in onset temperature with increasing cooling rate. The T_n° temperature for alloy 1x is approximately 651 to 651.5 °C compared with 652.5 °C for alloy 2x . The increased iron content has apparently reduced the undercooling necessary to nucleate Al$_3$Fe (the equilibrium intermetallic phase). The level of this difference might seem insignificant in comparison to the error in the data, indicated by the error bars, if it were not for the fact that this is a trend which will be seen when all the 1x series alloys are compared to the 2x series alloys (except for those with the Ti-B addition). An increase in iron content apparently slightly reduces the critical work of nucleation necessary for the nucleation of the eutectic. This effect is probably due to the fact that in the higher iron content alloys a larger volume fraction will solidify as eutectic. With larger 'pockets' of liquid of eutectic composition left

towards the end of solidification there will be more sites available for heterogeneous nucleation. The effect will be more pronounced in alloys where the eutectic has difficulty nucleating on the primary phase. This is the case with the Al_3Fe eutectic which has been reported as having difficulties nucleating on primary aluminium [36].

The initial sharp drop in nucleation temperature with increased cooling rate, in alloy 1x, is not maintained. At cooling rates in excess of 0.25 °C s^{-1} the change in nucleation temperature with cooling rate becomes less pronounced. In alloy 2x there is also an initially steep drop which levels off at cooling rates in excess of approximately 0.65 K s^{-1}. This effect could be due to a change in the intermetallic phase in the eutectic. The way in which the Al-Al_3Fe eutectic nucleation temperature varies with cooling rate is not necessarily the same as, say, the Al_6Fe eutectic; indeed, one would expect the relationships to be different for the two eutectics. Whilst there is no reason to suggest that the undercooling required for eutectic nucleation varies linearly with imposed cooling rate, if it is assumed to do (a linear model was used by Brusethaug *et al.* [3]), the 'kinks' in the nucleation temperature vs. cooling rate plots could be seen as indicating a change in the intermetallic type. The threshold value of cooling rate above which the Al-Al_3Fe eutectic is replaced by Al-Al_6Fe has been reported by various authors to be approximately 2 °C s^{-1} in alloys of varying compositions [9, 35, 36, 46, 48,]. However, Clyne and Young [8] reported the transition from Al_3Fe to Al_xFe (a phase similar in morphological appearance to Al_6Fe) at 0.7 to 1 °C s^{-1} in a hypoeutectic Al-Fe alloy containing 1 wt. % Fe. It is possible that the effects seen here result from the replacement of Al_3Fe by Al_xFe at the higher cooling rates.

4.2.3.2 Morphology of Intermetallic Phases Found in the Base Alloys

The micrographs in figure 4.07(a) to (f) show a selection of intermetallic particles extracted from the base alloys using the extraction technique described in section 2.3.2. The particles extracted from samples 1x01 and 2x01, shown in figures 4.07(a) and (b) respectively, show the typical plate-like morphology associated with the Al_3Fe phase. The particles lie flat on the carbon film and have a typical large dimension of 1 to 5 μm, although this dimension is somewhat meaningless as the particles have clearly been broken up during rolling. From the images it is clear that the morphology of the eutectic formed at low cooling rates is not the regular lamellar or rod-like associated with normal eutectics but irregular and typical of Al_3Fe which grows in a faceted and irregular manner [32]. The

images show that the particles are only slightly electron transparent which reflects their thickness compared to those solidified at higher cooling rates.

The particles extracted from the 1x80 are shown in figures 4.07 (c) and (d) and those extracted from the 2x80 samples are shown in figure 4.07(e) and (f). Their reduced scale reflects the increase in cooling rate. The scale of the whole microstructure is reduced because with a higher undercooling, the nucleation rate increases and individual grains cannot grow so large. This is a nucleation *and* growth effect. The morphology of 1x80 in figure 4.07(c) shows a rod-like regular eutectic phase which although broken up by the rolling process still maintains its form in silhouette and is distinct from the flat plates in 1x01. The rods are approximately 200 nm in diameter and are spaced about 400 nm apart (centre to centre). This supports evidence from the onset temperature measurements that an increase in cooling rate brings about a change in the type of intermetallic phase forming in the eutectic reaction. Figure 4.07(d) shows particles of a different morphology found in 1x80, similar to the plate-like Al_3Fe in 1x01. It is possible, therefore, that there is a mixture of intermetallic phases in this sample: Al_3Fe and a metastable regular eutectic such as Al_6Fe or possibly Al_xFe.

The particles from 2x80 did not show such a distinct change in morphology. The majority of particles still appeared to be flat and plate-like, albeit on a refined scale (see figure 4.07(e)). There were some elongated particles of a rod-like nature, see figure 4.07(f), with a similar dimension to those found in sample 1x80. This could be explained by the increased cooling rate needed for the transition to occur, evident from the onset temperature data (the apparent critical cooling rate for a phase transition was ≈ 0.25 °C s^{-1} for 1x and ≈ 0.65 °C s^{-1} for 2x). If a range of cooling rates exist over which the two phases, stable Al_3Fe and metastable Al_6Fe or Al_xFe, can nucleate then the closer to the critical cooling rate for the first occurrence of the metastable the sample is, the less of it will be evident.

4.2.4 Base alloys with trace additions.

The effect of the trace additions of 0.02 wt. % Mg, 0.04 wt % Ti and 0.04 wt. % Ti-B grain refiner on the variation of nucleation onset temperature with cooling rate have been assessed by comparison with the base alloys. Each addition, made to both the 1x and 2x alloy, will be dealt with separately.

The general effect of each addition can be seen by comparing alloys with the same addition but different Fe contents (that is, 1xMg with 2xMg (figure 4.05 (b)), 1xTi with

2xTi (figure 4.05(c) and 1xTi-B with 2xTi-B (figure 4.05(d),. There is some scatter but each addition seems to make the data follow a trend regardless of the Fe level. Furthermore, the trend is different for each addition. Mg, for example, reduces the nucleation temperature at high cooling rates compared to the base alloy, see figures 4.05(e) and (f). Ti has a similar effect, see figures 4.07(g), and (h). By contrast, Ti-B has the effect of increasing the nucleation temperature at most cooling rates, see figures 4.07(i) and (j). The fact that each of the additions, regardless of Fe content, show a trend, and that the trend is different for each addition, adds confidence to the validity of the results. The effects seen in the data are real effects of the additions and not due to experimental error or deconvolution error.

4.2.4.1 The Effect of the Addition of Mg to the Base Alloys

The $T_n{}^\circ$ for the alloy 1xMg was slightly lower, by 1°C, than that for the base alloy 1x whereas there is little difference between the values for 2x and 2xMg. The nucleation temperatures at lower cooling rates are similar to those in alloy 1x. The main difference between the 1x and 1xMg is seen at the higher cooling rates. In excess of 0.25 °C s^{-1}, where 1x deviates from the initial trend, the 1xMg data shows no such deviation (figure 4.05(e)). This suggests that the addition of Mg has either stabilised the Al-Al$_3$Fe eutectic or interfered with the nucleation of the metastable eutectic resulting in Al$_3$Fe being able to nucleate at higher cooling rates than when no Mg is present.

A similar behaviour is observed in alloy 2xMg, see figure 4.05(f). The nucleation temperatures are roughly the same at cooling rates below 0.6 °C s^{-1}. At higher cooling rates the values of nucleation temperature obtained for the different alloys diverge considerably, the difference being 8°C at 1 °C s^{-1}. The addition of Mg has had the effect of extending the range of cooling rates over which the Al$_3$Fe eutectic can form in both alloys and in doing so preventing the transition to another intermetallic in the range of cooling rates examined.

By comparing the alloys 1xMg and 2xMg the effect of the different Fe contents in alloys with the same level of Mg can be seen. Apart from the values of $T_n{}^\circ$, there is, in fact, very little difference in the nucleation temperatures at all cooling rates. The variation of nucleation temperature with cooling rate is approximately linear in both alloys.

4.2.4.2 Morphology of Intermetallic Phases in alloys with Mg Addition

The intermetallic phase extracted from the 1xMg01 and 2xMg01 alloys had the typical plate-like morphology associated with Al_3Fe as would be expected at these low cooling rates, see figure 4.07(g). The particles extracted from the faster cooled samples have a similar morphology but on a finer scale, see figures 4.07(h) and (i). Most were plate like which would agree with the nucleation temperature data which suggests that the addition of Mg stabilises Al_3Fe. However, there were some particles in the fast cooled specimens which were not plate-like. Both figures 4.07(h) and (i) show a plate-like Al_3Fe particle having a long dimension of over a micrometer next to some small rod-like particles of width 200 to 300 nm. These could be a different phase but may be a fragment of the larger particle broken off during rolling. Better evidence of a different phase is shown in figure 4.07(j) from 2xMg80. The figure shows two sets of regular long and thin particles. These are probably a metastable phase, indicating that the transition to the metastable species, if any, started to occur at the highest cooling rate.

The micrographs of the particles extracted from DSC samples with Mg additions support the evidence from the nucleation temperature data that the addition of Mg to these alloys stabilises the equilibrium phase Al_3Fe. Limited evidence for a transition, which probably occurs close to 80 °C min^{-1}, was seen in the morphology of the extracted particles but could not be detected by the nucleation temperature measurements. The way in which Mg affects phase selection will be discussed later.

4.2.4.3 The Effect of the Addition of Ti to the Base Alloys

The addition of Ti has not appreciably changed the T_n° in either alloy (see table 4.02). The variation of nucleation temperature with cooling rate in the 1xTi and 2xTi alloys are approximately the same regardless of iron content, with perhaps a slight deviation at the higher cooling rates, see figure 4.05(c). The comparison of results for the 1x alloy and the 1xTi alloy shows the effect of Ti, see figure 4.05(g). There is little evidence for a phase transition occurring except perhaps at the highest cooling rate as a straight line could be drawn through all but the last point. The nucleation of Al_3Fe has been stabilised by the addition of Ti .The way in which it has done this appears to be similar to the way in which Mg did. In fact, the data from 1xMg and 1xTi are very similar as can be seen when they are compared in figure 4.05(k).

The data from 2xTi and 2x, see figure 4.05(h), follow a similar pattern at low to medium cooling rates and begin to deviate at higher cooling rates (above 0.7 °Cs⁻¹). There is no phase change indicated in these data as there was in the 2x data. The gradient of a line drawn through the 2xTi data is approximately the same as that drawn through the low to medium cooling rate data in 2x. This is the same as the effect Ti has had on 1x and indicates that it is the nucleation temperature of the metastable phase which is affected, and not that of the Al_3Fe, by the addition in these alloys. There is again a similarity in the data from the 2xMg and 2xTi experiments as can be seen in figure 4.05(l).

In summary, in both alloys the Ti addition seems to have inhibited the nucleation of the metastable phase without altering the nucleation temperature of the Al_3Fe.

4.2.4.4 Morphology of Intermetallic Phases in Alloys with Ti Addition

The micrographs of phases extracted from 1xTi01 and 2xTi01, see figures 4.07(k) and (l), show the flat plate-like Al_3Fe phase consistent with all the low cooling rate samples. The dimensions of the plates are also in keeping with other samples. The 1xTi80 sample was contaminated and good images were impossible to obtain. Lack of time meant that a second sample could not be obtained. Particles from 2xTi80 were mainly flat plate like particles, see figure 4.07(m), typical of Al_3Fe. One example of a phase morphology not seen in any other sample was seen in the 2xTi80 sample, see figure 4.07n. This phase is clearly different to the others found in the sample and has a very long and branched rod like nature emanating from a single point. This would suggest that it nucleated from that point and grew outwards spreading wider as it advanced. The morphology of this phase is so different that it must be assumed to be a metastable phase. The nucleation temperature for this cooling rate could not be obtained as the fitting routine could not find a convergent solution, but there is a kink at high cooling rates in 1xTi80 which may be a result of a transition and may have occurred in 2xTi80. However, the fact that its nucleation site can be seen suggests that it nucleated on *something* such as a floating particle or piece of crud. Only one example was found in this sample. Whether it occurred as a direct consequence of the Ti addition is unclear.

There is limited evidence gained from the examination of the morphology of these particles to support that from the nucleation temperature data which suggest that Ti acts in a similar manner to Mg in that it suppresses the nucleation of the metastable phase (Al_6Fe or Al_xFe).

4.2.4.5 The Effect of the Addition of Ti-B Refiner to the Base Alloys.

The T_n° for temperatures for the 1xTiB and 2xTiB alloys were approximately 653 654°C respectively. The nucleation temperatures for the eutectics in the alloys with the Ti-B addition are higher in all cases than in the base alloys. The effect was similar in both alloys and is shown in figures 4.05(i) and (j). The nucleation temperature is higher at low cooling rates but tends to converge with those of the base alloys at high cooling rates. This is a different effect to that observed with Mg and Ti additions which lowered nucleation temperatures at high cooling rates. This effect could result from the enhanced nucleation of the metastable phase found at high cooling rates in the base alloys. When compared to one another, see figure 4.05(d), it can be seen that the different iron content makes little difference to the nucleation temperature as there is little difference between the nucleation temperatures for 1xTiB and 2xTiB, except at cooling rates where the values for 2xTiB are slightly lower than those for than 1xTiB.

4.2.4.6 Morphology of Intermetallic Phases in Alloys with Ti-B Addition

Flat and plate-like Al_3Fe existed at low cooling rates in these samples. An example is shown in figure 4.07(o) which has a similar scale to the same phase found in other samples.

At higher cooling rates where normally, without grain refiner, a higher degree of undercooling would be expected, the nucleant has the effect of providing heterogeneous sites for nucleation and thereby reducing the undercooling. The intermetallics extracted from the higher cooling rate samples have a clearly different morphology to those from non-grain refined samples, see figures 4.07(p) and (q), (and possibly from those assumed metastable phases found in small quantities in the Ti and Mg alloys solidified at high cooling rate). There is more regularity in this structure and although the particles are still flat they tend to be long and narrow and more strongly aligned . This is good evidence that the higher cooling rate samples contain a phase other than the equilibrium Al_3Fe. The addition of the grain refiner has enhanced the nucleation ability of the   metastable phase, possibly the same one found at higher cooling rates in the base alloys. From the graphs in figure 4.05(i) and (j) there is evidence that, by enhancing the nucleation of the metastable phase, the transition to the metastable phase has occurred at a lower cooling rate than in the base alloys.

4.2.5   EDX Results.

The EDX measurements made in the TEM are dealt with separately from the other results because there were some difficulties in interpretation of the results. The values of Fe levels could not be used to confidently identify the phases present without some assumptions being made. The problems encountered and the assumptions are discussed before the actual results are considered.

The EDX results are expressed in terms of atomic % Fe. The approximate values for the Fe content for each of the binary phases are given in at.% in table 4.03. The aim of the EDX measurements was to take advantage of the different levels of Fe in each of the intermetallic phases in order to identify the intermetallic phases in the DSC samples.

Phase	Al_3Fe	Al_mFe (m≈4)	Al_xFe (x≈4.5)	Al_6Fe
at. % Fe	25	20	18	14.3

Table 4.03 Approximate values of Fe content, in at. %, in the common binary Al-Fe intermetallic phases.

The number of readings which could be made on each sample varied because the number of separate particles able to be analysed varied and time constraints prevented more samples being made. For a reliable analysis from an individual particle to be obtained, the particle could not overlap, and had to be isolated from, others. Some samples contained a good number of isolated particles whilst others tended to have clusters of particles which prevented individual particle analysis. Overlapping particles posed two problems which prevented reliable analysis. Firstly, the thickness of individual particles was difficult to estimate and the thickness of overlapping ones was even more difficult to judge. Secondly, if two particles of different phases overlapped then, even if the thickness were known, the Fe concentration determined would be intermediate between the values for each of the individual phases and consequently ambiguous.

The results are shown in figure 4.08. The data are presented in the form of box charts. These are a way of showing the spread of data which gives an idea of the general trend. Each box represents the analyses taken from a number of particles in each sample. The box contains a horizontal line indicating the median average value. The upper and lower limits of the box represent the limits of ± 25 % of the variable population. Thus the box encloses 50 % of the data. Hence the position of the box on the y axis (at. % Fe) and its size

give an indication of the value of Fe content and of the spread of the data respectively. The bars extending above and below each box represent the minimum and maximum values obtained.

4.2.5.1 Problems Encountered with Thickness and Density Estimation

The need to enter a value of thickness and density into the analysis software was mentioned earlier. The values of density and thickness are needed so that the ZAF correction can be incorporated in to the calculation performed by the LINK software. The value used for density was an estimate based reported densities of 3.8 Mg m^{-3} 3.45 Mg m^{-3} for Al$_3$Fe and Al$_6$Fe respectively(see Table 1.02). The density for other intermetallics such as Al$_m$Fe and Al$_x$Fe have not been measured. The variation in calculated Fe concentration with density was measured for one sample by repeatedly analysing its EDX spectrum (for densities ranging from 2.8 to 4 g cm^{-3} at a constant thickness of 300 nm). A variation of 0.5 at. % was found over the range of stated densities. The spectrum from the same sample was then repeatedly analysed while varying the estimated thickness from 50 to 1000 nm (with constant density of 3 Mg m^{-3}). The variation in Fe content for this range of thicknesses was found to be 3.6 at %. The variation is shown in figure 4.09 . The error in the Fe concentration over the given range of density was, therefore, small whereas variations in the sample thickness were shown to have a large effect on the calculated value of Fe content. A more accurate value of thickness for each particle analysed could not be obtained due to time limitations.

The problem of thickness estimation was discussed earlier. An understanding of the way in which an erroneous estimation of thickness will affect measurements will help in explaining the large spread of data found in the results. If the value of thickness input for a particular particle is lower than the actual value then the calculated level within the particle will be too high. This was shown in figure 4.09. A similar situation applies with density in that too low a value of density will give an artificially high value of Fe concentration. In many cases, the data obtained contained at least some values of Fe content higher than 25 at. % despite the fact that none of the possible binary phases are known to contain more than 25 at. % Fe. Al$_3$Fe has the highest Fe content and all metastable phases contain lesser amounts. It must be assumed, therefore, that the values obtained are artificially high due to erroneous values of thickness and density being entered. The effect of a low density value is relatively small when compared to that of a low thickness value. The SEM micrograph of

intermetallic particles from a sample cooled at 80 °C min^{-1} viewed 'edge-on' shown in figure 4.10 show that the particles have a thickness ranging from around 100 nm up to nearly 1 μm. If particles this size were found in the sample having suffered the highest cooling rate, it can be assumed that particles in the slower cooled samples would be larger still. The values of Fe content can therefore be assumed to be artificially high in many cases and low in others. No assumption can be made regarding the size of the error without actual measurement of the thickness of each particle analysed. With this in mind the results of the EDX measurements will be examined.

In all but one of the alloys there is a drop in measured iron content from the sample cooled at 1°C min^{-1} to the sample cooled at 80 °C min^{-1}. This cannot be assumed to be solely due to an actual change in Fe content. The thickness of 300 nm entered for all particles has been shown to be too low for . some of the high cooling rate sample. The difference would have been greater for the larger particles in the slower cooled samples.The error in Fe content is therefore larger in the slow cooled samples than the fast cooled ones. This is illustrated in table 4.04 below which shows the estimated error in Fe content from two particles of the same composition but whose actual thicknesses are 500 and 1000 nm. If the data were to be adjusted in line with this then the Fe contents of the low cooling rate alloys would reduced more than those of the high cooling rate alloys.

Actual particle size /nm	Assumed particle size /nm	Difference /nm	error in at. %
500	300	200	$\approx + 1$ at. %
1000	300	700	$\approx + 2.5$ at. %

Table 4.04 Estimated error in calculated Fe content as a function of particle thickness (based on data shown in figure 4.09)

There is also the possibility that some of the particles analysed were thinner than 300 nm which would mean that some of the readings were artificially low. The fact that different phases have different morphologies and that the thickness of one phase varies from particle to particle adds to the unreliability of the EDX results.

4.2.5.2 EDX Results from the Base alloys.

The data from the DSC temperature measurement experiments on the base alloys suggest that Al_3Fe forms at low cooling rates in both alloys and some other metastable phase, co-existing with Al_3Fe, is found at the higher cooling rates. The second phase is more evident in alloy 1x than alloy 2x as the proposed critical cooling rate for the transition is lower. The box graph for alloy 1x, in figure 4.08(a), shows that most of the readings from 1x01 are above 25 at. %, the median value being approximately 26%. Bearing in mind the errors associated with thickness determination, it can be said that Al_3Fe was the predominant intermetallic phase at this cooling rate. The 1x80 box shows a much greater spread of data with a lower median value of 24.2 at %; some values were as low as 18.2 at. %. Again, considering that these values are probably artificially high, these results indicate that along with Al_3Fe, some of the particles analysed fall within the correct compositional range for Al_mFe or even Al_xFe. A similar case is seen in the 2x alloys with 2x01, figure 4.08(b), indicating predominantly Al_3Fe. The 2x80 box extends over a large range of compositions and to surprisingly to high values. Nevertheless, the median value is below 25 at.%, suggesting that some particles of a metastable phase were also found in this sample

4.2.5.3 EDX Results from Alloys with Trace Additions.

The conclusion drawn from the DSC experiment data regarding Mg additions was that it extends the range of cooling rates over which Al_3Fe can form. The box graphs of the data from 1xMg01 and 1xMg80, figure 4.08c, confirms this in that there is little difference between the two sets of data from high and low cooling rate. If they were adjusted to take account for thickness error than their similarity would be greater. (It must be noted however that only three readings were taken from 1xMg01). This is in stark contrast to the EDX data from 2xMg01 and 2xMg80, figure 4.08d, which shows a marked difference in the Fe level from high to low cooling rate. This does not confirm the temperature data or the morphological evidence. The nucleation temperature results for 2xMg do not include values for 80°C min^{-1} and there was limited evidence of a metastable phase in the morphology of samples extracted from this sample. There is the possibility, therefore, that a mixture of stable and metastable intermetallics nucleated at this cooling rate.

The values of Fe content in both 1xTi and 2xTi alloys are similar, figures 4.08(e) and (f). At low cooling rates the values are around that to be expected for Al_3Fe (with adjustment for thickness error). At high cooling rates the values are much the same. The

results from these alloys could be said to support the temperature measurement and morphological data which concluded that the Ti addition stabilised Al$_3$Fe increased the range of solidification velocities over which Al$_3$Fe can form.

It was concluded that the addition of Ti-B refiner had the effect of increasing nucleation temperatures at lower cooling rates. The EDX data, shown in figure 4.08(g) and (h), suggest that the low cooling rate phases in both alloys are Al$_3$Fe as most of the Fe levels are slightly above 25 at %. The values of Fe content measured in particles cooled at the higher cooling rate lie mainly in the low 20 at. % region and below. Although the EDX evidence is unreliable due to thickness and density estimation error the results from the EDX analysis of the samples with the Ti-B addition tie in well with the nucleation temperature and morphological evidence that a phase other than Al$_3$Fe is nucleating at higher cooling rates. Furthermore, this appears to be significantly lower in Fe content than the values obtained for phases extracted from the alloys containing Ti and Mg, indicating a possible different phase.

Unfortunately, little can be gained from the EDX results as they stand. In retrospect it would have been more useful to have gained some idea of the thickness of each particle before the analysis calculation was performed. Alternatively, a better guess could have been made at the thickness which took into account the difference in microstructural scale expected from samples solidified at considerably different cooling rates. A better analysis tool would have been the EPMA which does not require a thickness or density estimate or the analysis of TEM extraction patterns. However the technique used to extract the particles from the DSC samples was specifically designed for EDX in the TEM. The technique was successful in that intermetallic particles could be extracted from the matrix with relative ease and could be viewed and photographed. It was unsuccessful in that there was a high level of sample contamination due to inadequate cleanliness and that the analysis technique used was ineffective in positively and unambiguously identifying the extracted particles .

4.2.5.4 Results of EDX analysis for Mg and Ti.

The intermetallics extracted from the 1xMg 2xMg alloys were analysed for Mg and those from the 1xTi and 2xTi alloys were analysed for Ti. The results for each sample are shown in figure 4.11. The bar chart shows that the intermetallics from slow cooled Mg containing samples contain 0.25 to 0.7 at. % Mg and that those from the faster cooled samples have 0.3 - 1.7 at. % Mg. On the other hand, the intermetallics from the Ti

containing samples all contain less than 0.1 at % Ti. The difference was expected because of the different partitioning behaviour of the two elements with Al. Mg partitions to the liquid due to its limited solubility in Al whereas Ti partitions to the solidifying primary Al. A level of Mg higher than the bulk composition would therefore be expected in the intermetallics, and is indeed, observed.

A lower level of Ti would be expected in the intermetallics than in the bulk due to its partitioning to the solidifying primary Al dendrites. This is the case in the slow cooled samples where the average Ti level is less than 0.01 at % (or just above 0.01 wt. %). However in the faster cooled samples the average level of Ti is 0.05 to 0.07 at % (or $\approx$ 0.07 and 0.09 wt. % Ti as calculated by the LINK software). This is higher than the bulk level of 0.04 wt. %. The analysis of individual particles from the fast cooled samples showed that some particles contained none or very little Ti but four out of the eleven analysed contained more than 0.1 at % Ti.

The accuracy of the EDX measurement is known not to be reliable for the reasons discussed above. However, the high level of Ti in some of the fast cooled intermetallics is surprising. One explanation is that the particles containing the high levels of Ti were of a different species to those containing none or very little. This would support the conclusion that a mixture of intermetallic phases existed at the high cooling rates. The question still remains as to how the particles were able to solidify with that amount of Ti in their structure when it is known that the liquid that they were solidifying from was depleted in Ti.

4.2.6 Result of DSC experiments with Al-Ni alloy.

The results from the DSC experiments conducted on the Al - 1 wt. % Ni alloy solidified over the same range of cooling rates as the Al - Fe alloys discussed above are shown in figure 4.12. There is a very slight curvature to the plot although the curvature is by no means as severe as in the base alloy 1x and 2x plots. In fact it was possible to fit a good straight line through the data. The way in which nucleation temperature would be expected to vary with cooling rate will be discussed in section 4.3.

The Al-Ni data shows the variation in eutectic nucleation onset temperature for an alloy in which metastable phase formation is not possible. The data from the Al-Fe alloy solidified under the same conditions did not always show a straight line variation (especially the 1x and 2x alloys shown in figure 4.05(a)). A deviation from this linear relationship is seen at high values of cooling rate in these alloys and a straight line could not be drawn

through all the points in these plots. In others a straight line variation is seen with no discernable curvature (see figure 4.05(b) for the alloys with Mg additions). The Al-Ni plot with its near linear variation is proof that the 'kinks' seen in some of the Al-Fe plots are due to a phase transition at high cooling rates.

4.3   Discussion of DSC Experiments

The nucleation behaviour of the eutectic in binary alloys is complex. The first material to nucleate from the molten alloy is the primary aluminium which grows in a dendritic fashion. Iron has a very low solid solubility in aluminium and most of it dissolved in the melt will be rejected by the solidifying primary aluminium, thereby enriching the remaining liquid. When the remaining liquid reaches the eutectic composition it will solidify as an interdendritic eutectic comprising aluminium and an intermetallic phase (whose nature depends on solidification conditions and composition). Nucleation requires a certain amount of undercooling to provide a driving force. The amount of undercooling will depend on the ease with which the phase can nucleate. This is influenced by changes in free energy and surface energy on nucleation, the thermodynamic properties of the phase and the nature of heterogeneous nucleation sites available.

Al_6Fe has a lower melting temperature than Al_3Fe, and, therefore, under near equilibrium cooling Al_3Fe will always nucleate and dominate before it is possible for Al_6Fe to do so. Under fast cooling conditions it may be possible for Al_6Fe to nucleate before Al_3Fe has had time to do so. Therefore it is important to understand how the nucleation temperature is likely to vary with imposed cooling rate for a particular material. With a better understanding of the relationship between undercooling and cooling rate, it will be easier to understand the results from the DSC experiments. The plots of nucleation temperature vs cooling rate obtained from the DSC experiments show an approximate linear variation for a single intermetallic phase. Changes in the linear gradient are assumed to be a consequence of the change in the dominant intermetallic in the eutectic. There is no reason to assume that the variation will be linear unless the nucleation process has been modelled and shown to do so.

4.3.1 Nucleation Model

A simple model was developed to show how the nucleation temperature might vary with cooling rate. A classical homogeneous nucleation approach was used for simplicity. The purpose of developing this simple model was to show how nucleation temperature varies with cooling rate and to compare this to experimentally obtained data. It was not the aim to accurately fit the experimentally obtained data to the model as there were too few data to do so.

The steady state homogeneous nucleation rate, I, can be described in terms of the temperature, T, and the free energy barrier for nucleation, ΔG^*.

$$I = I_0 \, \exp\left(\frac{-\Delta G^*}{k_B \, T}\right) \qquad\qquad 4.16$$

where k_B is the Boltzmann constant, T is the temperature and I_0 is a pre-exponential factor whose value is approximately constant at small undercoolings [60]. The classical treatment of homogeneous nucleation gives an expression for ΔG^*:

$$\Delta G^* = \left(\frac{16 \, \pi \, \gamma_{s/l}^3 \, T_m^2}{3 \, (\Delta T)^2 \, L_v^2}\right) \qquad\qquad 4.17$$

where $\gamma_{s/l}$ is the solid/liquid interfacial energy, T_m is the melting temperature, ΔT is the undercooling ($\Delta T = T_m - T$) and L_v is the latent heat of fusion per unit volume of solid. This expression can be substituted into expression 4.16:-

$$I = I_0 \, \exp\left(\frac{-B}{T \, (\Delta T)^2}\right) \qquad\qquad 4.18$$

where, for small undercoolings B is a constant such that :-

$$B = \left(\frac{16 \, \pi \, \gamma_{s/l}^3 \, T_m^2}{3 \, k_B \, L_v^2}\right) \qquad\qquad 4.19$$

The isothermal nucleation time, t_n, is the time taken for an average of 1 nucleus to form in a volume V of material at constant temperature and can be expressed as

$$t_n = \frac{1}{IV} \qquad\qquad 4.20$$

The cooling curve for a liquid metal can be seen as series of infinitesimally small steps of length δt and height δT. In one step, the number of nuclei which would appear in a volume V of melt is given by: $I \, V \, \delta t$. By summing this over all the steps, the total number of nucleation events occurring as a function of time during the cooling of the melt can be found. Clearly, when the total number of events is 1, nucleation will have occurred in the sample. If the time taken for this to occur is t_n, the nucleation time, then this condition can be expressed as:

$$\int_0^{t_n} I \, V \, dt = 1 \qquad\qquad 4.21$$

If the cooling rate Φ is constant then:

$$\frac{dT}{dt} = \Phi \qquad\qquad 4.22$$

and if $T = T_m$ at $t = 0$,

$$\int_{T_n}^{T_m} \frac{I \, V \, dT}{\Phi} = 1 \qquad\qquad 4.23$$

and

$$\int_{T_m}^{T_n} I \, dT = \frac{\Phi}{V} \qquad\qquad 4.24$$

Which gives a relationship relating cooling rate to nucleation temperature. However, the integral is difficult due to the complexity of the term for I. An approximation for this expression can be employed where $I(T_n)$ is defined as the steady state nucleation rate at $T=T_n$.

$$I \, (T_n) = \frac{\Phi}{V} \qquad\qquad 4.25$$

since the curve of nucleation rate against temperature rises very sharply in the vicinity of T_n (see figure 4.13). The approximation defines T_n and assumes that the number of nucleation events occurring before it is reached is insignificant when compared to those occurring at T_n. Using equation 4.18 this can be written as:

$$I_0 \exp \left(- \frac{B}{T_n (\Delta T)^2} \right) - \frac{\Phi}{V} \qquad 4.26$$

which can be rearranged to give

$$\ln (\Phi) - \ln (I_0 V) - B \frac{1}{T_n (\Delta T)^2} \qquad 4.27$$

A plot of $\ln(\Phi)$ vs. $1/(T_n(\Delta T)^2)$ should yield a straight line of gradient -B and intercept $\ln (I_0 V)$. Using the experimental results, $\ln (\Phi)$ was plotted against $1/(T_n(\Delta T)^2)$ to confirm this relationship and help to determine whether a phase transition had occurred. The data from a single phase should lie on a straight line according to the model. A phase transition at high cooling rates to a metastable phase would be evident by the departure of the data from a straight line. The value of B is a characteristic of a particular material which could be used to help in identifying phases. The variable material parameters which make up B are $\gamma_{s/l}$, L_v and T_m. The interfacial energy term would vary considerably if the two competing phases are faceted and non faceted.

A spreadsheet (Microsoft Excel) was used to manipulate and plot the data to which a straight lines was fitted by a least means square method. The values of B and $\ln (I_0 V)$ were obtained from the fitted straight line. The diagrams in figure 4.14 show the plots with fitted lines. The largest departures from the straight lines are seen in the base alloys. Two different lines have been fitted to each set of data to show the transition. The values of $\ln(\Phi)$ obtained from the plots correspond to cooling rates of 0.25 °C/for alloy 1x and 0.67 °C/for alloy 2x which both correlate well with the values estimated from the plots in figures 4.05 (a). The advantage, therefore, of using the model is that it magnifies the effect of the transition making it easier to determine these critical values. The results for the 1xMg and 2xMg alloys are good straight lines over the full range of cooling rates. There is some deviation in the alloy 1xTi alloy but as it is not as severe as that seen in the base alloys ,and may be due to scatter in the data rather than a phase transition. The data for the alloys 1xTiB and 2xTiB

do not lay on a straight line but both deviate from it in a similar way. The initial point corresponding to the lowest cooling rate is rather low as on the T_g vs Φ plot. The remaining points seem to lie on a curve. If the Ti-B addition aids nucleation of a metastable phase at lower cooling rates as was inferred from morphological and EDX analysis of extracted particles, the points would not be expected to lie on a straight line. The curvature could be explained if, not two, but three intermetallic phases were nucleating over different ranges within the total range of cooling rates tested. More data would show whether this were true.

The model has been shown to be valid and to aid in the determination of phase transition critical cooling rates. For it to be possible to use the model to obtain more useful information more data would be needed since the graphs of ln (Φ) vs $1/(T_n(\Delta T)^2)$ accentuate the scatter in the data as well as any real effect. With more data it would be possible to discern between the two. It might also be possible to use the values of the gradient B to determine which phases nucleate and to investigate the nucleation process more quantitatively in these alloys.

4.3.2 Metastable Phase Identity

The identity of the metastable eutectic intermetallic phase which apparently replaces Al_3Fe in some of the alloys at elevated cooling rates cannot be confirmed from these results. Al_6Fe is not the only phase which can replace Al_3Fe in binary alloys at higher cooling rates; it has been shown in DC simulator experiments (see chapter 3) that the type of binary metastable phase found in binary alloys with trace additions can vary. (Al_mFe, Al_6Fe and Al_xFe were all positively identified by XRD in DC Simulator cast ingots of the same composition to these). However, the DC simulator experiments showed that at the high cooling rates in all but the alloy with the Ti-B addition, Al_6Fe was the only phase present. and that with the exception of alloy AlxMg the same phase was present in the regions of the lowest cooling rate examined. However the regular rod like morphology associated with Al_6Fe was not a striking feature of any of the phases extracted from the DSC samples. The cooling rates used in the DSC experiments would be those experienced towards the top 20 to 30 mm of the binary DC simulator ingots. Therefore, a comparison can only be made of the high cooling rate DSC samples to the phases occurring towards the top of the ingots. This would suggest that Al_6Fe was the metastable phase identified by nucleation temperature measurements and morphological examination (and EDX), particularly in the base alloys. It will be shown in the next section that the values of transition cooling rate, when Al_3Fe is

replaced by the metastable phase in the base alloys, does not agree with previously reported values for the transition from Al_3Fe to Al_6Fe. However, it was stated in Chapter 3 that the phase selection in the DC simulator, and indeed in large scale casting as a whole, is probably based on a complex interaction between nucleation and growth. It would not be possible, therefore, to draw firm conclusions as to the identity of the metastable phase seen in these DSC samples from results from the DC simulator castings.

The addition of Ti-B to the base alloys had a different effect to the Mg and Ti additions. The phases found in the top sections of the DC simulator ingots were mixtures of Al_3Fe and Al_6Fe for both Fe concentrations. The addition of Ti-B refiner would be expected to increase the influence of nucleation on phase selection. The regularity in the morphology of the phases extracted from the DSC samples with Ti-B additions and the fact that the EDX values of Fe concentration are significantly lower than in other samples might suggest that the metastable phase is Al_6Fe. The contradiction is that the addition of Ti-B appears to have allowed Al_3Fe to nucleate and coexist with Al_6Fe at lower cooling rates in the DC simulator ingots but has enhanced the nucleation of Al_6Fe in the DC simulator ingots at similar cooling rates. It is possible that its effect is to allow both phases to nucleate over expanded cooling rate ranges that overlap, i.e. allowed Al_3Fe to nucleate at higher cooling rates and Al_6Fe to nucleate at lower cooling rates. This might explain the odd variation in measured nucleation temperature with imposed cooling rate.

It is not possible to unambiguously identify the intermetallic phases extracted from the DSC samples and the comments made in the two paragraphs above are merely speculation. It can be assumed, however, that the phase occurring at the low cooling rates is the equilibrium intermetallic Al_3Fe.

4.3.3 Comparison with Previous Work on Binary Al-Fe Alloys

Increasing the Fe content from 0.2 wt. % to 0.4 wt. % has been shown to increase the critical cooling rate necessary for the transition from Al_3Fe to the unidentified metastable intermetallic phase. In previous work, the change from the Al_3Fe to the Al_6Fe eutectic has been investigated in mainly near-eutectic and hypereutectic Al-Fe alloys. Backerud [36] determined a threshold of 3 °C s^{-1} in Al - 1 wt. % Fe and Adam and Hogan [35] determined a value of 2 °C s^{-1} for Al - 2 wt. % Fe. A similar value was obtained by Hughes and Jones in Al - 2.2 to 4.7 wt. % Fe, albeit calculated from Bridgman data. In experiments on dilute Al-Fe alloys (0.04 to 0.55 wt. % Fe) Miki *et al.* identified a threshold of 1°C s^{-1} [21].

However, in Al - 0.58 wt. % Fe Kosuge and Mizukami [37] identified 2 °C s^{-1} as the upper limiting cooling rate for the Al$_3$Fe eutectic. The values obtained in this set of experiments for Al - 0.2 and 0.4 wt. % Fe are 0.25 and 0.65 °C s^{-1} respectively, somewhat lower than those reported in the work cited above. There is the possibility, however, that a transition to AlxFe has occurred. Clyne and Young [8] reported that a change in intermetallic morphology was observed in hypoeutectic alloys at cooling rates of 0.7 to 1 °C s^{-1}. The phase replacing Al$_3$Fe was found to be Al$_x$Fe. The morphological evidence in figures 4.07 support the view that Al$_3$Fe has been replaced by a more regular and less plate-like eutectic phase. The value of threshold cooling rate for the replacement of Al$_3$Fe obtained from the DSC experiments on 1x and 2x are approximate, however the different morphology of the particles extracted from the DSC samples is clear. It must also be emphasised that more than one eutectic intermetallic may have been present in a single sample solidified under non-equilibrium conditions. Further evidence of this can be found in other results discussed in chapters 3 and 5. The mixed morphology of some of the phases found at high cooling rates, again, supports this notion. It is possible that the transition from one type of intermetallic to another occurs over a range of cooling rates. If this is the case the onset temperature obtained from the eutectic peak on the DSC plot would be that of the phase nucleating at a lower undercooling.

A simple model is suggested to explain the change from one type of intermetallic to another. This model was used as an explanation of the behaviour by Brusethaug *et al.* [3]. For a given cooling rate the phase with the highest nucleation temperature will nucleate first and start to grow. The diagram in figure 4.15 shows schematically how other metastable phases can be introduced. The model will now be used to show how the trace additions have affected the nucleation temperatures

4.3.4 The Behaviour of the Binary Alloys with Mg and Ti Additions

It is possible to obtain information from the DSC experiments regarding the effect of trace additions. Each trace addition seems to have affected the T_n vs Φ curve (which is consistent for both Fe levels) and which is different from the effect of Fe concentration in the base alloy which indicates that the trends result from the trace element addition. The conclusion drawn from the results was that Mg and Ti extend the range of cooling rates over which the Al$_3$Fe eutectic can nucleate. This could be achieved in two ways. Firstly, the addition could affect the ability of the Al$_3$Fe to nucleate in such a way that the nucleation

temperature for a given cooling rate was higher, see figure 4.16(a). The figure shows schematically how the trace element addition would increase the range of cooling rates over which the Al$_3$Fe could form by reducing the undercooling required for its nucleation at a given cooling rate (Al$_6$Fe is used as the metastable phase as an example). Secondly, the trace addition could affect the nucleation temperature of the metastable phase. In figure 4.16(b) the trace addition has made it more difficult for Al$_6$Fe to nucleate at any given cooling rate. In reality the trace element could well produce both of these effects .There is also the possibility that it could enhance the nucleation of both phases but not by the same degree.

It is suggested that the addition of Mg and Ti has had an effect similar to that described in figure 4.16(b). The nucleation temperatures measured for the eutectic at low temperature are much the same for both base alloys and base alloys with the additions. However, the nucleation temperatures diverge at higher cooling rates indicating that it is the metastable phase, which is nucleating at high cooling rates in the base alloys, whose nucleation is inhibited in the alloys with the Mg and Ti addition.

The way in which such low levels of addition affect the nucleation characteristics remains unclear. It is worth speculating, however, on the mechanism by which they do so. The liquid left towards the end of solidification in the alloy containing Mg was enriched in Mg as was seen when the particles from these alloys were analysed for Mg. The liquid left towards the end of solidification in an Al alloy containing Ti was thought to be depleted in Ti, but again some of the particles were found contain more Ti than the bulk. How then, are both of these elements having the same effect ? It may well be that the way in which they affect the nucleation behaviour is entirely different but the effect is the same.

One suggestion is that the Mg affects the nucleation behaviour by actually changing the thermodynamics of the process. If the Mg partitions to the liquid to a large enough degree, then it is possible that the liquid will be sufficiently enriched in Mg to have its thermodynamic properties, such as melting temperature, and nucleation temperature significantly altered. To have the effect seen in these alloys the nucleation temperature of the metastable phase must have been lowered by the addition of Mg which could result from a reduction in the stability, and thus melting temperature, of the metastable phase. There is evidence that very small additions of certain elements can have a marked affect on the growth characteristics of an alloy. The modification of Al-Si alloys is a classic example where as little as 0.001 % Na added to the eutectic alloy is needed to drastically modify the eutectic structure [61]. Controversy remains on the mechanism of the effect but most

theories concentrate on the nucleation and/or growth of the eutectic Si. The thermodynamic changes are also a consideration in that the addition of Na depresses the eutectic temperature and shifts the eutectic composition towards the Si rich end of the phase diagram.

The fact that Ti affects the nucleation behaviour in a similar way to Mg is interesting. The excess Ti found in some of the particles may have been present in the lattice of the crystal but could have been present on the surface. It was only found to excess in the some of the high cooling rate samples. This could have arisen if Ti segregated to the Al-liquid interface and interfered with the nucleation of the metastable phase. If the potency of the surface as a nucleant for the metastable phase was reduced, the result would be that which was seen. This does not explain why it was only detected in some of the particles.

Alternatively, there is some evidence to suggest that the aluminium oxide film is affected by Ti and may be at the root of its effect. From the DC simulator experiments on Al-Fe-Si alloys, it was found that the addition of Ti tended to eliminate the FTZ even if there was a phase transition across the ingot. The Ti had an effect on the nature of the oxide film. It has been reported that Ti in commercial purity alloys at levels of 0.03 wt.% affects the nature of the oxide film grown during the electograining of lithographic sheet [62]. When DSC samples are examined after melting and solidification, the oxide film always appeared to have remained intact. The sample stayed the same shape throughout a set of experiments with feature such as burrs and scratches still visible after melting. In a DSC sample the oxide film has a large volume relative to the sample volume as a whole. If the Ti in the melt tends to 'stick' to the oxide film and become concentrated on it, or affects it nature in some other way, it is possible that it will affect the nucleation of some of the small pockets of liquid left in contact with it towards the end of solidification. It may be that the nature of the oxide film inhibits the nucleation of the metastable phase in some way and gives an advantage to the stable Al_3Fe.

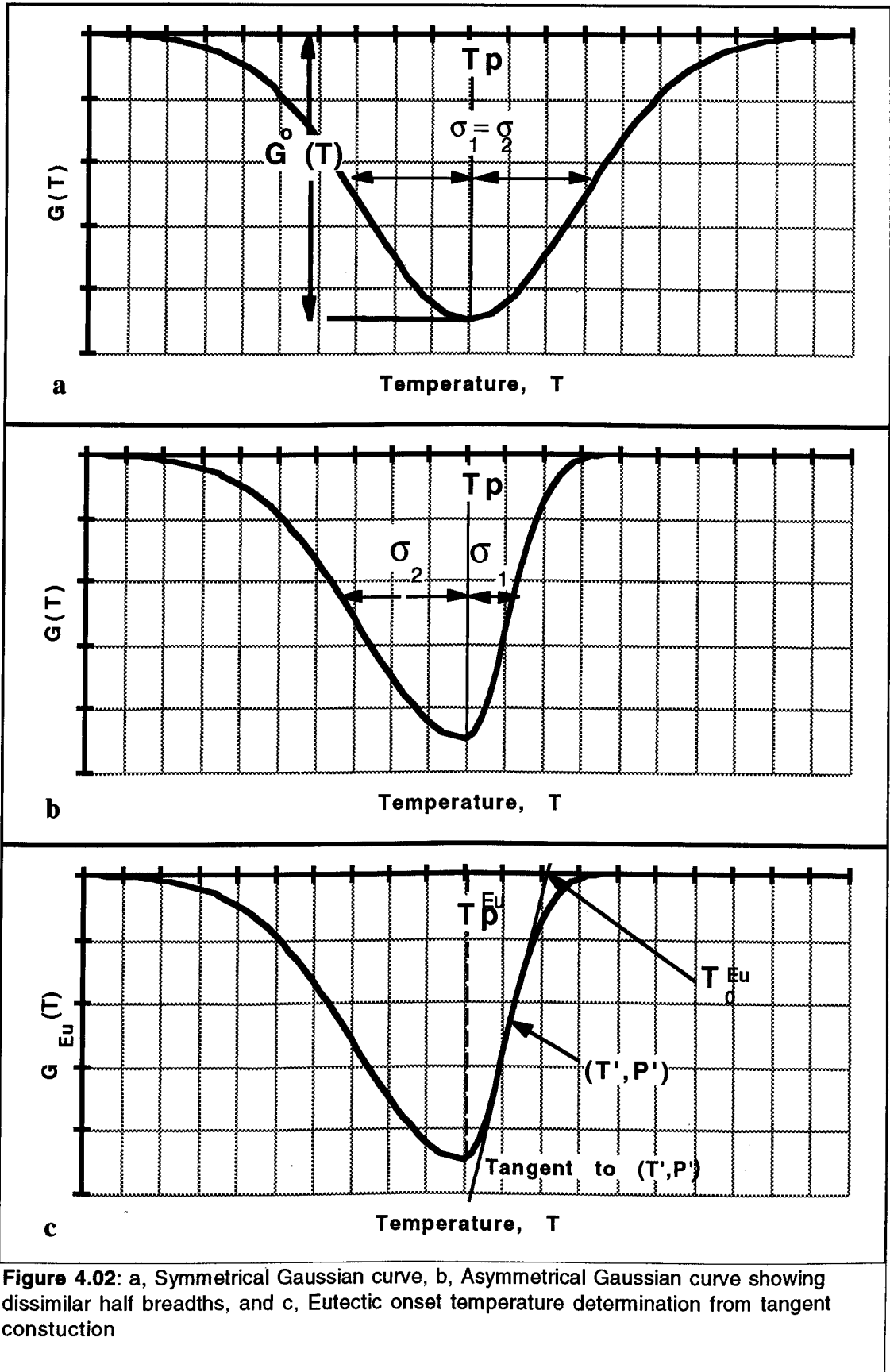### 4.4.4 The behaviour of the Binary Alloys with Ti-B grain refiner additions.

Grain refiners are used in commercial alloys to provide nucleation sites for the primary aluminium in order to homogenise the cast microstructure. The effect of Ti-B appears to have been to increase the nucleation temperature of the eutectic at all cooling rates. The results indicate that the addition of Ti-B has also enhanced nucleation of the metastable phase. A similar effect to this has been seen in the DC simulator experiments on

ternary alloys where the grain refiner promoted the nucleation of the metastable phases Al_mFe and cubic α over Al_3Fe and Al_6Fe, albeit at high cooling rates than were possible to use in the DSC. Using the simple nucleation model in figure 4.16(c), the way in which the grain refiner extends the range of cooling rates over which the metastable phase can form to lower values can be explained. The nucleation temperature of the metastable phase is increased for any given cooling rate. In this study, the morphology of the low cooling rate sample looked similar to the Al_3Fe found in other samples. The Ti-B addition did not enhance the nucleation of the metastable phase to such an extent that Al_3Fe was eliminated at all cooling rates. It remains unclear as to how the addition of Ti-B seem to have allowed Al_3Fe to form at lower cooling rates in the DC simulator experiments on binary alloys, but has apparently enhanced the nucleation of presumably Al_6Fe in the DSC sample. One possible explanation is that the grain refiner may have affected the growth of the intermetallics in the DC simulator experiments and that this effect would not have been seen in the DSC nucleation experiments. The growth of certain intermetallics among equiaxed dendrites may be favoured if they can easily branch or adjust their growth direction. This would not be required if the dendrites grew in a columnar fashion.

The Ti-B probably is able to promote the nucleation of one intermetallic phase over another by offering a better heterogeneous nucleation site. The crystallography of the Ti-B particle is hexagonal and it possibly promotes the higher symmetry metastable phases over the low symmetry monoclinic Al_3Fe.
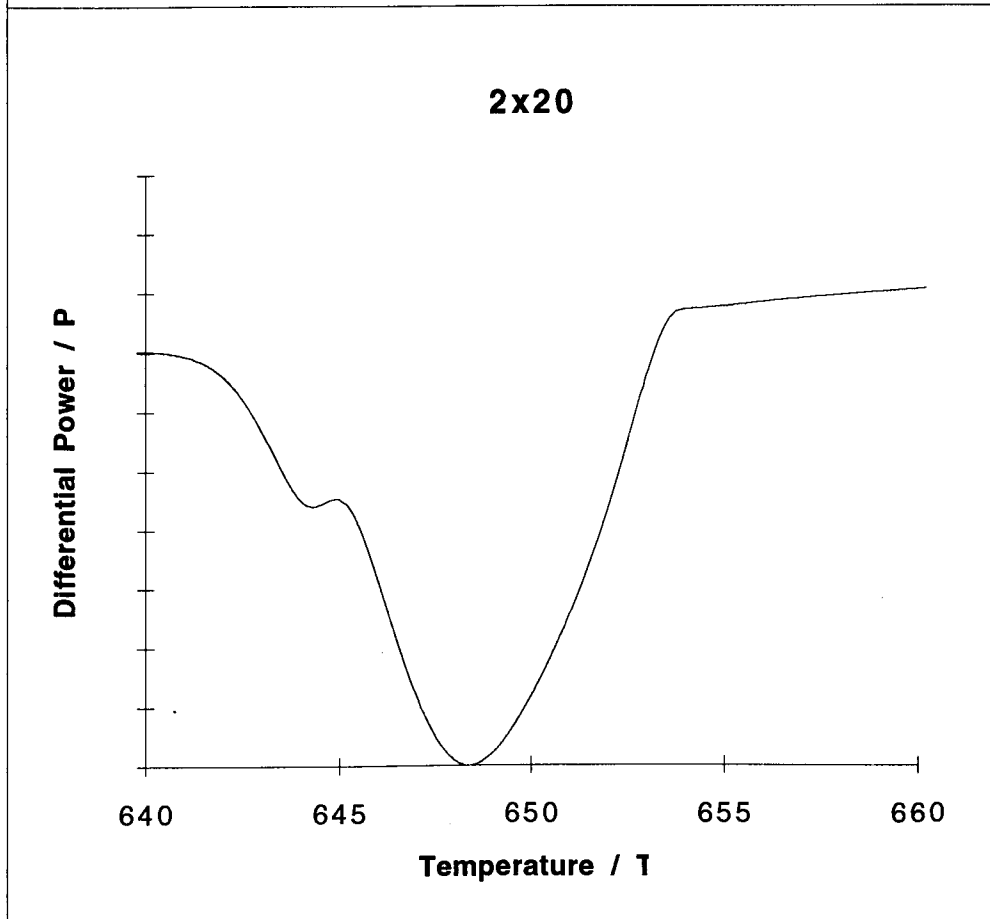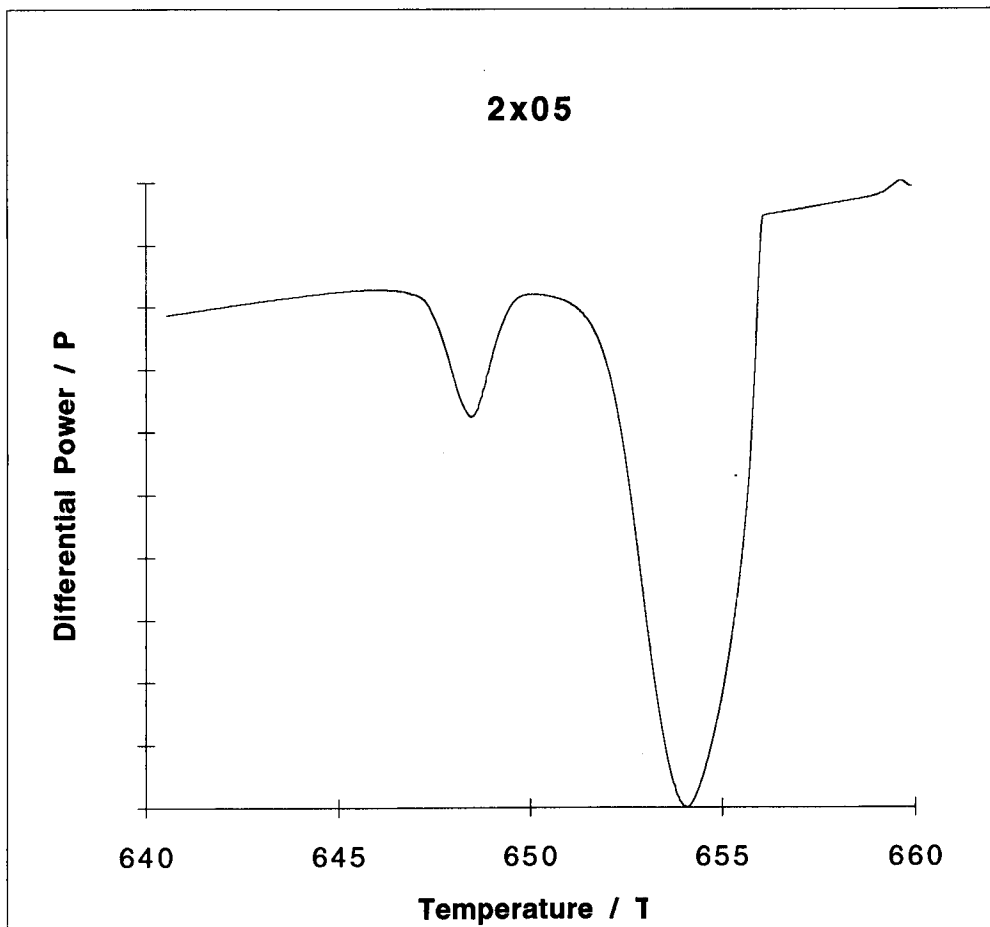
Figure 4.01: DSC plots showing the effect of cooling rate on the separation of the two peaks. (a.2x05 and b. 2x20)

Figure 4.02: a, Symmetrical Gaussian curve, b, Asymmetrical Gaussian curve showing dissimilar half breadths, and c, Eutectic onset temperature determination from tangent constuction

	Temperature	Differential	Baseline	Peak 1	Peak2	Fitted Curve		peak height	peak pos'n	sigma	Onset	
6776	620	10.42462	49.88	0.00	0.00	49.88	Linear	-2.020033461	621.9922274	1.76E-03		
6779	620	10.42923	49.88	0.00	0.00	49.88	Peak 1	-6.823856619	639.9534467	2.913504524	643.3880884	Eutectic
6782	620.066	10.43385	49.90	0.00	0.00	49.90				2.428658442		
6784	620.133	10.43692	49.93	0.00	0.00	49.93	Peak 2	-103.2113954	647.4909412	2.709431178	651.5746751	Aluminium
6787	620.2	10.44154	49.96	0.00	0.00	49.96				2.887635938		
6790	620.266	10.44615	49.99	0.00	0.00	49.99						
6792	620.333	10.44923	50.02	0.00	0.00	50.02	Least Sq peak	292520.9232				655
6795	620.4	10.45385	50.05	0.00	0.00	50.05	Least Sq base	1645912.756				650
6798	620.466	10.45846	50.07	0.00	0.00	50.07						
6800	620.533	10.46154	50.10	0.00	0.00	50.10	Baseline	-548.4971547	1.508237782	-0.000876		
6803	620.6	10.46615	50.13	0.00	0.00	50.13		0.00E+00	0.00E+00	0.00E+00		
6806	620.666	10.47077	50.16	0.00	0.00	50.16						
6808	620.733	10.47385	50.19	0.00	0.00	50.19						
6811	620.8	10.47846	50.21	0.00	0.00	50.21						
6814	620.866	10.48308	50.24	0.00	0.00	50.24						
6816	620.933	10.48615	50.27	0.00	0.00	50.27						
6819	621	10.49077	50.30	0.00	0.00	50.30						
6820	621.066	10.49231	50.33	0.00	0.00	50.33						
6824	621.133	10.49846	50.35	0.00	0.00	50.35						
6827	621.2	10.50308	50.38	0.00	0.00	50.38						
6828	621.266	10.50462	50.41	0.00	0.00	50.41						
6832	621.333	10.51077	50.44	0.00	0.00	50.44						
6835	621.4	10.51538	50.47	0.00	0.00	50.47						
6836	621.466	10.51692	50.49	0.00	0.00	50.49						
6839	621.533	10.52154	50.52	0.00	0.00	50.52						
6841	621.6	10.52462	50.55	0.00	0.00	50.55						
6844	621.666	10.52923	50.58	0.00	0.00	50.58						
6847	621.733	10.53385	50.61	0.00	0.00	50.61						
6849	621.8	10.53692	50.63	0.00	0.00	50.63						
6852	621.866	10.54154	50.66	0.00	0.00	50.66						
6855	621.933	10.54615	50.69	0.00	0.00	50.69						
6857	622	10.54923	50.72	0.00	0.00	50.72						

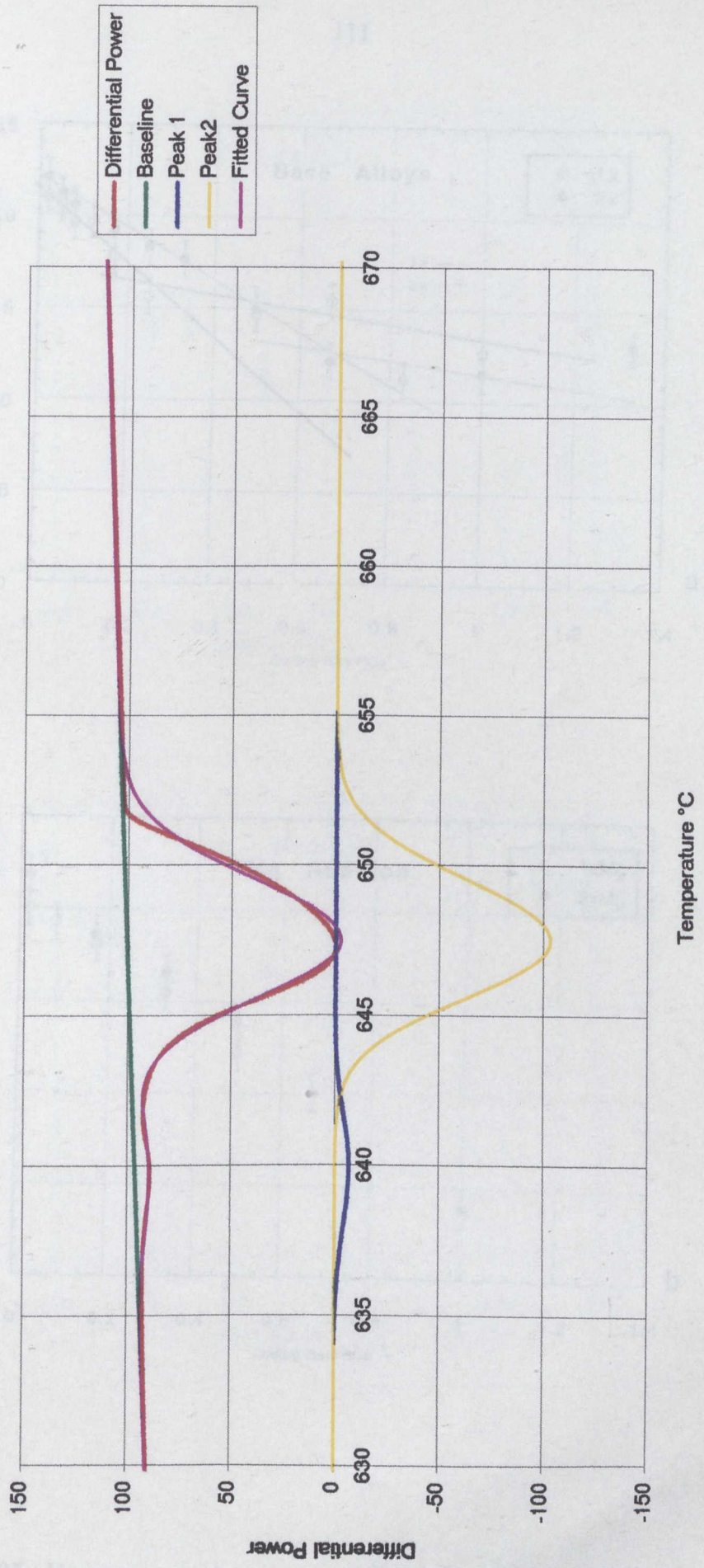**Figure 4.03** : Example of spreadsheet used to deconvolute DSC data.
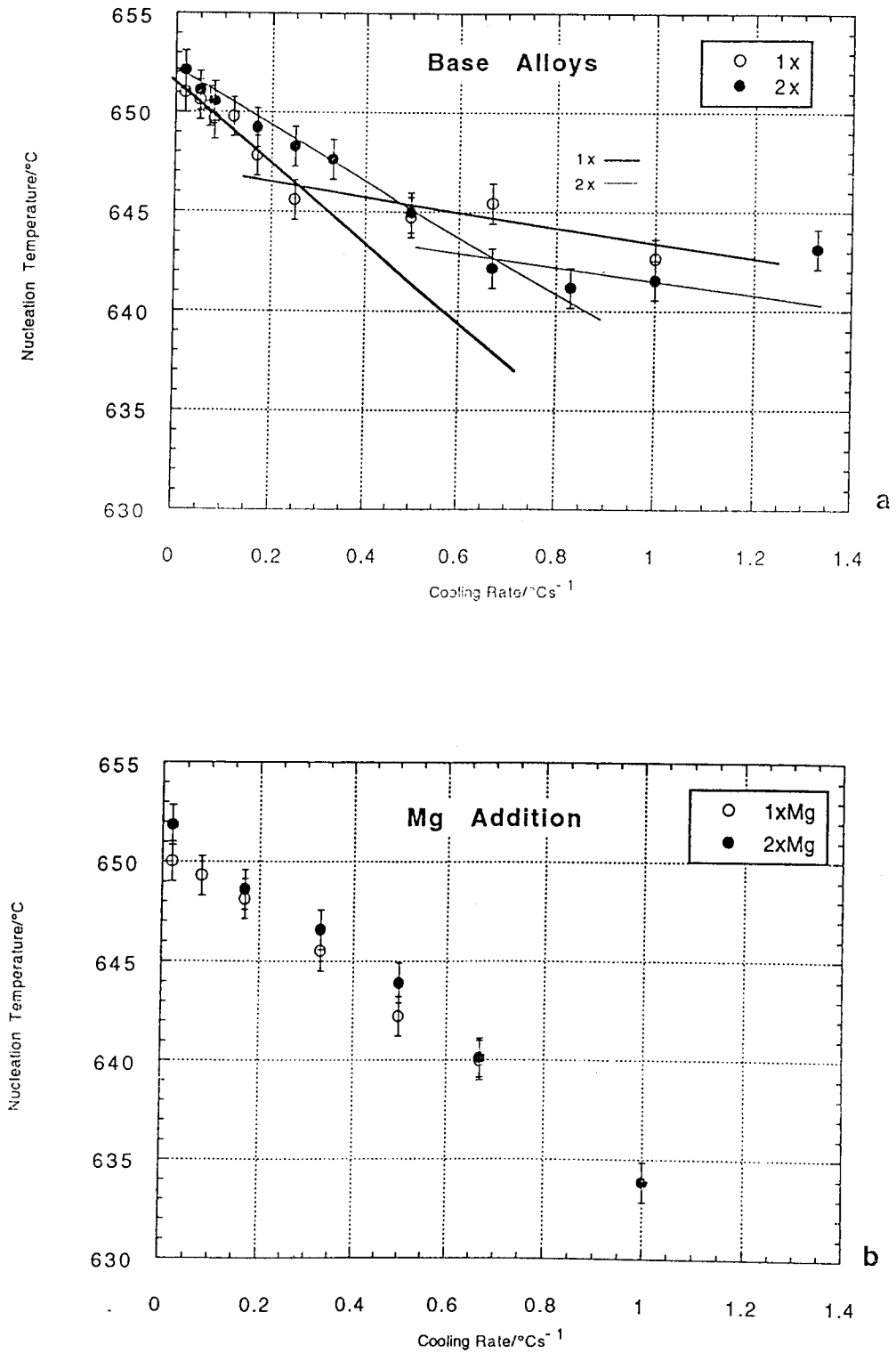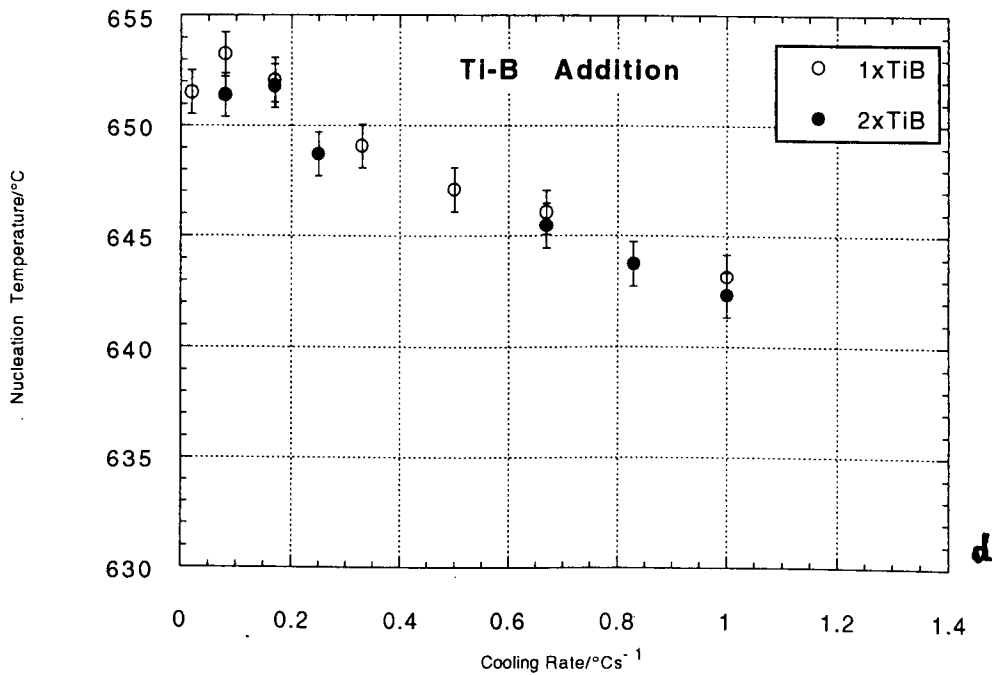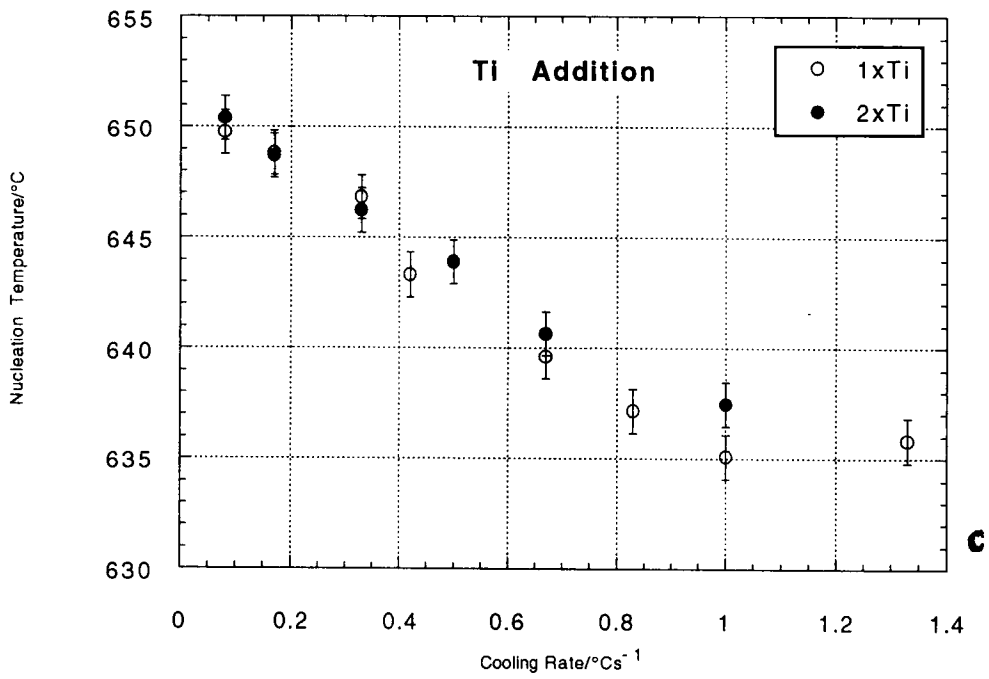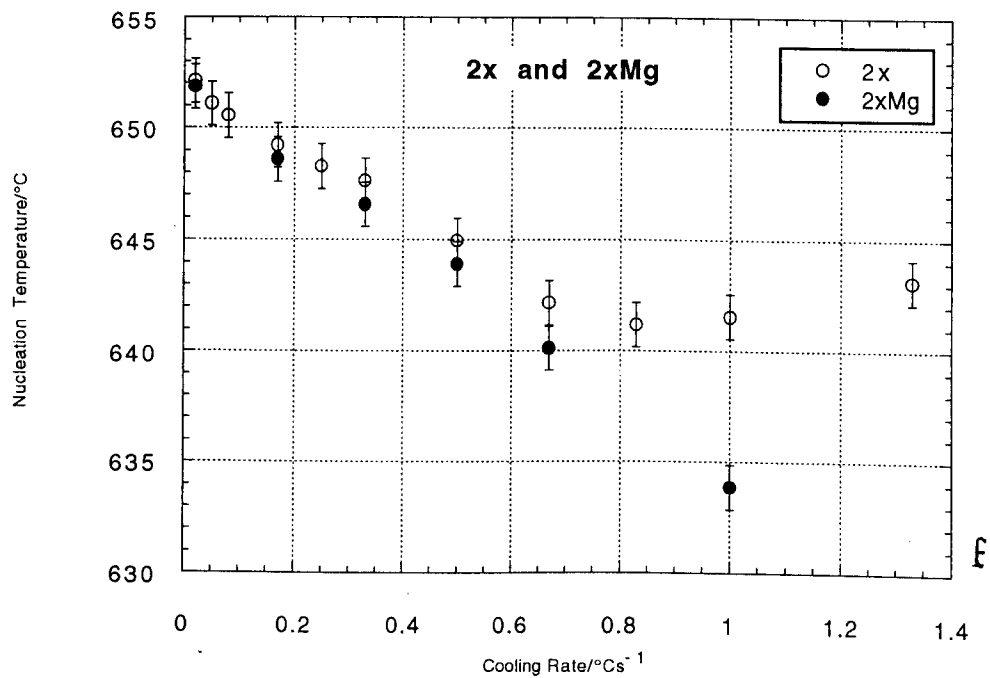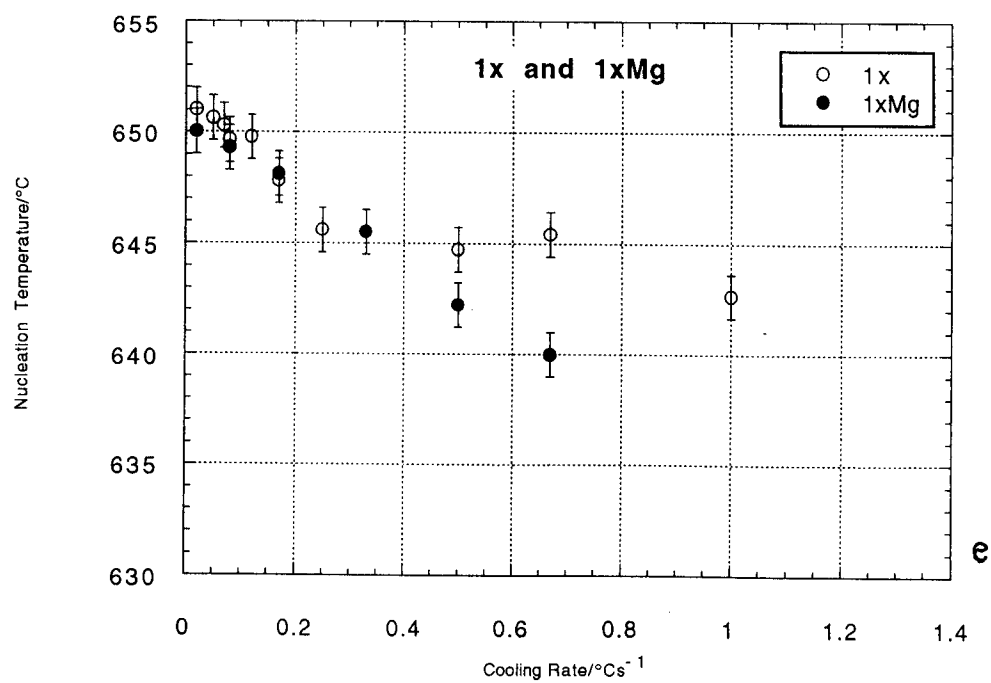
Figure 4.04: Example of fitted DSC peaks

Figure 4.05: Variation in nucleation temperature with cooling rate for DSC samples.

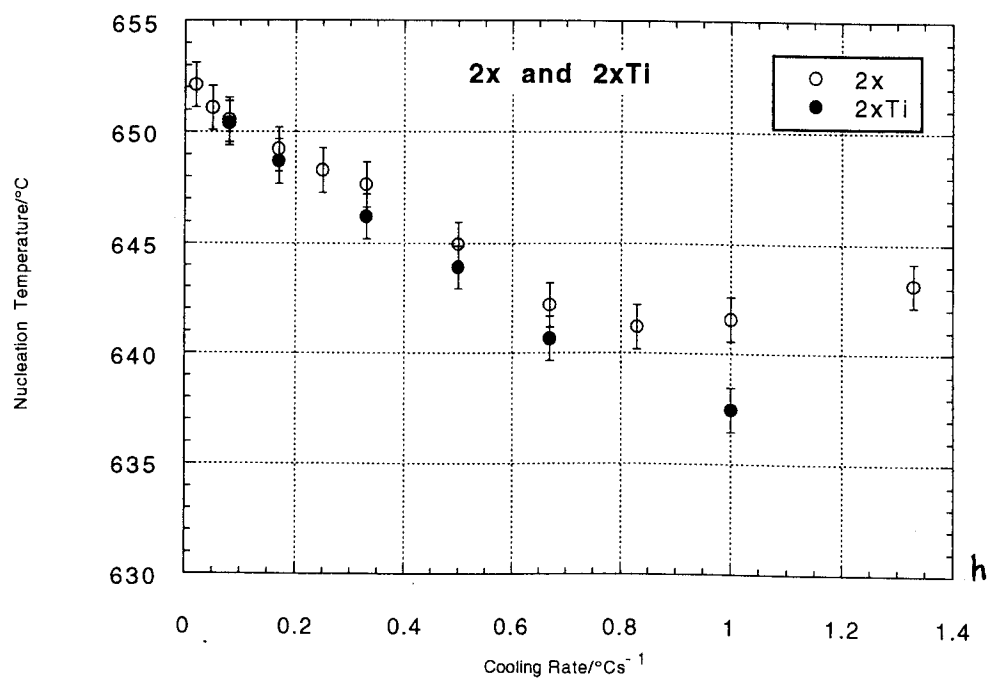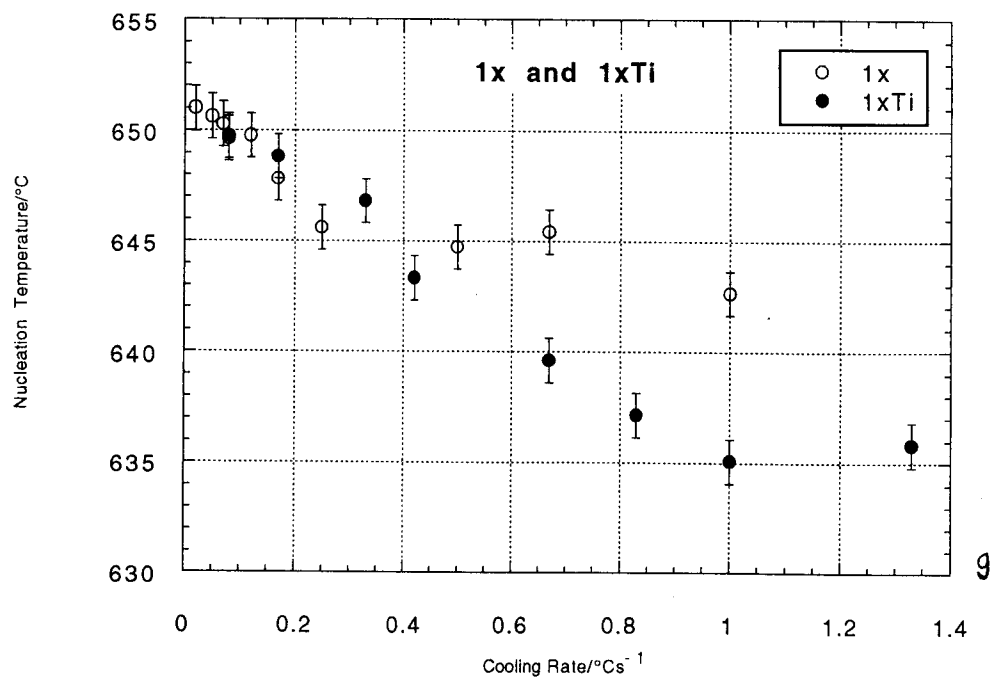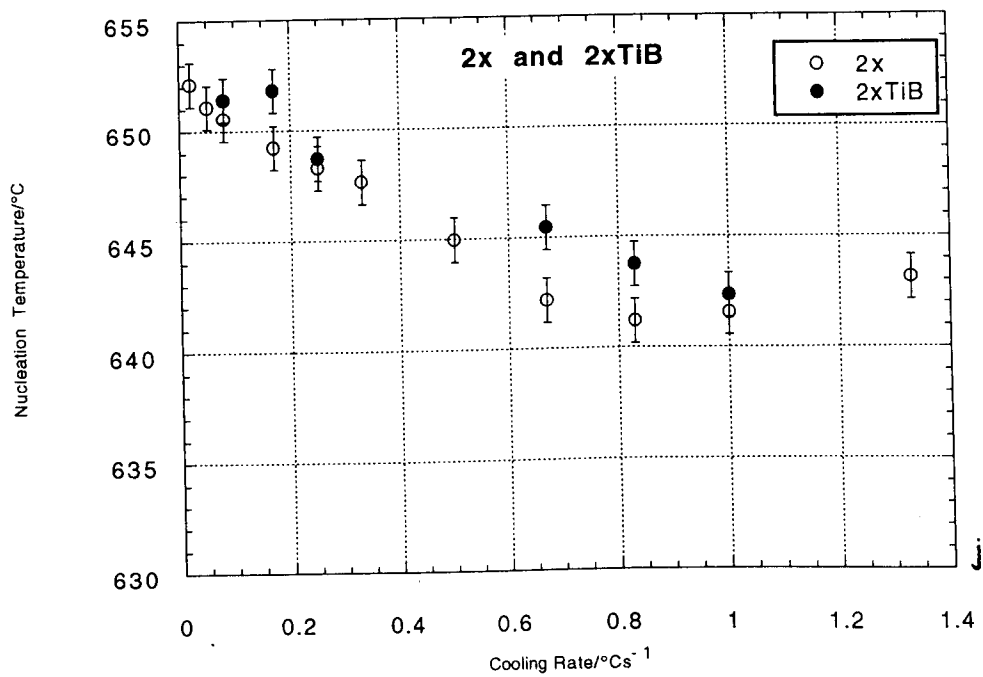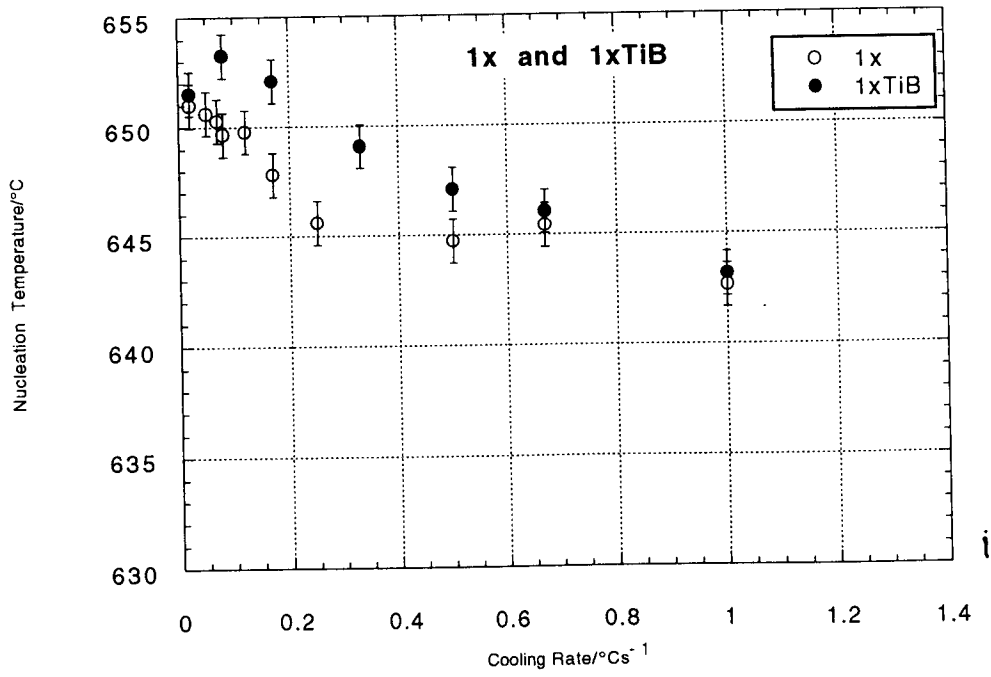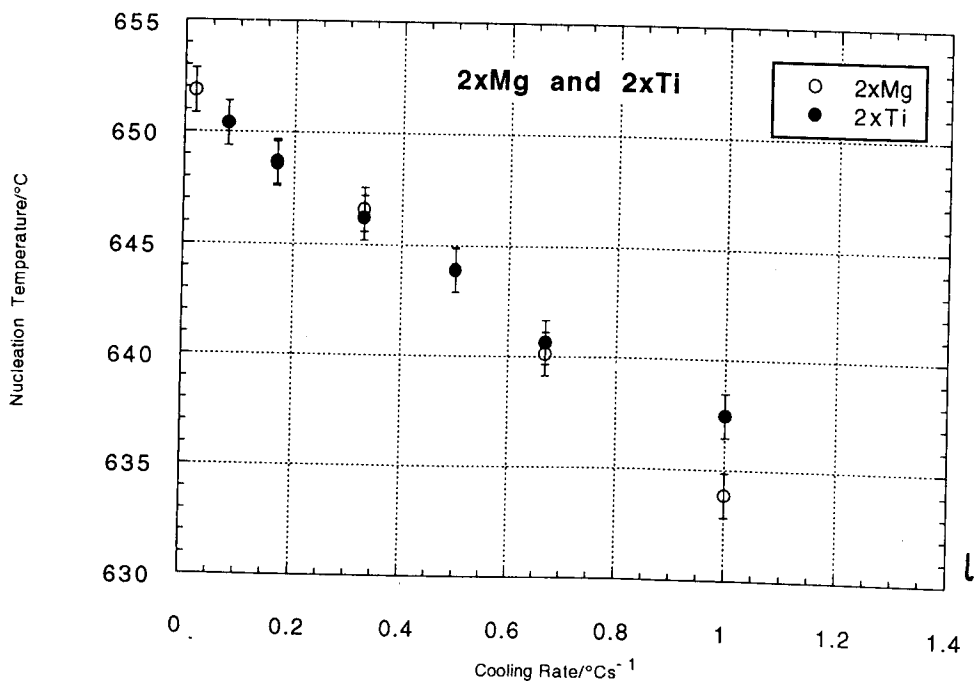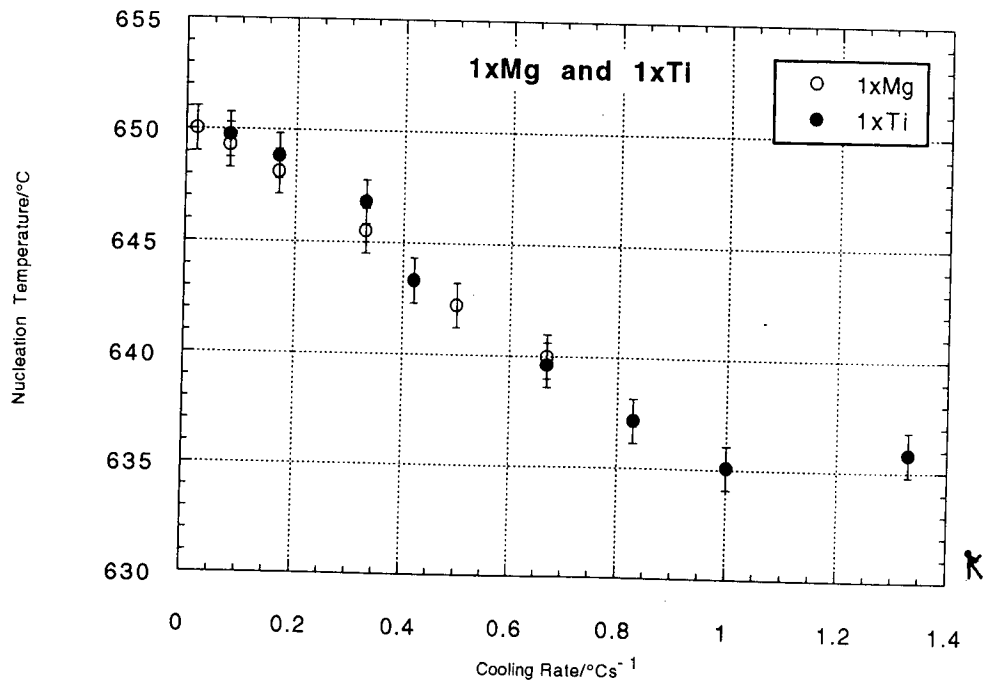**Figure 4.05:** Variation in nucleation temperature with cooling rate for DSC samples.

Figure 4.05: Variation in nucleation temperature with cooling rate for DSC samples.

Figure 4.05: Variation in nucleation temperature with cooling rate for DSC samples.
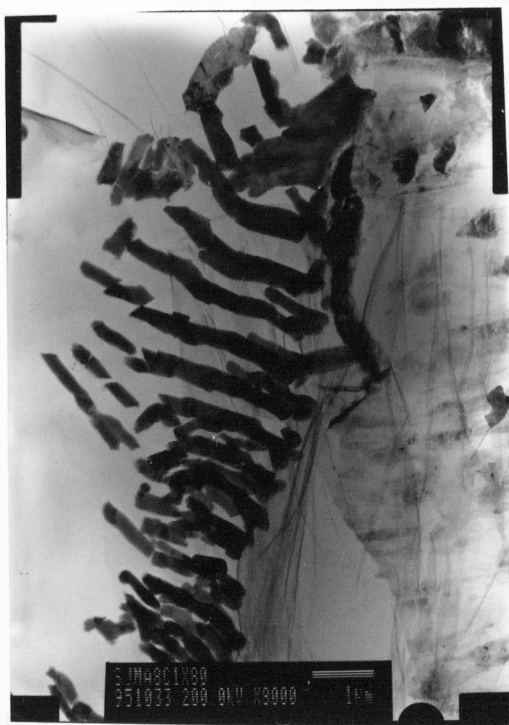
Figure 4.05: Variation in nucleation temperature with cooling rate for DSC samples.

Figure 4.05: Variation in nucleation temperature with cooling rate for DSC samples.
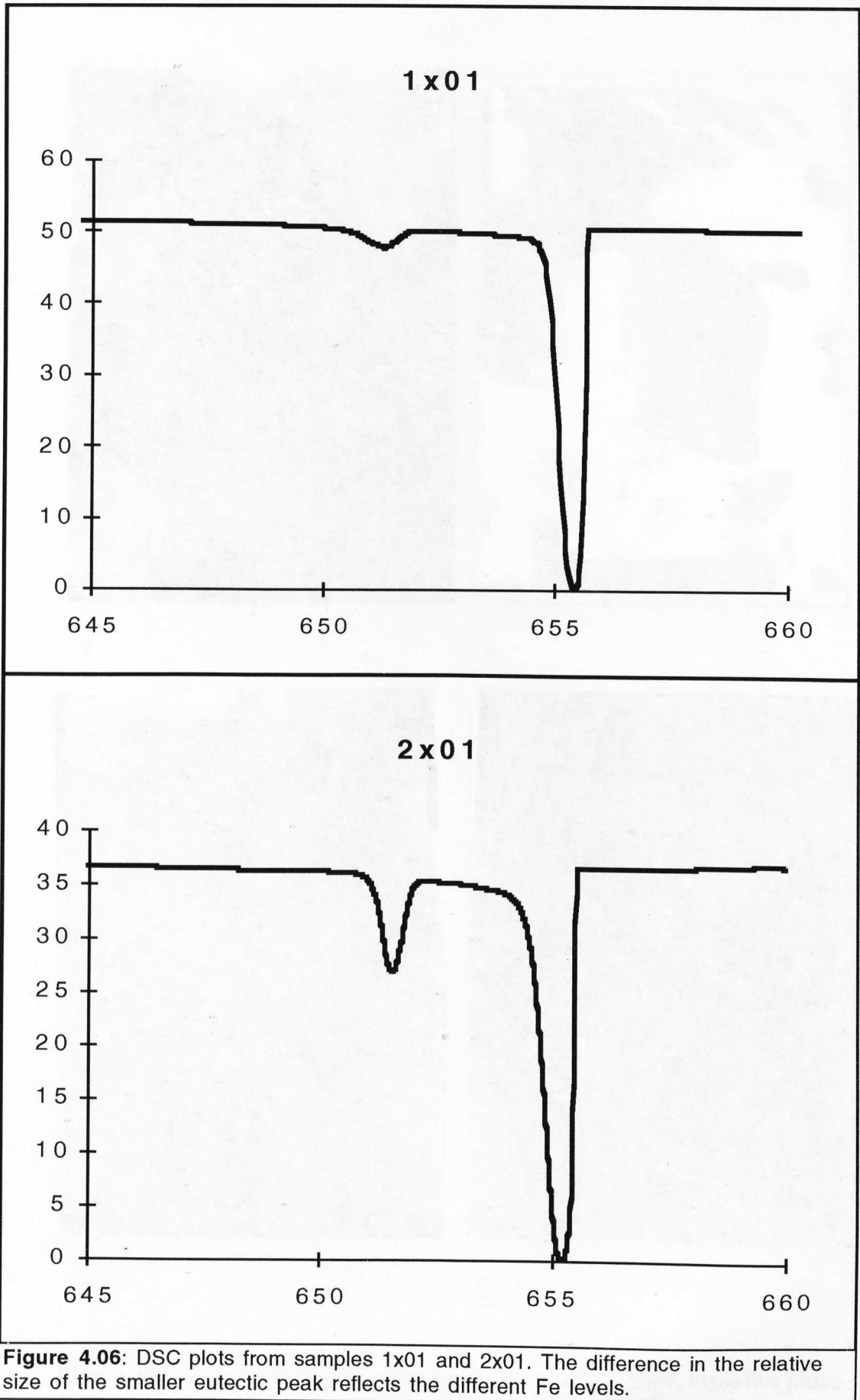
Figure 4.06: DSC plots from samples 1x01 and 2x01. The difference in the relative size of the smaller eutectic peak reflects the different Fe levels.
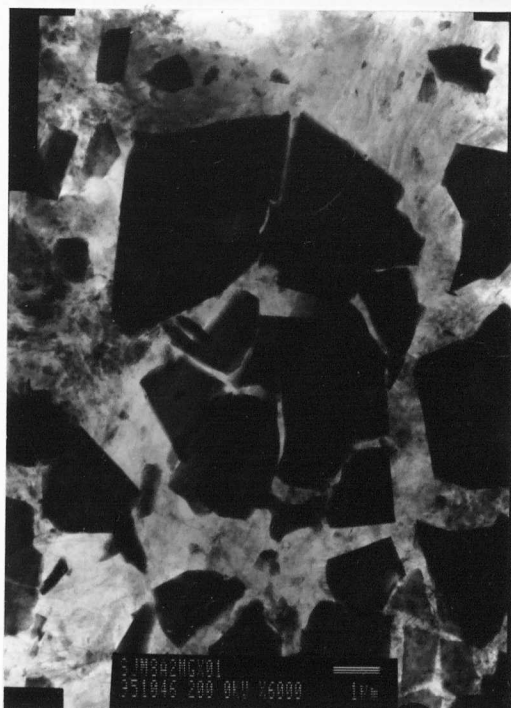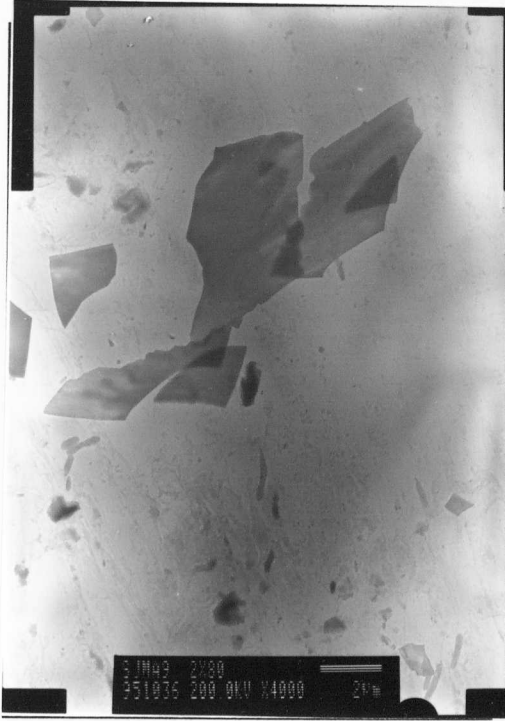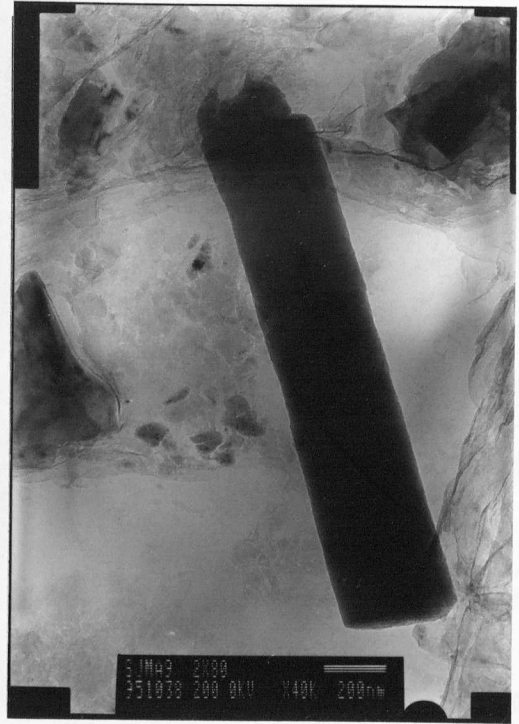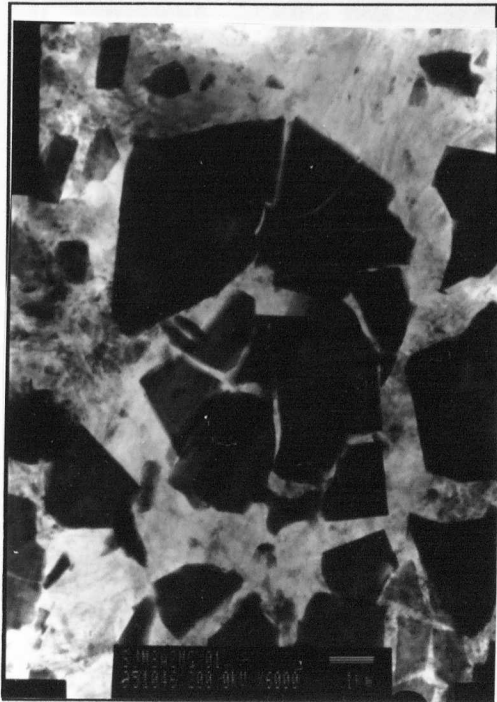
a.
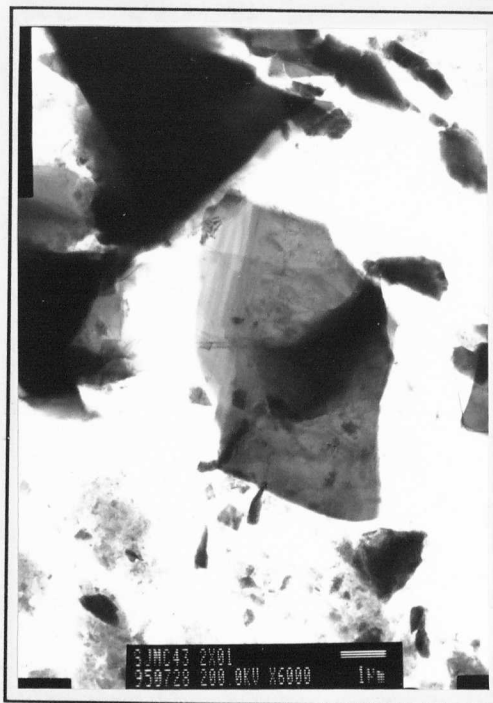
b.

c.

d.

Figure 4.07; **a**, 1x01, Plate-like phase (probably Al$_3$Fe), **b**, 2x01, Plate-like phase (probably Al$_3$Fe), **c**, 1x80, Rod-like regular eutectic phase, **d**, 1x80 Plate-like phase which has a different morphology to that shown in **c**.
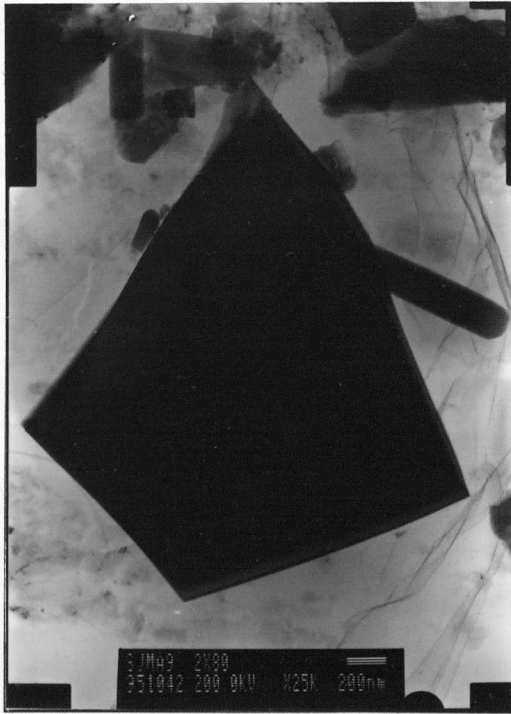
e.

f.

g.

h.

Figure 4.07; **e**, 2x80, Plate-like phase, **f.**, 2x80, Rod-like phase found in small quantities, **g**, 1xMg01. Plate-like phase, **h**, 1xMg80 Plate-like phase.
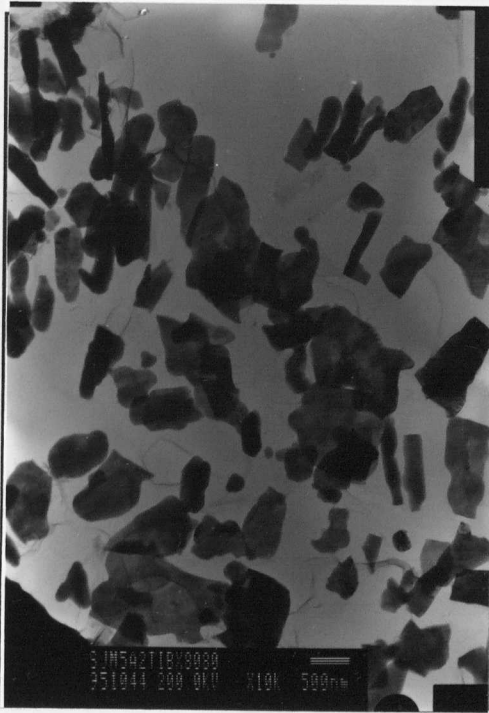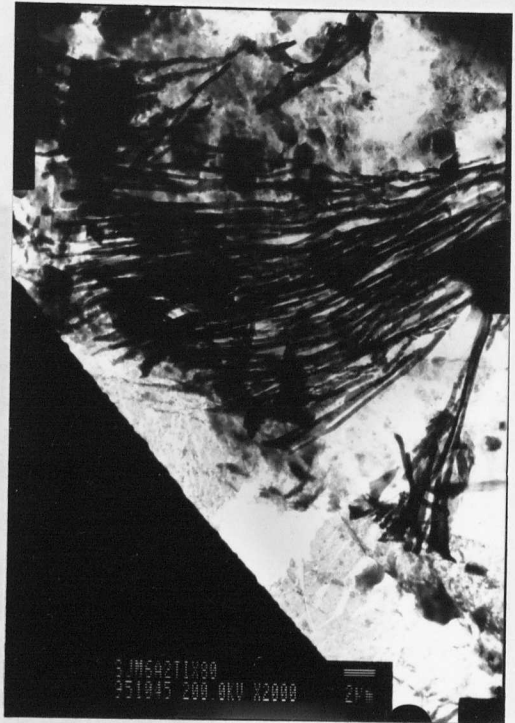
i.

j.

k.

l.

Figure 4.07; **i**, 2xMg80, Plate-like phase, **j**, 2xMg80, Rod-like phase found in small quantities, **k**,1xTi0, Plate-like phase, **l**, 2xTi01, Plate-like phase. Both **k** and **l** are likely to be Al_3Fe.

m.

n.

o.
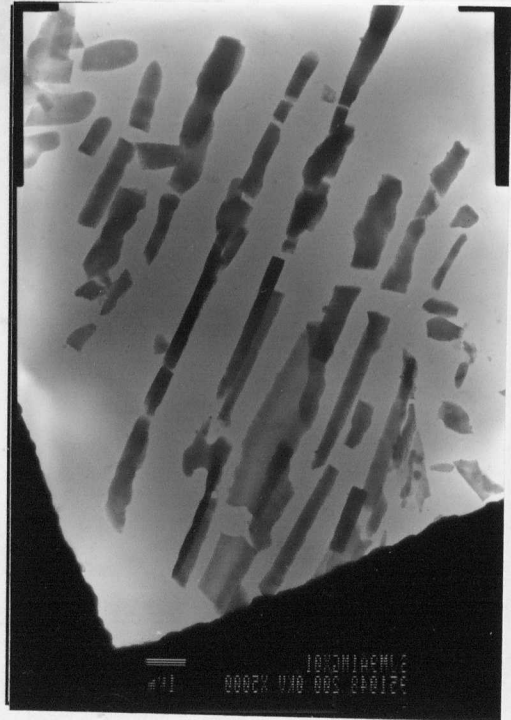
p.

Figure 4.07;. **m**, 2xTi80, Plate-like phase, **n**., 2xTi80, Phase morphology unique to this sample, **o**, 1xTiB80, Plate-like phase, **p**, 1xTiB80, and,**q**, 2xTiB80,(see overleaf) both show a phase morphology distinct from the assumed metastable phase morphologies found in other samples.
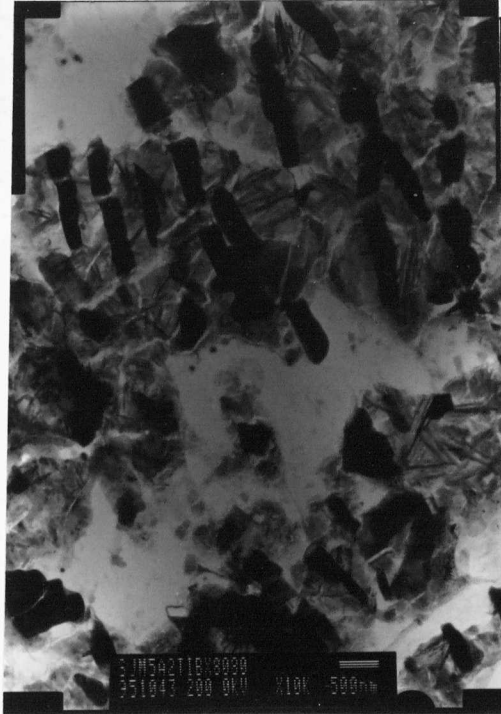
q.

Figure 4.07: q, 2xTiB80, regular eutectic phase morphology not seen in other samples (except figure 4.07 p)
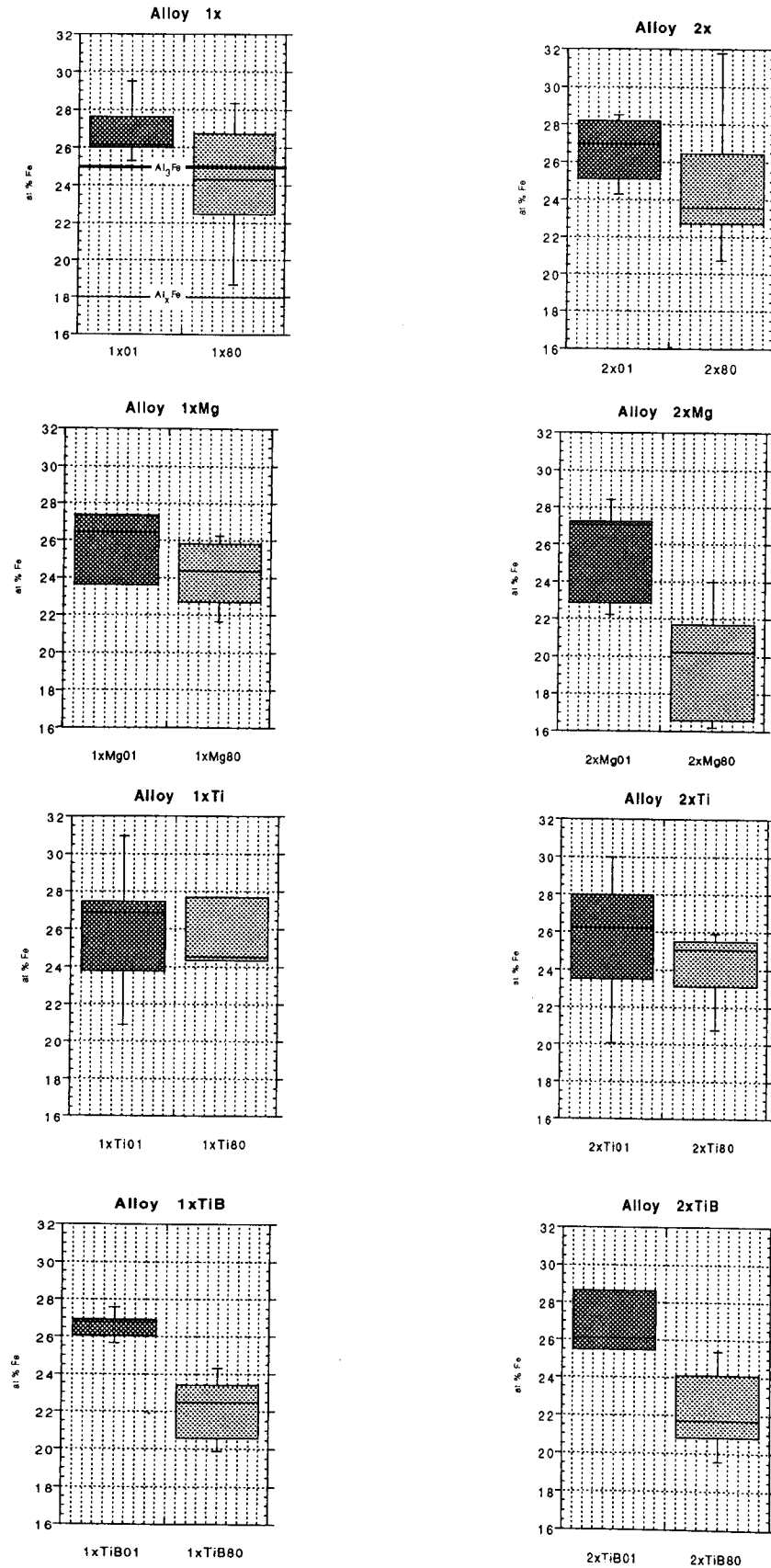
Figure 4.08: High-Low plots of EDX measurements of at.% Fe in DSC samples.
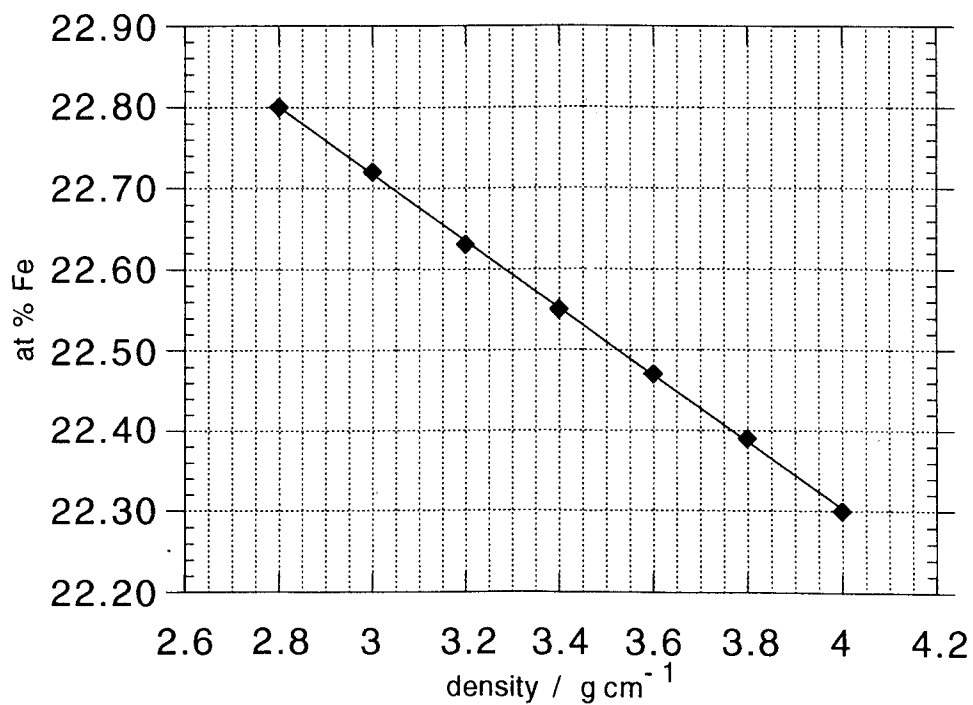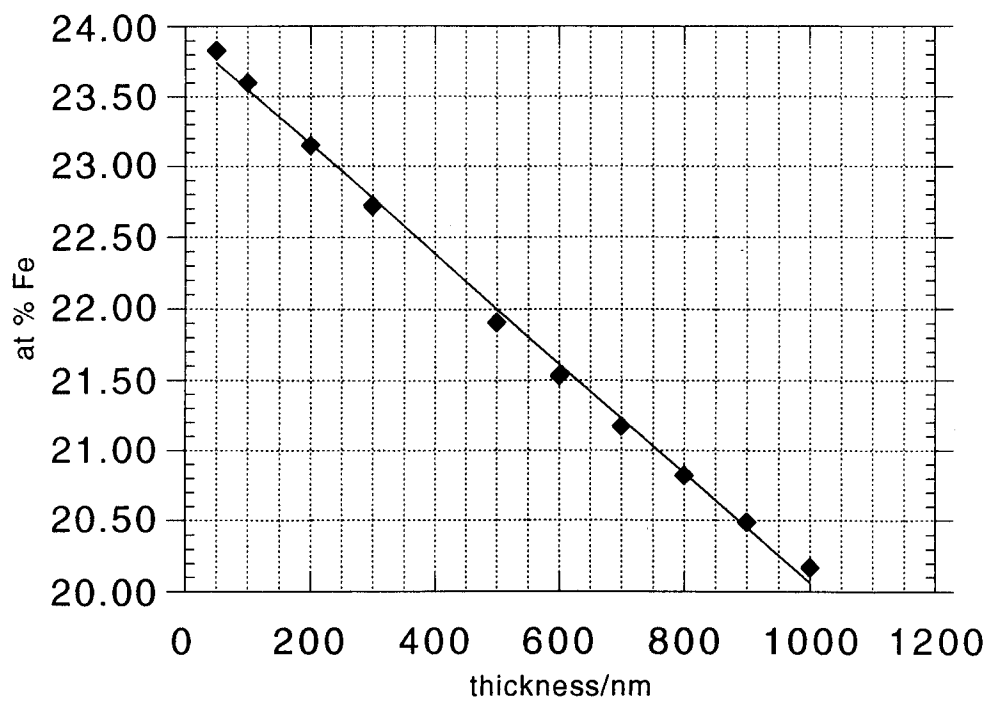
Figure 4.09: Variation in calculated at. % Fe with given thickness and density.
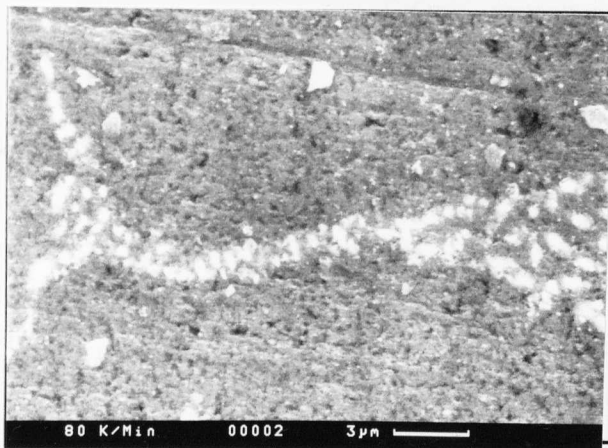
Figure 4.10: SEM image of high cooling rate DSC sample. The cross section through the thickness of the sample shows the thickness of the intermetallics.
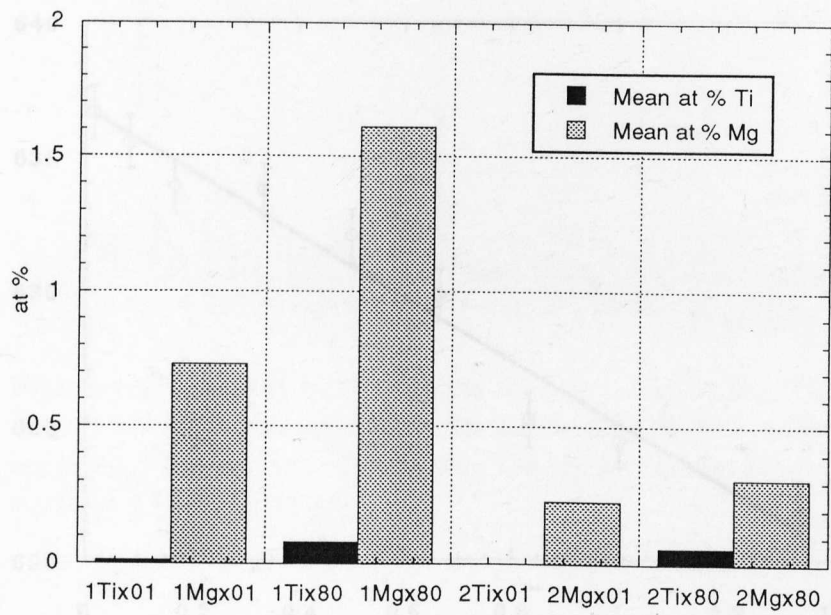
Figure 4.11: Average Mg and Ti level in xTi and xMg intermetallics determined by EDX
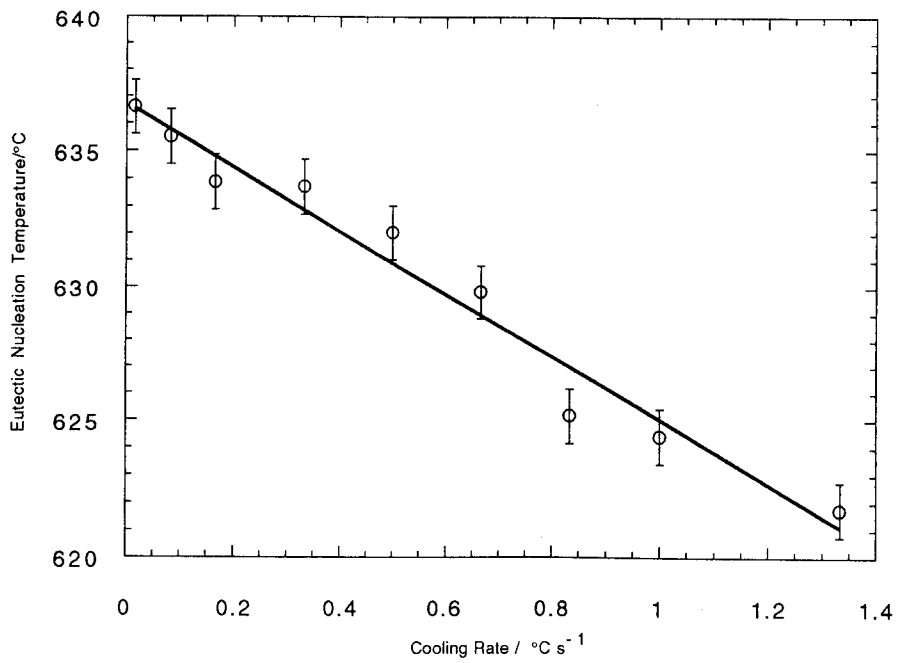
Figure 4.12: Variation in eutectic nucleation onset temperature with cooling rate for Al-1 wt. % Ni.
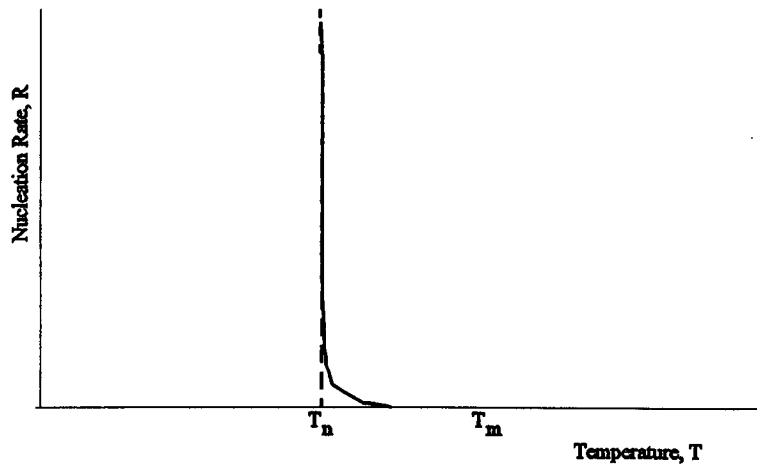
Figure 4.13 Schematic of nucleation rate vs. undercooling. The number of nucleation events occuring before the temperature defined as T_N is reached is considered insignificant. This allows the approximation $I(T_N) = \Phi/V$ (see equation 4.23) to be made.
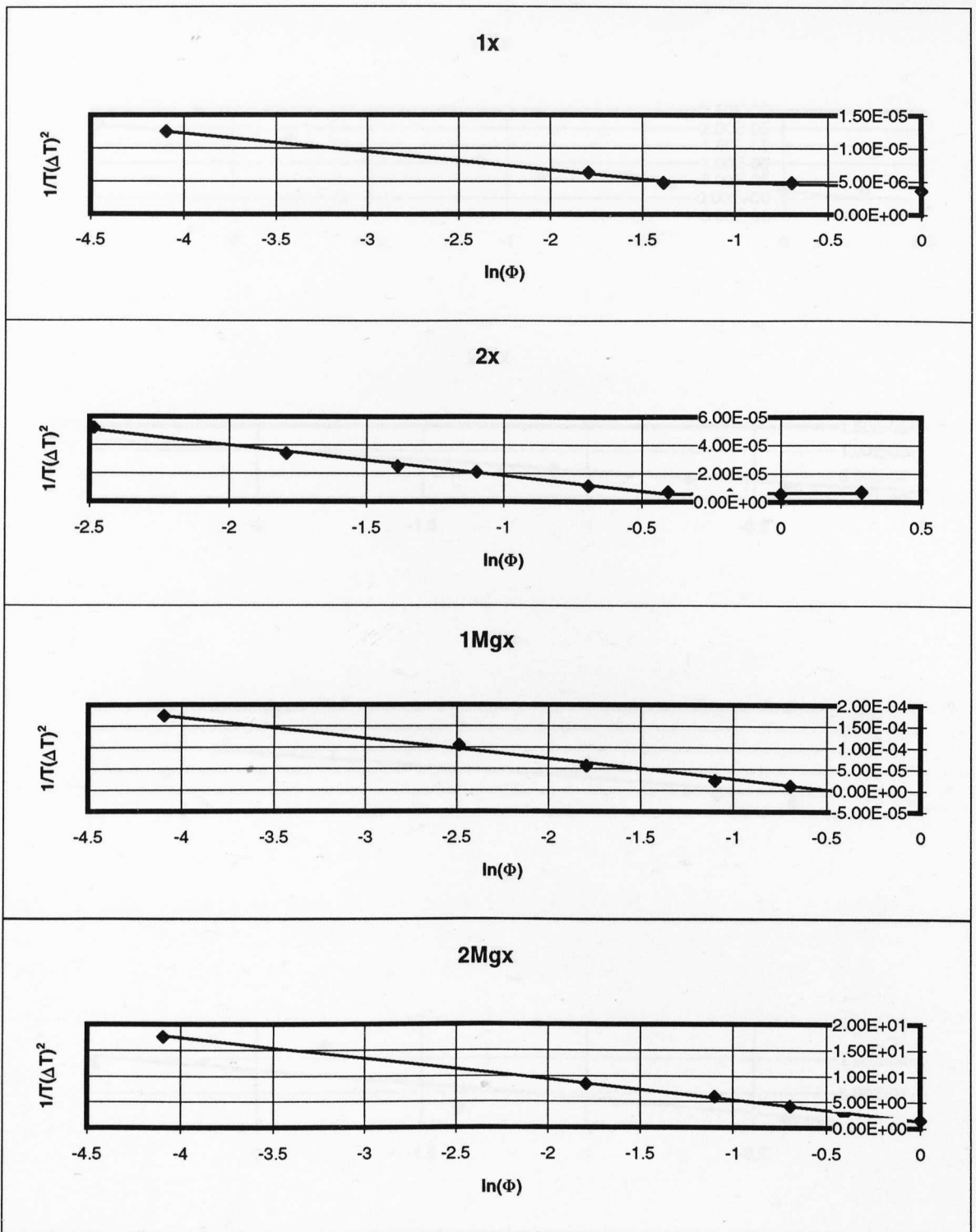
Figure 4.14: Plots of ln (Φ) vs $1/T(\Delta T)^2$ for each of the DSC alloys. The lines were fitted using the least mean square technique.
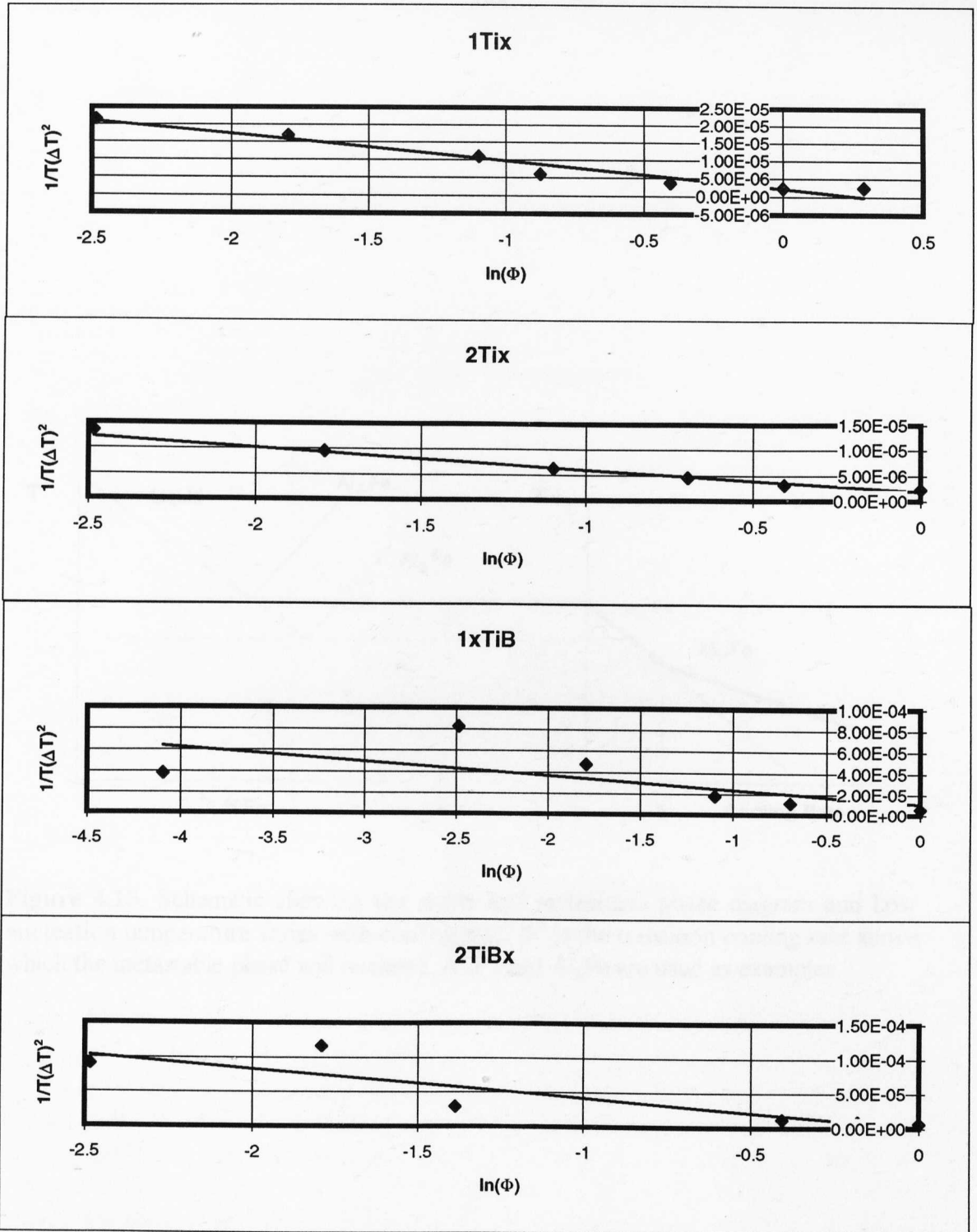
Figure 4.14: Plots of ln (Φ) vs $1/T(\Delta T)^2$ for each of the DSC alloys. The lines were fitted using the least mean square technique.
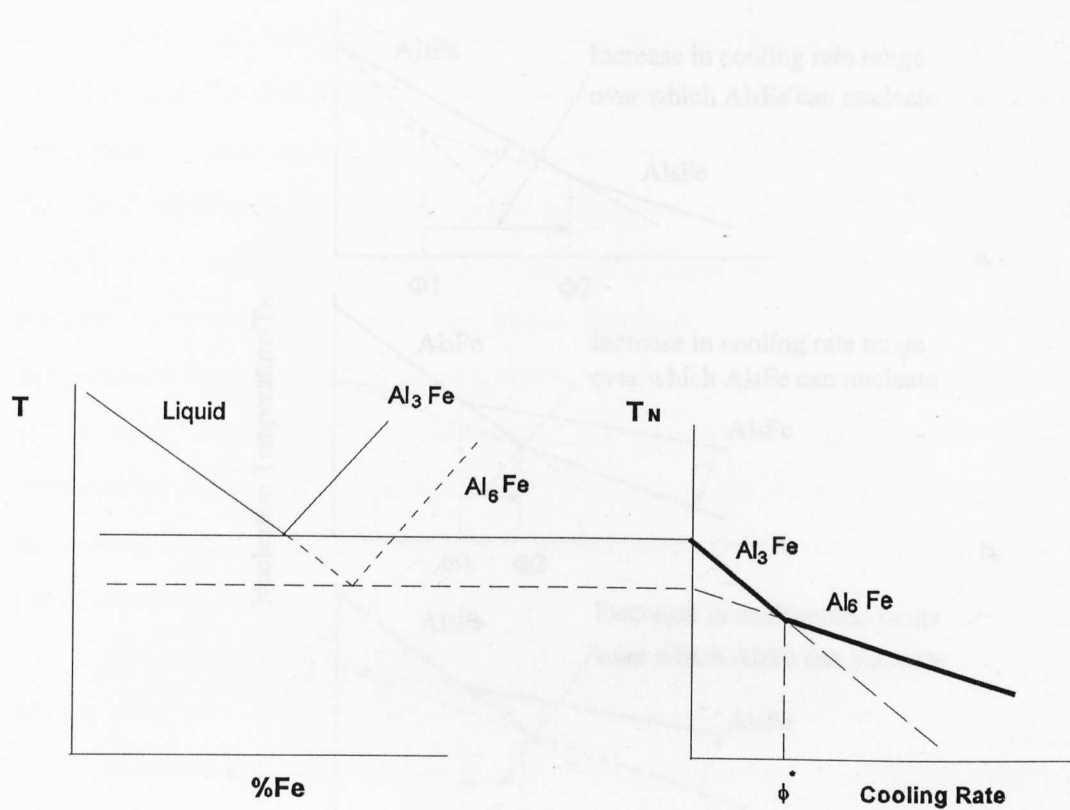
Figure 4.15. Schematic showing the stable and metastable phase diagram and how nucleation temperature varies with cooling rate: Φ^* is the transition cooling rate above which the metastable phase will nucleate. Al_3Fe and Al_6Fe are used as examples.

Figure 4.16 Schematic diagrams showing how the addition of trace elements which affect nucleation temperatures can shift the transition cooling rate (Φ). **a.** shows how an element which enhances the nucleation of Al_3Fe can increase the transition cooling rate. **b.** shows the proposed effect of the addition of Mg and Ti in these studies, whereby Al_3Fe is able to nucleate at higher cooling rates due to the supression of the metastable phase. **c.** shows the proposed effect of the addition of TiB grain refiner in these studies, whereby the metastable phase is able to nucleate at lower cooling rates due to the TiB providing it with favourable nucleation sites.

5.0   Bridgman Growth Experiments.

5.1   Introduction

The Bridgman furnace is a directional solidification furnace allowing growth velocity, U, to be accurately controlled. The growth velocity in a Bridgman furnace is controlled by the rate of withdrawal of the molten sample from a hot region of a vertical furnace through a sharp temperature gradient into a cold zone at a temperature well below the melting temperature. The metal solidifies as it passes through the temperature gradient. By controlling the growth velocity it is possible to gauge its effect on the resulting microstructure; in particular, it is possible to investigate its effect on phase selection. In these experiments, the growth temperature was measured by placing thermocouples into the sample before solidification and logging the temperature throughout the experiment. The difference in thermal conductivity between the liquid and solid meant that the growth temperature could be determined from the point of inflection on the temperature vs. time plot recorded during the experiment.

5.2   Aims

Experiments were conducted with binary eutectic alloys with and without trace additions present. The aim of the experiments was to identify the critical velocity, if any, at which the eutectic intermetallic phase changed due to competitive growth considerations. Alloys of eutectic composition were used because eutectics do not solidify over a range of temperatures. It was intended that a single inflection in the temperature vs. time plots, measured by a thermocouple inserted into the sample, would occur as the eutectic growth front passed the thermocouple. The composition used was that of the equilibrium eutectic Al-Al$_3$Fe with an invariant temperature of 655 °C. The Bridgman furnace. has been used by other workers with similar alloys to examine phase transitions and the effect of growth velocity on morphology [48,49,35.]. These experiments would show how alloy composition affected the transition velocity from one intermetallic phase to another and affected the growth temperature of the different eutectics over a range of solidification velocities.

The Bridgman furnace enables the growth front velocity and the temperature gradient at the interface to be controlled independently. The DSC experiments detailed in the previous chapter isolated the effect of cooling rate on the intermetallic phase selection. The cooling rate in a DC cast ingot gradually decreases from the inner edge of the shell zone to the centre. But, because the local solidification velocity profile has a different shape due

to the development of a sump of molten metal, see figure 5.01, the effect of local solidification velocity required examination. The Bridgman furnace allowed the influence of local solidification velocity to be isolated in much the same way that the cooling rate was in the DSC.

In a DC cast ingot, the local solidification direction is normal to the sump wall. If there were no sump present, the solidification front would be perpendicular to the casting direction and the solidification velocity would equal the casting rate. The sump develops as a result of the increasing thermal path through which heat from the solidifying metal has to diffuse. Consequently, the local solidification velocity varies with position in the ingot: the shape of the sump affects the solidification velocity profile. Figure 5.01 shows schematically the effect of the sump shape on local solidification velocity. The casting rate, C, is the rate at which the ingot is withdrawn from the mould. In a steady state, the local growth velocity equals the component of the casting rate normal to the growth front, $U_\perp = C \cos\theta$, whose variation across the ingot is also shown in figure 5.01. The maximum local growth velocity occurs at the edge and the centre of the ingot where the growth direction is parallel to the casting direction.

In practice it has been noted [52] that metastable phases found near the edge of DC cast ingots usually re-appear in the centre, causing a double FTZ. The cooling rate model used for explaining the FTZ assumes that high cooling rates near the edge result in metastable phases and lower cooling rates nearer the centre result in the metastable phase. The re-occurrence of metastable phases near the centre of some ingots cannot be explained if the single factor controlling phase selection is cooling rate but can be explained by variation in local growth velocity shown in figure 5.01.

5.3   Experimental

5.3.1 Choice of Alloy

An off-eutectic alloy pulled through a sharp temperature gradient will solidify over a range of temperatures with a mushy zone consisting of primary dendrite tips growing ahead of the interdendritic eutectic. In previous studies [49] the growth temperature has been measured by inserting a thermocouple in the molten sample prior to solidification. The temperature is logged and after a known period of time, when the solidification front has passed the thermocouple, the sample is quenched by dropping it through the hot zone of the furnace into the cold zone. The sample is then sectioned longitudinally, polished and etched

to show the solidification microstructure. The metal which was liquid before the quench will have solidified rapidly and will be apparent from the difference in microstructural scale. The distance from the solidification front to the thermocouple is measured. With the knowledge of the solidification velocity, the distance the solidification front has travelled and the temperature measured by the thermocouple, the growth temperature can be determined.

The main drawback of this technique is that it takes a considerable time to conduct each experiment. Each sample needs to have a new thermocouple inserted, which is time consuming and prone to failure and then requires careful metallographic preparation and examination. In the present study, the eutectic growth temperature was of primary interest and the alloys chosen were all based on the Al-Al$_3$Fe eutectic composition (Al 1.8 wt.% Fe). By using alloys of the eutectic composition, the transition from solid to liquid would occur at one temperature. (It was later noted that this was a mistake due to the nature of the Al-Al$_3$Fe coupled zone. This is discussed in detail later)Furthermore, since the thermal diffusivity of solid and liquid metal are different, a plot of temperature vs. time would show an inflection when the solidification front passed the site of the thermocouple. The advantage of this technique was that the need to metallographically examine each sample was overcome. The temperature could be logged, stored on disc and the sample remelted and reused repeatedly without the need for replacement thermocouples.

5.3.2 Alloy Preparation.

Sample	wt. % Fe	wt. % Mg	wt. % Ti	wt. % B
EUT	1.80	-	-	-
EUT Mg	1.82	0.02	<0.001	<0.001
EUT Ti	1.80	<0.001	0.041	<0.001
EUT Ti-B	1.81	<0.001	0.037	0.007

Table 5.01 Compositions of alloy prepared for Bridgman furnace experiments. (values were determined by spectrographical analysis).

Alloys of the Al-Al$_3$Fe eutectic composition of Al-1.8 wt. % Fe were made up from superpurity Al (99.999 wt. %) and Al-5 wt. % Fe, superpurity-based master alloy. 400 g batches of this base alloy were melted in an induction furnace and additions of 99.9 wt. %

Mg metal, superpurity-based Al-5 wt. %Ti master alloy and commercial purity 5:1 grain refiner (Al-5 wt. %Ti-1 wt. % B) made to give the alloy compositions shown in table 5.01

5.3.3 The Design and Operation of the Bridgman Furnace

Figure 5.02 shows a cross section of the Bridgman furnace. The Bridgman furnace consists of a vertical furnace connected to a temperature controller which maintained the furnace at 900°C. Situated lower down, inside the furnace, is a water bath contained within a water cooled jacket providing the heat sink. A thermal gradient of 5 °C mm^{-1} was maintained at the solid/liquid interface in all of the experiments.

Graphite crucibles, of 4 mm inside diameter, were used to contain the melt. In previous experiments conducted by other users at the Alcan International Laboratory, steady state solidification in these crucibles could be maintained at velocities up to 25 mm min^{-1}. Above this velocity, it was found that the solidification front was never able to attain steady state but was always travelling slower than the rate of withdrawal *i.e.*, the transient length (the part of the sample where the solidification front accelerated from rest to the set level) was longer than the sample itself.

Figure 5.03 shows a schematic diagram of the experimental set-up. A 0.30 mm diameter horizontal hole was drilled through the crucible at a distance of 100 mm from its base. An alumina sheath (0.25 mm inside diameter, 0.30 mm outside diameter) was then cemented into the hole. A K-type thermocouple, whose tip had been swaged by the manufacturers down to a diameter of 0.25 mm, was fed into the sheath so that its tip was situated in on the centreline of the crucible. The alumina sheath allowed thermocouples to be removed after an experiment and reused. (The thermocouples were very fragile and prone to mechanical failure and often needed to be replaced). The thermocouple was connected to an ADU MM700 Series data logger, controlled through a lap top computer (AST Premium 386SX/25 PC).

The crucible containing the thermocouple was cemented into a holder on the end of the withdrawal rod and the assembly inserted into the furnace. A rolling, double 'O' ring seal at the bottom of the water bath allowed the crucible and withdrawal rod to be moved up and down within the furnace without water leaking from the bath. Once the seal was in place, the bath was filled with water to a pre-set level and the coolant water system and an argon gas supply to the furnace were switched on. The furnace was heated to 900°C and maintained at that temperature throughout the experiment.

The crucible was filled with molten alloy by raising the top of it above the top of the furnace and placing a tightly fitting graphite funnel on to the end. A long graphite stop was used to plug the hole in the base of the funnel while the alloy was melting. The solid metal to be melted was cut into small pieces weighing approximately 6 g in total and placed in the funnel before it was lowered into the furnace. When the metal was molten, the funnel and top of the crucible were raised up and the stop rod was removed. The molten metal was then helped into the crucible by careful prodding with an alumina rod. The funnel was removed and the crucible was lowered back down to a pre-set level and held for at least two minutes to ensure thermal equilibrium.

The solidification velocity was selected and entered into a computer programme linked to the speed controller. This dictated the speed at which the stepper motor at the base of the furnace turned a threaded rod (of known thread pitch). The threaded rod was located in a fixed nut attached to the withdrawal rod. The rotation of the rod pulled the equipment frame and crucible down through the furnace forcing the solidification front to travel at a velocity dictated by the withdrawal speed. When the temperature read by the thermocouple reached 700°C the data logger was activated and temperature and time data were plotted in real time and recorded on disc until the temperature reached 600°C. These data were stored on floppy disc for subsequent analysis.

Each alloy was grown over a range of velocities in separate experiments. The velocities chosen were 3, 4, 5, 6, 7, 8, 10, 12, 13, 15, 17 and 20 mm min^{-1}. This range of velocities was below the steady state growth limit and straddled the Al_3Fe/Al_6Fe transition velocity of 6mm min^{-1} which was reported in similar experiments using similar temperature gradients [35,49].

5.3.4 Determination of Growth Temperature from Bridgman Data

The thermocouples used in these experiments were not independently calibrated due to their fragile nature. The tip diameter was approximately 0.25 mm in the swaged condition but the manufacturers would only guarantee their accuracy in the unswaged condition. Because a different thermocouple was used for each alloy any error introduced due to the lack of calibration would have been systematic for a particular alloy. It would not have introduced the scatter seen in the data , but only an offset from the true values.

The plots shown in figure 5.04 (a) and (b) are typical of the temperature time profiles logged in these experiments. The inflections marking when the solidification front passed

the thermocouple can be seen. They are, however, not as 'sharp' as was hoped, making growth temperature determination difficult. These problems will be discussed in the results section of this chapter. When there was more than one inflection, as seen in figure 4.05 (b), the lower one was taken to be the eutectic growth temperature for reasons which will also be explained in the next section.

Because the inflection point was not as clear as was originally hoped an attempt was made to locate it more reliably using a computer spreadsheet. The basis of the approach was to plot dT/dt against T. However, even though data was filtered at source by the data logger to take out any noise from other equipment, it was still found to be too noisy and not continuous enough to accurately pick out a solid/liquid transition temperature using this method. The sample rate of the data logger was limited to 5 samples per second which tended to give a stepped, non-smooth plot. A smoothing function built into the spreadsheet (Microsoft Excel) did filter out most of the noise but also smoothed out the inflection. Experimenting with the interval over which the data was differentiated and with other smoothing techniques were unsuccessful in determining the growth temperature. The only viable technique was to pick out the inflection by eye by enlarging the area of interest and using a tangent to the curve to pick out the kink.

5.3.5   XRD and Metallography of Bridgman samples.

Eutectic intermetallic phases were identified by cutting a 10 mm long section, 70 to 80 mm from the base of the samples grown at 3, 10, and 20 mm min^{-1}, and processing it in the same manner as that for DC simulator samples described in chapter 2, section 2.2.2. By identifying the intermetallic phases present in these samples it would be possible to determine whether there had been a phase change and, if so, in which range of velocities it had occurred (3 to 10 mm min^{-1} or 10 to 20 mm min^{-1}).

A section, cut from just above where the SIBUT sample was taken, was removed for metallographic examination. Longitudinal and transverse sections were made from this sample and mounted in Bakelite. These were ground on 200 to 600 grit emery paper before being polished using 15 then 6 μm diamond paste on rotating polishing wheels. The metallographic contrast was obtained by a final polish on colloidal silica which eliminated any remaining scratches and provided a mild etch. Optical microscopy of both longitudinal and transverse sections was performed on a Reichert-Jung MeF3 microscope.

5.4   Bridgman Experiment Results.

5.4.1   Limitations of the Bridgman Growth Experiments.

Problems were encountered in obtaining good temperature measurements using the technique described above. These problems will be described before the results are presented so that the scatter in some of the data is understood.

There is a large scatter in the data obtained for the growth temperatures at varying cooling rates. This is due partly to the inaccuracy of the temperature measurement data and partly to the uncertainty in the determination of the growth temperature from this data. At slow growth rates, the inflection in the plot of T vs t was difficult to pick out. The reason is seen in figure 5.04 (a) and (b) where two T vs t plots are shown from alloys grown at high and low growth rates. The data from the slowly grown sample has a non-sharp transition whereas the inflection from the faster growth is more sharp. It will be shown that, although a eutectic composition was used, the alloy grew in a manner more usually seen in hypoeutectic alloys *i.e.*, with primary aluminium dendrites growing ahead of the eutectic interface. With a mushy zone present in the sample it is difficult to determine a single eutectic growth temperature. The reason for the presence of a mushy zone in an alloy of nominally eutectic composition can be understood by considering the shape of the coupled zone in this alloy system

The coupled zone in a eutectic alloy is the range of compositions over which a fully eutectic microstructure can be achieved at given growth temperature. If the coupled zone is superimposed on to a phase diagram, the type of microstructure expected for a particular growth temperature and composition may be determined. Figure 5.05(a) shows, schematically, a typical coupled zone for a normal eutectic alloy solidifying into a positive temperature gradient. The coupled zone itself is a representation of the competitive growth theory where the two competing components are primary dendritic α and the α–β eutectic (or primary dendritic β and the eutectic, depending on which side of the eutectic composition the system lies). The shape of the coupled zone shows that at very low and high undercoolings of the interface below the eutectic temperature, there is a range of compositions over which a fully eutectic microstructure can be expected. This is because, at these combinations of growth temperature and composition, the eutectic can be expected to grow faster than either primary phase.

At high velocities a fully eutectic microstructure can grow at compositions other than the eutectic composition because, as well as the periodic compositional variation which exists along the eutectic interface, there also exists a planar front solute pile-up ahead of the interface. Thus, the eutectic composition exists, locally, at the interface, while the bulk composition in the liquid is still hypoeutectic. That a fully eutectic microstructure is not observed at all compositions and growth temperatures below the eutectic temperature is due to competitive growth between the two primary phases α and β and the α β eutectic. For the planar eutectic interface to become unstable, leading to the growth of α or β dendrites ahead of the interface, it is necessary for either the α-L or β-L interface to be perturbed such that the growth rate of the perturbation is faster than the growth rate of the eutectic (in bridgman growth the perturbation grows at a higher temperature than the eutectic front. For a eutectic growth front growing into a positive temperature gradient at low growth velocities, the solutal gradient associated with the planar front is low and no zone of constitutional supercooling exists ahead of the interface; the α-L and β-L interfaces are stable with respect to perturbations of any wavelength. As the velocity increases, so will the solutal gradient and the liquid ahead of the interface can be constitutionally supercooled leading to the formation of dendrites of α- or β- phase depending on the composition of the liquid. The further the bulk composition is from the eutectic and the higher the growth velocity, the steeper will be the solutal gradient at the interface and the more prone will the interface be to instability. This accounts for the characteristic 'anvil' shape of the upper part of the coupled zone. As the growth velocity increases, the microstructural scale of the eutectic decreases *i.e.* the interlammelar or inter-rod spacing is reduced. As a consequence of this, a point will be reached when the perturbation wavelength of the α-L or β-L interfaces which can grow at a velocity (temperature) greater than that of the eutectic interface becomes larger than the spacing of the phases themselves and planar front eutectic growth is again favoured over primary growth of either α or β.

In contrast to the case for a normal eutectic, the coupled zone in the Al-Al$_3$Fe system is skewed [35]. This effect is shown in figure 5.05(b). The asymmetrical shape of the Al-Al$_3$Fe coupled zone is due to the faceted nature of the Al$_3$Fe phase. Faceted phases have a growth disadvantage over non-faceted phases due to the relative difficulty in atomic attachment. This inhibits the growth of primary Al$_3$Fe and gives primary Al dendrites a growth advantage over the eutectic, allowing them to grow faster even at hypereutectic concentrations. The consequence of this is that it is possible, depending on growth velocity,

for a dendritic microstructure with interdendritic eutectic to form at and above the eutectic composition.

In the Bridgman experiments, the growth interface was non-planar as a result, with primary aluminium dendrites growing ahead of the Al-Al$_3$Fe eutectic. The thermocouple in the Bridgman samples at low solidification velocity would first have sensed the dendrite tip growth temperature and then the temperature of the eutectic growing behind. This can be seen on the plot of T vs. t for the slow growth velocity, see figure 5.04(b), where there appear to be two inflections. On plots such as these, the growth temperature of the eutectic was taken to be the lower inflection. Identifying this lower inflection by eye was difficult and error was introduced as a result.

At higher growth velocities only one inflection was picked up as the growth front passed the thermocouple. This could mean one of two things. Firstly, that the growth was fully eutectic, meaning that the growth temperature was within the fully eutectic range of the coupled zone. This is unlikely as the Al-Al$_3$Fe coupled zone skews away from the eutectic composition making it impossible for alloys of this composition to grow in a fully eutectic manner. Secondly, and more likely, the single inflection is a reflection of the greater velocity at which the interface passes the sensor. The interface took less time to pass the thermocouple but the sampling rate of the datalogger was the same as for low velocities, resulting in lower resolution of small temperature changes. It will be shown that this was the case because microstructural examination showed that primary dendrites existed in samples grown at all growth rates. It was found, however, that the main intermetallic growing at higher growth rates was Al$_x$Fe. Nothing is known about the nature of the coupled zone for the Al$_x$Fe except that it is probably symmetrical due to the regularity of its morphology and that it probably lies between the coupled zones for Al-Al$_3$Fe and Al-Al$_6$Fe which are shown schematically in figure 5.06 [35].

5.4.2 Reappearance of Equilibrium Al$_3$Fe at High Growth Velocities

Previous users of the Bridgman growth apparatus used for this set of experiments had been able to maintain steady state growth up to velocities of 20-25 mm min^{-1} using similar crucibles to the ones used in this study. The photographs of the microstructures of the samples grown at high growth rates indicate that this may not be the case in these experiments. Figure 5.07 shows transverse and longitudinal sections of high growth rate samples. This was typical of the morphology of all samples grown at the higher speed. There

is clear evidence that there has been some lateral growth in these samples. Dendrites of primary aluminium appear to have grown in sideways and at an angle from the crucible wall. The lateral growth probably results from the growth interface at the centre of the sample lagging behind that at the edge. In effect, a sump has formed which is too deep for the constant growth velocity across the sample to be maintained. As the sample passed through the sharp temperature gradient between the hot and cold part of the furnace, the solid/liquid interface at the very edge of the sample grew at approximately the same speed as the withdrawal rate. However adjacent to this part of the sample, where the sump has the steepest gradient, the growth direction was not parallel to the withdrawal direction. This allowed lateral growth in from the sides of the sample in a similar way to that occurring in DC casting (see figure 5.01). At the centre of the sample the local growth rate is the same as the withdrawal rate as the growth direction and withdrawal direction are parallel.

This is effect is illustrated in figure 5.08, which shows how local solidification rate in a Bridgman sample may have varied at three different growth rates. In the sample grown at low growth rate, the slight variation in local solidification rate was not significant. The growth rate did not exceed that needed for Al_xFe to outgrow Al_3Fe (U^C_x). At the medium growth rate there is more variation across the sample width but the local growth rate does not fall below U^C_x so that only Al_xFe is seen in the sample. However, at high growth rates the sump is at its deepest and its sides are at their steepest. The lateral growth from the sides is so slow that does not exceed U^C_x. The result, in term of the intermetallic phases, is a mixture of phases with Al_xFe concentrated at the edge and the centre and Al_3Fe concentrated between. More Al_3Fe would be expected with increasing growth velocities (above that needed for the mixture of phases to grow) at the expense of Al_xFe.

The quoted growth velocity (at higher values of U) cannot therefore be assumed to be the same across the thickness of the sample. The values of growth temperature measured in these samples are not then as accurate as those measured at lower growth rates for two reasons, the first being the problem of resolution outlined in the previous section and the second being related to the local solidification velocity variations described above and thermocouple position. The measured growth temperature would depend on the positioning of the thermocouple. If the thermocouple tip was not situated at the centre of the sample it would have been possible for it to measure any of a range of growth temperatures. This view is enhanced by the results of the SIBUT extraction and XRD analysis. The high velocity samples grown at 20 mm min^{-1} (except in samples with the TI addition) all have

Al_3Fe as the major intermetallic. The intermetallics extracted from the base alloy grown at 17 mm min^{-1} were identified as being Al_xFe indicating that steady state growth was maintained up to this level. Growth temperatures measured at the higher growth rate must therefore be viewed with scepticism.

5.4.3 Results

The dependence of growth temperature on the square root of growth velocity for the alloys studied are shown in figure 5.09. The square root of the growth velocity was used as the Jackson-Hunt relationship for regular eutectics relates the square root of the velocity U linearly with the growth temperature T_g [63]: $\sqrt{U}$ - T_g C. The results of the XRD analysis of SIBUT extracted intermetallics are shown in table 5.02 with the majority phases shown first and any minority phases shown in parentheses. As with the DC simulator samples, the XRD technique was able to identify mixtures of phases as long as the volume fraction of any phase in a sample was above $\approx$10%. Optical micrographs of the Bridgman grown samples are shown in figures 5.10.

5.4.3.1 Growth Temperature Measurements

The error bars on the data points in figure 5.09 are representative of the resolution of the thermocouple. The radius of the thermocouple with sheath was 0.15 mm. The temperature gradient at the interface was 5 °C mm^{-1} giving resolution of 0.75 °C.

	Imposed solidification velocity / mm min^{-1}			
Alloy	**3**	**10**	**17**	**20**
Eut	Al_3Fe	Al_xFe	Al_xFe	Al_3Fe
Eut + Mg	Al_3Fe	Al_xFe (Al_3Fe)	-	Al_3Fe (Al_xFe)
Eut + Ti	Al_3Fe	Al_xFe	-	Al_xFe
Eut + Ti-B	Al_3Fe	Al_xFe	-	Al_3Fe

Table 5.02 Eutectic intermetallic phases found in Al - 1.8 wt.% Fe (with trace additions) grown in a Bridgman furnace at different velocities. When a mixture of phases was identified, the minority phase is shown in parentheses.

5.4.3.2 Base Alloy

The base alloy was superpurity-based Al -1.8 wt. % Fe. The variation in growth temperature with imposed velocity is shown in figure 5.09(a). Table 5.02 shows the identity

of the phases extracted from samples grown at 3, 10, 17, and 20 mm min^{-1}. Photographs of the microstructure of samples grown at 3 and 10 mm min^{-1} are shown in figure 5.10.

The plot shown in figure 5.09(a) shows a large scatter in the data caused by the measurement error explained above. The results from the particle extraction show that Al$_3$Fe is the major intermetallic found at 3 mm min^{-1} whereas Al$_x$Fe is found at both 10 and 17 mm min^{-1}. The transition from the Al-Al$_3$Fe to the Al-Al$_x$Fe eutectic has occurred at some velocity between 3 and 10 mm min^{-1} ($\sqrt{U}$ of 0.22 to 0.44 (mm s^{-1})$^{1/2}$ on the graph). Previous work [35,49] suggests that the transition velocity for the Al$_3$Fe to Al$_6$Fe transition occurs at 6 mm min^{-1} and that this value is largely independent of the of Fe content in binary Al-Fe alloys. The value of U for the transition between Al$_3$Fe and Al$_x$Fe has not been reported. It was expected that the shape of the T$_g$ vs. $\sqrt{U}$ plot would give an indication of the transition velocity as it has in previous work (see figure 1.09) where the change in gradient clearly shows the transition from Al$_3$Fe to Al$_6$Fe. However, the scatter in the data in this work makes this determination difficult. The data do not appear to lie on a single straight line which indicates that, were the growth temperature determination more accurate, a change in gradient may have been visible. Lines have been drawn in as a suggestion of the possible linear variation of the two phases. These lines are not mathematically fitted and are intended only as a guide. They cross at a value of $\approx$ 0.37 (mm s^{-1})$^{1/2}$ or just over 8 mm min^{-1} which corresponds with the observation from SIBUT results that the transition occurs between 3 and 10 mm min^{-1}.

The systematic error in the thermocouple measurement resulting from the fact that they could not be calibrated (due to their frailty) would not introduce scatter but would introduce a single systematic error for each alloy, the error being different for each alloy. It would not affect the gradient of the linear relationship but only its intersection with the temperature axis. The results cannot therefore be used as they are to estimate the equilibrium melting temperature of the Al$_x$Fe eutectic. Displacing the values of T$_g$ down by about 2 °C would bring the proposed Al$_3$Fe eutectic data points down so the intercept of the straight line drawn through these points with the growth temperature axis gives the equilibrium temperature of 655°C (which is the accepted value). A similar displacement of 2 °C to the higher growth rate data would give an estimated value for equilibrium temperature of the Al$_x$Fe eutectic of about 650°C. It must be emphasised that this value is at best a rather crude estimate.

5.4.3.3 Microstructure of the Base Alloy Samples.

Figures 5.10 (a) and (b) show the optical micrographs of the base alloy grown at 3 and 10mm min^{-1} (termed E03 and E10 respectively). Micrographs of sections parallel to the growth direction are termed longitudinal and those of sections normal to the growth direction are termed transverse. Both longitudinal and transverse sections were required to provide a full picture of the individual particle morphology.

Sample E03, see figure 5.10(a), contains coarse particles of Al$_3$Fe in the interdendritic eutectic between the primary Al dendrites. The dendrites of primary Al are fine and regularly spaced with very short secondary arms. The intermetallic particles are discrete, faceted plates elongated in the growth direction. There is no evidence of any other type of intermetallic morphology in this sample.

In sample E10 XRD indicated that Al$_x$Fe was the major intermetallic phase present. This is reflected by the markedly different microstructure observed in this sample when compared to E03(figure 5.10(b)). The primary aluminium dendrites are somewhat larger and their spacing is greater. There are larger areas of interdendritic eutectic which has a very different appearance to that seen in sample E03. The eutectic is very fine and whilst individual particles of intermetallic are difficult to resolve, they appear to be mostly lamellar. A second morphology is evident which looks similar to Al$_3$Fe but on a finer scale, situated in small clumps amongst the Al$_x$Fe and sometimes in larger islands (fig 5.09b, i and ii). The XRD identification technique will only detect mixtures of phases as long as the component phases make up more than 5 to 10 % of the total mixture so it is probable that the supposed Al$_3$Fe seen here was not detected by XRD.

An alternative explanation for the mixed morphology is displayed by the micrographs in figure 5.11. These high magnification SEM images of extracted Al$_x$Fe show the fine morphology of the phase grown in a Bridgman sample. It is possible that the coarser intermetallic seen in the optical micrographs, which was taken to be Al$_3$Fe, could be areas of very closely spaced fibrous Al$_x$Fe. Figure 5.11(a) shows that the closely spaced fibres in some of the intermetallic colonies are only just resolvable. The optical micrographs would not have resolved such detail as the spacing is less than 1μm. Figure 5.11(b), at an even higher magnification shows the morphology in more detail. This could explain why there appear to be some isolated coarse particles in amongst the finer ones. The larger 'islands' in the sample where the eutectic appears to have wider spacing (see figure 5.01(b) iii) are probably Al$_x$Fe which, having grown at an angle, has an apparently wider spacing when

sectioned perpendicular to the growth direction. Other areas, however, must be assumed to consist almost entirely of Al_3Fe, particularly in view of their similarity to the structures observed in E03 (see figure 5.10(b) iv).

The difference in phase morphology between sample E03 and sample E10 is marked and is more confirmation that the transition occurs between these two growth rates. The fact that there is apparently some Al_3Fe present in the E10 sample (which was not picked up by XRD along with the Al_xFe) means that the transition probably occurs over a range of solidification velocities. This would contribute to the degree of difficulty encountered with the determination of the transition velocity in the plots of T_g vs. $\sqrt{U}$.

Sample E20 had a mixture of fine and coarse eutectic morphologies (see figure 5.09(c)) most of which consisted of the Al-Al_3Fe eutectic according to the XRD analysis. The eutectic was made up mainly of the coarse Al_3Fe with some areas nearer the centre of the rod of a finer eutectic similar in appearance to the Al_xFe in E10. The occurrence of the equilibrium eutectic in this sample is attributed to the problem of lateral growth discussed earlier in this chapter.

5.4.3.4 Base Alloy with Mg Addition (EMg)

The plot of T_g vs. $\sqrt{U}$ for the EMg alloy is shown in Figure 5.09(b). There is no obvious kink in the data which would indicate a phase transition. However, can be seen from XRD analysis of SIBUT-extracted intermetallics (table 5.02) that a phase transition did occur between 3 and 10 mm min^{-1}, although the extractate from the EMg10 sample contained both Al_xFe and Al_3Fe, the latter present at a lower level. Since Al_3Fe was detected by XRD in the EMg10 sample, but not in the E10 sample, it may be inferred that the transition to Al_xFe occurred at a higher growth rate in sample EMg than in the base alloy. In the base alloy grown at 10 mm min^{-1} (E10) the only evidence of Al_3Fe was that seen in the microstructure and not in the XRD trace. This effect is illustrated in figure 5.12. The increased critical velocity for the transition from Al_3Fe to Al_xFe ($U^c_{x\ (Mg)}$)brought about by the addition of Mg is shown. The phases resulting at the three different growth rates are shown below. The large difference is at medium velocity where a mixture of both Al_3Fe and Al_xFe becomes possible. At the high velocity, the model predicts primarily Al_3Fe and a lesser amount of Al_xFe (which, if low enough, may not have been detected by XRD)

It is probable that the addition of Mg has extended the range of growth rates over which Al_3Fe can grow. If it is the case that the addition has promoted the growth of Al_3Fe by whatever means, any change in gradient on the T_g vs $\sqrt{U}$ plot would be seen at a higher velocity. Because of the scatter in the data, several data points are needed before a trend can be established. As the Al_3Fe to Al_xFe transition did not take place until higher growth rates, it was not possible to obtain enough growth temperature measurements from the Al_xFe eutectic to establish a trend.

5.4.3.5 Microstructure of the EMg Samples

Figures 5.10(d) and 5.10(e) show the micrographs of the base alloy with the Mg addition grown at 3 and 10 mm min^{-1} respectively. The samples grown at the low velocity contained fine directional dendrites of α-Al with interdendritic Al_3Fe eutectic. The dendrites are finer than those seen in the base alloy grown at the same rate and there appears to be less branching. This is probably due to the partitioning of the Mg to the liquid resulting in a reduced dendrite tip radius. The addition of Mg has altered the appearance of the microstructure, when compared to E03, although the shape of the intermetallic particles is similar.

The optical micrographs of the EMg10 sample (figure 5.10(e)) again show a finer dendritic morphology than E10. The eutectic is mixed with the fine Al_xFe making up the larger part but coexisting with a coarser Al_3Fe. The Al_xFe eutectic is lamellar and appears to be slightly coarser in scale than that seen in the E10 sample. There are many coarse Al_3Fe particles, mainly at the interface between the dendrites and the interdendritic spaces. The Al_3Fe was not found in discreet islands as in sample E10 but close to, and mixed with, the Al_xFe. Again, the addition of Mg has had a small but noticeable effect on the microstructure of the sample.

EMg20 showed the non-unidirectional growth pattern characteristic of non-steady state growth similar to that observed in the base alloy grown at the same rate (E20). There were regions present of both coarse and fine eutectic, the coarser Al_3Fe eutectic being dominant.

5.4.3.6 Base alloy with the Ti addition (ETi).

The results of XRD analysis of intermetallic phases present in SIBUT extractate from the EMg samples are shown in Table 5.02 are and similar to those of the base alloy in

that the transition to the Al_xFe eutectic has occurred between 3 and 10 mm min^{-1}. The plot of T_g vs. $\sqrt{U}$ for alloy ETi is shown in figure 5.09(c). Again, lines have been drawn on the plot to suggest the variation in growth temperature with $\sqrt{U}$ and indicate the proposed transition from the $Al-Al_3Fe$ to $Al-Al_xFe$ eutectic. The gradient of the line going through the first four points is close found at low growth velocities in the base alloys. The last three data points have a large scatter probably because of the problems related to lateral growth outlined at the beginning of the chapter. Nevertheless, the addition of Ti appears to have increased the growth temperature of the Al_xFe eutectic. This has had the effect of decreasing the critical velocity for the transition from $Al-Al_3Fe$ to $Al-Al_xFe$ and extending the range of velocities over which Al_xFe can form to lower values.

The phase extracted from the ETi20 sample was Al_xFe. This was the only occurrence of this phase on its own in a sample solidified at 20 mm min^{-1}. All three other extracted samples grown at this rate contained mainly Al_3Fe. This can be explained using the illustration in figure 5.12 which shows the resulting intermetallic phases which would be expected if Ti were to lower the critical value of growth velocity for the transition from Al_3Fe to Al_xFe ($U^c_{x(Ti)}$). The model shows that when the growth front deviates markedly from the planar front, at high velocities, more Al_xFe would be expected to grow in the alloy with Ti addition than in the base alloy. This corresponds with the results of the SIBUT analysis.

5.4.3.7 Microstructure of the ETi Samples

Figure 5.10(f) and 5.10(g) show the optical micrographs of the base alloy with Ti addition grown at 3 and 10 mm min^{-1} respectively (termed ETi03 and ETi10). The microstructure of sample ETi03 is similar to the samples of other alloys grown at low velocity with primary aluminium dendrites surrounding the $Al-Al_3Fe$ interdendritic eutectic. The microstructure is closer in appearance to sample E03 than sample EMg03 in that the transverse section shows similar amount of secondary dendrite arms. Sample EMg03 had no evidence of this (compare figures 5.10(a) ii, 5.10(d) ii and 5.10(f) ii). Microstructures of sample ETi10 are shown in figures 5.10(g). The scale of the microstructure appears to be finer than is the case in E10 and the interdendritic eutectic is different. Although some large particles of coarser phase are present, the main part is made up of the $Al-Al_xFe$ eutectic. Figure 5.10(j) shows, in higher magnification, that the $Al-Al_xFe$ eutectic is made

up of regularly spaced lamellae of Al_xFe between thicker layers of Al. The lamellae are longest in the growth direction.

The microstructure of the sample ETi20 showed evidence of lateral growth. There was a mixture of eutectic intermetallics present, with the finer lamellar (Al_xFe) morphology being dominant.

5.4.3.8 Base Alloy with Ti-B Grain Refiner Addition (ETiB).

The majority of the Ti and B present in a commercial grain refiner form the insoluble compound TiB_2 which acts as a nucleant for the primary aluminium dendrites. Grain refiners are added to rid a cast structure of directional dendrites in areas of fast cooling and to produce a homogenous structure. They are intended to modify the nucleation process but the nature of the growth is affected as a result. Free dendrites tend to form in the liquid which are not constrained to grow in a single direction. Figure 5.13 (a) shows schematically the way in which growth occurs in a grain refined Bridgman sample in comparison to a non-grain refined sample (figure 5.13(b)). At a certain undercooling in the liquid, primary aluminium will nucleate heterogeneously on TiB_2 and grow in the form of equiaxed dendrites over a range of temperatures. As the solidification proceeds, in between dendrite arms the liquid becomes enriched in solute until eventually it solidifies as a eutectic when the eutectic composition is reached. As a result the eutectic grows as a continuous matrix whose growth rate is dictated by the withdrawal rate of the sample. So, even though the growth rate of the dendrites is not necessarily the same as the sample withdrawal rate, that of the eutectic is.

The plot of T_g vs $\sqrt{U}$ for the sample ETiB is shown in figure 5.09(d). Guidelines have been drawn on the plot to show a possible trend. The gradient change corresponding to the phase transition, which according to XRD results (see Table 5.02) occurred between 3 and 10 mm min^{-1}, appears to occur at about 8 mm min^{-1}. *i.e.* at a very similar value to that suggested for the base alloy. The phases extracted at from the samples grown at 3, 10 and 20 mm min^{-1} are the same in both the base alloy and ETiB. This strongly suggests that the addition of Ti-B refiner does not affect the growth characteristics of the eutectic at all. This is quite conceivable, considering that TiB_2 is insoluble in the liquid and acts as a physical site for nucleation of the primary aluminium and implies that the effect of the different dendrite morphology is small. It can be concluded that the additions of Ti-B refiner do not affect intermetallic phase selection by altering transition velocities. The effect seen in the DC Simulator, where Ti-B had a large effect on phase selection, must, therefore, be related to

the cooling rate and hence nucleation of the intermetallic phases, and not the growth rates of the competing phases.

5.4.3.9 Morphology of ETiB

Figure 5.10(h) shows optical micrographs of ETiB03. The difference in dendritic morphology between this sample and others grown at the same rate is clear. The dendrites are not directional and columnar but are equiaxed and randomly positioned. The eutectic Al_3Fe forms a continuous matrix surrounding the primary aluminium dendrites. The transverse and longitudinal sections (5.10(h) iii and iv) show that the eutectic grew in a directional manner with the intermetallic particles elongated in the growth direction. The degree of orientation is not as high, however, as in samples showing columnar growth because the growth front was disturbed by the floating dendrites in the mush. However the fact that the intermetallic particles are oriented predominantly in the growth direction means that the eutectic grew with a planar front similar to the schematic representation in figure 5.13(a).

The major crystallised phase found in sample ETiB10 extraction was Al_xFe. Micrographs of sample ETiB10 are shown in figure 5.10(i) .The dendritic microstructure is the similar to that observed in sample ETiB03 but on a finer scale. The interdendritic eutectic is again mixed and consists of a few small regions of coarse Al-Al_3Fe eutectic but mostly very fine lamellar Al-Al_xFe eutectic similar to those seen in sample E10. Once again there is a degree of orientation to the growth direction which is disrupted locally by the equiaxed dendrites.

The eutectic in sample ETiB20 consists mainly of coarse Al-Al_3Fe although there was some intermetallic present with a different, rod like morphology, however. The rod like morphology of the eutectic seen in figure 5.10(j) is not seen elsewhere in these experiments. It strongly suggests that Al-Al_6Fe eutectic was present in this sample. None of this phase was detected in XRD analysis of the SIBUT sample but this could be because it was present in too small an amount to be detected, or because that it is not, in fact, Al_6Fe.

5.5.   Discussion of Bridgman Experiments.

The results of the Bridgman experiments on Al-Fe alloy with eutectic composition conclude that at above a growth velocity of approximately 8 mm min^{-1} the Al-Al_3Fe eutectic is replaced by the Al-Al_xFe eutectic and that this eutectic is found at growth velocities up

to 17 mm min^{-1}. Above this growth velocity the equipment could not maintain a planar growth front and problems were encountered with non-planar growth. The addition of Mg to the base alloy extended the range of solidification velocities over which the Al-Al$_3$Fe eutectic could grow. This result was also seen in the DC simulator experiments where the addition of Mg to both binary Al-Fe and ternary Al-Fe-Si was found to favour the formation of Al$_3$Fe. The DSC experiments showed that the addition of Mg promoted the nucleation of Al$_3$Fe at higher cooling rates than in the base alloys. The result seen in the DC simulator experiments can therefore be viewed as a combined effect of Mg on the nucleation and growth of the eutectic. The addition of Ti to the base alloy in the Bridgman experiments had the effect of lowering the transition velocity. This was not an effect that was seen when Ti was added to the alloys cast in the DC simulator experiments. However, the DSC results showed that its effect on the critical cooling rate was the same as that for Mg. This will be discussed in chapter 6. The effect of the addition of Ti-B to the alloys cast in the Bridgman furnace was small. No change was seen in the transition velocity from that of the base alloy and the phases detected by XRD were the same as those seen in the base alloy. There was some morphological evidence that the Al-Al$_6$Fe eutectic had grown in the samples grown at intermediate and high growth velocity although by no means conclusive.

5.5.1 Model for phase selection based on Growth Rate.

The competitive growth model for competing phases can be used to explain why phase transitions occur at certain growth velocities in the Bridgman growth experiments on the base alloys. at low growth velocities, the equilibrium eutectic Al-Al$_3$Fe can be expected to grow. The undercooling at the growth interface at low growth velocities is above the eutectic temperature of the metastable phases. Once the growth temperature is below the eutectic temperature of the metastable phases it is thermodynamically possible for them to grow. However, they will only be able to grow once their growth velocity can exceed that of the equilibrium eutectic. This can occur because at higher imposed growth velocities they have a growth advantage over the equilibrium eutectic which cannot adjust its spacing as easily due to its rigid and faceted growth mode. The non-faceted eutectics can adjust their spacing more easily and are able to grow at a higher growth velocity for a given temperature. This is represented schematically in figure 5.14   which shows the growth regimes of three competing eutectics. This model will be used to help explain some of the effects seen in the Bridgman experiments.

5.5.2 Base Alloy

Previous Bridgman directional solidification experiments have been carried out by Liang and Jones [49] on a high purity Al-3 wt.% Fe alloy and by Adam and Hogan [35.] on high purity based alloys ranging from Al-2 to 4 wt.% Fe. It was found that for the 3 wt.% Fe alloy the transition from the Al_3Fe eutectic to the Al_6Fe eutectic occurred at 6.6 mm min^{-1} $(110 \mu m\ s^{-1})$. The results for the 2 wt.% alloy were similar. The values of critical velocity for the transition from the $Al-Al_3Fe$ to the $Al-Al_xFe$ eutectic for the four alloys tested in this study are shown in table 5.03. The critical velocities for the change over is approximately 8 mm min^{-1} (133 $\mu m\ s^{-1}$) for the base alloy. This value is an estimate only but is similar to the value obtained by Liang and Jones who identified the Al_6Fe eutectic by its regular lamellar appearance. The phase found at the higher growth velocities in this study was identified as Al_xFe by XRD and had a lamellar structure. It is possible that the phase that Liang and Jones identified as Al_6Fe was in fact Al_xFe. The more positive identification has been made possible by the use of the SIBUT apparatus and XRD. The Al_6Fe found by Adam and Jones was identified using TEM diffraction patterns. Its morphology was stated to be faceted parallel fibres or rods in a continuous aluminium matrix, which is the more typically reported morphology of the $Al-Al_6Fe$ eutectic [ref.].

Alloy	Base	EMg	ETi	ETiB
U^c_x / mm min^{-1}	8	9+	5.5	8

Table 5.03 Approximate critical growth velocities for the $Al-Al_3Fe$ to $Al-Al_xFe$.

The difference between the alloy used in this study and work cited above is the composition. The alloy used in this study is of eutectic composition (but grew in a hypoeutectic fashion due to the skewed nature of the coupled zone) whereas those alloys used in previous work were hypereutectic. Adam stated that the equilibrium eutectic $Al-Al_3Fe$ structure was confined to compositions below 2 wt.% Fe. Higher levels of Fe resulted in primary Al_3Fe prisms forming. Above 2 wt.% Fe, therefore, Al_3Fe grows ahead of the eutectic growth front. The presence of the $Al-Al_xFe$ eutectic in hypoeutectic alloys at higher growth rates was also detected by Young and Clyne [8] in Bridgman growth experiments at growth rates ranging from 6 to 120 mm min^{-1}. They found that at intermediate growth rates corresponding to cooling rates of 0.5 to 5 °C^{-1} (actual growth rates are not stated) a new phase was found in the eutectic mixture. Its morphology was similar to that of the Al_xFe identified in this study. However the XRD Bragg reflection angles and intensities do not

correspond to those found in this work. There is not, it seems, a consensus as to the exact composition and crystal structure of the Al_xFe intermetallic, but only that a phase which is not Al_6Fe is sometimes found at elevated growth rates and cooling rates in Al-Fe alloys. The conclusion from Young and Clyne is that the transition from the Al_3Fe to Al_6Fe eutectic occurs via an intermediate phase denoted Al_xFe. It is possible that at lower levels of Fe (approx ≤ 1.8 wt.% Fe; the eutectic composition) Al_xFe forms in preference to Al_6Fe. The reason is unclear but could possibly be related to the position of the $Al-Al_xFe$ eutectic coupled zone on the Al-Fe phase diagram. If it was situated between those for $Al-Al_3Fe$ and $Al-Al_6Fe$, then it may be possible that only a small range of compositions and growth velocities exist which will result in its growth.

It has been stated that the Bridgman directional growth apparatus isolates the effect of solidification velocity from any nucleation effects. This is true of a continuous phase. However the morphology of the eutectic intermetallic phase, in particular the Al_3Fe, appears to be discontinuous and probably requires repeated nucleation whereas the Al_xFe eutectic appears to be more continuous. In the hypoeutectic alloy the repeated nucleation may have been hindered due to the 'pinching off' eutectic colonies by secondary dendrite arms. In the nominally hypereutectic case, growing with a planar eutectic front this would not have occurred. It is possible that the difference in the eutectic observed in at elevated growth temperatures in this study and the work sited above could be due to this effect especially if Al_xFe has a nucleation and growth advantage over Al_6Fe when there is a mushy zone present.

5.5.3 Effect of Trace additions.

It was concluded from the results that the effect of Mg was to enable Al_3Fe to form at higher growth velocities whereas the effect of Ti was to allow the $Al-Al_xFe$ eutectic to grow at lower velocities. The addition of Ti-B refiner had little effect on the eutectic phases or the transition growth rate. The estimated transition velocities for the alloys with trace additions are shown in table 5.03. The effects of each element can be seen on a schematic plot of T_g vs $\sqrt{U}$, shown in figure 5.15.. It has been known for some time that minor addition of some elements at low levels can affect the phase selection in DC cast and simulated DC cast Al-Fe and Al-Fe-Si alloys [4,14,13]. The model describes the way in which the addition of a trace element would raise or lower the transition velocity by changing the growth temperatures of one of the intermetallic species. The purpose of conducting the Bridgman

growth experiments in which the growth rate was isolated from the cooling rate and also adding individual trace elements was to examine whether the addition affected the growth temperature of the solidifying intermetallics. Their effect on growth temperature will now be discussed.

The actual mechanism by which trace elements affect the growth behaviour of intermetallic phases has not been investigated, but it is know that they can have a dramatic effect on the microstructure. The most common use of a trace element in this respect is that of sodium in the modification of Al-Si eutectic alloys. This was discussed in the last chapter where it was pointed out that debate still occurs as to the way in which sodium acts to modify the silicon phase. The purpose of these experiments was not to discover the mechanism by which trace elements affect phase selection but simply to gauge their effects, if any.

The addition of Mg has increased the maximum growth rate at which Al_3Fe is observed. This is evident both from the phase identification data and from the growth temperature measurements. Figure 5.12, (which shows change in the critical growth velocity on the addition of Mg ($U^c_{x(Mg)}$) in Bridgman samples) when viewed alongside phase identification results confirms that this is probably achieved by raising the critical velocity for the transition. The schematic in figure 5.15(a) shows schematically how this effect could be brought about by raising the growth temperature of the equilibrium phase at any given growth rate. A similar effect was seen in the DSC experiments where the Mg addition extended the range of cooling rates over which Al_3Fe could form. Larger undercoolings (or faster growth rates) are needed before the metastable phase Al_xFe is able to grow faster than the Al_3Fe. It can be concluded that Mg affects Al-Fe eutectic phase selection by promoting the growth (and nucleation) of the equilibrium phase Al_3Fe. The manner in which this is achieved is not known.

One suggestion is that the effect is a thermodynamic one. It is known that the Mg partitions to the liquid on solidification because of its limited solubility in primary aluminium. The higher level of Mg found in the liquid just before the eutectic solidifies may be enough to significantly alter the eutectic temperature. The value of eutectic temperature would be expected to be lowered because the Al-Al_3Fe eutectic temperature is higher than that for the eutectic formed with Mg. This would lower the growth temperature for any given growth rate. However, the nature and shape of the eutectic part of the metastable phase diagram for Al_xFe is not known. The addition of Mg would be expected to have a similar effect on the

Al-Al$_x$Fe eutectic as the it did on the Al-Al$_3$Fe eutectic, that is, to lower growth temperatures. It would not, however, necessarily alter the growth temperature by the same degree. The situation seen in these experiments could be achieved if the effect of Mg on the Al-Al$_x$Fe eutectic was greater than on the Al-Al$_3$Fe eutectic.

It is also possible that the effect observed is due to the solubility of Mg in the competing intermetallics. If Mg is soluble in Al$_3$Fe and not in Al$_x$Fe it will depress the Al-Al$_x$Fe growth temperature more than the Al-Al$_3$Fe since large solute pile up would occur.

Another suggestion as to how Mg could raise the growth temperature of the stable eutectic concerned with the effect which it may have on the atomic attachment kinetics. Al$_3$Fe is a faceted phase which grows by a stepwise growth mode giving it a growth disadvantage over non-faceted phases. The concentration of Mg in the Al$_3$Fe could enhance the atomic attachment by altering the nature of the growth interface. If Mg made it easier for atoms to attach to the interface the growth temperature would be increased for a given growth rate. This could be brought about if Mg increased the twin density in the Al$_3$Fe, for example. This would reduce the separation of favourable sites for atomic attachment a given growth temperature. Verification of this mechanism would be provided by using TEM analysis of the intermetallic particles with and without Mg present, when an increased twin density should be observed.

By contrast with the effect of Mg, the addition of Ti reduced the growth rate at which the transition from Al-Al$_3$Fe to Al-Al$_x$Fe occurs compared to the base alloy. The range of growth rates over which Al$_3$Fe could grow was reduced and that of Al$_x$Fe extended to lower values. The effect, predicted by the model in figure 5.12 is seen in the results. This is not surprising considering that Ti forms a peritectic with Al such that it partitions to the solid on solidification whereas Mg, which forms a eutectic, partitions to the liquid. Figure 5.15(b) show schematically the result of an addition such as Ti which raises the growth temperature at all growth rates of the metastable Al$_x$Fe. The result is to move the critical growth rate for the transition back to lower values, in line with what is observed experimentally. The way in which Ti does this remains unclear. It is unlikely to be a thermodynamic effect as the Ti partitions to the Al leaving the liquid depleted in Ti. The effect of the extra 0.04 wt.% Ti in the Al is unlikely to have a significant effect on the thermodynamics in the same way that the presence of Mg in liquid could.

The addition of Ti-B grain refiner has had very little effect on the growth temperature of the eutectic. The approximate value of the critical growth rate for the

transition to Al_xFe is very close to that of the base alloy and is well within the range of experimental error. The addition of grain refiner to castings is made to nucleate primary aluminum dendrites in order to refine the microstructure as a whole. The action of the grain refiner on the solidification structure in the Bridgman growth was discussed in the results section of this chapter. The small effect on the orientation of the eutectic seems not to affect the phase transition to any noticeable degree. However, evidence from both the DSC experiments and from the DC simulator experiment shows that it does have a pronounced effect on phase selection. It must be concluded, therefore, that the effect of the grain refiner is to adjust the nucleation temperatures of the intermetallic phases and not the growth temperatures.

5.5.4 An Alternative Explanation for The Re-occurrence of Al_3Fe at High Growth Rates.

The reoccurrence of Al_3Fe at high growth rates in all Bridgman samples except ETi was attributed to slow lateral growth resulting from the formation of a sump in the samples. An alternative suggestion for the observation may be found in the well known Jackson-Hunt relationship between growth rate and undercooling [63]. For a normal eutectic, the relationship $U / \Delta T^n = C$ (where $\Delta T = T_m - T_g$ and $n = 2$) is used. A linear relationship, therefore, exists between $\sqrt{U}$ and T_0. Adam and Hogan [35] obtained relationships for the $Al-Al_3Fe$ and $Al-Al_6Fe$ eutectics based on experimental measurements. They stated that, for the anomalous $Al-Al_3Fe$ eutectic, the value n in the above expression was not 2 but 2.6. A plot of $\sqrt{U}$ vs. T_g for this eutectic would not give a .linear relationship. Consider the situation could exist where a normal ($n = 2$) and an anomalous ($n > 2$) eutectic were in competition. Figure 5.16 shows, schematically, a plot of $\sqrt{U}$ vs. T_g for such a case where the value of the equilibrium melting temperature is lower for the normal eutectic than the anomalous eutectic as would necessarily be the case(Al_3Fe and Al_xFe have been used in the figure as the anomalous and normal eutectics respectively). At the lowest and highest growth rates, the $Al-Al_3Fe$ eutectic can grow at a higher temperature whereas at the intermediate growth rates the reverse is true.

This hypothesis would account for the re-occurrence of the equilibrium eutectic at the highest growth rates. It does not, however, explain the coexistence of two different intermetallic phases in the same sample. The explanation offered earlier in terms of non-steady state lateral growth does and is thus more likely to be the reason.

$$\bar{U}=\bar{U}_\perp+\bar{U}_\parallel$$
$$U_\perp = U\cos\theta$$
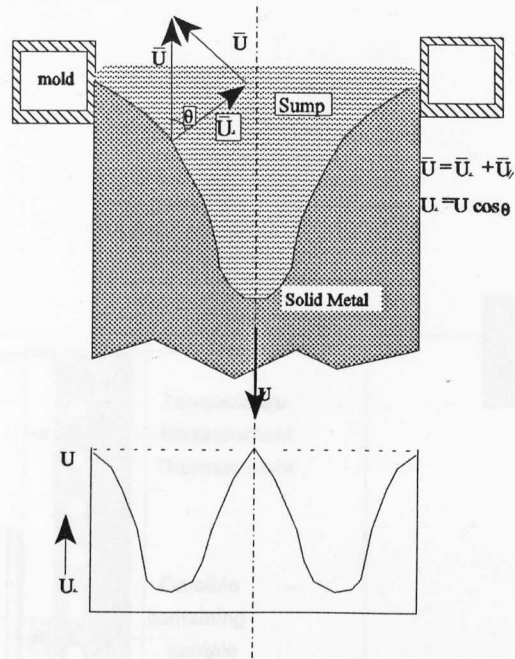
Figure 5.01 The effect of sump shape on local growth velocity in the DC cast ingot.
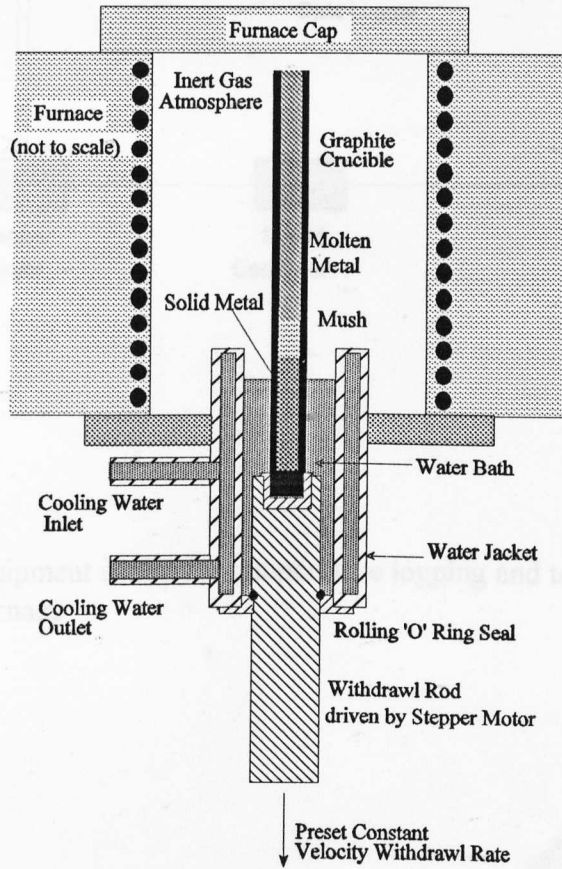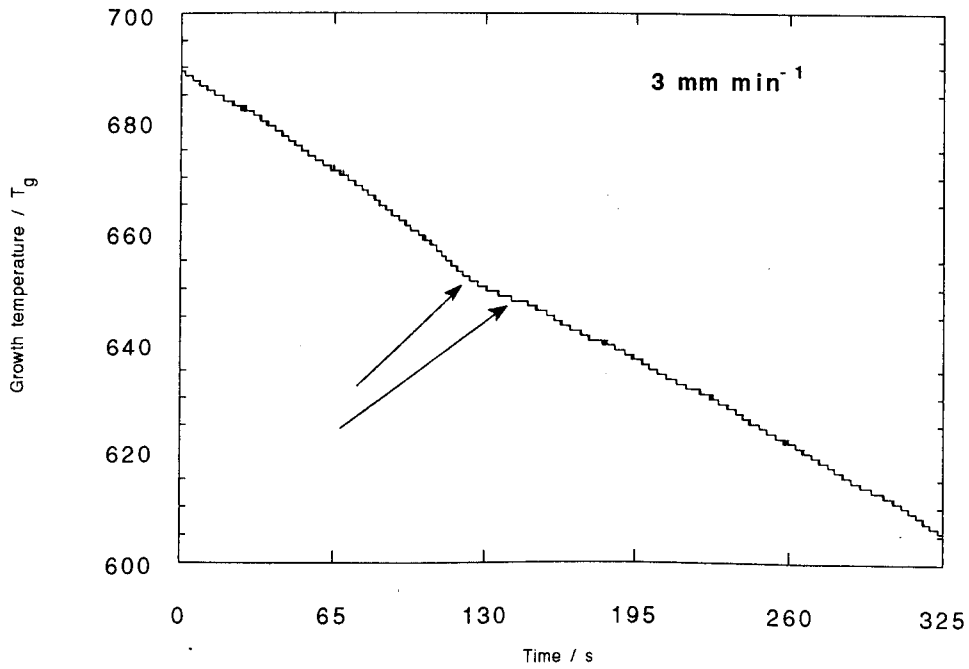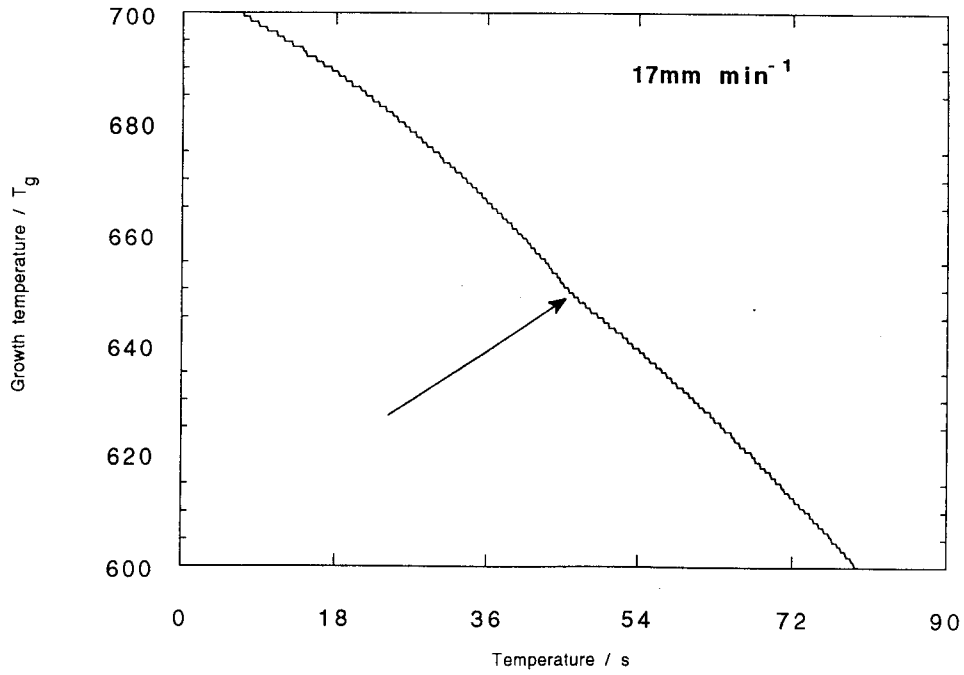

Figure 5.02 CrossSection of Bridgman Furnace.
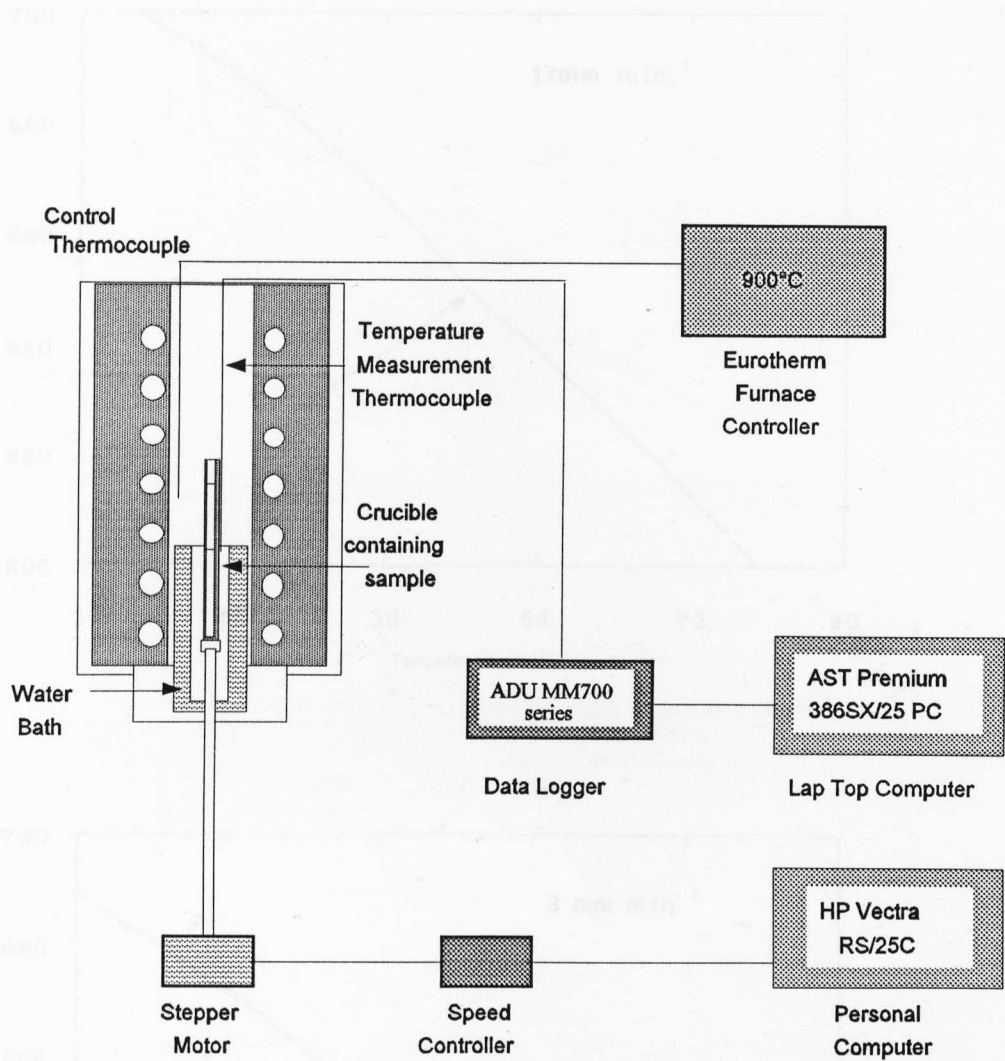
Figure 5.03. Equipment set up for temperature logging and temperature control in the Bridgman Furnace

Figure 5.04: Time / Temperature plots recorded at 3 mm min^{-1} and 17 mm min [-1]. The arrows mark points of inflection on the curves.
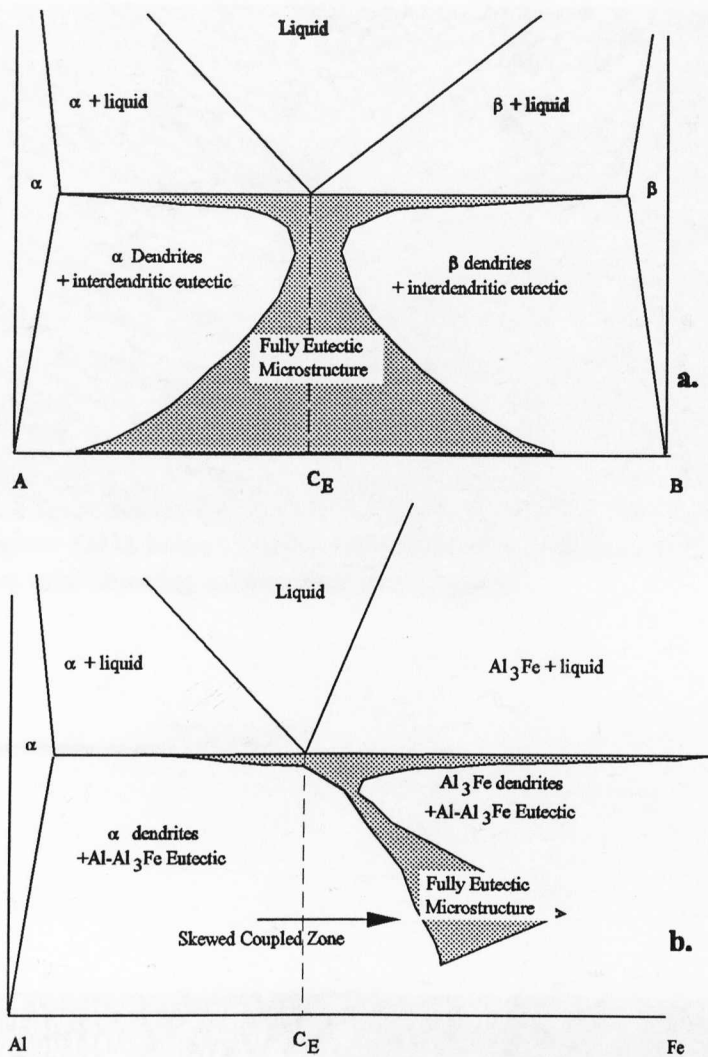
160

Figure 5.05. Different coupled zone shapes on binary eutectic phase diagrams. **a.** shows a symetrical coupled zone for a normal eutectic, **b.** shows a coupled zone skewed to the right due to the faceted growth mode of the intermetallic Al_3Fe.
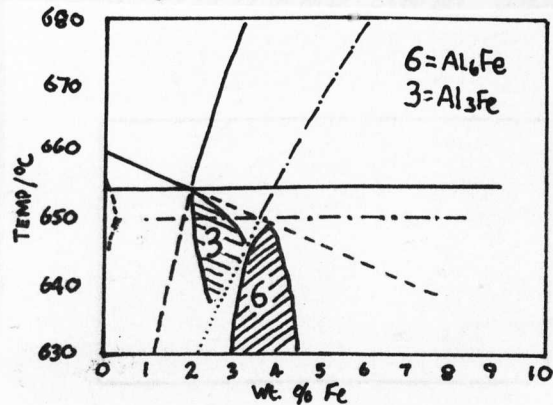
Figure 5.06 Representation of coupled zones for the Al-Al_3Fe and Al-Al_6Fe eutectics (After Adam and Hogan [35]).
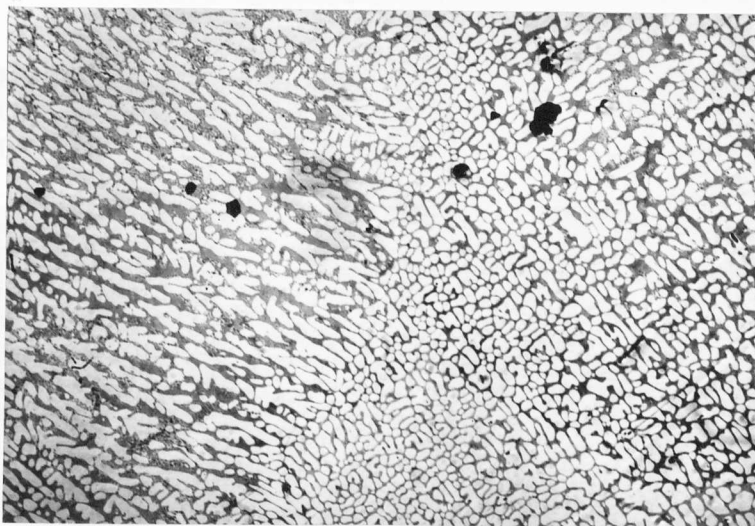
Figure 5.07a Longitudinal section of a sample grown at 20 mm min^{-1} showing evidence of lateral growth.

———————200 μm
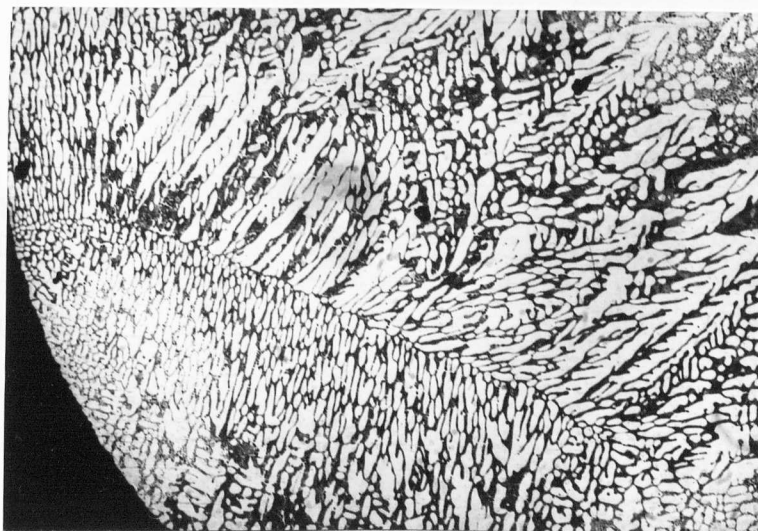
Figure 5.07b. Transverse section of a sample grown at 20 mm min^{-1} showing evidence of lateral growth.

R   = Imposed Growth Rate
U   = Local Growth Rate
U^C_X = Critical Growth Rate for AlxFe

Liquid   Liquid   Liquid

Solid   Solid   Solid

Low R   Medium R   High R

All Al₃Fe   All AlxFe   Mixed Al₃Fe an AlxFe

Figure 5.08 Schematic diagrams showing the effect of different growth velocities on the local solidification velocity profile of a Bridgman sample and the resulting phases. The diagrams show how it may be possible for Al_3Fe to grow in samples grown at relatively high velocity.
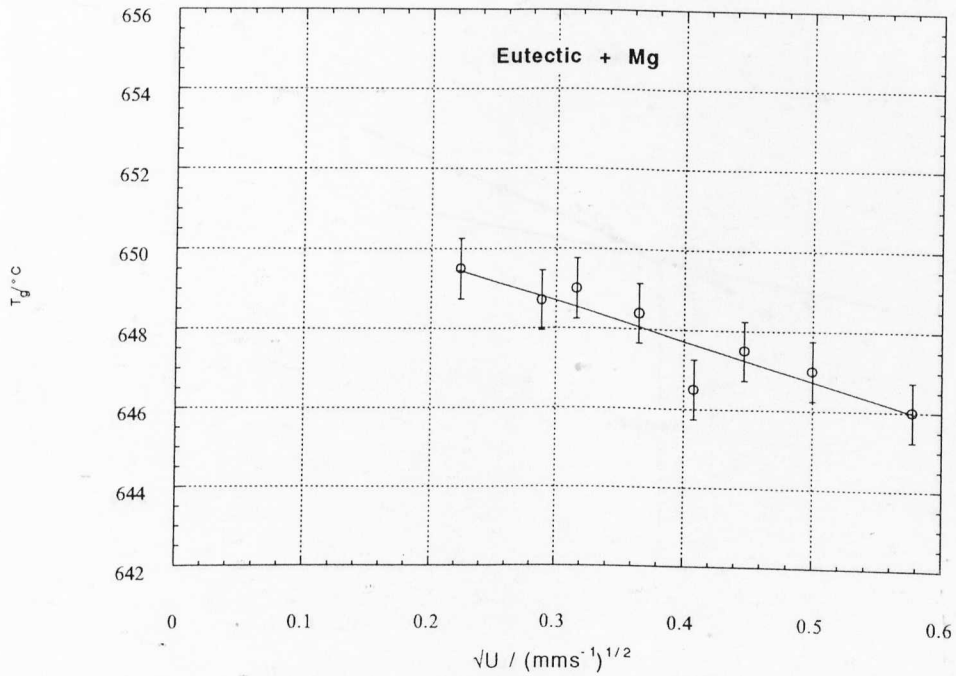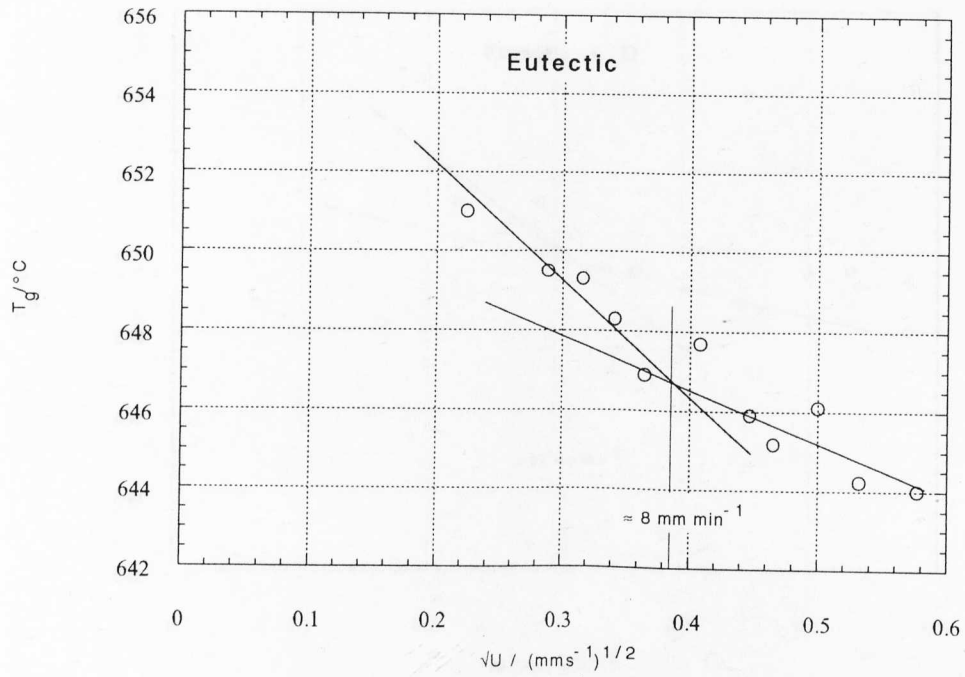
Figure 5.09: Plots of √U vs growth temperature T_g from Bridgman growth experiments.

Figure 5.09: Plots of √U vs growth temperature T$_g$ from Bridgman growth experiments.

Growth direction

i

ii

1 mm

iii

iv
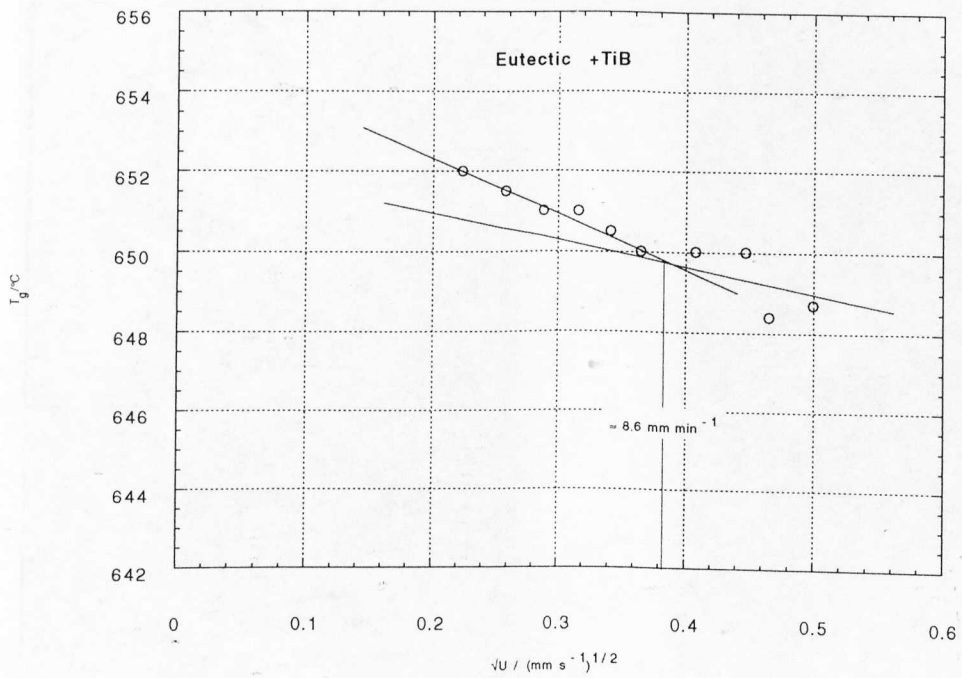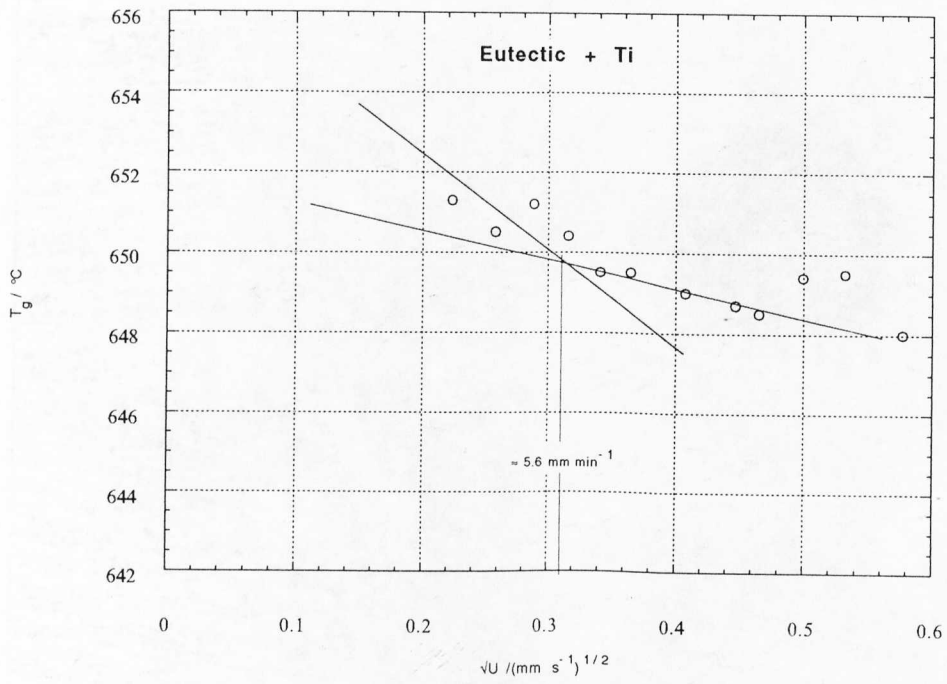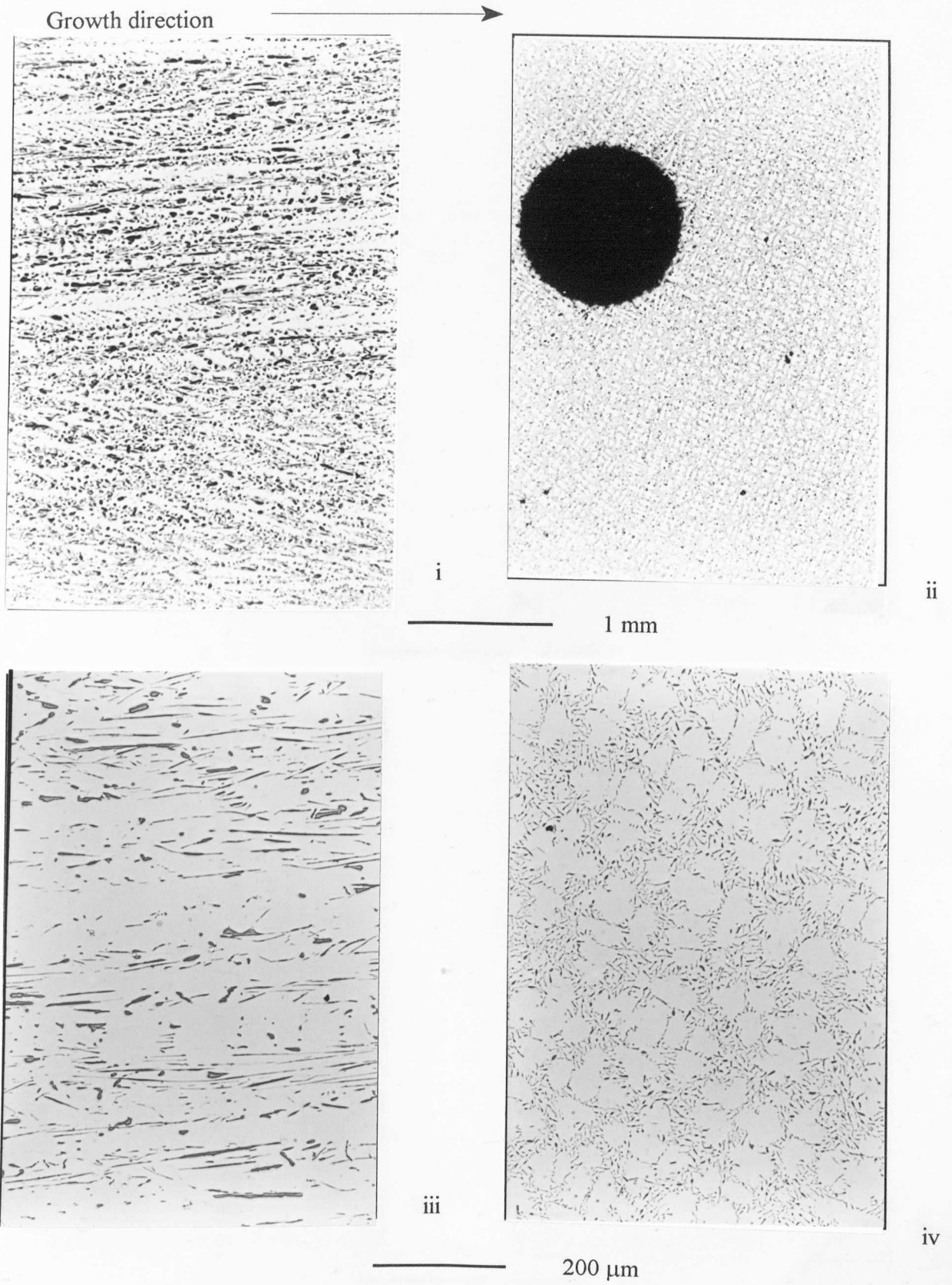
200 μm

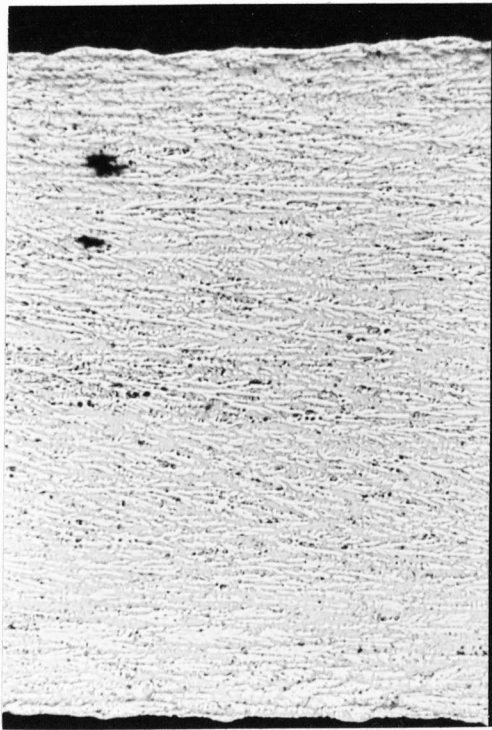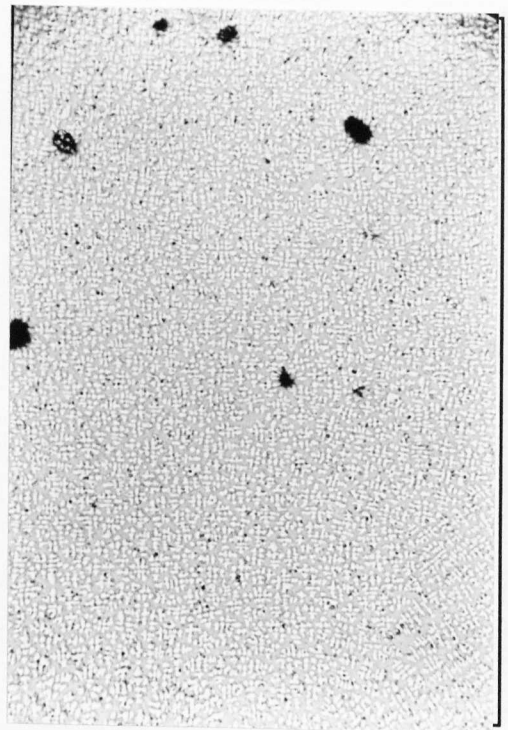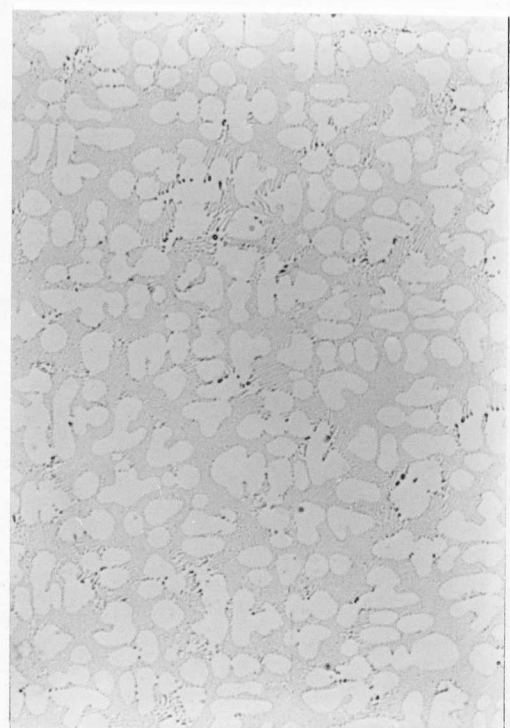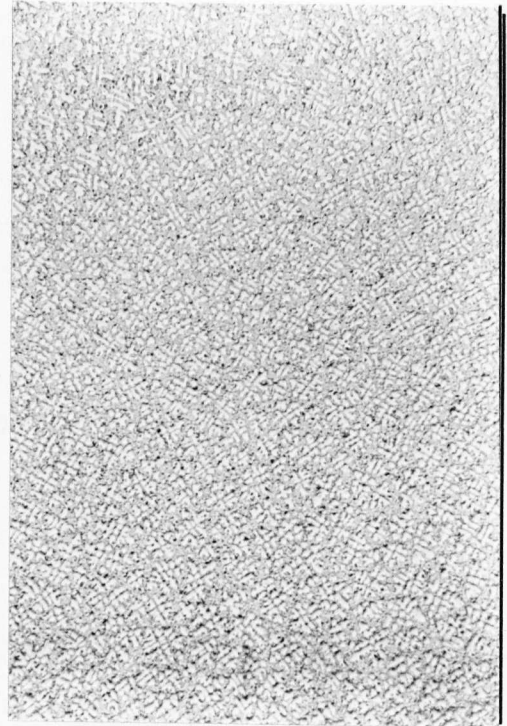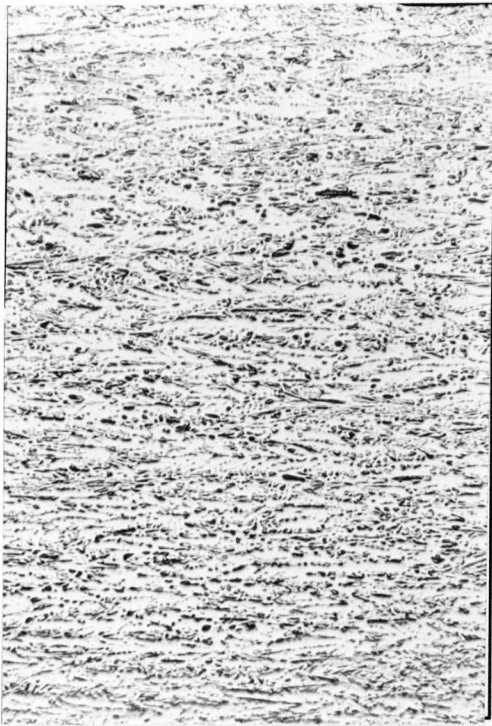**Figure 5.10 a**. Bridgman Growth Samples: Alloy E03

Growth direction

1 mm
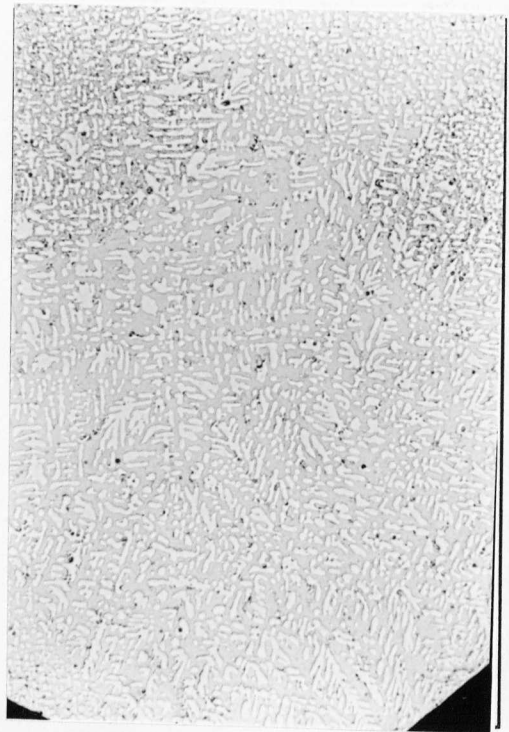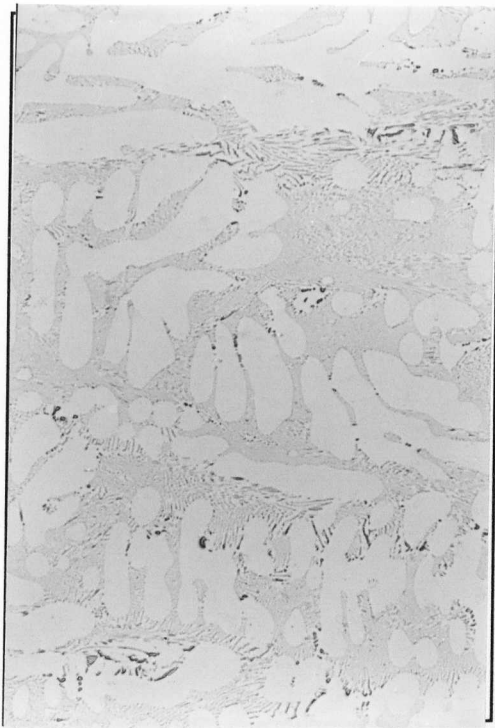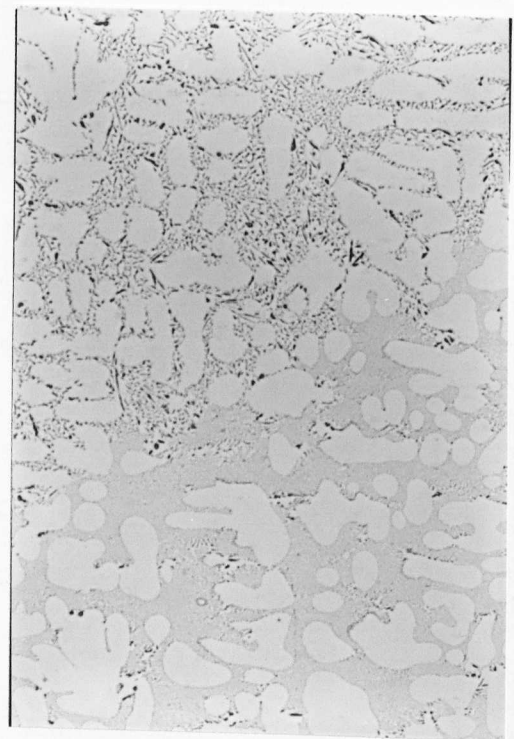
200 μm

Figure 5.10 b. Bridgman Growth Samples: Alloy E10

Growth direction →

i

1 mm

ii

ii
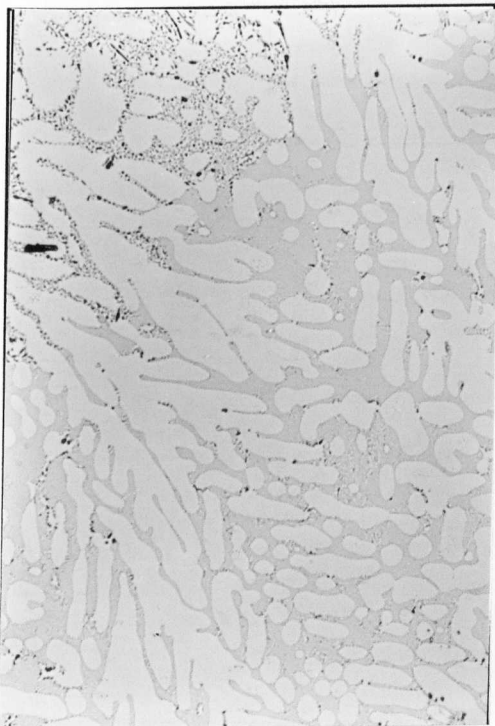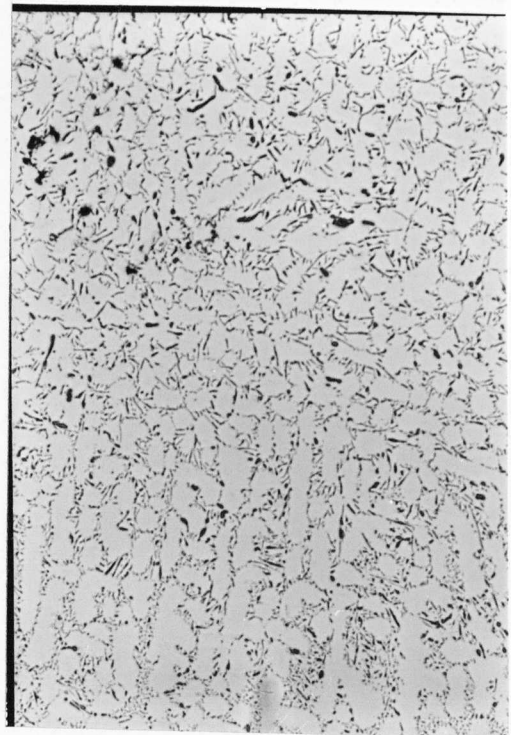
iv

200 μm

Figure 5.10 c. Bridgman Growth Samples: Alloy E20
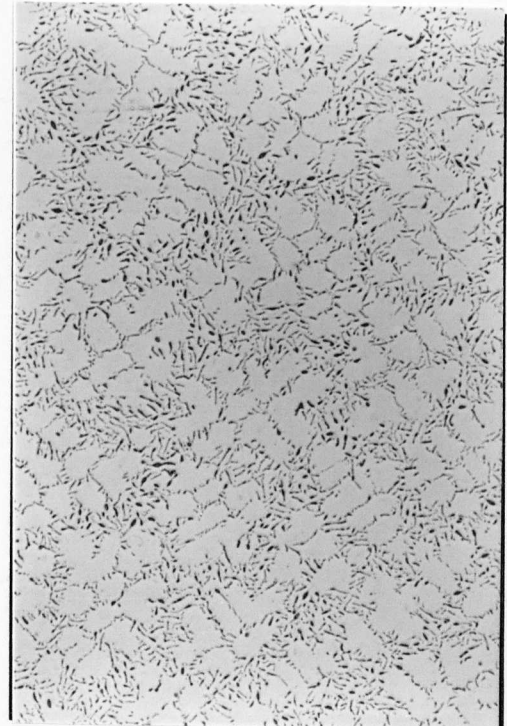
Growth direction

i

ii

1 mm

iii

iv
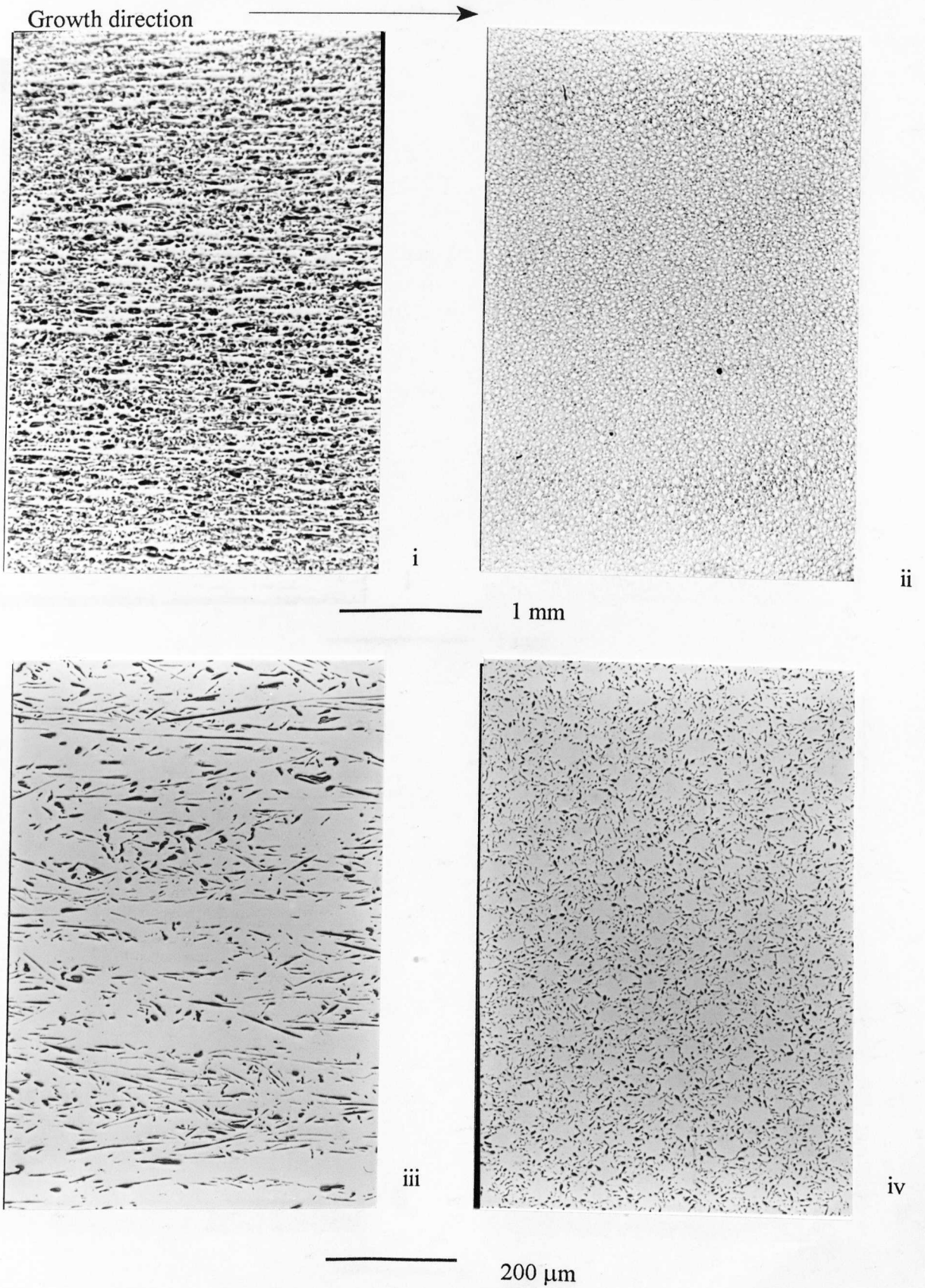
200 µm

Figure 5.10 d. Bridgman Growth Samples: Alloy EMg03

Growth direction →

i

ii

——————— 1 mm

iii

iv

——————— 200 μm

Figure 5.10 e. Bridgman Growth Samples: Alloy EMg10
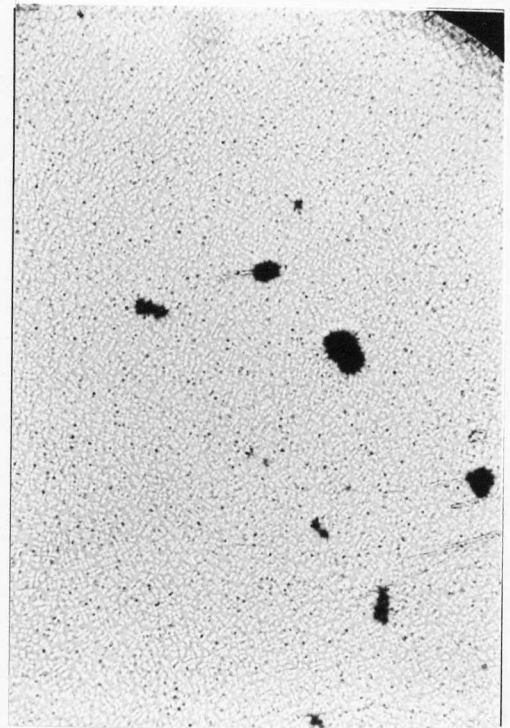
Growth direction →

i

ii

1 mm

iii

iv

200 μm

Figure 5.10 f. Bridgman Growth Samples: Alloy ETi03
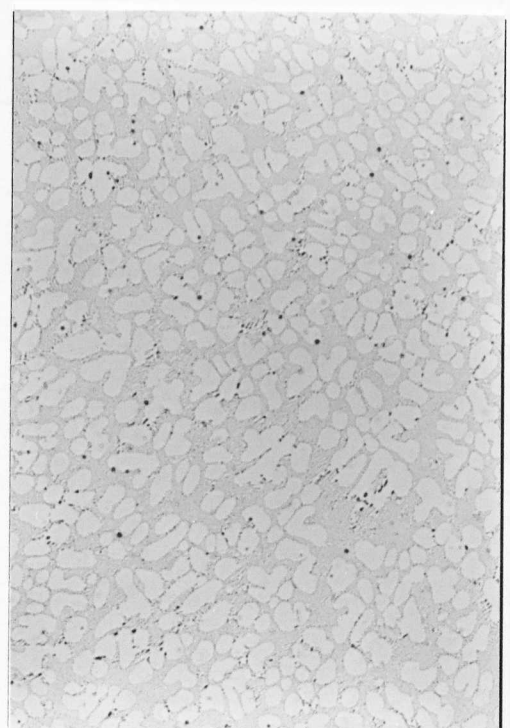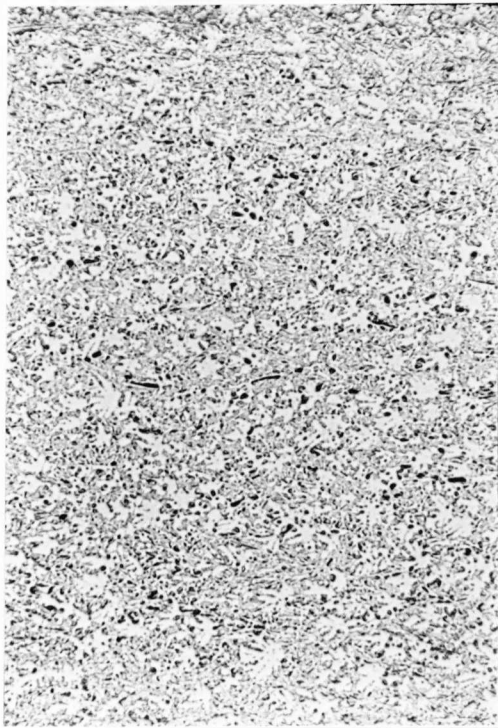
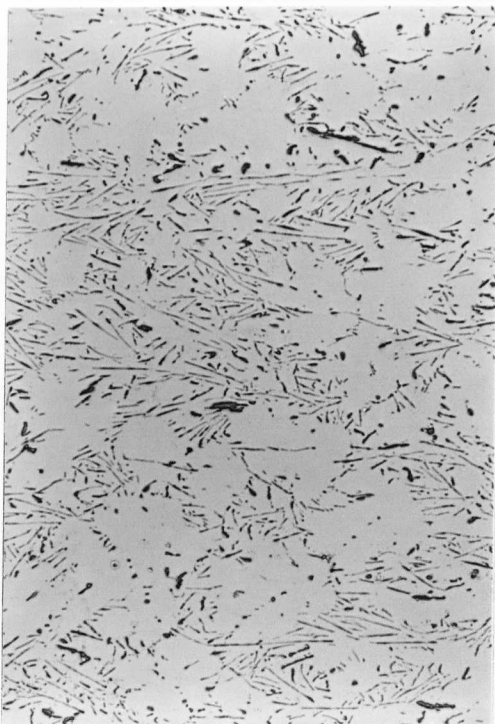Growth direction ⟶

i

ii

1 mm

iii

iv

200 μm

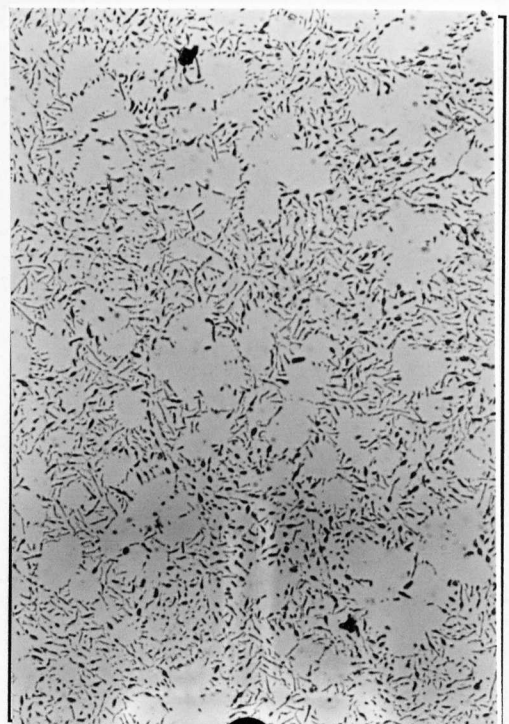**Figure 5.10 g**. Bridgman Growth Samples: Alloy ETi10

Growth direction ⟶

i

ii

1 mm

iii

iv

200 μm

Figure 5.10 h. Bridgman Growth Samples: Alloy ETiB03

Growth direction

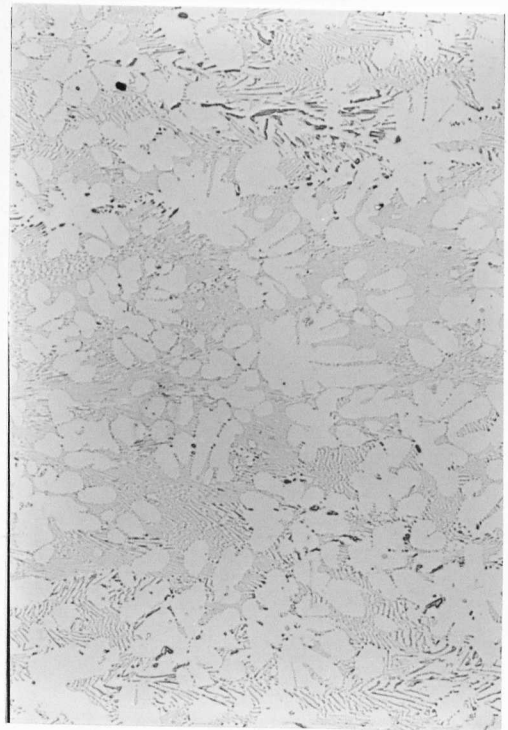

1 mm
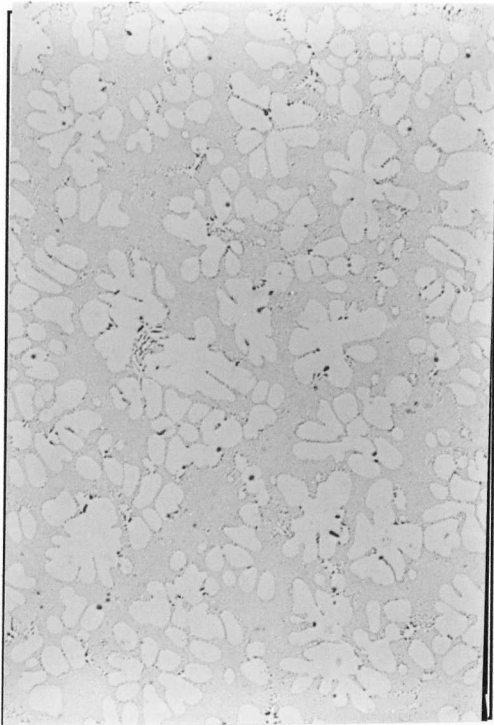
200 µm

Figure 5.10 i. Bridgman Growth Samples: Alloy ETiB10

Growth direction →
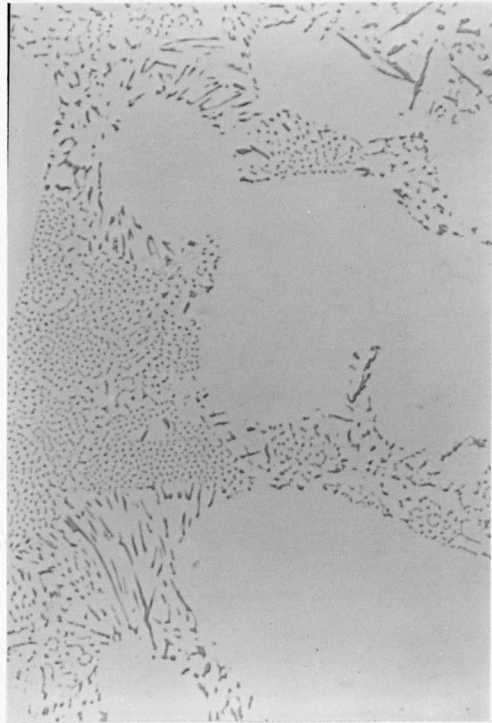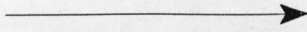
———— 100 µm

Figure 5.10 j. Bridgman Growth Sample: Alloy ETiB20, showing free dendrite surrounded a rod like phase.

Figure 5.11a Al$_x$Fe particles. The optical micrographs (figure 5.10) could not resolve the fine detail shown here. The apparent mixed morphology of samples identified as containing only Al$_x$Fe can be explained by these images. The dense black phase of different appearance to the majority of the intermetallics is probably very fine and closely spaced eutectic Al$_x$Fe.
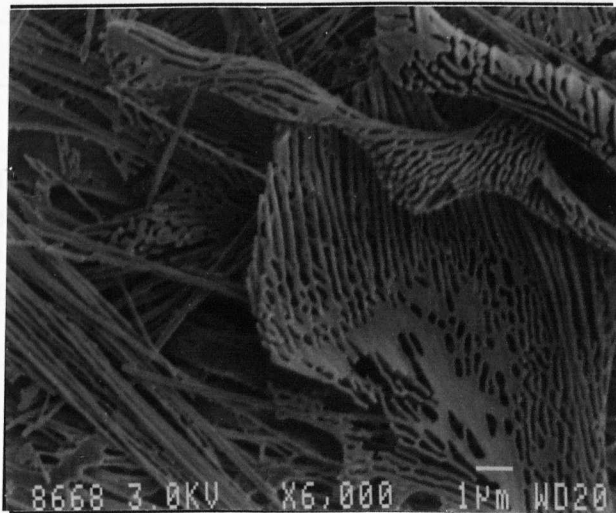
Figure 5.11b This image shows the morphology of Al$_x$Fe in more detail.

Low Growth Rate   Medium Growth Rate   High Growth Rate

U

Mg Raises
Transition
Velocity

$U^C_{X(Mg)}$

U^C_X

$U^C_{X(Ti)}$

Ti Lowers
Transition
Velocity
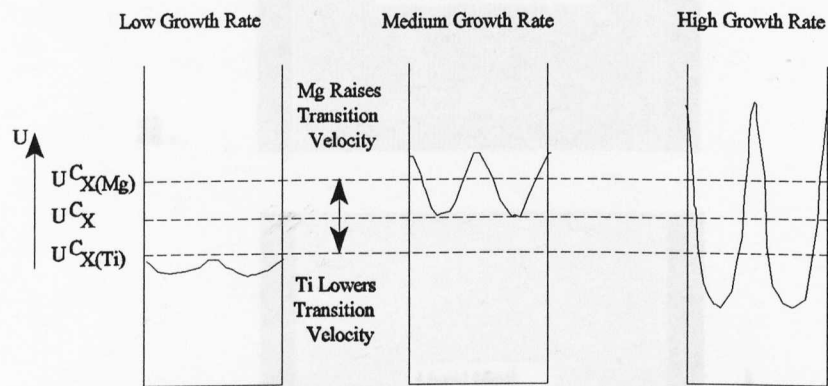
	Low Growth Rate	Medium Growth Rate	High Growth Rate
No additions	All Al$_3$Fe	All Al$_x$Fe	Mixed Al$_3$Fe and Al$_x$Fe
Mg addition	All Al$_3$Fe	Mixed Al$_3$Fe and Al$_x$Fe	More Al$_3$Fe
Ti addition	All Al$_3$Fe	All Al$_x$Fe	More Al$_x$Fe

Figure 5.12 Schematics of local solidification velocity (see fig 5.08) showing the effect of trace addition such as Ti and Mg which alter the critical velocity for phase transitions. The resulting phase mixtures are shown in the table. These correspond to the results of the phase identification by SIBUT extraction.
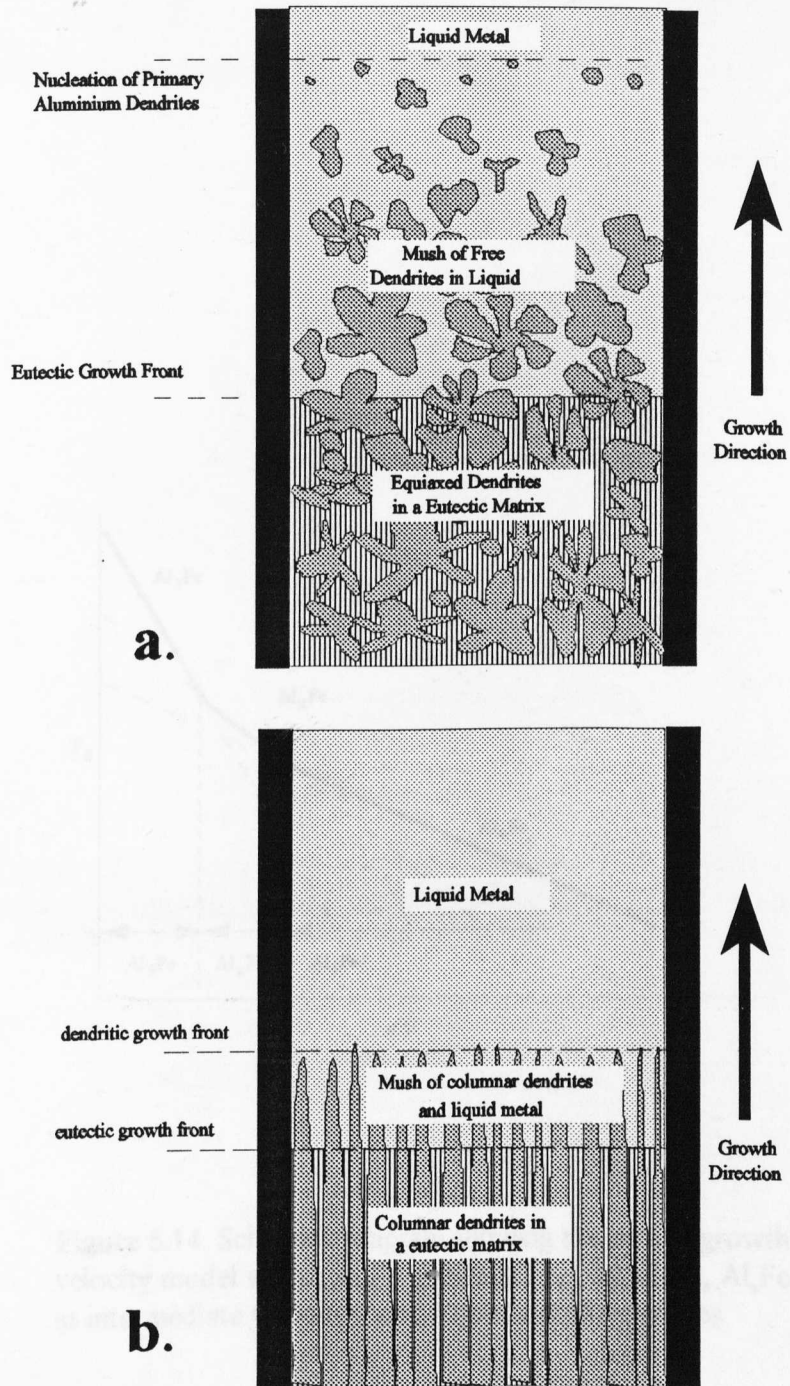
Figure 5.13. Schematic diagram showing the difference in growth mode between, **a.** grain refined Bridgman growth and, **b.** non-grain refined Bridgman growth.
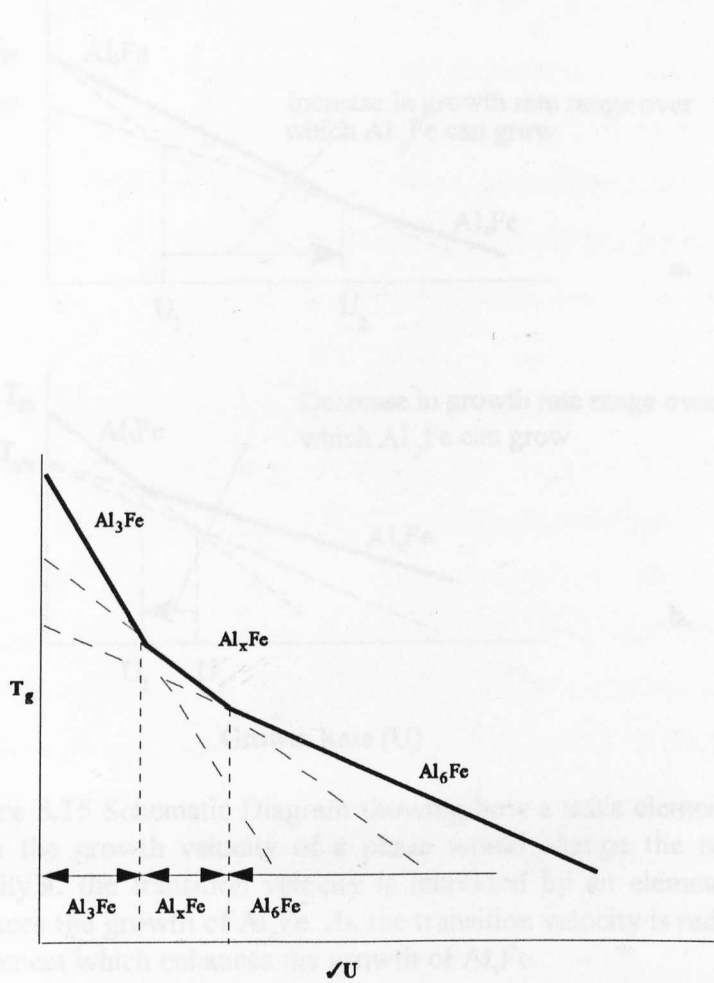
Figure 5.14. Schematic diagram showing the simple growth velocity model where Al$_3$Fe grows at low velocities, Al$_x$Fe at intermediate velocities and Al$_6$Fe at high velocities
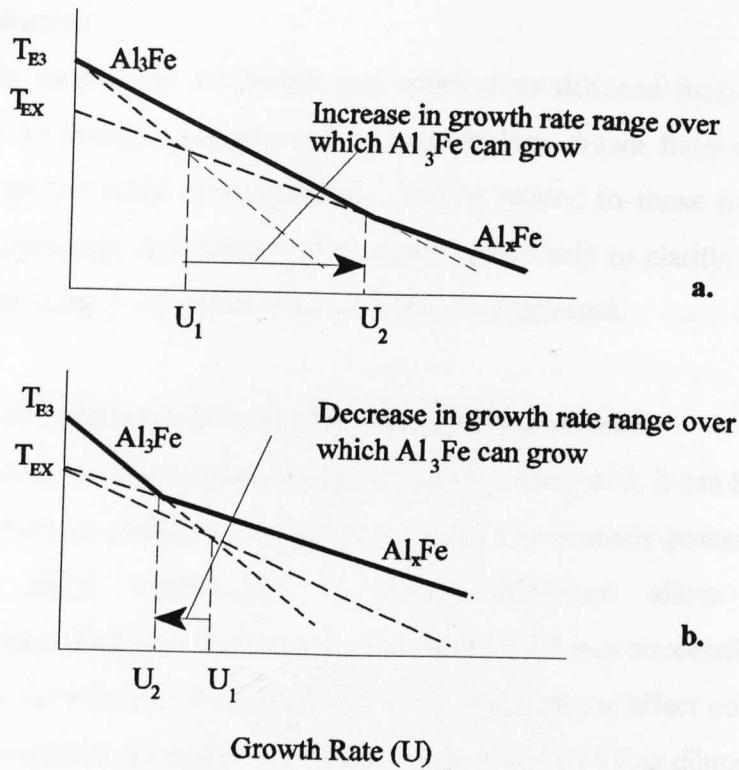
Figure 5.15 Schematic Diagram showing how a trace element which alters the growth velocity of a phase would change the transition velocity. **a.** the transition velocity is increased by an element which enhances the growth of Al_3Fe. **.b.** the transition velocity is reduced by an element which enhances the growth of Al_xFe.
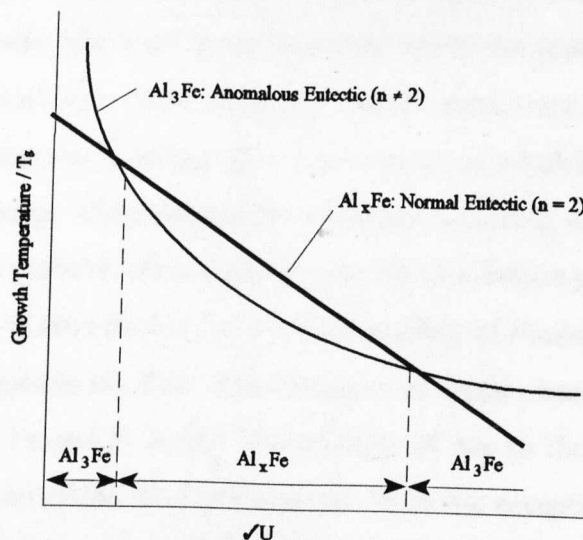
Figure 5.16 A schematic diagram which could explain the re-occurrence of Al_3Fe at high growth velocities. The straight line relationship is obeyed by normal eutectics, whereas anomalous eutectics would show the curved relationship. The growth regimes of two such competing eutectics are shown.

6.0   Conclusions and Further Work

6.1   Introduction

In this chapter the summaries and conclusions deduced from the experimental chapters will be brought together and the conclusions drawn from the DC simulator experiments on the effect of composition will be related to those from the DSC and Bridgman experiments. Any further work which would help to clarify, improve upon or complement the work done in this study will then be suggested.

6.2   General Conclusions from the DC Simulator Experiments

From the DC simulator experiments described in chapter 3, it can be concluded that the SIBUT extraction technique coupled with XRD is an extremely powerful technique for unambiguous phase identification in dilute aluminium alloys and that the macroetching/anodising technique used to reveal the FTZ was successful. It can also be concluded that the addition of trace elements can have a strong effect on the intermetallic phase selection and the formation and characteristics of the FTZ in dilute Al-Fe-Si alloys. The magnitude of the effect depends on the nature of the addition and the base alloy composition. The appearance of the FTZ is not restricted to the transition between two particular intermetallic phases: a FTZ resulted from the cubic α/Al$_3$Fe, cubic α/Al$_6$Fe, Al$_6$Fe/Al$_3$Fe and Al$_m$Fe/Al$_6$Fe transitions, the latter being by far the most pronounced. The transition in intermetallic type is not always accompanied by the appearance of a FTZ (cubic α to Al$_3$Fe, and, sometimes, Al$_3$Fe to Al$_6$Fe): in fact, some trace additions (e.g. Ti, Mn) cause the FTZ to disappear even though a phase transition which in other alloys produces a visible FTZ still exists. When two phases are found coexisting in the same region of the ingot the sample was probably taken from an area where a diffuse phase boundary existed. An increase in the Fe:Si ratio from 2:1 to 4:1 has the effect of eliminating the cubic α phase in favour of Al$_6$Fe outside the FTZ. The formation of certain intermetallic phases can be inhibited by certain Fe and Si levels. The addition of Mg to the base alloys tended to promote the formation of the Al-Al$_3$Fe eutectic. With the exception of alloys with TiB$_2$ additions, alloys based on Al-0.2 wt. % Fe-0.1 wt. % Si contained no Al$_6$Fe and alloys based on Al-0.4 wt. % Fe-0.1 wt. % Si contained no cubic α. TiB$_2$ promotes the formation of cubic α and eliminates a visible FTZ in the alloys with a Fe:Si ratio of 2:1. In the alloy with an Fe:Si ratio of 4:1, however, TiB$_2$ promotes the formation of Al$_m$Fe and leads to the most visible FTZ.

6.2 The use of DSC and Bridgman experiments in Explaining the Effects Seen in the DC Simulator

The addition of Mg to the ternary alloys cast in the DC simulator hindered the formation of cubic α and may have favoured the formation of Al_3Fe (along with V, Ti and Mn) in alloys with a FE:Si ratio of 2:1. In the binary alloys there was also evidence that the addition of Mg promoted the formation of Al_3Fe in the alloy with the lower Fe content. It would appear that the addition of Mg favours the equilibrium phase especially in the presence of Si and lower concentrations of Fe. The same effect was seen in the DSC experiments at both Fe concentrations used where it was concluded that Mg increases the range of cooling rates over which Al_3Fe can form by hindering the nucleation of the metastable phase (which was not identified). Again, in the Bridgman experiments the addition of Mg, it was concluded, had the effect of promoting the growth of the equilibrium phase, but this time over Al_xFe. The way in which it did so was unclear. The effects seen in the DC simulator experiments, therefore, can be seen as a combined effect of Mg on the growth and nucleation aspects of intermetallic phase selection.

The effect of the addition of Ti to the alloys cast in the DC simulator was not as straightforward. Its addition was found to promote Al_3Fe and to some extent Al_6Fe in alloys with an Fe:Si ratio of 2:1. There was little effect on the alloy with the higher Fe:Si ratio of 4:1 perhaps because the higher levels of Fe and Si obscured any effect. Again, in the binary alloys the effect was small in terms of phase selection. The major effect seen by the addition was to eliminate a visible FTZ in all but one alloy. This must be seen as an effect on the oxide film. This effect has been reported to be due to the Ti in solid solution in the primary Al and not to any effect it has on the intermetallic [62]. In the DSC experiments, the effect of the addition of Ti was similar to that of Mg in that it promoted the formation of Al_3Fe at higher cooling rates than in the base alloys. The binary alloys of the same composition cast in the DC simulator did not show this effect at similar cooling rates. In the Bridgman experiments, the effect was to lower the transition temperature of the $Al-Al_3Fe-$ $Al-Al_xFe$ transition. It is difficult to relate this effect to the DC simulator experiments as no Al_xFe was detected in the alloys cast with this addition.

The addition of Ti-B grain refiner was found to have a much larger effect that the addition of Ti reflecting the effect on nucleation of TiB_2 particles. In the ternary alloys cast in the DC simulator, the effect was to promote cubic α at all cooling rates in the alloys with a Fe:Si ratio of 2:1 and Al_mFe at high cooling rates in the alloy with a Fe:Si of 4:1. It was

concluded that this effect was due to the lower symmetry of the TiB_2 favouring the nucleation of other phases with low symmetry. In the binary alloys where no cubic α was possible, Al_xFe was and Al_mFe were found in the alloys with the lower and the higher Fe content, respectively, at high cooling rates. A mixture of Al_6Fe and Al_3Fe was found in regions of lower cooling rate where in the base alloy only Al_6Fe was found. This suggests that in these alloys Ti-B additions allow Al_3Fe to co-exist with Al_6Fe at lower cooling rates than it would in the absence of grain refiner. At similar cooling rates, in the DSC experiments it was found that Ti-B promoted the nucleation of an unidentified phase (possibly Al_6Fe) although Al_3Fe was found to co-exist in the same samples. It may be the case, that in the absence of Si the effect of Ti-B refiner in these alloys is to make it possible for different phases nucleate at the same cooling rate. This would be possible if there were a limited number of particles available to act as nucleants as indeed would be expected in these alloys where most of the TiB_2 is used as a nucleant by the primary aluminium. The remaining few could influence nucleation of metastable phases at some sites but not at others. The effect of the addition of Ti-B refiner on the Bridgman samples was found to be minimal. The solidification structure was affected but, it seems that this did not affect the growth characteristics of the eutectic. The conclusion can be drawn, therefore, that the effect of Ti-B grain refiner additions on phase selection in the alloys cast in the DC simulator was due to altered nucleation behaviour and not to any effect it had on the growth behaviour.

6.3 Further Work

In order to complement and improve upon the experiments already conducted in this study, the following suggestions are made.

1   More experiments using the DC simulator on the same alloys would prove the reproducibility of the results obtained. The range of Fe and Si levels used could also be extended in order to more clearly identify trends. The DC simulator was used in this work to get a rough idea of the effects variables employed. To that effect it was succesful, but to prove the reproducibility, it would be wise to standardise the experimetal procedure more rigidly. It is evident from the variation in the size of the shell zones that the experimental technique was subject to variation. This could be alleiviated by automating the process.It would also be advantageous to measure growth velocity in the equipment by the simple use of thermocouples placed at known heights throughout the sample. This would provide a

comparison with the Bridgman experiments.

2   The positive identification of phases extracted from DSC samples would have been extremely useful. In retrospect it would have been better to use TEM diffraction pattern analysis to provide identification. The use of the EDX analysis of Fe concentration as a quick tool for phase identification failed.

3   From the DSC experiments described in chapter 4, it can be concluded that the nucleation of intermetallic phases in dilute Al-Fe alloys is complex. The simple model relating the nucleation temperature to the cooling rate has been shown to be valid for the limited data obtained in this work. It was possible to identify phase transitions using the model with greater ease than without. There is the possibility that with more data the value of the gradient obtained from plots of $\ln (\Phi)$ vs $1/(T_n (\Delta T)^2)$ could be used to characterise the phase which is nucleating. The positive identification of particles extracted from DSC samples would prove the validity of this technique.

4.   The results of growth temperature measurement from Bridgman experiments in this work were somewhat unreliable due to the wrong choice of alloy. The growth temperatures would have been easier to confirm by quenching the sample after the growth front had passed a thermocouple inserted into the side and examining the microstructure as described at the beginning of chapter 5 or by using 3 wt % Fe alloys which have been successfully used in similar experiments by other workers [49]. It would be interesting to examine the effect of varying the speed of withdrawal during a single experiment in the Bridgman furnace using an alloy with a truly eutectic growth front. The way in which one eutectic replaces another and the solidification velocity at which the transition occurs would be evident from the microstructure. This provides evidence of how nucleation and growth interact in phase selection. A range of alloy copositions could be used, from low Fe, off eutectic to higher Fe fully eutectic alloys in order to gauge the effect of composition and the shape of the solidification front on phase selection.

5   Although the use of peak deconvolution in the determination of nucleation onset temperatures was successful, which was evident from the closeness of the fitting to the experimental data, it would be advantageous to use more sensitive equipment to measure solidification. Alternatively, this could possibly be achieved by using smaller samples which would enable the peaks to be resolved at higher cooling rates. The disavantage of this technique would be to risk reducing the height of the eutectic peak to such an extent that it was impossible to see.

7.0 References.

1. Registration Record of Int. Alloy Designation and Chem. Comp. limits for Wrought Aluminium and Wrought Aluminium Alloys.The Aluminium Assoc., Washington D.C. (1991).

2. T. Otani, T. Kato, K.Arai, R. Osaka in *Proc. Light Metals Conf.* , Chicago, (1981) pp 855-870.

3. S. Brusethau .g, D. Porter and O. Vorren in Int. *Light Metal Cong. Proc.*, Vienna, Austria, 22-26 Jun. '87, pp. 472-476.

4. S. Asami T. Tanaka and A. Hideno; *Furakawa Rev* 1 .70-74.

5. H. Westengen; *Aluminium*,58 (1982) . 398-401.

6. P.Skerpje; *Met.Trans. A* 18A (1987) 189-200.

7. H. Westengen; *Z. Metallkde* 73 (1982) 360-368.

8. R.M.K. Young and T.W. Clyne; *Scripta Met.* 15 (1981) .1211-1216.

9. I Miki, H. Kosuge. and K Nagahama; *J Jap. Inst. L.Met.* 32 (1975) 1-9.

10. T.J. Brobak, S. Brusethaug in *Int. Light Metal Cong. Proc.*, Vienna, Austria,22-26 Jun. '87 pp. 477-480.

11. Ping Liu, T. Thorvaldson and G.L. Dunlop; *Mat. Sci. and Tech.* 2 (1986) 1009-1018.

12 T. Otani, T. Kato, K.Arai, R. Otsuka in *Proc. Light Metals Conf.* , Chicago, 1981.pp 855-870.

13 H. Kosuge, *Keininzoku;* 30 (1980) . 27-226.

14 H. Tezuka and A Kamino in , *Proc. 3rd Int Conf On Aluminium Alloys.* 1 (1992) pp. 117-122.

15 Y. Langsrud, *Key Eng. Mats,* 44 & 45 (1990) . 95-116.

16. P.J. Black; *Acta Cryst* ., 8 (1955) 43.

17 P.J. Black , *Acta Cryst* ., 8 (1955) 175.

18 R.C.Hudd and W.H. Taylor; *Acta Cryst,.* 15 (1965) 441.

19 P.Villarsh and L.D.Calvert, in Pearsons Handbook of Intermetallic Phases, Amer. Soc. Metals, 1985.

20 D.Munson; *J.Inst .Met.,*95 (1967) 217.

21 I.Miki, H.Kosuge & K.Nagahama; *J.Jap.Inst.Light Metals,* 25 (1975) 1-9.

22 D.A. Porter and H. Westengen , in Quantative Micro Analysis with High Spatial Resolution, The Metals Soc.,1982 94.

23 P.Skerpe, J.Gjonnes and Y.Langsrud; *Ultramicroscopy,* 22 (1987) p. 239.

24 P.Skerpe, Acta Cryst , 44b (1988) p.486.

25 M. Chandrasekeran, Y.P.Lin , R.Vincent and G.Staniek; *Scripta Met.* 22 (1988) 797.

26 E.H. Dix; *Proc. ASTM* 25 (1925) p.120.

27 A.D.I.Nichol; *Acta Cryst.*, 6 (1953) .285.

28 P.J.Black, O.S. Edwards and J.B. Forsyth; *Acta Cryst.*, 14 (1961) .993.

29 E.H. Hollingworth, G.R.Frank and R.E. Willet; *Trans. Met. Soc. AIME,* 224 (1962) 188.

30 A.M.B. Douglas; *Acta Crys.*, 3 (1950) p.19.

31 C.J. Simensen and R. Vellasamy; *Z. Metallkde.,*68 (1977) .428.

32 L.F. Mondolfo ,*Aluminium Alloys: Structure and Properties,* Butterworths, London, 1976.

-33 J. Murray; *Mat. Res. Soc. Symp* 19 (1983) pp.257-258.

34 Ping Liu and G.L. Dunlop;, *Acta Metal.* 36 (1988) .1481-1489.

35   C. McL. Adam and L.M. Hogan; *J. Austral. Inst. Met* . 17 (1972) .81-90.

36   L. Bäckerud; *Jernkontorets Annaler,*152 (1968) .109.

37   H. Kosuge and Mizukami; *Kiekinzoku,* 22 (1972) .437-434.

38   K.Robinson and P.J. Black; *Phil. Mag.,* 44 (1953).1392.

39   M.Cooper and K. Robinson; *Acta Cryst.,*20 (1966) .614-617.

40   M.Cooper; *Acta Cryst.,*23 (1967) .1106-1107.

41   A.L. Dons; *Z. Meatllkde.* 73 (1982) .360.

42   G.Phragmen; *J.Inst Met.,* 77 (1958) 498.

43   V.G. Rivlin and G.V. Raynor; *Int. Met. Rev.,* 3 (1981) .1211.

44   C.Y. Sun et al;, *J.Inst Met* 95 (1967) .384.

45   L.Bendersky, M.J.Kaufman, W.J.Boettinger and F.S. Biancaniello; *Mat. Sci. Eng.* 98 (1988) 213.

46   H. Kosuge. and I.Mizukami; *J Jap. Inst. L.Met.* 25 (1975) .48-58.

47   W.A. Tiller, "Recent Research on Cast Iron",Gordon and Breach, New York 1968.

48   I.R. Hughes and H. Jones; *J. Mat. Sci.* 11 (1976) 1781-1793.

49   D.Liang and H. Jones; *Z.Metallkd.*83 (1992) 224- 226.

50   C.J. Simensen, A.I. Spjelkavik; *Fresnius Z. Anal. Chem.* 300 (1980) 177-182

51   C.J. Simensen, P. Fartum, A. Anderson; *Fresnius Z. Anal. Chem.*319 (1984) 286-292

52   P.V. Evans ,Private communication, 1994.

53   B.Ellard, Private communication ,1993.

54   Internal Report, Alcan International Ltd, Banbury, 1995.

55   A. Griger, V. Stefaiay, E. Kovacs-Csetenyi, T. Turmezey; *Key Eng. Mats.*44 and 45 (1990) 17-30.

56   Y.Langsrud; *Key Eng. Mats.,* 44 and 45 (1990) 95-116.

57   W.Kur z, R. Trivedi; *Acta Met. et Mater.* 38 (1990) 1-17.

58   R.F. Cochrane, P.V. Evans, A.L. Greer; *Mater. Sci. and Engg.* A133 (1991) 803 - 806

59   C. Wagner, J. Vazquez, P. Villares, R. Jimenez-Garay; *Materials Letters* 18 (1994) 280-285

60   W.Kur z and D.J. Fisher; Fundamentals of Solification, Trans Tech Publications ltd, 1989, Aedermannsdorf Switzerland

61   I.J. Polmear;*Light Alloys,* Edward Arnold London1989

62   G.J. Marshall, J.A. Ward; *Mat. Sci and Tech,* 11 (1995) 1015-1023

63   K. Jackson, J.D. Hunt; Trans.Met. Soc. AIME, 236 (1966) 1129-1142